UNIVERSITY OF BIRMINGHAM

LARVAL ZEBRAFISH ELECTROCARDIOGRAPHY ELECTRODYNMAIC MODELLING AND SENSOR DESIGN

by

JAMES EDWARD CROWCOMBE

A thesis submitted to
The University of Birmingham
for the degree of
DOCTOR OF PHILOSOPHY

School of Engineering
College of Engineering and Physical Sciences
The University of Birmingham
September 2016

Abstract

This thesis presents the first model of the electrical activity of the larval zebrafish heart as well as the design and fabrication of novel electrode arrays that were created to measure the electrocardiogram. The model consists of realistic 3D geometry of a 3 day's post fertilisation zebrafish heart and body with a bidomain electrical model that uses the Fitzhugh-Nagumo equations as the ionic model. The model is able to replicate experimentally observed conduction velocities and action potentials by using region specific parameters and simulate electrocardiograms that are comparable to measurements. The electrode arrays are constructed from flexible polyimide films with gold microelectrodes. These devices have the potential to improve the measurement of the electrocardiogram for drug screening applications as an alternative to the use of micropipette electrodes. Gold plating and PEDOT:PSS coating techniques were applied to the devices to successfully reduce electrode impedance with the effectiveness of each technique categorised using impedance spectroscopy. The devices were tested *in vivo* with larval zebrafish with limited success and so *in vitro* tests were conducted using an artificial current source.

Acknowledgements

Firstly, I would like to thank my supervisor Dr. Edward Tarte for allowing to me the opportunity to explore a number of interesting topics and for all of the guidance and assistance throughout this project.

Thank you also to Dr. Richard Barrett for providing advice and tutelage of microfabrication techniques and for providing samples used in this work. I'd also like to thank my fellow PhD students James Churm for assistance with the design and fabrication. Thanks also to Rhiannon Hurst who provided material on the zebrafish as well as well as looking after the zebrafish and providing assistance with measurement experiments.

I am also grateful to Professor Atilla Sik who offered advice and guidance and allowed me to test the microfabricated devices in his lab. Thanks also to Dr. Sundeep Dhillon who provided results and performed measurements as well as providing material to improve the model.

Finally, I would like to thank my family for their continued support throughout this process.

Contents

Glossary of terms

Miscellaneous Terms

Symbol/Abbreviation	Description
C	Capacitance
∇	Spatial Derivative
e	Charge of an electron, $e = 1.6 \times 10^{-19}$ C
T	Temperature
k_b	Boltzmann constant, $k_b = 1.38 \times 10^{-23}$ $m^2kgs^{-2}K^{-1}$
N_A	Avogadro's Number, $N_A = 6.02 \times 10^{23}$ mol^{-1}
F	Faraday's constant, $F = 9.64 \times 10^4$ $Cmol^{-1}$
R	The universal gas constant, R = 8.31 $JK^{-1}mol^{-1}$

Biological and Electrophysiological Terms

Symbol/Abbreviation	Description
V_i/φ_i	Intracellular electric potential
V_e/φ_e	Extracellular electric potential
V_m	Transmembrane potential, the potential difference between the inside and outside of the cell membrane ($V_i - V_e$)
P_κ	Permeability of κ ion, m^2
z_κ	Valence of κ ion
u_κ	Mobility of κ ion ($m^2V^{-1}s^{-1}$)
D_κ	Fick's Constant for κ ion (m^2s^{-1})
c_κ	Concentration of κ ions (mol/l)
$\vec{j}_{\kappa e}$	Flux of κ ions that pass through a unit area of membrane per unit time (mole/m^2s)
L_D	Debye Length of electrode interface, m
σ	Conductivity of a solution, (S/m)
σ_i	Intracellular conductivity, (S/m)
Σ_e	Extracellular conductivity, (S/m)
R_t	Charge transfer resistance of electrode interface, Ω
OHP	Outer Helmholtz plane
$\varepsilon_0, \varepsilon_r$	Permittivity of free space (8.85 x 10^{-12} F/m)/Relative permittivity of a dielectric respectively
in vivo/in situ/in vitro	Whole biological systems/in situation where phenomenon occurs/cell cultures

FHN	Fitzhugh-Nagumo equations, phenomenological heart/nerve model
Bidomain	Continuum model of heart tissue incorporating interconnecting intracellular and extracellular domains
Excitable cell	Cells that elicit a response in response to stimulus
AP	Action potential, excitable cell response to stimulus above threshold
APD	Action potential duration, time duration of an action potential
Depolarisation	Increase in membrane potential, upstroke of an action potential
Repolarisation	Decrease in membrane potential, downstroke of an action potential
Larval zebrafish	Referred to as 0-5 days post fertilisation
dpf	Days post fertilisation
hpf	Hours post fertilisation
HTS	High Throughput Screening, A key/important step in drug effect determination

Technological Terms

Symbol/Abbreviation	Description
MEA	Multi-electrode array
ECG	Electrocardiography, Electrocardiogram. Measurement of the hearts electrical activity on the body surface
Photolithography	Use of light to pattern objects
Handle/carrier wafer/wafer	Pre-treated with 250 nm oxidised surface layer (100) silicon wafer
Durimide 7020, 7505	Varieties of PSPI used during fabrication for different thicknesses
PSPI (Durimide)	Photosensitive polyimide, used for substrate layer and insulation layer of devices
MF-26A	Chemical ancillaries used to develop photoresist
SPR-220-7	Photoresist used to pattern metal layers
HTR-D2, RER600	Chemical ancillaries used to develop PSPI
EIS	Electrochemical Impedance Spectroscopy
PCB	Printed Circuit Board
TMAH	Tetramethylammonium hydroxide, ingredient of MF-26A
Electrode Impedance	Measure of opposition to current with applied voltage
Chloroauric acid	Gold plating solution, that is used to gold plate electrodes to reduce electrode impedance
PEDOT:PSS	poly(3,4-ethylenedioxythiophene), conductive polymer that is used to coat electrodes to reduce electrode impedance
DUT	Device Under Test

List of figures

List of tables

1. INTRODUCTION

This thesis describes the development of a novel model that was created of the larval zebrafish heart and body to simulate the electrocardiogram (ECG). In addition to this, the design and fabrication of novel microfabricated electrodes is described toward the development of a high through put (HT) system to measure the larval zebrafish ECG. In the following introduction, the motivations, themes and objectives of this thesis are described along with a brief outline of each section.

1.1 Motivation

Heart related diseases are one of the largest causes of deaths worldwide. With sudden cardiac death causing 450,000 deaths each year in the USA alone [1]. Amongst the most common heart problems are cardiac arrhythmias and QT prolongation (increased delay between ventricular depolarisation and repolarisation). In order to increase the understanding of these dysfunctions it is necessary to study the electrical properties of the heart during early development. Over the last ten years the zebrafish has been increasingly used to study these dysfunctions and has been suggested as a useful model for studies of human cardiac electrophysiology and development [2].

This is due to the surprisingly close electrophysiological similarity between human and zebrafish hearts. The shape and duration of zebrafish myocyte action potentials (APs) are largely similar to those of human myocytes, as orthologues of the cardiac ion channels found in humans also exist in zebrafish e.g. zERG (orthologue of human hERG) [3]. Cardiac activity can be assessed quickly following fertilisation in comparison to other animal models, as

zebrafish development occurs very rapidly with a beating heart present at 24 hours post fertilisation (hpf) or 1 day post fertilisation (dpf) [4, 5].

One of the most important and useful ways in which cardiac electrical activity can be measured and hence used to diagnose disorders, is to measure the electrocardiogram (ECG). The ECG is a time-resolved vector measure of electrical activity of the heart on the body surface. It is important as it is non-invasive and reveals a large amount of detail as to how the heart is functioning as well as evaluating potential drug side effects. Measuring the human ECG is a well-developed and standard technique that is well understood and widely used with patients. Whereas, measurement of the larval zebrafish ECG is a developing technique that has been performed on both adult and larval zebrafish at varying stages of development [1, 6-11]. In addition to the action potential similarities, the human and zebrafish ECG morphologies are similar and so are the QT intervals (delay between ventricular depolarisation and repolarisation) and heart rates [11-13]. The QT interval is an important parameter to measure as a prolonged QT interval can lead to the development of arrhythmias such as Torsade de Pointes [14]. These arrhythmias can be irritating (palpitations) or even life threatening. The causes of QT prolongation can either be genetic or acquired (e.g. from drug treatments). Therefore, restrictions have been increased around the use of drugs that are known to prolong QT and standards have been increased for the drug screening process to identify drugs that have this effect [15]. In addition, the mechanisms behind QT prolongation are poorly understood [16], as are the drug compounds that can cause it and so novel screens can help to better understand this [11, 17].

As their ECG is similar to mammals and they respond very similarly to drug treatment as humans, zebrafish embryos and larvae can be useful screening tools with several additional

benefits over other animal models. These include the small amount of chemicals necessary for drug testing, fast and inexpensive embryo production, rapid generation of transgenic animals and fewer regulatory restrictions in care and maintenance [1, 11].

These advantages of using the larval zebrafish mean that it is an ideal candidate for use in high throughput screening (HTS). HTS is a key tool in the drug discovery process which is generally used to screen a library of a large number of compounds on either a group of cells, a receptor, or even a metabolic enzyme [18, 19], using a standard 96 well plate [19]. The goal of such a process is to identify 'hits' or 'leads' within the library which have the desired effect on the target. The results will not necessarily identify the final drug but provide leads to help with the pharmacological refinement process. HTS can be used to assess bioavailability (absorption and accumulation), pharmacokinetics (drug persistence) and toxicity. The zebrafish gives the opportunity to study the effects of a compound on an entire living system. In addition, drugs are often rejected due to causing cardiac malfunctions and the screening out of compounds with these side effects using the zebrafish has been suggested as being cost efficient over the alternatives [20, 21]. Previous work in this area has focused on video imaging [20] and automatic heart rate extraction which offers less detail than measuring the ECG.

Larval zebrafish ECGs are currently measured using micro pipette electrodes [11]. These are widely used to measure the electrical activity of cells and are highly capable of measuring such signals. However, such an electrode is not compatible with HTS as a lot of manual positioning is required. In HTS targets are dispensed in to a well automatically [22] with no control over rotation of the zebrafish. Therefore, electrode arrays need to be developed that are capable of measuring the ECG of the zebrafish for such a system. Multichannel electrode arrays constructed using microfabrication techniques have become standard tools in

a range of biomedical applications [23, 24], including measurement of the adult zebrafish ECG [8]. This thesis introduces the design and fabrication of such arrays towards the development of a HTS zebrafish system. This style of electrode has been shown to be capable of measuring the ECG but improvements are needed in order for a full HTS system to be developed.

In addition, and to compliment measurements, computational models provide a platform for investigating aspects of physiology that are difficult to study within intact organisms for both ethical and/or practical reasons, such as animal welfare and costs. Despite being computationally intensive these models have become increasingly realistic and informative. They have begun to be more widely used due to the greater availability and increase in computing power with models of the heart even being constructed for individual patients to aid diagnosis [25]. Simulations of the heart can address its electrical or mechanical properties and current models incorporate either or both of these aspects [26-28].

Models of the heart range in scale from a single cell [29], to sheets of tissue [30], a partial heart [31, 32] and also to a whole heart [33-35]. This thesis focuses on simulating the electrical activity of the zebrafish heart and thus determining the waveform of the ECG which is known as the forward problem of electrocardiography [36-38]. Whilst the mechanical properties of the heart may affect the resultant ECG (see [28]), the relationship between electrical and mechanical properties of the heart increases model complexity and hence computational intensity.

As most cardiac research is conducted with the aim of developing therapies for human diseases, the majority of previous work in this field focuses on the human heart. Models that incorporate the human body have been generated to investigate ECG generation as well as its parameters, including drug effects [39, 40], although some modelling using other mammalian

hearts (e.g. sheep, dog, etc.) is also available [41, 42]. Some models have even been made of fish hearts, e.g. a fluid flow model of the larval zebrafish heart [43] and a mechanical model of the carp heart [44], but no previous electrical simulations exist for the zebrafish larva.

This thesis introduces the first electrical model of the zebrafish larval heart and body. This model was created for the purpose of simulating the ECG to make predictions to aid in functional measurements by determining the best positions to place electrodes on the larval zebrafish. As a result, the model can successfully simulate the heart's activation wave and produce an ECG that is comparable to those measured from 3 dpf zebrafish but there is room for improvement.

1.2 Overview

In order to understand the electrical activity of the heart that is responsible for initiating and maintaining the mechanical function of the heart, chapter 2 briefly describes the basic anatomy and electrophysiology of the heart in general and specifically for both humans and zebrafish. The electrical activity is explained, starting with its origins in the cell membrane leading to action potentials that propagate along cells and to other cells. It is then explained how this behaviour leads to propagating waves throughout the heart muscle. The chapter then continues by describing how the electrocardiogram is generated from this activity. The forward problem and inverse problem of electrocardiography are also described along with how this relates to modelling the larval zebrafish heart electrical activity and ECG.

In chapter 3, common methods for modelling the heart and the ECG are introduced. Starting with electrical model of the body that is common to most ECG models which treats the body as a volume conductor. This is followed by different methods that have previously been used to model the current sources produced by the heart. Equivalent cardiac generators/sources

are introduced which simplify the complex electrical activity of the heart as an equivalent simpler source such as a monopole or dipole. These are useful for an approximate solution of the problem requiring less information and computational load to construct. An overview is then given of the different more realistic models that have been used to model the heart that aim to replicate some or all aspects of the real biological source. These models have the advantage in that their predictions are more realistic but this comes with increased complexity. A brief description is then given of the finite element method which is used in the software package COMSOL Multiphysics that was used to create the models described in the results chapters of this thesis (Chapters 5, 6, 7, 8).

Chapter 4 provides background to the electrode design and fabrication work. Firstly, the different types of electrodes that can be used to measure the larval zebrafish ECG are described, material choice is explained that is based on material properties for the desired application. An overview is then given of the electrode-electrolyte interface and an equivalent circuit model (used in chapter 8) is introduced as it is important to understand the physical mechanisms required to measure signals with metal electrodes including the importance of electrode size and electrical impedance. This is followed by a description of the methods used to fabricate the electrodes, with a brief guide to techniques such as spin coating, photolithography and methods of etching materials. This is then followed by a description of electrochemical impedance spectroscopy which is the main method used to test the fabricated devices. An overview is then given of techniques that can be applied to microfabricated electrodes to reduce their impedance and thus increase their ability to measure a signal. The chapter finishes with an overview of the previous development towards a zebrafish HTS system including electrode designs and results. This project was developed as a collaborative effort between the School of Engineering at the

University of Birmingham which developed the electrodes and the Medical School which supplied the zebrafish and measurement equipment.

Chapter 5 is the first of the results chapters and covers the early stages of development of the larval zebrafish heart model. Including the use of the equivalent cardiac sources (from chapter 3) in various COMSOL models. A simple ellipsoidal body geometry is used throughout the chapter along with three variations of a dipole source finishing with a simple Fitzhugh-Nagumo model. The results show that each dipole model is equivalent to each other, the voltage distribution within the zebrafish body can be investigated and a simple ECG can be generated using these simple models. The magnitude of the voltages is large close to the heart and quickly reduces with distance as is expected from a dipole which means recording electrodes need to be placed close to the heart. A Fitzhugh-Nagumo model is then explained which adds some realism with wave propagation and action potentials but is incapable of simulating the ECG.

In chapter 6, the previous models are expanded upon by introducing and explaining the development of a bidomain heart model of a 3 dpf zebrafish with improved geometry. This model uses modified Fitzhugh-Nagumo equations to give each region of the zebrafish heart individual action potentials and conduction velocities which are consistent with measurements from the literature. In turn, this improved model is capable of simulating ECGs that are comparable to those which are measured using a micropipette electrode in three positions across the zebrafish body. The limitations of the model are also explained along with how it could be improved in the future.

The previous two chapters explain the heart models that were created in this work and chapter 7 describes static models that were created of the electrode geometry. Specifically, different shapes and sizes of electrodes are explored by placing them in both uniform and dipole

electric fields and comparing the voltage on them (electrode voltage). The electrode shapes and sizes are ranked based on their ability to measure the equivalent empty volume voltage for different electrode positions. The results of these models suggest that compact shapes such as a circle or square perform best. Then a simple model of the zebrafish skin model is added to the geometry to show how electrode voltage is reduced due to the presence of the skin and why contact with the fish is required to measure a good signal. Finally, the square and circle geometries are added to the bidomain model which shows that the increased voltage sensitivity of smaller electrodes leads to an improved measurement of the ECG.

The final part of the work in this thesis is described in chapter 8. This chapter covers the steps taken toward the development of the zebrafish HTS system. The previous electrode models showed how important electrode size is to voltage sensitivity and the electrode-electrolyte model showed how electrode impedance is inversely proportional to electrode area. This means that the required small electrodes have a large impedance. In order to reduce this the use of the plating/coating techniques described in chapter 4 are described to lower the impedance of the microfabricated electrodes. The effects of the plating were measured using electrochemical impedance spectroscopy and the model is then used to analyse the results. This is followed by a description of electrode fabrication and use with the zebrafish along with the problems encountered with both electrode release and measuring a signal. Due to the lack of a measured signal a redesign of the electrodes is then described along with an updated fabrication process. A confirmation of the plating techniques on the new electrode designs is then presented followed by more tests with the zebrafish. Unfortunately, no ECG signals could be measured therefore the electrodes were tested using an artificial signal to show their functionality which is then compared to the results of a COMSOL model.

This thesis concludes with chapter 9, which highlights the significant achievements of the thesis as well as areas that could be improved upon in future work. The limitations and possible improvements for the heart model are discussed. The reasons for ineffectiveness of the microfabricated electrodes are also discussed along with improvements that could be made.

2. THE HEART AND THE ELECTROCARDIOGRAM

This section introduces the basic anatomy and electrophysiology required to give context to the heart models described in chapters 3, 5 and 6. The cardiovascular system including the heart of both humans and the zebrafish is described. Followed by the origins of electrical activity within the heart, from a single cell to the entire heart and how from this activity, the electrocardiogram is generated.

2.1 Anatomy and function

The circulatory system is one of the body's most important organ systems. This system is responsible for distributing nutrients, oxygen, hormones and cellular waste products throughout the body. It consists of blood, a network of blood vessels and the heart. The heart is a muscular pump which rhythmically contracts forcing blood to circulate the body. Despite obvious differences in size between the larval zebrafish and humans the function and anatomy of the circularity system is quite similar.

2.1.1 Function

The human heart consists of four chambers, left atrium, right atrium, left ventricle and right ventricle surrounded by muscular walls (Figure 2.1 A). It is approximately the size of a closed fist, contains 2-3 billion muscle cells [45], weighs 331 g [46] and is located in the chest just behind the sternum. The human circulatory system is split into two loops; one for the lungs (systemic) and one for the rest of the body (pulmonary).

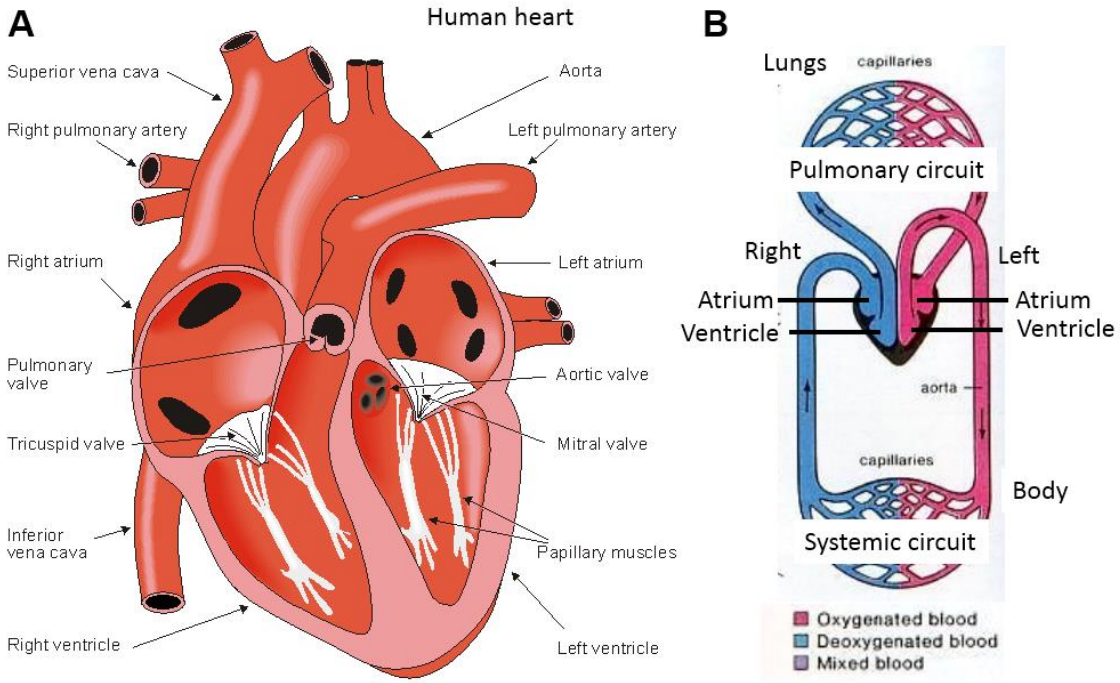

Figure 2.1 A) Human heart schematic anatomy from [38], B) circulatory system diagram from [47] with additional labels.

A diagram of the human circulatory system is shown in Figure 2.1 B. At the start of the cycle blood from the body that is low in oxygen enters the relaxed right atrium via the superior and inferior vena cava. The atrial wall muscle contracts forcing blood through the tricuspid valve into the right ventricle (atrial systole). When the ventricle is filled with blood the tricuspid valve closes which stops blood flowing back into the right atrium. The right ventricle then contracts which pushes blood out of the heart via the pulmonary valve and into the pulmonary artery which leads to the lungs (ventricular systole), the valve then closes preventing back flow of blood. After the blood is oxygenated by the lungs it returns to the heart via the pulmonary veins and into the left atrium. The left atrium then contracts and blood moves through the mitral valve and into the left ventricle, then the mitral valve closes when the chamber is filled. Following this, the left ventricle contracts forcing blood out of the heart through the aortic valve and into the aorta which leads to the rest of the body. The right and left atriums contract at the

same time as do the right and left ventricles. This allows blood to be pumped to the lungs and the rest of the body in one cycle.

The 3 dpf zebrafish is the most common aged zebrafish to use for ECG experiments as at this the stage there is a fully functioning heart and positioning is easier due the lack of a swim bladder [4, 5]. A typical 3 dpf zebrafish is shown in Figure 2.2 A, from dorsal and lateral views. At 3 dpf, the heart is approximately 100 µm in size and contains ~300 cells [48], that are coupled by gap junctions [49, 50]. The cardiac structure is simpler than that of the human heart with a tubular structure as shown in Figure 2.2 B.

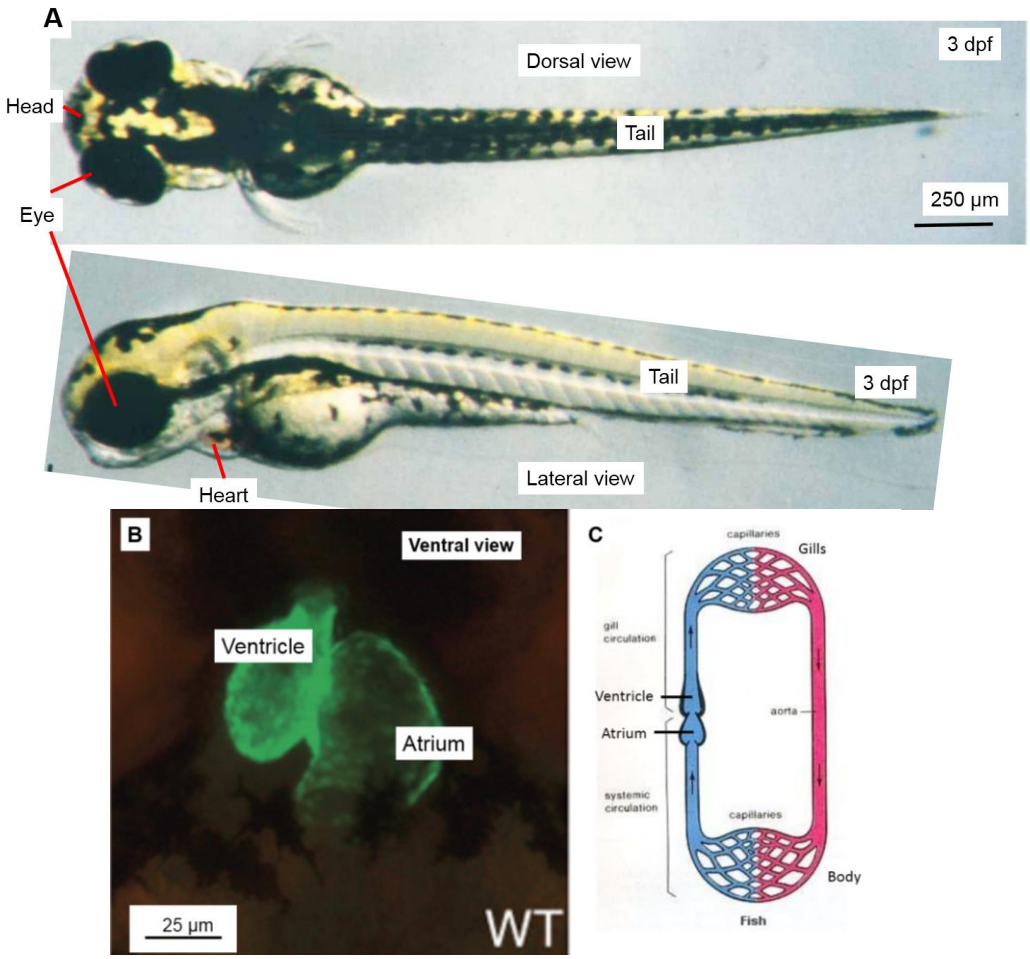

Figure 2.2 A) 3 dpf zebrafish dorsal and lateral views, [51] B) 3 dpf zebrafish heart from [52], C) circulatory system diagram from [47] with additional labels.

The zebrafish has a simpler circulatory system (Figure 2.2 C) than the human consisting of just one loop which is known as single cycle circulation. Because of this, the zebrafish heart contains only two chambers, an atrium and a ventricle. At the start of the cycle, blood enters the heart into the atrium. The atrium then contracts, which forces blood into the ventricle. This is followed by the contraction of the ventricle which forces blood out of the heart, through the gills and around the rest of the body and back to the heart.

2.1.2 Cardiac cells

Cardiac cells are mechanically secured to each other at intercalated discs forming complex structures in humans consisting of spiralling chains of fibres that are formed from many cells. A less complex structure is present in larval zebrafish due to the smaller heart size and lower number of cells. Electrical coupling of cells is achieved via high resistance gap junctions (Figure 2.3). Gap junctions consist of two connexions which are each an assembly of six connexion proteins. A channel is formed by the connexions which connects the cytoplasm of adjacent cells together allowing electrical signals to propagate from cell to cell. The typical time scale of these propagations from to cell to cell is in the order of 10 to 100 μs for the cytoplasm with similar values for the gap junctions [53], these times vary between heart regions. Due to these, sometime, multiple connections between cells, cardiac tissue can be said to behave as a functional syncytium, which means that it behaves as if it were one cell even though individual cells have their own properties.

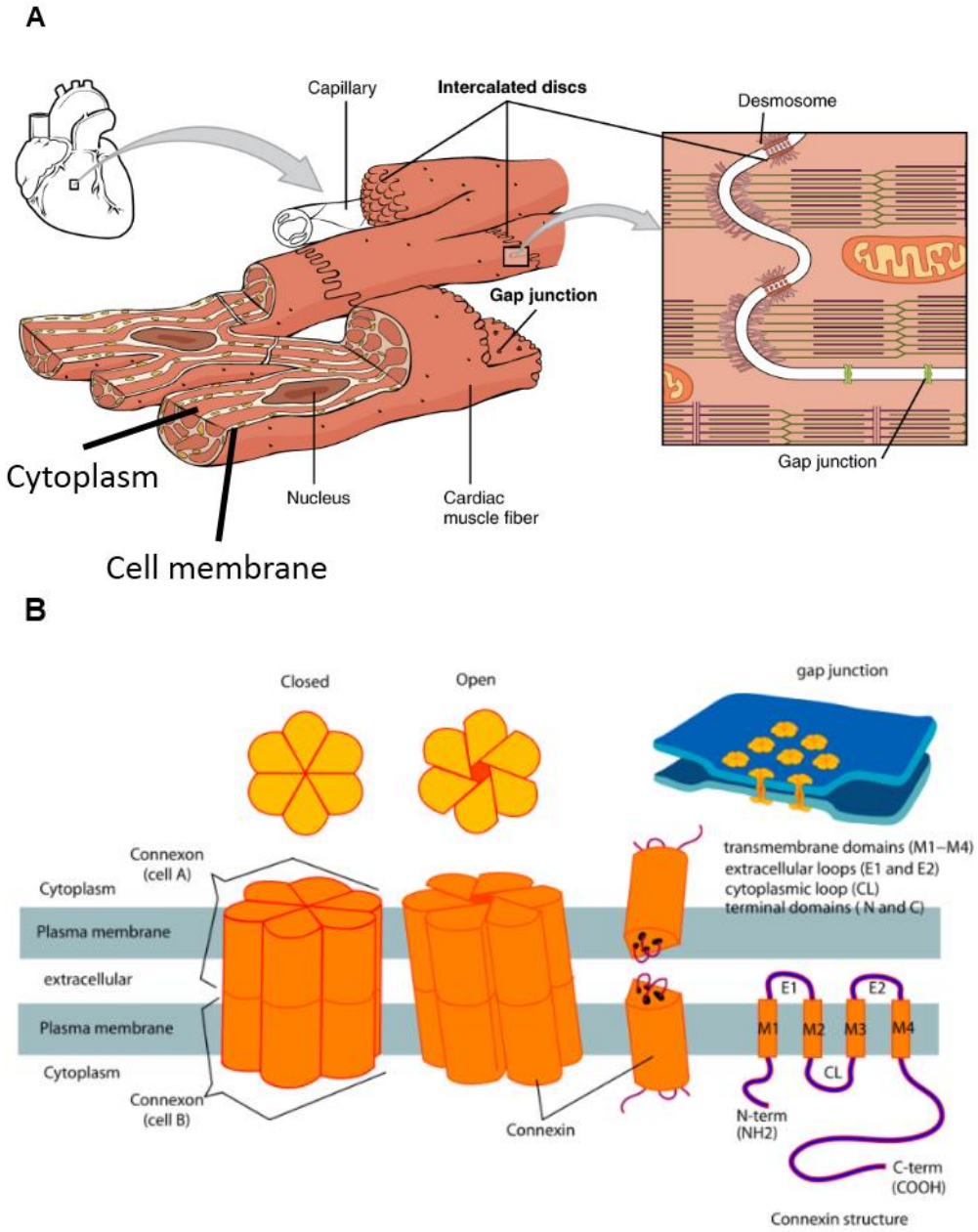

Figure 2.3 A) Cardiac cell anatomy and structure from [54], B) expanded view of gap junction structure [55].

The muscular walls of the heart are made from individual cells called cardiomyocytes which are the basic building block of the heart and are collectively known as the myocardium. They are generally long cylindrical cells in humans containing one or two nuclei and many mitochondria. They are approximately 4700 μm^2 in the human and 300 μm^2 in the larval zebrafish (at 3dpf). Other structures are also present such as T-tubules which allow electrical

activation to spread quickly within the cell and the sarcoplasmic reticulum which regulates calcium ion concentration. Each cardiomyocyte is connected to one or more cells at intercalated discs which provide both mechanical (by desmosomes) and electrical coupling (via gap junctions). Complex structures consisting of spiralling chains of fibres that are formed from many cells are present in human hearts with less complex arrangements in the zebrafish heart due to the much lower number of cells. The cellular membrane which surrounds each cell gives rise to their electrical properties.

The heart also contains a variety of other cell types and structures such as fibroblasts, blood vessels, nerves and specialised conduction cells. These conduction cells have a key role in ensuring the heart pumps in a rhythmic and efficient way. The human heart has a highly developed conduction system where as a 3 dpf zebrafish has yet to fully develop its own system. However, there are two elements of the conduction system that are present in both human and larval zebrafish which are the sinoatrial node (sinoatrial region in zebrafish) and the atrioventricular node (atrioventricular band in zebrafish). The sinoatrial node (SA node) consists of pacemaker cells which initiate the electrical activation of the heart and the atrioventricular node (AV node) delays conduction between the atrium and ventricle. These are explained more in a later section.

One of the other most notable features of cardiac cells is the cell membrane (Figure 2.3). The cell membrane plays an important role in the electrical behaviour of these cells with cardiac electrophysiology being the study of this behaviour and the wider electrical activity of the heart. Ion movement through the membrane is facilitated by the presence of ion channels which are formed by ion-selective proteins and allow the transport of sodium, potassium, chlorine and

other ions across the membrane. These membrane ion channels are separate structures which exist alongside the gap junctions between cells.

2.2 Cardiac electrophysiology

In both the human and larval zebrafish hearts the rhythmic contraction/pumping of the heart is initiated and maintained by electrical activation of the heart muscle which triggers contraction. The origin of this activity is within the cells. Cardiac cells are part of a group known as excitable cells which also include nerve cells and means that if they are exposed to a stimulus above a certain threshold they illicit a response called an action potential. An action potential is generated by the flow of ions across the cell membrane from the intracellular space (inside of the cell) to the extracellular space (outside of the cell) or *vice versa*. Differences in the relative concentrations of these ion species lead to voltage gradients across the cell membrane. The sum of these gradients is known as the transmembrane potential or simply membrane potential and is defined as the difference in voltage between the voltage inside of the membrane and outside of the membrane:

$$V_m = \varphi_i - \varphi_e \tag{2.1}$$

Where φ_i is the intracellular voltage and φ_i is the extracellular voltage. In this section, the origin and initiation of the electrical activation of the heart is described at the cellular level (for a typical cardiomyocyte) in the cell membrane, then the propagation of electrical signals in a small section of heart tissue is described followed by how this scales to the whole heart.

2.2.1 Cellular static behaviour

An excitable cell can be considered to be a closed volume containing charged molecules (intracellular space) which is separated from a field of ions in a solvent (extracellular space) by the cell membrane. The cell membrane plays an important role in the electrical properties of

cells by regulating the movement of ions between the extra and intracellular spaces. The ease with which ion species can cross the membrane is the membrane permeability which is different for each ion. Activation of the cell triggers changes in this permeability which allows ions to cross the membrane under the influence of two forces.

The concentration of each ion differs greatly either side of the membrane which means there is a concentration gradient for all permeable ions. This leads to ions moving from a region of high concentration to a region of low concentration which is known as diffusion. This flow of ions leads to a build-up of ions either side of the membrane which consequently creates an electric field across the membrane which is felt by any ion moving across it. Therefore, to describe ion movement across the cell membrane both diffusional and electric field forces need to be described. An equilibrium is reached when these forces balance each other for all permeable ions. A short mathematical description of these forces for a single ion species, κ, is given below which can also be found in Malmivuo [38] in more detail.

The flux of ions driven by an electric field or migration ($\vec{j}_{\kappa e}$) is given by:

$$\vec{j}_{\kappa e} = -u_{\kappa} \frac{z_{\kappa}}{|z_{\kappa}|} c_{\kappa} \nabla \varphi \tag{2.2}$$

Where $\vec{j}_{\kappa e}$ refers to the number of ions that pass through a unit area of membrane per unit time (mol/m^{2}s). u_{κ} is the ionic mobility (m^2/Vs), z_{κ} is the valence of the κ ion, c_{κ} is the ionic concentration and φ is the potential (V) and $z_{\kappa}/|z_{\kappa}|$ is the sign of the ion. The electric field is given by $-\nabla\varphi$ and $u_{\kappa}$is dependent on the size of the ion and the solvent viscosity.

The flux of ions for a given concentration gradient ($\vec{j}_{\kappa D}$) is given by Fick's Law:

$$\vec{j}_{\kappa D} = -D_{\kappa} \nabla c_{\kappa} \tag{2.3}$$

Where $\vec{J}_{\kappa D}$ refers to the number of ions that pass through a unit area of membrane per unit time (mol/m^{2}s), D_κ is Fick's diffusion constant (m^2/s) and c_κ is the ionic concentration of κ (mol/cm^3). D_κ is dependent on the size of the ion and the solvent viscosity.

The migration couples the electric field force $-\nabla\varphi$ and Fick's law couples the diffusion 'force' ∇c_κ to the resulting ionic flux. In both equations, as the flux is limited by the collision with solvent molecules there is a connection between u_κ and D_κ. This connection was found by Nernst [56] and by Einstein [57] and is given by:

$$D_\kappa = \frac{u_\kappa RT}{|z_\kappa|F} \tag{2.4}$$

Where R is the gas constant (8.314 J/(mol·K), T is the absolute temperature (K) and F is Faraday's constant (A/mol).

From this relation it is possible to write an expression for the total flux due to both diffusion and migration:

$$\vec{J}_\kappa = \vec{J}_{\kappa D} + \vec{J}_{\kappa e} = -D_\kappa \left(\nabla c_\kappa + \frac{c_\kappa z_\kappa F}{RT} \nabla\varphi \right) \tag{2.5}$$

This equation is known as the Nernst-Planck equation and describes the flux of an ion due to the presence of a concentration gradient and an electric field. The ionic flux ($\vec{J}_\kappa$) can be converted into an electric current density ($\vec{J}_\kappa$) by multiplying by the number of charges carried by each mole (z_κF):

$$\vec{J}_\kappa = \vec{J}_\kappa z_\kappa F \tag{2.6}$$

As the membrane is extremely thin any variations across it can be considered one dimensional in a direction normal to the membrane. This direction is labelled x and so the Nernst-Planck equation becomes:

$$\vec{J}_\kappa = -D_\kappa \left(\frac{d}{dx} c_\kappa(x) + \frac{z_\kappa F c_\kappa(x)}{RT} \frac{d}{dx} \varphi(x) \right) \tag{2.7}$$

The significant ions that cross a cardiac cell membrane are potassium (K^+), sodium (Na^+), calcium (Ca^{2+}) and chlorine (Cl^-). Starting with the assumption that, at rest the membrane is only permeable to K^+ ions and that in reality the intracellular concentration of K^+ ions is larger than the extracellular concentration leads to K^+ diffusing across the cell membrane. This leaves an equal number of Cl^- ions inside of the membrane. Then due to the electrostatic attraction between the two opposing ions, K^+ ions accumulate on the outside of membrane and Cl^- ions accumulate on the inside. This process does not continue indefinitely as the electric field (created by the opposing ions) exerts a force that opposes the diffusion of K^+ through the membrane and an equilibrium is reached where the two forces are balanced. This does not require a large amount of K^+ ions compared to the amount available so the intracellular and extracellular concentrations of potassium can be considered to be unchanged. The transmembrane potential ($V_i - V_e$) at this equilibrium is then known as the equilibrium potential. This equilibrium potential can be derived from the Nernst-Planck equation as a function of concentration. If the flux of κ^{th} ion is zero, the Nernst-Planck equation becomes:

$$\vec{J}_\kappa = 0 = -D_\kappa \left(\frac{d}{dx} c_\kappa(x) + \frac{z_\kappa F c_\kappa(x)}{RT} \frac{d}{dx} \varphi(x) \right) \tag{2.8}$$

Which can be rearranged to give:

$$\frac{d}{dx} c_\kappa(x) = -\left(\frac{z_\kappa F c_\kappa(x)}{RT} \frac{d}{dx} \varphi(x) \right) \tag{2.9}$$

Then by integrating from the intracellular to the extracellular space the equilibrium voltage (V_κ) of the κ^{th} ion is given by:

$$V_\kappa = \varphi_i - \varphi_e = -\frac{RT}{z_\kappa F} \ln \frac{c_{e,\kappa}}{c_{i,\kappa}} \tag{2.10}$$

Where φ_i is the intracellular potential, $\varphi_e$is the extracellular potential, $c_{e,\kappa}$ is the extracellular concentration and $c_{i,\kappa}$ is the intracellular concentration. An equation for each permeable ion can then be found by substituting for their relevant concentrations.

Of course, in real tissue the cell membrane is permeable to multiple ions, this can be modelled using the Goldman-Hodgkin-Katz equation. If the influence of external charges is negligible and there are no fixed charges in the membrane, then the electric field is constant across the membrane. If this is true, then the transmembrane potential varies linearly across the membrane:

$$E_{\mathrm{x}} = -\frac{d}{dx}\,\varphi(x) = -\frac{V_{\mathrm{m}}}{h} \tag{2.11}$$

Where E_{x} is the electric field within the membrane, φ is the potential, V_{m} is the transmembrane potential and h is the thickness of the membrane in the x direction. Combining this expression with the Nernst equation gives the Goldman equation:

$$V_{\mathrm{m}} = \frac{RT}{F}\,ln\left[\frac{P_{\mathrm{K}}[K^+]_{Ext} + P_{\mathrm{Na}}[Na^+]_{Ext} + P_{\mathrm{Cl}}[Cl^-]_{Ext} + P_{\mathrm{Ca}}[Ca^{2+}]_{Ext}}{P_{\mathrm{K}}[K^+]_{Int} + P_{\mathrm{Na}}[Na^+]_{Int} + P_{\mathrm{Cl}}[Cl^-]_{Int} + P_{\mathrm{Ca}}[Ca^{2+}]_{Int}}\right] \tag{2.12}$$

Where P_{K}, P_{Na}, P_{Cl}, P_{Ca} are the permeability's and $[K^+]$, $[Na^+]$, $[Cl^-]$ and $[Ca^{2+}]$ are the concentrations of potassium, sodium, chlorine and calcium ions respectively. This model is valid when the total flux of all ions is zero, which is only valid when the cell is relatively static i.e. at rest. This results in the resting potential of a cardiac cell being negative. The voltage is measured across the cell membrane relative to the outside zero with the sign determined by the voltage inside of the cell. At rest, K^+ and Cl^- are more abundant within the cell with Na^+ and Ca^{2+} the opposite. To model the active behaviour of the membrane a more complex model is required which was first developed in 1952 by Alan L. Hodgkin and Andrew F. Huxley [58] from experiments with giant squid axons and is described in detail in [38].

2.2.2 Cellular active behaviour

The following section gives a qualitative description of the active behaviour. The key point of this is that as mentioned previously, the permeability of the ion channels within the membrane are sensitive to changes in the membrane voltage which means that specific ion channels 'open' or 'close' to each ion based on the membrane potential. This leads to the generation of action potentials as described for the two main types of excitable cell within the heart, pacemaker cells and the regular cardiomyocytes.

Pacemaker cells

Activation of the heart is initiated at the sinoatrial node. Pacemaker cells have a property known as automaticity which means that they are self-excitatory and produce an action potential without application of an external stimulus. The pacemaker action potential has three phases which are described below and shown in Figure 2.4 A. The phases are named based on the action potential of the cardiomyocyte which has more stages:

- Phase 4: Initially, there is a large abundance of Na^+ ions outside of the cell with a negative V_m. The initial negative membrane potential increases (towards positive) due to the influx of sodium ions (Na^+) which enter due to diffusion. There is no true resting state as Na^+ ions are constantly entering the cell which causes the membrane potential to gradually increase.
- Phase 0: When the potential increases past a certain point, which is called the threshold, the calcium (Ca^{2+}) voltage gated ion channels open and Ca^{2+} ions rapidly enter the cell due to their high concentration outside of the cell, this causes the membrane potential to rapidly increase up to a maximum positive potential, this is known as the action

potential upstroke or depolarisation. Then the Ca^{2+} channels close which is triggered by the maximum potential.

- Phase 3: The increase in membrane potential triggers the opening of the potassium (K^+) ion channels. The high concentration of K^+ within the cell causes them to leave the cell which reduces the membrane potential back to its initial value, this is known as the action potential downstroke or repolarisation. Then the K^+ channels close. To allow this cycle to be repeated, the concentration of K^+ ions and Na^+ ions is reset by a sodium-potassium pump (an enzyme) which brings K^+ ions into the cell and removes Na^+ ions from the cell using energy from the metabolism of the cell [38].
- Phase 4: The cycle then repeats itself as Na^+ ions continue to enter the cell. In addition to the sodium-potassium pump removing Na^+ ions from the cell, the concentration of Na^+ ions is reduced by their movement across gap junctions to neighbouring cells triggering depolarisation in them, as explained further in section 2.3.

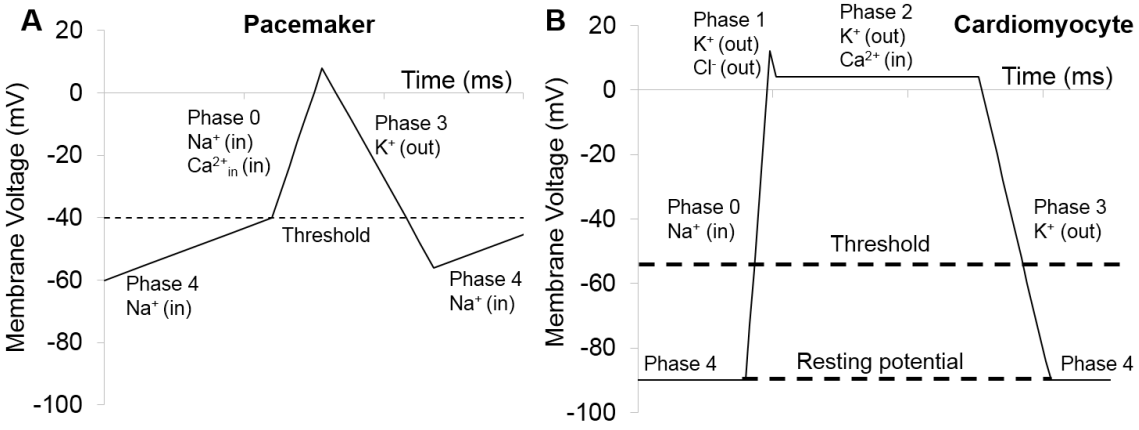

Figure 2.4 Schematic diagrams of A) pacemaker and B) cardiomyocyte action potentials.

Cardiomyocytes

Similarly, the activation of the regular cardiomyocytes can be broken down in to phases (Figure 2.4 B). There are five phases to the action potentials of cardiomyocytes which are:

- Phase 4: The resting state as described previously. The membrane potential is negative and constant.
- Phase 0 (depolarisation): After receiving sufficient stimulation from Na^+ or Ca^{2+} ions entering the cell from neighbouring pacemaker cells or cardiomyocytes, V_m rises above a threshold. This causes the Na^+ voltage gated ion channels within the cell membrane to open rapidly which means Na^+ ions move into the cell, this increases V_m up to its maximum, the channels then close.
- Phase 1: The K^+ and Cl^- voltage gated ion channels open which allows a small amount of K^+ and Cl^- ions out of the cell, this decreases V_m by a small amount, then the chlorine channels close.
- Phase 2: A this point the Ca^{2+} ion channels open allowing Ca^{2+} ions into the cell and at the same time K^+ ions are still leaving the cell from phase 1 which leads to a plateau in V_m.
- Phase 3: After a few hundred ms (exact value depends on cell type) Ca^{2+} ions stop entering the cell but K^+ ions still continue to leave the cell which reduces V_m and returns the cell back to the resting state. This is repolarisation (downstroke) and the K^+ channels then close.
- Phase 4: The cell returns to its resting state where the concentration of sodium ions is greater outside of the membrane and the concentration of K^+ ions is greater inside the membrane leading to a negative V_m. There is then a small period of time where the cell becomes insensitive to any stimulus above the threshold which is known as the refractory period.

The exact nature of this process differs between heart regions due to the multitude of cardiomyocytes types found within the heart. They all have the same basic operation but there are key differences which are essential to the hearts function for both humans and zebrafish.

2.3 Depolarisation and repolarisation waves

The scaling of the cellular activity to sections of cardiac tissue and the whole heart can be illustrated by considering a small section of tissue containing pacemaker cells surrounded by regular cardiomyocytes.

Initially, all the cells in the section of tissue are at rest which means that their membrane potential is negative but due to the constant influx of Na^+ ions into the pacemaker cells, one of them depolarises increasing the membrane potential. Some of the Na^+ ions that enter the cell move across the gap junctions to the neighbouring cells causing an increase in membrane potential and depolarisation in these cells. This in turn causes Na^+ ions from the first set of neighbouring cells to enter their own neighbouring cells and so on until this depolarisation reaches the regular cardiomyocytes. Depolarisation in these cells is then triggered in the same way and so on with their neighbours until depolarisation spreads throughout the entire region.

At a larger scale and for a large number of cells, the cell to cell propagation of depolarisation begins to look like a continuous wave as there are so many cells that the uneven nature of the propagation at the wavefront evens out. This was also assumed to be true for the larval zebrafish but of course this is a much poorer approximation for such a small heart. This is discussed later in Chapter 5.

Repolarisation is quite different as it is not actually a propagating phenomenon as the repolarisation of one cell does not directly lead to the repolarisation of its neighbours. Repolarisation occurs due to the duration of the cells action potential. Therefore, if the duration

of every action potential is the same repolarisation would occur in the same order as depolarisation. However, real heart tissue has distinct regions with different duration action potentials so heart tissue may not necessarily repolarise in the same order in which it depolarised. For example, consider if there are two regions of tissue, region one with a long APD and region two with a short APD. If region one depolarises first it will then repolarise second, provided region two is activated quickly. However, repolarisation is still generally approximated as a wave as long as these differences in regional properties are taken into account.

2.4 The Electrocardiogram (ECG)

In this section the generation and form of the measured ECG is described that is a result of the depolarisation and repolarisation waves path through the heart. The cellular electrical activity can be measured by inserting microelectrodes inside cardiac muscle cells (intracellular) whereas, as mentioned earlier, the ECG is a body surface measurement. This means that it represents the extracellular activity of the heart.

2.4.1 Signals produced by activation

In order to explain the generation of the full ECG it is helpful to understand the signals produced by both depolarisation and repolarisation in a small section tissue as measured from the surface of the body. Figure 2.5 represents the body with two electrodes placed either side. A signal is measured by the positive electrode (on the left) for both depolarisation and repolarisation with the polarity determined by direction of travel (towards or away from the positive electrode), giving four cases in total. The polarities of these signals are, for each case in turn:

- Case A: Depolarisation wave towards positive electrode = positive signal.

The transmembrane voltage ahead of the waves path is negative as this region is still at rest (as shown by the minus signs in Figure 2.5). The activated region behind the wavefront is in the plateau stage of the action potential (phase 2) and therefore it is positive. If both regions are assumed to be uniform this leads to the creation of a double layer source (positive and negative layer sources separated by a small distance) at the wave front with the positive side orientated in the direction of propagation. Then, due to this orientation the resulting signal is positive with the actual time varying signal in a more realistic example dependent on geometry and electrode position. This approximation is an important point that is explained more in Chapter 3 and used with the models described in Chapter 5.

- Case B: Depolarisation wave away from negative electrode = negative signal.

This is the opposite of case A where the source is orientated away from the electrode with the negative side orientated towards it instead, which leads to a negative signal.

- Case C: Repolarisation wave towards positive electrode = negative signal.

A similar method can be used to explain the resulting signal in this case. The transmembrane potential is positive ahead of the repolarisation wavefront (plateau) and negative behind (resting). This results in the opposite orientation of the double layer source for each case resulting in a negative signal for the repolarisation wave travelling towards the positive electrode.

- Case D: Repolarisation wave away from positive electrode = positive signal.

A positive signal would be measured when the wave is travelling away from the positive electrode.

Figure 2.5 E shows what happens when the wave is not travelling directly towards an electrode. The detected signal is proportional to the component of the velocity in the direction towards the electrode (ignoring any change in the wavefront for different directions).

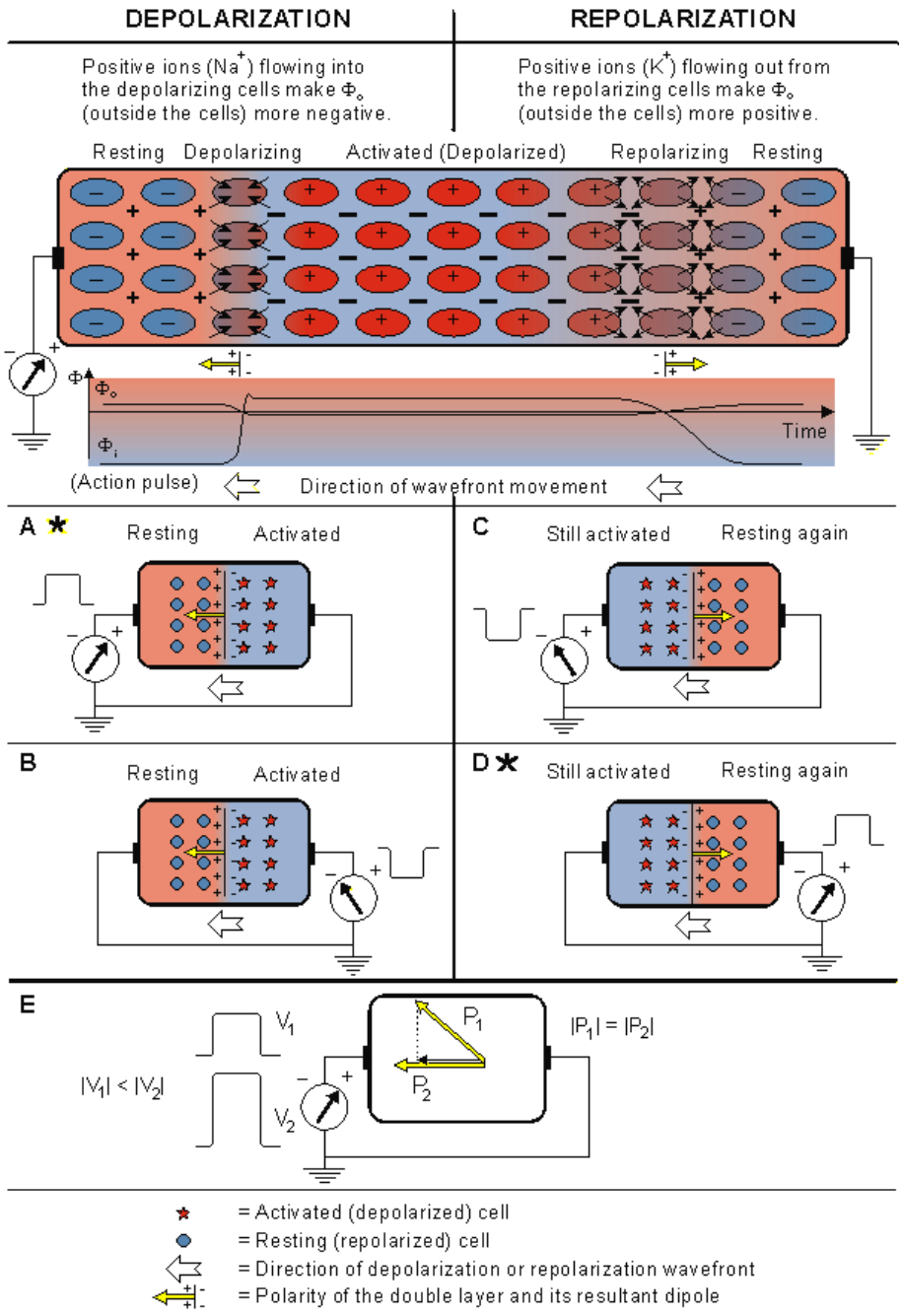

Figure 2.5 Signals produced by propagating activation fronts in extracellular electrodes from [38].

2.4.2 Generation

This section describes how the ECG is generated due to the path of the depolarisation and repolarisation waves through the heart. It is important that the path that the depolarisation waves takes through the heart leads to activation of the heart in such a way that efficient pumping occurs. This is achieved in the human heart via specialised conduction system consisting of specialised conduction cells where the wave conduction velocity is high in order to improve the spread of activation. Activation of the larval zebrafish heart is rather simpler due its tubular structure and early stage of development.

As shown in the previous section, the polarity of a detected signal is dependent on electrode position and therefore so is the shape of the ECG. This has led to a standard system of electrode positions called the 12 Lead ECG system being developed. This allows for standard electrode positions which results in ECGs being measured in the same way and at the same positions between patients. For the larval zebrafish there is no such standard system with electrodes approximately positioned in the same way for each measurement which leads to some variability in the measured signal. Larval zebrafish ECG measurements are most similar to the unipolar leads of the 12 Lead ECG system that are placed across the chest as electrodes are placed on the zebrafish body surface with a distance ground.

The conduction system of the human heart consists of the sinoatrial node, Bachmann's Bundle, intermodal pathways, the atrioventricular node, bundles branches and the Purkinje fibres (Figure 2.6 A). This figure shows which area of the heart generates which section of the ECG and Figure 2.6 B shows a schematic image of the ECG with the key features labelled. Propagation of the depolarisation wave begins at the SA node, from here depolarisation spreads into the surrounding tissue in the right atrial wall and quickly along Bachmann's bundle to the

left atrium. This results in the entirety of both atriums becoming depolarised at nearly the same time which then makes them contract in unison. This activation of the atrium shows on the ECG as the P wave (Figure 2.6 B). At the same time, the depolarisation wave is travelling along the intermodal pathways to the AV node. The AV node is the only place where the wave can enter the ventricle. Conduction is slow through this region allowing time for the contraction of the atria to fill the ventricles. Activation then travels along more fast conducting fibres before branching in to the left and right bundle branches that run together parallel to the base of the heart in the septum (which generates the Q wave) and then diverge into the Purkinje fibres. The wave then spreads quickly from the base of the heart and up through the ventricles causing them to contract at once. Ventricle depolarisation is detected as the R wave in the ECG. Repolarisation of the heart does not occur in exactly the same way as depolarisation. Epicardial cells on the outer surface of the ventricle have a shorter duration AP than endocardial cells on the inner surface. This means that the epicardial cells repolarise before the endocardial cells. Ventricular repolarisation results in the T wave and this change in duration is responsible for its polarity. Atrial repolarisation occurs at the same time as ventricular repolarisation and so is covered by the R wave. Common intervals are marked on Figure 2.6 B that are used in diagnosis. The PR interval is the delay between atrial depolarisation and ventricular depolarisation and the QT interval is the delay between ventricular depolarisation and ventricular repolarisation.

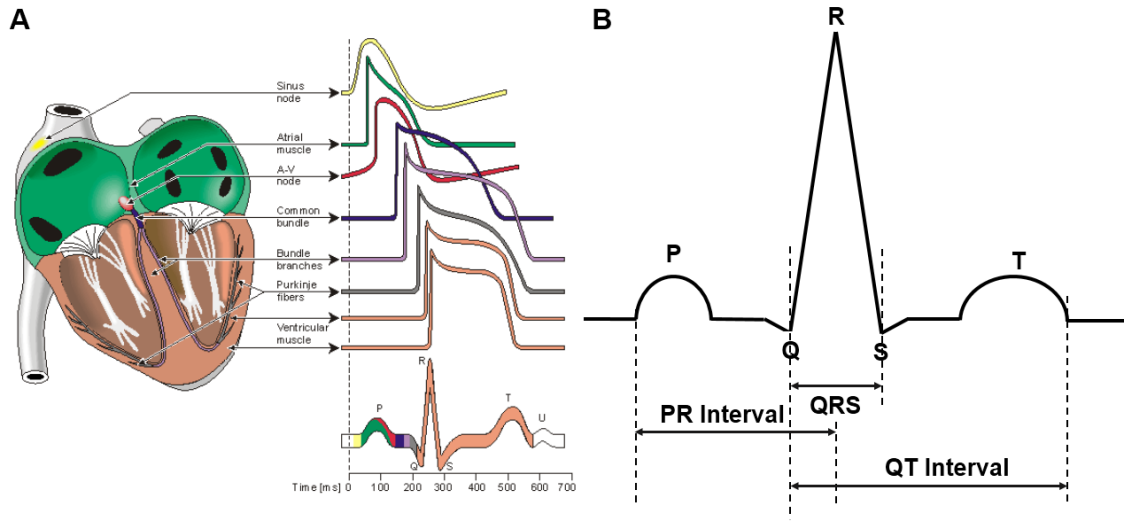

Figure 2.6 A) Human heart conduction system with action potentials for each region and resultant ECG, B) schematic typical Lead II (left leg – right arm) human ECG with labels [38].

The path of activation through the larval zebrafish heart can be seen from an activation map which plots the time course of activation as one image with separation between lines equal to 5 ms (Figure 2.7 A). Depolarisation is initiated in the SA region which spreads into the atrium which fully depolarises before the wave enters the AV band. The wave is then delayed in this region (tighter lines) before entering the ventricle where depolarisation spreads fully. A typical ECG recorded from a position over the ventricle of a 3 dpf zebrafish is also shown (Figure 2.7 B). This shows what is to be expected from an ECG measured at this position with positive P waves and R waves due to the wave travelling towards the electrode. Followed by a negative T wave which shows repolarisation occurs in the same order as depolarisation. This is discussed in more detail in chapters 5 and 6.

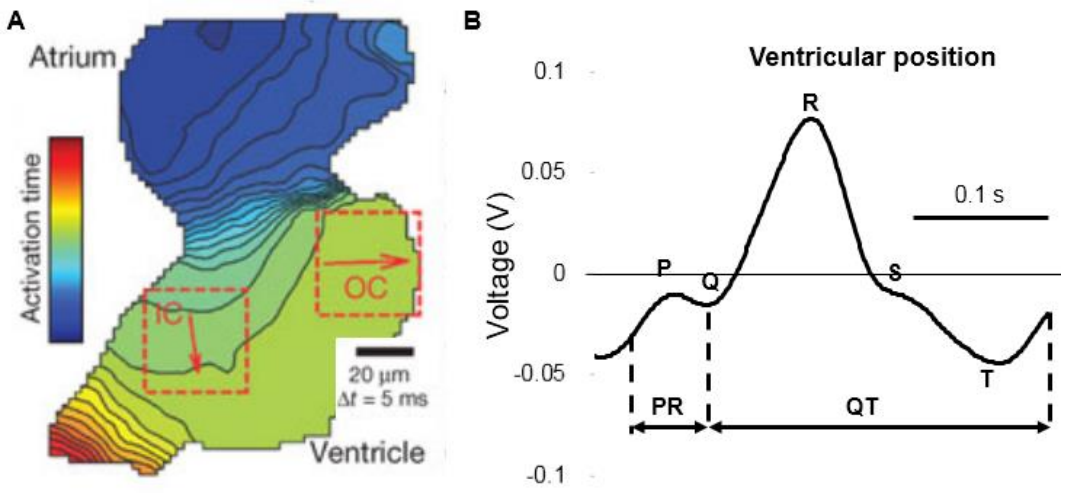

Figure 2.7 A) 3 dpf zebrafish heart activation map [59], B) a typical 3 dpf zebrafish ECG from a ventricular position. Supplied by Sundeep Dhillon.

The larval zebrafish ECG shares many similarities with the human ECG. The same gross features are present even though the size and shape of the hearts are quite different. The reason for the similarity in the shape is that both hearts follow largely the same activation sequence. The human heart, although it has four chambers instead of two, activates both atriums followed by both ventricles. This is the same sequence as in the zebrafish heart where the atrium is activated followed by the ventricle. The signal from the atriums of both hearts are detected as the P wave on each ECG. Repolarisation of the atrium occurs at the same time as ventricular depolarisation so it is masked in both hearts leading to a solitary R wave. Then the ventricle repolarises in both hearts, producing a T wave.

The usefulness of the ECG as a diagnostic tool can be seen as its form reveals if the heart is functioning correctly or otherwise by showing if depolarisation and repolarisation is occurring within normal parameters, allowing diagnosis of many cardiac dysfunctions.

This concludes the summary of cardiac anatomy and the generation of the ECG, in the next chapter the methods used to model this activity are described.

3. MODELLING THE HEART AND THE ECG

One of the main objectives of the work presented in this thesis was to model the electrical activity of the larval zebrafish heart to simulate the ECG to aid measurements. Therefore, this section introduces various models and methods of modelling this activity. There is a large amount of literature about modelling the human heart but there is no previous work relating to the modelling zebrafish larval heart (apart from the fluid flow model [43]). Therefore, it was assumed that the same modelling techniques that are applied to the human heart could also be applied to the larval zebrafish heart. The basis for all the heart models is that the body is a volume conductor and the heart is as a current source. Models of the heart can either be stationary or static (not varying with time) as well as time dependent. Stationary models can also become pseudo time dependent by using multiple solutions with variations in the current source to replicate different points in time.

A large amount of different current sources have been previously used to model the heart ranging from simple (point dipoles) to realistic (full ionic models). These sources are separated into two main categories, equivalent cardiac generators/sources (simple) and tissue models (realistic).

Common methods for modelling the electrical activity of the human heart and/or ECG include tissue (discrete and continuum), cell automaton and equivalent cardiac generator models. There are advantages and disadvantages to each sort of model. The heart models described in this thesis either use an equivalent cardiac generator or a continuum model. The final model presented in this work uses a continuum model, specifically the bidomain model. This model was chosen as it is compatible with ionic models that are capable of simulating the

key properties of the hearts electrical activity such as action potentials and wave propagation as well as fulfilling the main aim of the heart modelling work which was to simulate the ECG. This model made it possible to utilise much of the data available in the literature (explained in chapter 6). It is also a widely used model that has been extensively used to model both the human heart and the ECG and so there is extensive work in the literature describing its implementation [35, 38]. The disadvantage of this model (also discussed in chapter 6) is that it is not suited to modelling a small number of cells as is the case with the larval zebrafish heart. Alternatively, there are cell automaton models which generally consist of a number of elements that may represent a single cell or many cells where an activation state is applied to each element (e.g. resting or excited) [60]. The states of multiple elements can then be set to simulate activation of the heart at different instances of time. These models have the advantage that they are well suited to a low number of cells. They also have the disadvantage that they are a simplified representation of activation and they require determination of cell positioning to be most effective [35, 61]. It was not possible to determine the position of cells within the larval zebrafish heart due to limited imaging equipment and there is much more literature regarding ECG simulations using a bidomain model. Therefore, a cell automata model would have limited advantages over an equivalent cardiac generator model, which were used and are inferior to a bidomain model. This is because the size and position of the elements that could have been used would reduce the realism of this type of model. If the cell positions could have been determined, a cell automaton could have been created. However, if this was the case, a more ideal solution would have been to create a discrete tissue model rather than a cell automaton model. Therefore, it was decided the bidomain model was the best option available to create the most realistic model possible given the available data.

This chapter first describes a volume conductor followed by overviews of different current sources and ends with a brief description of the finite element method and the use of COMSOL Multiphysics in which the heart models were built. Much of the information presented in this section is in the style of and gathered from [38] unless otherwise stated.

3.1 Volume conductor

A volume conductor is defined as a volume that has a resistivity in which a current source resides. There are two main types of volume conductor which are homogenous and inhomogeneous. Homogenous volume conductors simplify the real biological features into a single conducting medium surrounding the current source. An inhomogeneous volume conductor is more representative of the actual physical situation and contains features such as the lungs or bones with corresponding resistivity values. A homogeneous volume conductor was used for all the models in this thesis due to available data and close proximity of the zebrafish heart to the body surface.

3.1.1 Mathematical description

The voltage distribution in a volume conductor (the body) that results from a current source can be modelled by considering a current source that is placed in an infinite and homogenous volume conductor with conductivity, σ [38]. This current source creates an electric field ($\bar{E}$) and a conduction current ($\sigma\bar{E}$). The total current density is therefore given by:

$$\bar{J} = \bar{J}^{i} + \sigma\bar{E} \tag{3.1}$$

As the system is quasi-static the electric field can be expressed at each time as the negative gradient of a scaler potential φ, equation (*3.1*) can therefore be changed to:

$$\bar{J} = \bar{J}^{i} - \sigma\nabla\varphi \tag{3.2}$$

And also due to quasi-static conditions the capacitive effects of the tissue are negligible with a short amount of time for charges to redistribute. The divergence of $\bar{J}$ describes the rate of charge density with respect to time and as the charge density must be zero, $\nabla \cdot J$ is also zero. This leads to the Poisson equation:

$$\nabla \cdot J^i = \nabla \cdot \sigma \nabla \varphi + \nabla \cdot J = \sigma \nabla^2 \varphi \tag{3.3}$$

Or when the source is encased in a closed volume, Laplace's equation:

$$\sigma \nabla^2 \varphi = 0 \tag{3.4}$$

As a closed volume is used throughout this work, Laplace's equation is used with appropriate boundary conditions to determine the potential distribution resulting from a variety of different current sources.

3.2 Equivalent cardiac generators

An equivalent cardiac generator or source is a source or a set of sources that when placed in a realistically shaped volume conductor will produce potentials on the surface of the conductor equivalent to those from a real heart. The end result of this is that the real biological sources are replicated but the exact mechanism which generates the real potentials are not. The macroscopic overall effect of the heart current source is modelled by using the overall effects of the depolarisation and repolarisation wave. The reason equivalent sources can be used is that (as explained in chapter 2) the wavefront of the depolarisation and repolarisation waves can be approximated as a double layer at any point in time. A double layer consists of two parallel layers of charge, one positive and one negative separated by a small distance. Therefore, the electrical activity can be further approximated by lumping each side of the double layer into a positive and negative point separated by a small distance, forming a dipole. This source can

then be broken down even further by only modelling one side of the wavefront with a monopole. Point sources do not physically exist but they can replicate real sources which behave equivalently to a point source. The simplest representation of the entire wave is then a dipole (used in [62]) and the realism of a model can be increased by increasing the complexity and therefore the realism of the source by using multiple dipoles [63], multipoles [64] and moving dipoles [65-67], as has been done in the literature.

The equivalent sources used in this thesis are all variations of a single dipole. They are stationary/pseudo-time dependent and represent a fixed point in the cardiac activation cycle. The following sections derive the analytic solutions for a monopole followed by a dipole.

3.2.1 Monopole

The simplest type of source is a point source or monopole. It consists of a fixed direction and variable orientation and magnitude. The following is a derivation of the potential due to a monopole located at the origin in a region of infinite extent with a known conductivity as a function of the radial distance from the source. In this situation, current must flow in straight lines radially away from the source (Figure 3.1).

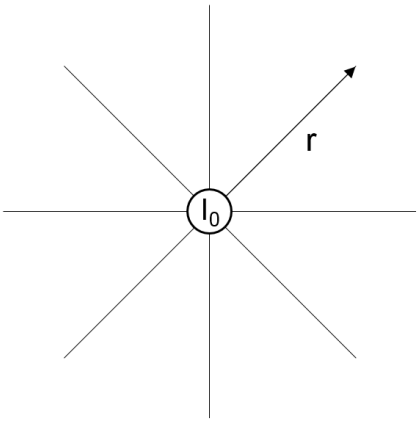

Figure 3.1 A monopole in an infinite conducting medium. I_0 is the current, r is the distance away from the source. The lines represent the current flow.

The current density at a point away from the source is then the total current divided by the surface area:

$$J = \frac{I_0}{4\pi r^2} \tag{3.5}$$

Where J is the current density, $I_0$is the magnitude of the current source and r is the distance away from the source. The current density can also be expressed as a vector:

$$\bar{J} = \frac{I_0}{4\pi r^2}\overline{a_r} \tag{3.6}$$

Where $\overline{a_r}$ is a unit vector in the direction of r. The current density is constant at each value of r with a scalar potential (φ) associated with the current source also constant at each r value. The electric field can be expressed as the negative gradient of the scalar potential:

$$\bar{E} = -\nabla\varphi \tag{3.7}$$

And the current density can be expressed in terms of the electric field (Ohm's law):

$$\bar{J} = \sigma\bar{E} \tag{3.8}$$

Then by combining (*3.7*) and (*3.8*) with (*3.6*):

$$\bar{J} = \frac{I_0}{4\pi r^2}\overline{a_r} = -\sigma\nabla\varphi \tag{3.9}$$

Only the r component of (*3.6*) is valid, therefore the equation becomes:

$$-\sigma\frac{d\varphi}{dr} = \frac{I_0}{4\pi r^2}\overline{a_r} \tag{3.10}$$

Which can be solved by integrating with respect to r:

$$\varphi = \frac{I_0}{4\pi\sigma r} \tag{3.11}$$

This equation shows that the potential is constant when the radius is constant and that the potential is at its maximum closest to the monopole and then falls away as r increases. The potential is proportional to 1/r.

An actual monopole cannot exist in bioelectric sources due to the need to conserve charge but multiple positive and negative monopoles that together have zero net charge can occur, the simplest example of which is the dipole.

3.2.2 Point dipole

The simplest form of a dipole is a fixed positive monopole (source) and a fixed point negative monopole of equal but opposite strength (I_0) separated by a small distance (d), where d $\rightarrow$ 0 and $I_0 \rightarrow \infty$. The dipole moment or magnitude is $p = I_0 d$. The fixed dipole has three variables in polar coordinates, the magnitude of the source and the two angles which describe its orientation. The orientation of a dipole is defined as the direction from the source to the sink. The dipole vector is given by:

$$\bar{p} = I_0 \bar{d} = I_0 d \overline{a_d} \tag{3.12}$$

Where the direction is defined from the negative to the positive point source with $\overline{a_d}$ being a unit vector in that direction. Figure 3.2 shows the geometry of a dipole with no specific origin with the sink $(-I_0)$ located at the origin of the coordinate system. The source (I_0) is located a small distance away (d) from the sink.

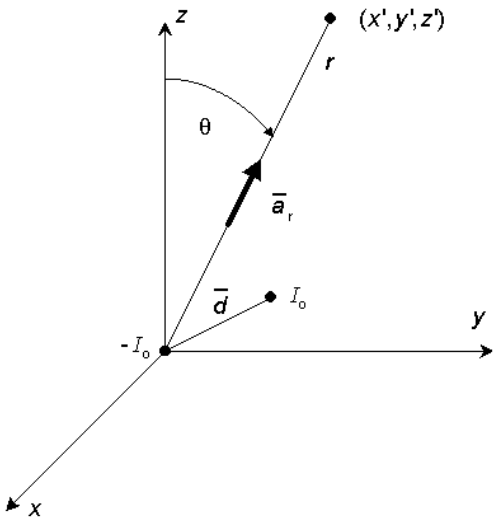

Figure 3.2 A dipole consisting of a source and sink (I_0 and $-I_0$) separated by a distance d (d->0). A point (A) is located at (x', y', z') from [38].

The dipole field is the field caused by moving the source away from the sink. This field can be calculated by using the expression for the positive monopole (Equation (*3.11*)) and evaluating how the potential field is changed by moving it. This is found by taking the first derivative with respect to the dipole direction ($\bar{d}$) and then multiplying by d:

$$\varphi_d = \frac{\partial\left(\frac{I_0}{4\pi\sigma r}\right)}{\partial d} d \tag{3.13}$$

This directional derivative is equal to the $\bar{d}$ component of the gradient:

$$\varphi_d = \nabla\left(\frac{I_0}{4\pi\sigma r}\right) \cdot \bar{d} \tag{3.14}$$

And by using $p = I_0 d$ (*3.14*) becomes:

$$\varphi_d = \frac{p}{4\pi\sigma} \nabla\left(\frac{1}{r}\right) \cdot \overline{a_d} \tag{3.15}$$

If the dipole is orientated along the z axis the gradient is calculated using:

$$\nabla\left(\frac{1}{r}\right) = \frac{1}{r^2}\,\overline{a_r} \tag{3.16}$$

Where $\overline{a_r}$ points from source to field. The dipole field is given by:

$$\varphi_d = \frac{p}{4\pi\sigma r^2}\,\overline{a_r}\cdot\overline{a_z} \tag{3.17}$$

As the magnitudes of $\overline{a_r}$ and $\overline{a_z}$ are equal, their dot product becomes equal to $\cos\theta$. So the dipole field is given by:

$$\varphi_d = \frac{p\cos\theta}{4\pi\sigma r^2} \tag{3.18}$$

This equation shows that the potential of a dipole varies according to $1/r^2$ as opposed to 1/r for the monopole. The potential is fixed by r when moving radially from the dipole but there is also an angular dependence on the voltage which was not present for the monopole. Therefore, the potential distribution does not form concentric spheres but varies around the dipole. Figure 3.3 shows a plot of the potential produced by each source ((*3.11*) and (*3.18*)). r ranges from 1 to 20 in both and the conductivity is 1. I_0 is 1 for the monopole and $1\text{x}10^6$ for the dipole. d is $1\text{x}10^{-6}$ and θ is zero. These values result in potentials of the same size for both sources. The potential starts at the same value and then falls more quickly for the dipole due to the dependence on $1/r^2$.

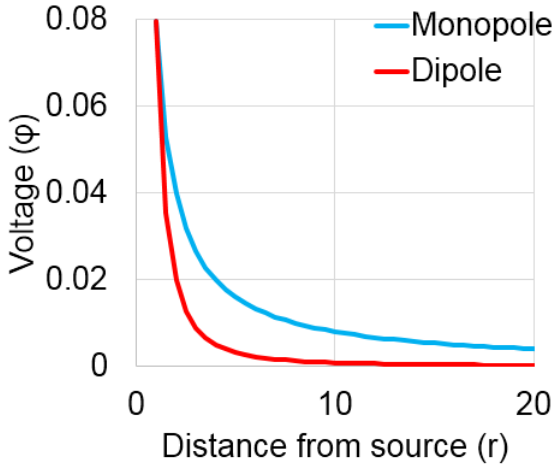

Figure 3.3 Plot showing the dependence of the potential on the distance from the source for a monopole and dipole.

In addition to a single dipole, multiple dipoles can be used to replicate a section of activity that splits and moves in two or more directions. Together multiple dipoles form higher order

multipoles such as quadrupoles (2 dipoles) or octapoles (4 dipoles) which are formed by even numbers of dipoles. Moving dipoles can also be used which involves using a normal point dipole and varying its position to simulate the path of the wave.

3.3 Tissue models

Simple equivalent cardiac generators work well for modelling the normal healthy heart but aren't as realistic when modelling an abnormal heart or the finer details of activity [68, 69]. Tissue models use current sources that are aiming to partially or fully recreate the physical biological sources which makes them more complex but also more accurate in their predictions. All tissue models are generally time dependent as they replicate the change in the cellular ionic currents through time which means action potentials and wave propagation are modelled. There are two types of tissue model, discrete models which mainly deal with the microscopic structure of the heart and continuum models which deal with larger sections of tissue or the whole heart and the ECG.

The general structure of a tissue model is that there is an ionic model of the cell which describes the ionic current that is paired with a capacitive current, the wave is then modelled using diffusion.

Ionic models describe electrical activity of excitable cells by modelling the flow of ions across the membrane via the series of channels, pumps and exchangers that are present in the membrane and inside of the cell. Such models are usually created by fitting equations to experimentally recorded data. The first example of this is the Hodgkin-Huxley model [58] mentioned earlier. Many other models have been developed since this was introduced, specifically for cardiac cells, among them, the work of Noble [29] in 1962 or Luo and Rudy [70] in 1991. The detail added to these models is constantly increasing producing ever more

complex models with a brief history given by Henriquez in [35]. However, sometimes this detail is not needed and less realistic models known as phenomenological models can be used that are still able to simulate the main or key properties of cardiac tissue to achieve the desired result such as the Karma model [71]. When selecting or developing a model a number of things need to be considered such as what system the model is of, the aim of the modelling, the available data and what additional data can be measured. A compromise is then reached and a model is selected or modified from the available options. What follows is an overview of the ionic model (Fitzhugh-Nagumo) used in this thesis (in various forms) as well as the bidomain model.

3.3.1 The Fitzhugh-Nagumo equations

Developed from the Hodgkin-Huxley model, the Fitzhugh-Nagumo equations are a phenomenological ionic heart model. This means that they do not replicate the exact mechanisms of the hearts electrophysiology but they do replicate the main features such as the threshold for excitation, action potentials and refractory period. They were originally proposed by Richard Fitzhugh in 1961 [72] as a reduction from the Hodgkin-Huxley [58] equations. Fitzhugh took the equations for the multiple ion channels and combined them into one 'fast' current and one 'slow' current. The fast current groups the currents which are responsible for the depolarisation (chapter 2) or action potential upstroke (mainly Na^+) and the slow current groups the currents which are responsible for the repolarisation (mainly K^+). This reduction or simplification meant that the resulting equations were easier to solve and interpret and phase plane analysis could be used [72]. Later Nagumo [73] presented an equivalent circuit of the equations which gives them their name, the Fitzhugh-Nagumo (FHN) equations (Figure 3.4).

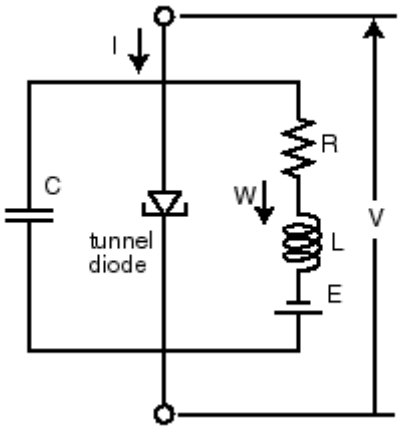

Figure 3.4 Circuit diagram of the FHN equations. C is a capacitor, R is a resistor, L is an inductor. From [73].

They were originally used to model nerve action potentials but a modification by Rogers et al made the action potentials produced by them more applicable to cardiac action potentials [74]. The original equations appear in the literature in a number of different forms [75, 76] with the form used by Rogers et al and in this work given by:

$$\frac{du}{dt} = c_1 u(u-a)(1-u) - c_2 v \tag{3.19}$$

$$\frac{dv}{dt} = b(u - dv) \tag{3.20}$$

These equations describe change in two variables u and v over time. u is equivalent to the membrane potential and v is a recovery variable. a, b, c_1, c_2 and d are 'membrane parameters' that define the shape of the AP. The action potential produced by these equations is shown in Figure 3.5, using parameters a = 0.12, b = 0.011, c_1 = 0.175, c_2 = 0.03 and d = 0.55. The equations describe the activity at a single point, in order to model the movement of the action potential through space a diffusion term is added which makes a reaction diffusion system.

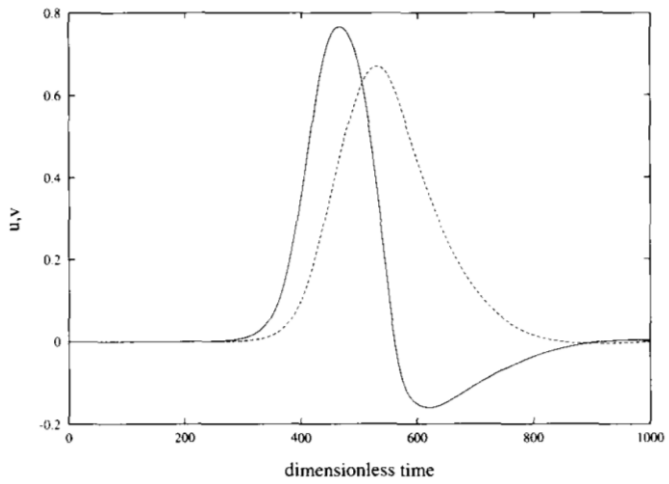

Figure 3.5 Plot showing u (solid line) and v (dashed line) verses time. From [74].

This action potential resembles that from a nerve, with a hyperpolarisation at the end of the repolarisation, Rogers *et al* found that multiplying by u in the last term of the first equation removes this hyperpolarisation resulting in an action potential more similar to those of cardiac cells (Figure 3.6). The Rogers version of the FHN equations are:

$$\frac{\partial u}{\partial t} = \nabla \cdot D\nabla u + c_1 u(u-a)(1-u) - c_2 uv \tag{3.21}$$

$$\frac{\partial v}{\partial t} = b(u - dv) \tag{3.22}$$

Where D is the diffusion coefficient which is anisotropic. The parameter values are shown in Table *3.1* with the action potential produced by these parameters shown in Figure 3.6. These parameters are general and were chosen by trial and error to produce a travelling wave solution by Rogers *et al* [74].

Table 3.1 – Parameter values for the Rogers FHN equations.

Parameter	Value
a	0.13
b	0.013
c_1	0.26
c_2	0.1
d	1
D	1-4

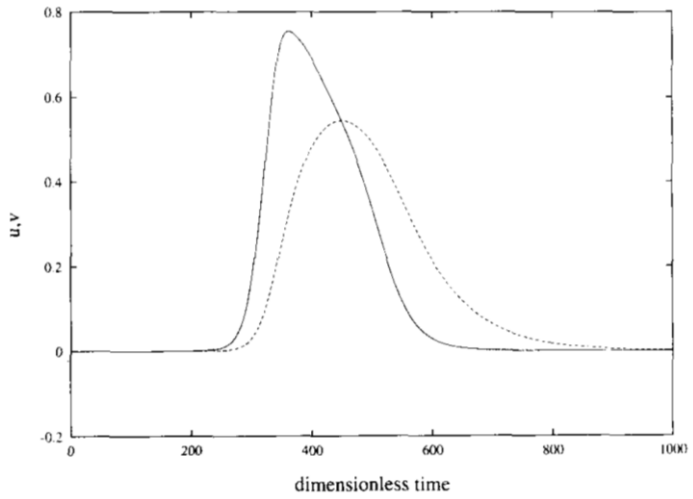

Figure 3.6 Plot showing u (solid line) and v (dashed line) verses time. A Rogers modified Fitzhugh-Nagumo action potential with no hyperpolarisation. From [74].

The FHN equations use arbitrary units, Rogers *et al* converted these to real units by comparison to measured results. They did this by equating one time unit to 0.63 ms and one space unit to 0.99 mm. Dokos *et al [31]* used a different method by scaling the equations so that one time unit corresponded to one second and one voltage unit corresponded to one volt. These further modified equations are shown below:

$$\frac{\partial u}{\partial t} = kc_1(u-B)\left[a-\frac{(u-B)}{A}\right]\left[1-\frac{(u-B)}{A}\right]+kc_2v(u-B) \tag{3.23}$$

$$\frac{\partial v}{\partial t} = ke\left[\frac{(u-B)}{A}-dv-b\right] \tag{3.24}$$

Where the scaling parameters are k, which scales the time, A, which scales the voltage and B, which offsets the voltage. This is the form of the equations that are used in chapter 6 which explains the exploration of these parameters that was needed to replicate zebrafish action potentials. There is no diffusion term as these equations can be used to simulate cardiac activity at a single point or a diffusion term can be added (as in Eq. (*3.21*)) to simulate a travelling wave.

The FHN equations were chosen for the heart model as they could be used with the data that was available. They have been previously used to model the ECG [77], however, the ECG

is generated by the extracellular potentials on the surface of the heart which are not modelled by the FHN equations by themselves. Therefore, an addition to the model is needed which can be used to model the intracellular and extracellular potentials, this model is known as the bidomain model.

3.3.2 The Bidomain model

An essential prerequisite to the bidomain model is that the heart can be treated as a syncytium. Of course, the reality is that the heart consists of many cells connected together by gap junctions. The electrical resistance of the gap junctions is approximately equal to the resistance of the entire cytoplasm of a cell but this resistance is confined to a much smaller area. This means that the junctional resistance can be considered to be a point resistance whereas the cytoplasmic resistance is distributed. These two resistances are averaged together to form a volume conductor that fills the entire intracellular space. The same can be done for the extracellular space where there are no point resistances, but the cellular structure still has an effect on the resistance, so the resistance is again averaged over multiple cells forming another continuous conducting medium. Together these two mediums form a bidomain that fills the heart tissue. This model can then be used to model the heart using suitable parameters. To simulate the ECG, there is also a third region which represents the exterior of the heart or the body.

The bidomain equations are derived as follows [37, 38] starting with the definition of the membrane potential (as before):

$$V_m = V_i - V_e \tag{3.25}$$

Current is assumed to only flow between the extracellular region and the body according to the defined boundary conditions. Ohms law states:

$$\boldsymbol{J} = \sigma \boldsymbol{E} \tag{3.26}$$

Where J is the current density, σ is conductivity and E is the electric field. Using the quasistatic approximation [78]:

$$\boldsymbol{E} = -\nabla \mathrm{V} \tag{3.27}$$

Where V is the voltage. Then for the two domains combining (3.26) and (3.27):

$$\boldsymbol{J}_i = -\sigma_i \nabla \cdot V_i \tag{3.28}$$

$$\boldsymbol{J}_e = -\sigma_e \nabla \cdot V_e \tag{3.29}$$

Any current that leaves one domain must flow into the other due to current conservation therefore the change in current density between the two domains is equal in magnitude and opposite in sign:

$$-\nabla \boldsymbol{J}_i = \nabla \boldsymbol{J}_e = A_m I_m \tag{3.30}$$

Where I_m is the transmembrane current, given by:

$$I_m = C_m \frac{\partial V_m}{\partial t} + i_{ion} \tag{3.31}$$

Where C_m is capacitance per unit area and i_{ion} is the ionic current. Then, combining (3.28), (3.29) and (3.30) gives:

$$\nabla \cdot (\sigma_i \nabla V_i) = A_m I_m \tag{3.32}$$

$$\nabla \cdot (\sigma_e \nabla V_e) = -A_m I_m \tag{3.33}$$

The bidomain equations are compatible with a variety of ionic models. The FHN equations can be used by inserting them into equation (3.32) and (3.33) for the ionic current (i_{ion}).

These equations can then be solved using an appropriate ionic model and boundary conditions. Which are described in chapter 6. This model has been used widely to model both the heart and the resulting ECG [40]. It is useful for modelling an entire heart due to its

averaging of cellular effects. It is computationally intensive [79] but recent advancements in computing power has increased its use along with being able to implement it using commercial software packages such as the COMSOL model presented by Sovilj *et al* [80].

This model uses a simplified human heart and body geometry together with the bidomain equations and the Fitzhugh-Nagumo equations as the ionic model to simulate the 12 Lead ECG as shown in Figure 3.7. The geometry is constructed from simple shapes based on approximate real sizes. The heart consists of individual regions which are given specific properties by varying the parameters of the equations in each region to produce individual action potentials and conduction velocities. The path of the activation wave is also replicated within the model. This results in a reasonably realistic voltage distribution on the surface of the model torso with ECGs such as the lead II simulation (D).

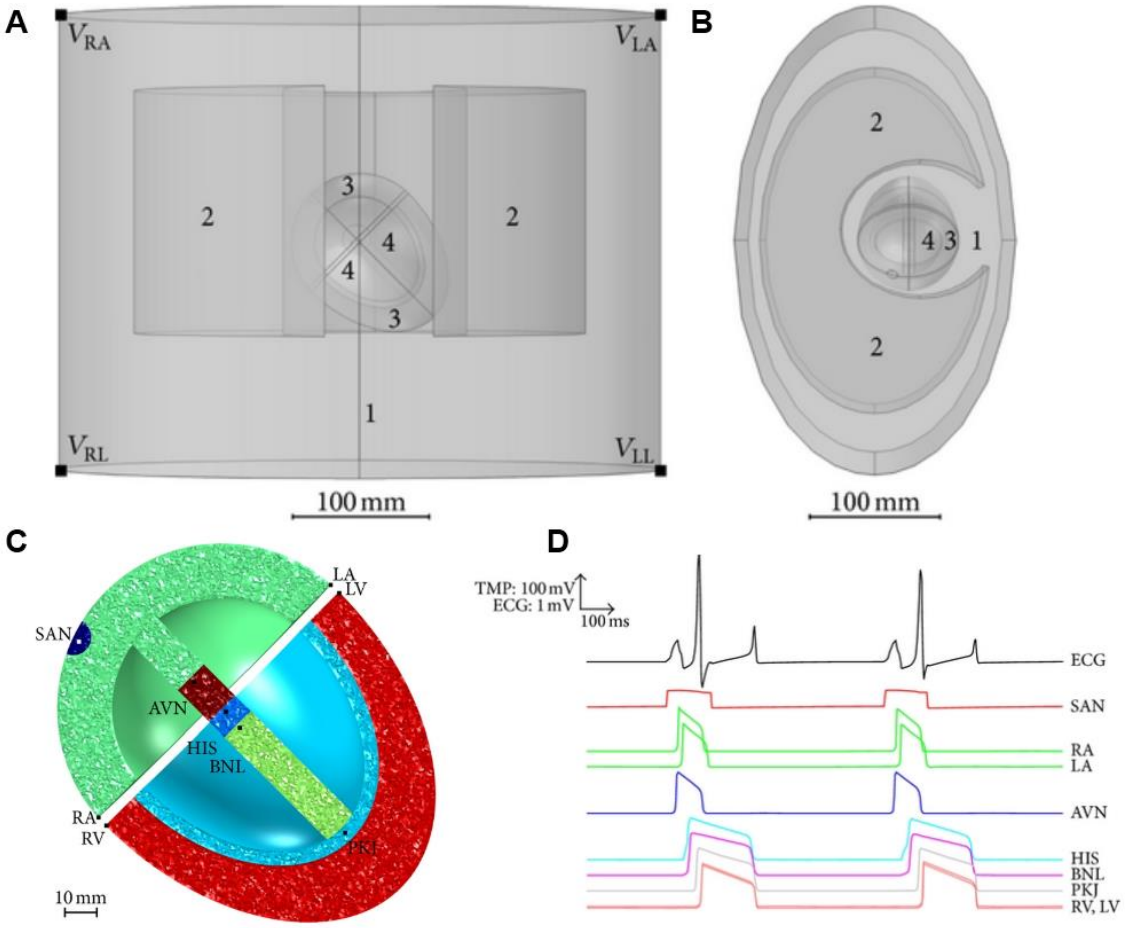

Figure 3.7 A) Simplified human heart and torso geometry. 1 torso, 2 lungs 3 and 4 heart. Electrode positions are marked, B) top view of the geometry, C) simplified heart geometry with distinct regions, D) model results showing Lead II ECG with associated action potentials for each region [80].

The main disadvantage of bidomain models is that a continuum doesn't replicate the hearts fine structure, which is important for small regions of tissue like the larval zebrafish heart, in the same way a discrete model of every cell would which is discussed in chapter 6.

3.4 ECG Modelling

ECG modelling falls in to two categories, the first being the forward problem [36] which relates to determining the potential on the surface of the body from a known source. In this problem the source is known as well as the properties of the body (volume conductor). This problem has a unique solution which can always be known by calculating the field produced by the selected

source in the volume conductor. The accuracy of the solution is only limited by how accurate the selected source and volume conductor are to the biological reality. This is a situation that does not occur during ECG measurements as only the field is measured from an 'unknown' source.

The other problem is known as the inverse problem [81] and occurs during clinical use of the ECG, the potential on the body surface is measured and clinicians want to know the exact nature of the source that is generating the potentials in order to diagnose dysfunctions effectively. This problem does not have a unique solution [60] but there are a number of ways to solve it with acceptable accuracy. Possible solutions to this problem include the empirical approach and the use of a simplified source model. The empirical approach is the one taken by clinicians who use pattern recognition to recognise abnormalities in ECGs based on previously recorded ECGs of the same abnormality. A simplified source model is chosen that can be solved that replicates the measured data.

The method used to model the zebrafish heart is the forward problem as the potential on the body surface is calculated from a current source. However, some assumptions have been made about the source as well as looking at the ECGs recorded from the zebrafish which means it is partially the inverse problem as well.

3.5 Modelling methods

In order to model the electrical activity of the heart, the equations which describe the activity need to be solved. This has been done previously analytically as well with a variety of numerical methods including the finite difference method (FDM), boundary element method (BEM) and the finite element method (FEM) which is used in this thesis. Analytic methods are limited to simple geometries [62, 82] and so limited whereas the other methods have a wider use. The

method chosen for this work was FEM. This method was chosen over the other numerical methods as it is more capable of handling complex geometries than FDM (like those found in biological systems) and it is more flexible than BEM when solving non-linear equations (like those that describe the heart's electrical activity) [83-85]. In addition, software based on the finite element method was available (COMSOL Multiphysics) to use, with which it was possible to create and solve heart and electrode models. This section briefly describes FEM as well as the use of COMSOL Multiphysics.

3.5.1 The finite element method

The finite element method (FEM) or finite element analysis (FEA) is a numerical method for finding an approximate solution to a set of governing equations with specified boundary conditions over a prescribed geometry [84]. It involves splitting the geometry into small sections (finite elements) in a process known as meshing which together form a network of finite elements known as a mesh. FEA has been used extensively to study a wide variety of problems including the heart and the ECG [25].

Individual elements can vary in size as well as shape. The models described in chapter 5-8 use only triangular (2D) and tetrahedral (3D) elements. Elements are connected to one another at the edges by node points, so for example, a triangular element contains 3 node points. More intricate geometries require more elements to accurately represent them, as shown in Figure 3.8. The circle is represented by too few elements in (A) becoming an octagon but a square still retains its shape, with a finer mesh the circle is much better replicated (B).

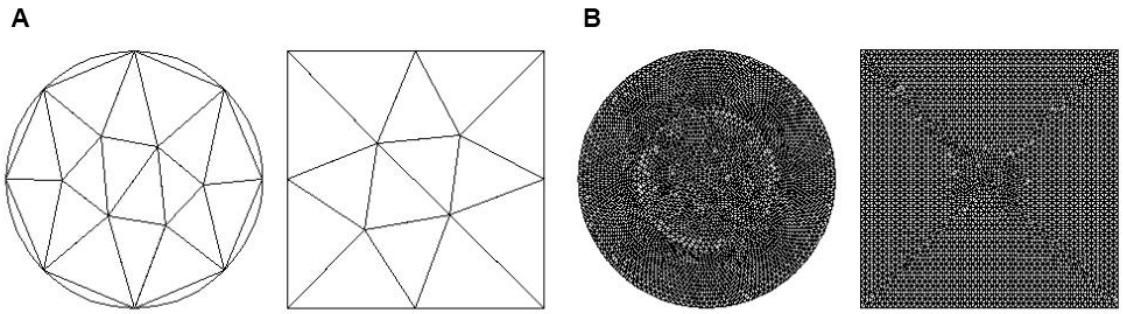

Figure 3.8 A square and a circle represented by different mesh sizes generated using COMSOL, A) a very coarse mesh, B) a very fine mesh.

Using the governing equations, an equation or a series of equations are applied to each node with an interpolation function used to approximate the dependent variable over each element. The result of this is a set of simultaneous equations, with the objective being to determine the unknown coefficients of these equations to find the best approximation to the real solution of the governing equations. For a continuum there are an infinite number of equations but because there are a finite number of nodes there are a finite number of equations.

Due to this, care is needed to ensure a fine enough mesh is chosen to represent the geometry as well as any rapid changes in the dependant variables used, which in heart models is the AP upstroke. The disadvantage of this is that larger numbers of elements mean a longer solution time.

3.5.2 COMSOL Multiphysics

The models presented in this thesis were created using COMSOL Multiphysics 4.3-5.2. which is a commercial finite element modelling software package. It offers the ability to solve a wide range of problems ranging from general partial differential equation (PDE) solving to specific modules that are tailored to structural mechanics or electrodynamics amongst many others. These modules each have individual physics interfaces which allow application of boundary conditions, initial values and coefficients specific to each application. A key feature of COMSOL is that multiple

physics interfaces/different governing equation can be combined hence the name Multiphysics. This coupling is performed using appropriate boundary conditions and PDE terms. The software then solves all equations as one system.

The specific modules used in this work are the AC/DC module with the electric currents interface for modelling the body in the heart models as well as the electrodes in the electrode models. This module was used along with the mathematics module and the coefficient PDE interface which was used with the Fitzhugh-Nagumo equations. Both time dependent and stationary simulations could be performed with each module used. The heart models take advantage of the multiphysics option to couple the two interfaces using the boundary conditions described in chapters 5 and 6.

Different solvers are also available for stationary, time dependent and frequency domain problems. Meshing is usually performed using the preconfigured mesh sizes which are generally adequate. However, different mesh types or mesh properties can be selected if required. A parametric sweep can also be added which allows the user to input a range of values for a given parameter or parameters. A solution is then found for each variable for each value of the parameters and the results can be compared using post processing tools or the model data can be exported. Simple geometry can be constructed within COMSOL using blocks/circles and work planes or more complex geometry can be imported into COMSOL from CAD or 3D modelling software. Details of how each model used each of these feature is given in chapters 5-8.

4. ELECTRODES FOR ECG

This chapter provides context and background information for the electrode models (chapter 7) and practical work (chapter 8) described in this thesis. As stated previously, zebrafish ECG measurements have been obtained for zebrafish at various ages from larvae to adult [1, 6-11]. There are two main types of electrode used which are micropipette electrodes (for larvae [11] and metal electrodes (for adults [86]). Application of the metal electrodes to the larval zebrafish is the goal of the project, as they have the potential to be suitable for high throughput. This chapter starts with a description of each electrode type followed by a description of a model of the metal electrolyte interface. An overview of methods to fabricate these metal electrodes is then given as well the methods to test them and then finally an overview is given of the previous work that chapter 8 continues.

4.1 Electrode types

There are a number of considerations to be made when selecting an electrode for a measurement, this includes the choice of materials, biocompatibility as well as electrode size, shape and electrical impedance.

4.1.1 Effect of electrode impedance

Electrode size and shape refer to the size and shape of the conductive area of the electrode [87]. Electrode impedance is defined as the opposition of the electrode to a current when in a potential field. Therefore, a lower electrode impedance allows a larger current to pass for a certain voltage and attenuates the signal less than a higher impedance electrode. The spatial sensitivity and signal-to-noise ratio effect the recorded signal quality and are dependent on electrode size and shape [88]. Any increase in size reduces the spatial sensitivity but reduces impedance [89].

This is true for smaller electrodes as they intercept a smaller proportion of the field which improves measurement of the local signal. Increased impedance with small electrodes mean that measured voltages are reduced as well as increasing noise [88]. Therefore, a compromise is needed between spatial sensitivity and electrode impedance [90]. This phenomena is known as spatial filtering [91].

Any increase in electrode impedance results in a reduced input voltage to a connected amplifier as well as an increase in thermal noise. The voltage reduction due to the impedance [88] is shown in Figure 4.1.

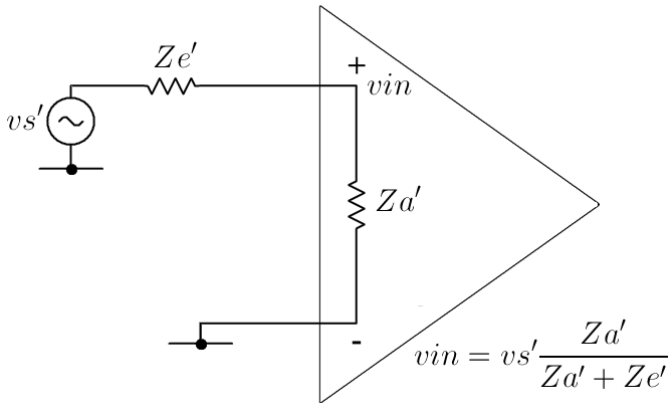

Figure 4.1 Effect of impedance on input voltage to amplifier [88].

The thermal noise is given by [90]:

$$\Delta V_N = \sqrt{4k_B ZT\Delta f} \tag{4.1}$$

Where $\Delta V_N$is the thermal noise (V), k_B is Boltzmann's constant, Z is the real part of electrode impedance, T is the temperature and Δf is the bandwidth of the signal. Figure 4.2 shows the effect of this for different signal magnitudes by plotting the signal to noise ratio (SNR) against different impedance magnitudes. This is for 25^{o}C with a bandwidth of 1 GHz with typical signal magnitudes for zebrafish ECG experiments (~µV). This shows that for the same signal magnitude, a higher impedance results in a smaller SNR. Smaller signals obviously also have

a lower SNR, which means the electrode impedance needs to be as low as possible and the SNR needs to be above one in order to differentiate the signal from the noise.

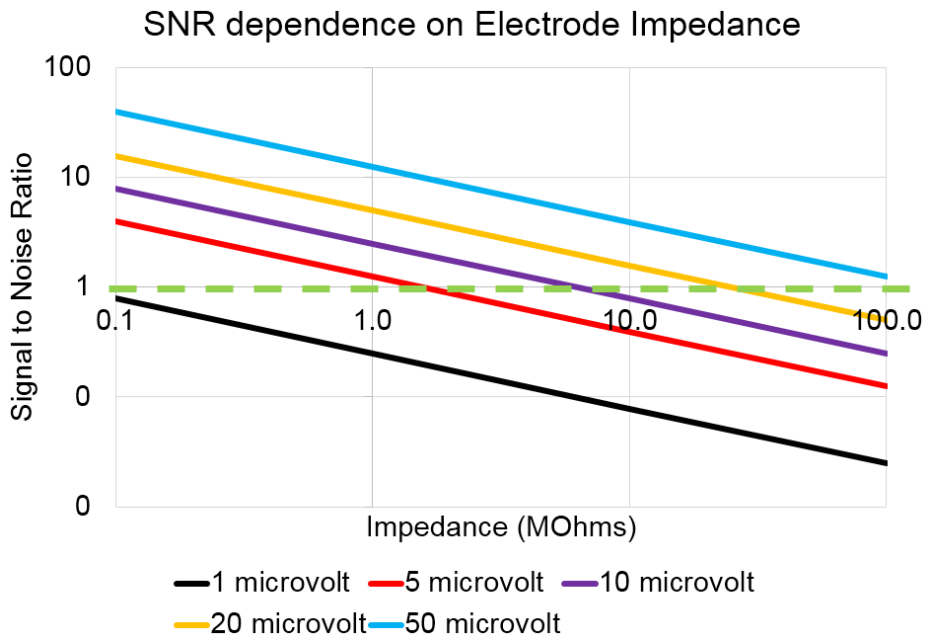

Figure 4.2 Signal to noise ratio for different electrode impedances and magnitudes of signal.

4.1.2 Micropipette electrodes

The current method for measuring the larval ECG is to use micropipette electrodes. This allows a high quality signal to be measured due to its construction (Figure 4.3) which insulates (using glass) the metal interface to the external electronics from the potential field. This means a large area of metal can be used without compromising on spatial resolution resulting in a relatively low impedance. These electrodes are available in a range of sizes depending on the application with a 2 µm diameter tip used for larval zebrafish ECG recordings. Different sizes of tip (opening) have no effect on the impedance provided that the metal and electrolyte remain unchanged but the tip diameter does affect the spatial resolution of the electrode. A typical measurement procedure is described in chapter 6. These electrodes can also be used to measure signals at the cellular level such as APs using voltage clamp techniques. In addition, they also have a low impedance of around 1 MΩ [92]. The disadvantage of these types of electrodes for

ECG measurements is that for each measurement, time consuming positioning of the zebrafish and electrode are required which is amplified by the need for a large number of measurements to confirm drug effects. In addition to this, it can be useful to measure signals from more than one position on the body surface, which means additional positioning and mass production of these electrodes can be difficult [93].

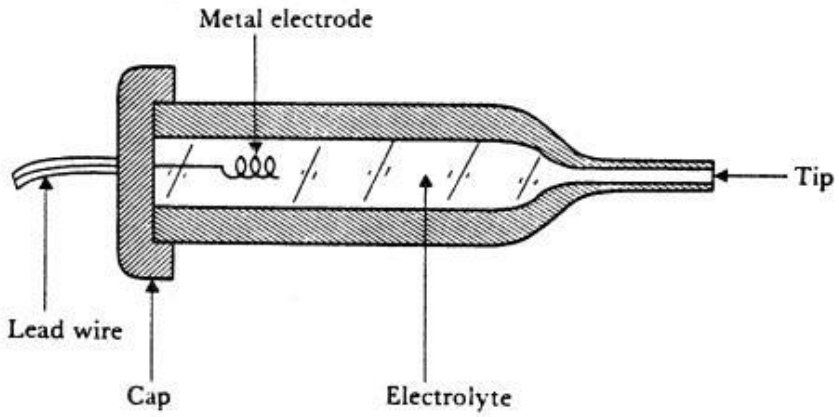

Figure 4.3 Micropipette electrode structure [94].

4.1.3 Metal electrodes

An alternative to the micropipette is metal micro electrodes which are generally made by sharpening small diameter metal wires [95], or as used in this thesis, with standard microfabrication techniques [96]. A large amount of work has been done to develop microfabricated electrode arrays (MEAs) that have been used throughout many aspects of neurophysiology to record extracellular potentials. Using established microfabrication techniques, it is possible to deposit thin films of conductive material that form electrodes and connection pads onto patterned insulating structures made from polymer, glass or other materials. Advances in this technology have led to an increase in the range of materials and the number of electrodes per unit area as well as decreased electrode sizes. Patterning of the materials allows for a large variety in MEA design, with the aim being that an array can be

designed to encase the larval zebrafish removing the need for positioning and allowing progress towards a high throughput system.

The general structure of a microfabricated electrode consists of two components; a thin conductive layer of metal and layers of insulating substrate material that enclose it. A large variety of configurations and materials have been used. The most common materials used for the substrate are silicon-based, glass or polymer and the conductive film is usually deposited metal.

These materials are carefully chosen depending on the application requirements. For example, a flexible and durable material is advantageous to use as insulation and a substrate in order to have a flexible final device. A popular choice for such devices is the polymer, polyimide. The dimensions of photosensitive polyimide (PSPI) can be precisely set by the processes of etching or photo-lithography. These processes are described later and allow the position of electrodes relative to each other and to the biological tissue to be finely controlled. The disadvantage is that the nature of metal electrolyte interface (described in the next section) results in a higher electrode impedance that is frequency dependent.

Biocompatibility is a key consideration when selecting materials for use with biological tissue. The main objective of an electrode is to record the electrical activity of the tissue but the tissue tries to protect itself from outside interference. The main concern is that the materials chosen are not toxic or will damage the tissue in any other way. This leads to two categories, surface biocompatibility and structural biocompatibility. Surface biocompatibility is the contact between the devices and the tissue concerning the morphological/biological/chemical and physical properties of the materials used. This relates more to chronic neural implants which are designed to remain inside the body for a long time. For surface electrodes, there is

less of a concern especially when ECG electrodes are likely to only be in contact for a short time. Structural biocompatibility is achieved by attempting to mimic the surrounding tissue properties for example the flexibility.

4.2 Metal electrolyte interface

The signals conducted through electrode recording systems are based on electron conduction in a metal whereas electrical conduction in the heart occurs due to the transport of ions across the cellular membrane. Therefore, any attempt to use metal electrodes to measure these electrical signals relies on an understanding of the interface between the metal electrode and electrolyte solution. An overview is given here of each of these phenomena along with a model which was described by Barrett [97] for a microfabricated nerve interface. This model was developed from the work of Kovacs [98] and Fischer [99] and is used to analyse results in chapter 8. The electrodes described in this thesis (initially) all use gold as the active site for its good flexibility and known biocompatibility [100]. Therefore, the model describes the electrochemical interface between thin film gold and an electrolyte.

This interface can be modelled using an equivalent circuit shown in (Figure 4.4) which is known as Randle's model [98]. The solution resistance is connected in series to the interface which models the direct charge transfer (charge transfer resistance (R_T) and Warburg impedance (R_w/ς_w)), connected in series with a capacitor (interfacial capacitance ς_I) in parallel. By determining the effect of each component in this circuit the total impedance spectra of the interface can be predicted.

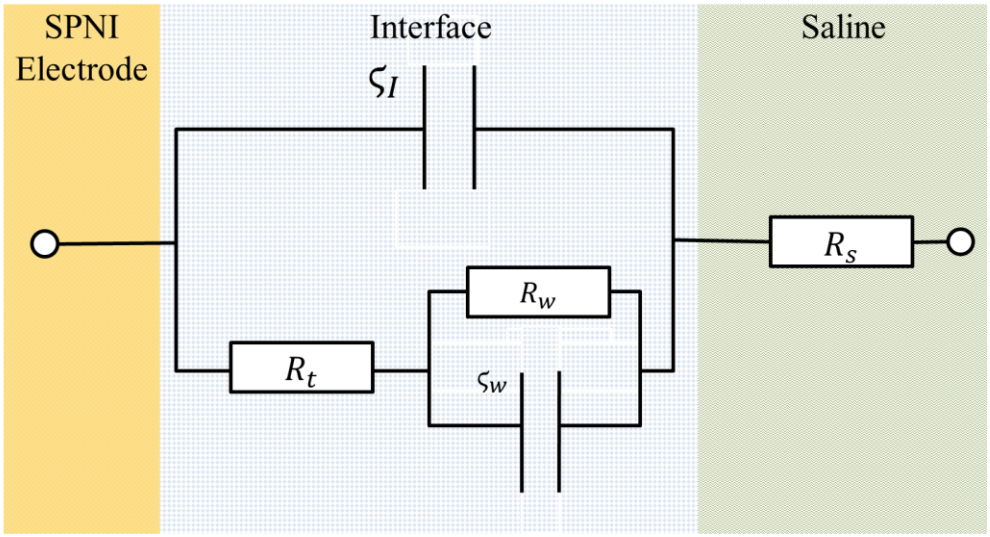

Figure 4.4 An equivalent circuit model of the electrode-electrolyte interface [98].

4.2.1 Interfacial Capacitance

Initially, the electrolyte solution and the metal electrode are electrically neutral. When the metal is placed in the solution reactions can occur causing electrons to be transferred across the interface. Eventually, an equilibrium is reached with these reactions where there is no net current flow. Impurities drive these reactions for a gold electrode as an oxide is unlikely to form. These impurities could be contaminants on the surface of gold that were either evaporated with the gold or were picked up during other processes.

Free electrons in the metal are attracted to positive ions in the solution and so travel to the electrode surface. There is an electric field generated between the electrons at the electrode surface the positive ions in the solution. This creates a variation in ion concentration in the solution, from a maximum at the electrode surface to a bulk value in the rest of the solution. The charged metal surface means that polar water molecules orientate themselves towards it. This determines the closest point at which charged ions in the solution can reach and is a distance known as the outer Helmholtz plane (OHP) shown in Figure 4.5.

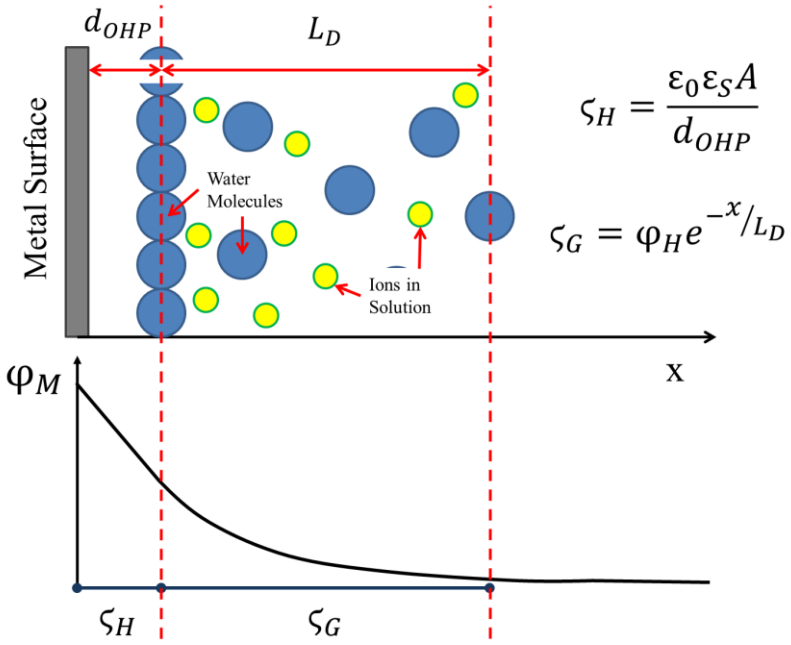

Figure 4.5 Diagram of interfacial capacitance between ions in solution and the metal surface [99].

An initial theory was developed by Helmholtz to treat potential distribution at the interface as a simple capacitor. Resulting in the capacitance per unit area (ς_H) given by:

$$\varsigma_H = \frac{\varepsilon_0 \varepsilon_r}{d_{OHP}} \tag{4.2}$$

Where ε_r is the dielectric permittivity of the solution, ε_0 is the permittivity of free space and d_{OHP} is the distance of the OHP from the electrode surface. This model was flawed as charges do not stay concentrated entirely at the OHP but move into the solution which lowers the entire interface capacitance. Gouy and Chapman (G-C) modified this model to include this by including an ionic cloud near the interface where the electrical and thermal effects are included using an ionic distribution averaged over time. Which resulted in a capacitance per unit area (F/m^2) given by:

$$\varsigma_G = \frac{\varepsilon_0 \varepsilon_r}{L_D} \cosh\left(\frac{ze\varphi_0}{2k_b T}\right) \tag{4.3}$$

$$L_D = \sqrt{\frac{\varepsilon_0 \varepsilon_r k_b T}{2N_0 e^2}} \quad (4.4)$$

Where ς_G is the G-C capacitance, φ_0 is the potential at the electrode, x is the distance from the electrode, $L_D$is the Debye length, $k_b$is the Boltzmann constant, z is the valence of the ion, T is the temperature, N_0 is the solution bulk concentration and e is the charge of an electron. The G-C model does not give a finite plateau for capacitance with increasing potential, which is observed in real systems due to the OHP acting as a dielectric. Therefore, another model known as the Stern model is used to account for this effect. This model combines the Helmholtz and G-C models to give a layer of bound ions at the OHP, beyond which there is a diffuse ion cloud. Which means the total interfacial capacitance is given by:

$$\frac{1}{\varsigma_I} = \frac{1}{\varsigma_H} + \frac{1}{\varsigma_G} \quad (4.5)$$

Where ς_I is the interfacial capacitance per unit area, ς_H is the Helmholtz capacitance and ς_G is the G-C capacitance. The associated impedance for this component of the interface can be found by applying $Z_C = \frac{1}{jwC}$. However, in general this capacitance cannot be modelled using pure capacitors even without the other components [101]. A frequency dispersive capacitance is used instead which is modelled using a constant phase element with the impedance given by:

$$Z_\varsigma(\omega) = \frac{1}{\varsigma_I (j\omega)^n} \quad (4.6)$$

$$Z_\varsigma(\omega) = \frac{1}{\varsigma_I (\omega)^n \left[\cos\left(\frac{n\pi}{2}\right) + \mathrm{j}\sin\left(\frac{n\pi}{2}\right)\right]} \quad (4.7)$$

Where n is an ‘idealness’ constant between 1 and 0, where n=1 is a pure capacitor [102]. This dispersive capacitance is thought to be related to the electrode surface roughness which cannot

be made completely flat at the microscopic level and as such is an important factor to consider in an impedance spectroscopy model [101].

4.2.2 Charge transfer resistance

The interface capacitance does not fully describe the electrical properties of the interface as there is also a resistance, which is necessarily considered in parallel to the capacitance. This is because in certain conditions a DC potential may cause current to flow across the interface. For small voltages (up to 50 mV) as were used in the impedance spectroscopy work in chapter 8, the resistance to this current flow is given by:

$$R_t = \frac{k_b T}{J_0 z e} \tag{4.8}$$

Where J_0 is the exchange current density and z is the valence of the ion involved.

4.2.3 Warburg impedance

Electrode/electrolyte interfaces are mostly dominated by the charge transfer resistance. This changes with a large current density which means reactants cannot diffuse and increased reaction rates deplete the local reactants. For a sinusoidal applied potential at high frequencies, ions struggle and then fail to follow the field. This results in no diffusional impedance for which there is the Warburg model for frequency dependent diffusional impedance for a unit area (Ωm^2), given by:

$$R_w = K_w \frac{1}{\sqrt{f}} \tag{4.9}$$

Where $K_w$is the Warburg constant:

$$K_w = 10^{-7} \frac{k_b T}{q^2 N_0 \sqrt{\pi D}} \tag{4.10}$$

Where D is the diffusion constant for the ions. Usually represented as a combination of capacitance and impedance (as in Figure 4.4), it is better represented as a single element [98]. Charge transfer resistance dominates the behaviour of the interface with the Warburg impedance playing a relatively small part for a gold electrode but it is included for completeness.

4.2.4 Solution resistance

The final part of the model concerns the solution resistance experienced by the current as it spreads out into the solution which depends on the shape of the electrode and resistivity of the solution for a flat electrode. For a rectangular electrode this is:

$$R_s = \rho \frac{\ln \frac{4l}{w}}{\pi l} \tag{4.11}$$

Where ρ is the resistivity of the solution, l is the length of the electrode and w is the width of the electrode.

4.2.5 Resulting impedance spectra

The total impedance of the interface can be calculated by combining the impedance of each component using $Z_R = R$ and $Z_C = \frac{1}{\varsigma_I (j\omega)^n}$. This is given by:

$$Z = \frac{(R_t + R_w)\left[1 + (R_t + R_w)\omega^n \varsigma_I \left(\cos\left(\frac{n\pi}{2}\right) - j \sin\left(\frac{n\pi}{2}\right)\right)\right]}{\left(\varsigma_I \omega^n (R_t + R_w)\cos\left(\frac{n\pi}{2}\right) + 1\right)^2 + \left(\varsigma_I \omega^n (R_t + R_w)\sin\left(\frac{n\pi}{2}\right)\right)^2} + R_s \tag{4.12}$$

The impedance magnitude and phase can then be calculated by splitting this into real and imaginary parts:

$$\Re[Z] = \frac{(R_t + R_w)\left(1 + (R_t + R_w)\omega^n \varsigma_I \cos\left(\frac{n\pi}{2}\right)\right)}{\left(\varsigma_I \omega^n (R_t + R_w)\cos\left(\frac{n\pi}{2}\right) + 1\right)^2 + \left(\varsigma_I \omega^n (R_t + R_w)\sin\left(\frac{n\pi}{2}\right)\right)^2} + R_s \tag{4.13}$$

$$\Im[Z] = \frac{-(R_t + R_w)^2 \zeta_l \omega^n \sin\left(\frac{n\pi}{2}\right)}{\left(\zeta_l \omega^n (R_t + R_w)\cos\left(\frac{n\pi}{2}\right) + 1\right)^2 + \left(\zeta_l \omega^n (R_t + R_w)\sin\left(\frac{n\pi}{2}\right)\right)^2}$$

The magnitude and phase can then be calculated using:

$$|Z| = \sqrt{\Re[Z]^2 + \Im[Z]^2} \tag{4.14}$$

$$Arg[Z] = arctan\left(\frac{\Im[Z]}{\Re[Z]}\right) \tag{4.15}$$

A spectrum can then easily be plotted for each for a range of frequencies using Microsoft Excel with the parameters given in Table 4.1, along with suitable values for the electrode size. This is done for various electrodes in chapter 8.

Table 4.1 – Parameter values for interface model.

Symbol	Parameter, Units	Value	Reference
ε_0	Permittivity of free space, $m^{-3}kg^{-1}s^4A^2$	8.854 x 10^{-12}	-
ε_r	Saline solution permittivity	79.4	[98]
d_{OHP}	Distance of OHP, Å	5	[98]
L_D	Debye Length, m	7.92 x 10^{-10}	[103, 104]
z	Valence of NaCl	1	-
e	Charge of an electron, C	1.6 x 10^{-19}	-
φ_0	Potential at the electrode, mV	40	-
k_b	Boltzmann Constant, 10^{-23} m^2 kg s^{-2} K^{-1}	1.38	-
T	Solution temperature, K	298	-
N_0	Saline bulk concentration	8.9 x 10^{22}	-
J_0	Exchange current density of gold, A/cm^2	2 x 10^{-9}	[105]
D	Diffusion constant of ions, m/s^2	1.49 x 10^{-9}	-
ρ	Resistivity of saline at 25°C, Ωm	0.72	[100]

Some example spectrums produced by this model are shown in Figure 4.6 A and B show the effect of area on magnitude and phase for different electrode areas. This shows that the impedance magnitude is inversely proportional to the electrode area and that the impedance largely depends on the capacitive component of the interface. This changes at high frequencies where the impedance falls and the solution resistance dominates, as this is not frequency

dependent there is a plateau. This can also be seen in the phase as each area starts at -90° (capacitive) and then falls towards zero (resistive). The larger electrodes reach the solution resistance at a lower impedance. The effect of the idealness is shown in C and D with a 177 μm^2 electrode (typical zebrafish sizing). Where idealness is a constant between 0 and 1, (1 is an ideal capacitor as introduced in section 4.2.1). n<1 results in higher impedances and a reduced drop off in impedance with frequency and less solution resistance dominance at high frequencies. The phase expectedly shows less capacitive behaviour, changing towards resistive behaviour at higher frequencies.

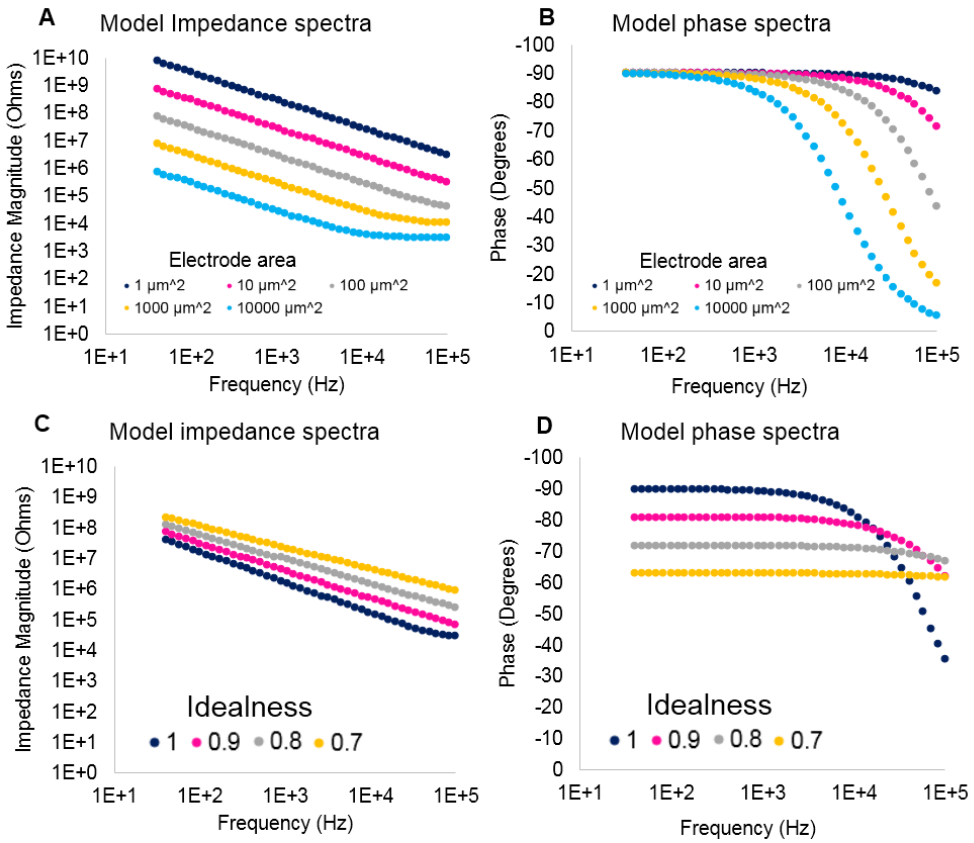

Figure 4.6 Model impedance magnitude and phase spectra for a range of electrode areas (A and B) (n=1) and idealness factors (D and C) (A=177 μm^2).

4.3 Microfabrication methods

This section introduces the methods that have been used to fabricate microelectrode arrays for use on larval zebrafish as well as the methods used to connect the arrays to external electronics as well as electrode testing methods. This section starts with a brief process outline which is followed by descriptions of each process. Fuller descriptions of each process can be found in [96, 106].

4.3.1 Process outline

The steps taken to fabricate zebrafish electrode devices are outlined below starting with the silicon wafer (numbers refer to Figure 4.12). A more exact (thicknesses etc.) method is given in the appendix in relation to the devices described in chapter 8.

1. Layer 1 – Sacrificial layer on silicon wafer (varying thicknesses)
    - Chrome
    - Aluminium
    - Allows release of devices from wafer
2. Layer 2 - Substrate PI
    - Various thicknesses spun on to wafer at different speeds
    - Exposed and then developed using HTRD2 + RER600
    - Forms the outline of each device
3. Layer 3 – Metallisation
    - Gold and Chrome (for adhesion)
    - For wiring, connection pads and electrode sites
4. Layer 4 – Metal patterning
    - SPR 220 photoresist spun on to sample

- Exposure and then development in MF-26A

Wet etching

- To remove unwanted Gold and chrome
- Forms wiring, connection pads and electrode sites

Plasma/UVO cleaning

- To remove remnants of photo resist and improve adhesion of next layer

7. Layer 5 – PSPI insulation/passivation
    - Various thicknesses spun onto wafer
    - Insulates all wiring except for electrodes and connection pads

    Plasma/UVO cleaning
    - Final descum to remove unwanted material

    Hard bake in furnace
    - To remove oxide and give final properties
9. Release in NaCl
    - Anodic dissolution of the sacrificial layer

4.3.2 The Silicon Wafer

The fabrication processes described in this thesis begins with a (100) silicon wafer with a 250 nm oxidised surface layer, known as a ‘handle’, ‘carrier’ or just ‘wafer’. Wafers are used in microfabrication processes as they provide a flat uniform surface, are unreactive and thermally stable. Zebrafish devices are fabricated on a 4” diameter wafer which allows for many different devices and multiple designs to be fabricated at the same time. The use of an aluminium sacrificial layer means that the wafer is placed straight into the thermal evaporator system as the first process.

4.3.3 The sacrificial layer

The use of polyimide as a substrate layer necessitates the need for a sacrificial layer as it adheres well to the silicon wafer which means devices cannot simply be peeled off. The release of micro fabricated structures has been widely investigated with the most common methods being wet etching and dissolution in a solvent. A variety of materials have also been used such as metals, semiconductors and insulators.

Aluminium was chosen as the sacrificial material as it has been used previously [107, 108] and reduces the amount of shrinkage compared to alternatives like PMMA [97] which means it is easier to interface with external electronics. Chrome is deposited by thermal evaporation (described in the next section) first to prevent islands forming during release, followed by the aluminium layer. The aluminium is removed at the end of the fabrication process and the electrode devices are released by placing the wafer in a 2 M NaCl solution and connecting an area of exposed aluminium to a gold counter electrode. The differences in ionic structure between the gold and the aluminium means a current flows which gradually removes the aluminium from the wafer surface via anodic dissolution [107, 108]. This process generally takes 24 to 48 hrs. However, there were some problems with this as outlined in chapter 8. This method was used rather than using an aluminium etchant as it has been shown in the literature to be effective with similar polyimide devices and it is more compatible with them as it limits exposure to chemicals that could damage the devices [107].

4.3.4 Fabrication of thin metal films

Fabrication of the aluminium sacrificial layer and the thin metal films that form the connections, electrodes and tracks is performed using thermal evaporation and sputtering. Like any material, metals have a boiling point and by heating a metal to this point it sublimes forming a gas. A

film can then be formed by placing a target close to the evaporating metal, the hot gaseous metal will then condense as it hits the cooler target forming a pure layer. The metals are heated by placing them in an aluminium chloride crucible that contains a tungsten wire coil, a current is then applied to the coil causing it to heat up, which in turn heats the metal. Sputtering of metals is similar in that the metal is heated but this is achieved by bombardment with a highly energetic plasma rather than a tungsten coil. This causes the metal to evaporate in an anisotropic, non-homogenous way called a sputter coating. This method allows for greater coverage of samples which are not perfectly flat such as those containing plastic layers. The thickness of the metal films can be controlled by varying the current applied (temperature) and the time the sample is exposed, where more current and more time results in a thicker film.

Two evaporation systems (Figure 4.7) were used in this work, the Polaron thermal evaporator (Quorum Technologies, Discontinued) and the Cressington coating system (Cressington, 308R). The Polaron system was used to thermally evaporate chrome and aluminium and the Cressington system was used to thermally evaporate aluminium, gold and sputter coat chrome. The wafer is placed upside down in a vacuum chamber and pumped down to $<2x10^{-6}$ mbar (Cressington) before the metal can be evaporated or sputtered. A vacuum is needed as this increases the mean free path of the metal particles which allows them to reach the sample. For the sacrificial layer, a chrome film is first either evaporated (Polaron) or sputtered (Cressington) onto the surface of the sample, this provides a ‘back plate’ to the aluminium to maintain an electrical connection during the etching of the aluminium when the sample is released. A layer of aluminium is then evaporated onto the sample. To form the metallisation layer a combination of chrome and gold is deposited using the Cressington evaporator. Gold does not adhere well to polyimide so chrome is used as an adhesive layer.

Chrome is sputtered for 30 s forming an ~18 nm layer then ~100 nm of gold is evaporated. The thickness of these thin films can be measured as they are deposited in the Cressington system which uses an oscillating quartz crystal thickness monitor. No shutter was used to protect the sample when using the Polaron system as it is not equipped with a shutter. A shutter was used with the Cressington system during evaporation of gold and sputtering chrome during initial heating of the metal. For aluminium depositions using the Cressington system, it was found that using the shutter made it difficult to expose the metal to the sample at the ideal temperature as the required current varied due to damage to the tungsten crucible by the aluminium and so no shutter was used. For these depositions, the current was slowly increased until deposition started to be measured using the thickness monitor and then the current was held/slightly increased until the required deposition thickness had been reached.

Figure 4.7 Polaron system (left), Cressington coating 308R system (right).

4.3.5 Spin coating polyimide resins

Thin, homogenous layers of polyimide are fabricated by depositing a small amount of resin onto the centre of a wafer which is then rotated (spun). The thickness of the resulting film is a function of the spin speed, viscosity and the amount of resin deposited. A faster spin speed

results in a thinner film. The exact relationship between spin speed and film thickness is provided by the supplier of the material in what is called a ‘spin-profile’ [109, 110]. This allows for the thickness of the layer to be controlled by changing the spin speed. The resin is formed by dissolving the polyimide in a solvent, the concentration of this solvent is reduced firstly during the spinning process and then by exposing it to elevated temperatures in a ‘soft bake’ using hotplates and a temperature ramp.

A similar process is used to create a thin film of photoresist, which is a light sensitive material which can be used to pattern a surface and is used to protect parts of the wafer during wet etching. The photoresist used in this thesis is SPR-220-7 (Megaposit, Shipley).

The exact thickness of a polyimide or photoresist film can be measured using a Dektak surface profiler (Bruker Corp). This works by dragging a stylus across the surface of the sample and measuring any changes in its height. As room conditions and the amount of deposited material can affect the resulting film thickness these were kept as stable as possible.

The spinning process does not always produce a perfectly flat film as thicker regions can form on the edge of the wafer which are known as ‘edge-beads’. An edge-bead can lead to problems during the photolithographic process (explained later). It is most likely to form when spinning the photoresist and can be removed using a small amount of acetone and gently wiping around the edge of the wafer.

4.3.6 Soft baking of polyimide resins and photoresist

The process of removing the solvent from the spun resin or photoresist is known as soft baking. The solvent is evaporated by placing the wafer on a hotplate and elevating the temperature. This hardens the spun resin and leaves it in a semi-cured state which allows for easier handling. Photosensitive polyimide (PSPI) was soft baked using a temperature ramp of 30 °C → 90 °C

at 3 °C per minute. This slow ramp was used to prevent bubble formation. For the photoresist SPR-220-7, a drop-down soft bake was used where the sample was held at 90 °C for 2 minutes on one hotplate, it was then transferred to a second hotplate and held at 130 °C for 6 minutes. This procedure prevents deformations in thicker layers. After soft baking the samples they were left to cool for at least 5 minutes.

4.3.7 Photolithography

Photolithography is the process of changing the chemical structure of a material by exposing it to light. Deposited films are patterned by exposing areas of the film to light which changes the chemical structure making them less or more soluble to chemical developers. The regions that become more soluble will therefore be 'developed' (etched away) by submerging the film in an appropriate developer. The areas which are exposed to light are selected using a 'photomask' (mask) which blocks light from some areas and allows it to reach others, this creates a pattern which can then be defined using the developers. Only the desired regions remain after development as shown in Figure 4.8. There are two types of photolithographic processes, positive and negative. A negative process leaves the exposed region intact after development and a positive process removes the exposed region. The types of photo sensitive polyimide used in this thesis (Durimide 7020 and 7505, Fujifilm) are both negative materials and the photoresist (SPR-220-7) is a positive material. The masks were therefore designed accordingly.

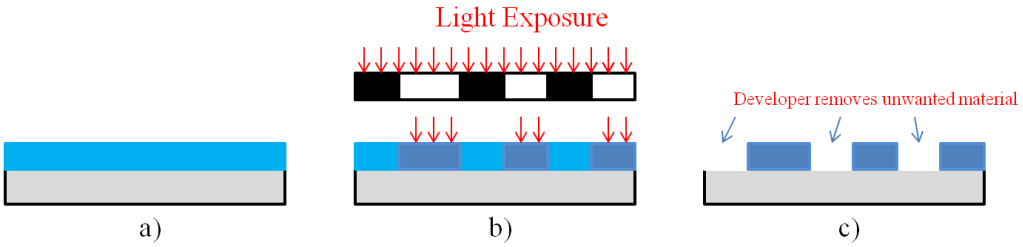

Figure 4.8 The photolithographic process for a negative resist (the exposed material remains intact after development). A) Deposited film on wafer, B) desired areas of film are exposed to light, C) unwanted material is removed by developer. From [97].

UV light was exposed to the samples in the wavelength range of 380-400 nm using a Canon mask aligner. The PSPI is developed using the ancillaries HTR-D2 and RER-600. With development of the SPR-220-7 performed using MF-26A (Shipley).

4.3.8 Etching gold and chrome

The metal layers are patterned using chemical wet etching which removes unwanted material to leave the desired pattern. Photolithography is used with SPR-220-7 to protect areas on the sample and then all the unprotected areas are removed during the etching, the photoresist is then removed revealing the patterned metal.

Gold is etched by submersing the sample in potassium iodide solution for approximately 40 seconds and then rinsing with deionised water. The sample is then placed in chrome etchant (Sigma) for 15 seconds to etch the chrome. A microscope coverslip that was coated with the same amount of metals was used as a test to make sure these timings successfully removed the metals.

4.3.9 Cleaning

Two surface cleaning treatments were used in this work to remove unwanted organic matter and improve the quality of the fabricated electrodes. These are oxygen plasma etching (OPE) and UVO cleaning.

Plasma etching uses a plasma of ionised oxygen particles to bombard the surface of the sample and etch away any unwanted material. Oxygen particles are ionised using two electrodes (anode and a cathode), a large potential is applied between the two which causes any free electrons in the gas to move towards the anode. The movement of these electrons ionises oxygen molecules which turns into a cascade that creates the plasma. OPE is used twice in the fabrication process, once after wet etching and again after the insulation layer using a Femto model from Diener Electronics.

UVO cleaning uses short wavelength ultra-violet radiation aimed at the sample to excite or dissociate organic contaminants. This was performed using a Jelight UVO cleaner.

4.3.10 Hard baking of polyimide devices

This step removes the remaining solvent from the polyimide layers and gives the polyimide its final material properties. Without this step the polyimide is not as durable and more susceptible to taking up water. The wafer is baked in a nitrogen environment to prevent burning of the polyimide at the elevated temperatures (>200 °C). The temperature ramp that was used is shown in Figure 4.9.

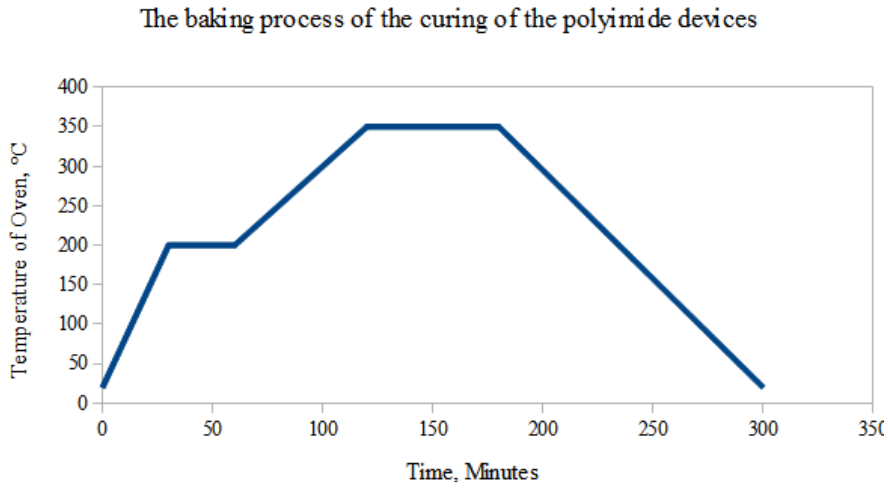

Figure 4.9 Hard bake temperature ramp for curing polyimide devices [97].

4.4 Methods to reduce electrode impedance

As described previously, the impedance of an electrode is an important parameter in achieving a good signal, as is the voltage sensitivity of the electrodes. With no way to achieve the required voltage sensitivity without small electrodes, there are methods described in the literature that have been developed to reduce the impedance of electrodes without increasing their overall dimensions. This has been achieved using a variety of methods which have the main effect of increasing the surface area of the electrodes via depositing materials on to the electrode surface. Amongst these methods are the electroplating of metals [111] and the use of conductive polymers [112, 113].

4.4.1 Electroplating

This is the technique of using an electric current to deposit metal ions on to the surface of a target electrode. The electrodeposition process is achieved by placing two electrodes (anode and cathode) in an electrolyte. The anode is either the source of material to be deposited or the counter electrode and the cathode is the target or working electrode. The electrolyte contains dissolved metal ions and salts to permit the flow of electricity. Gold plating is the method used in this thesis and Chloroauric acid (Sigma) solution was used which contains gold ions (Figure 4.10). A DC voltage is then applied across the two electrodes resulting in gold ions being deposited on to the working electrode. The thickness of the deposited layer is determined by the magnitude of the voltage and the length of time it is applied. Electroplating results in a roughened surface which increases the surface area of the electrodes. More details of the methods used are given in chapter 8.

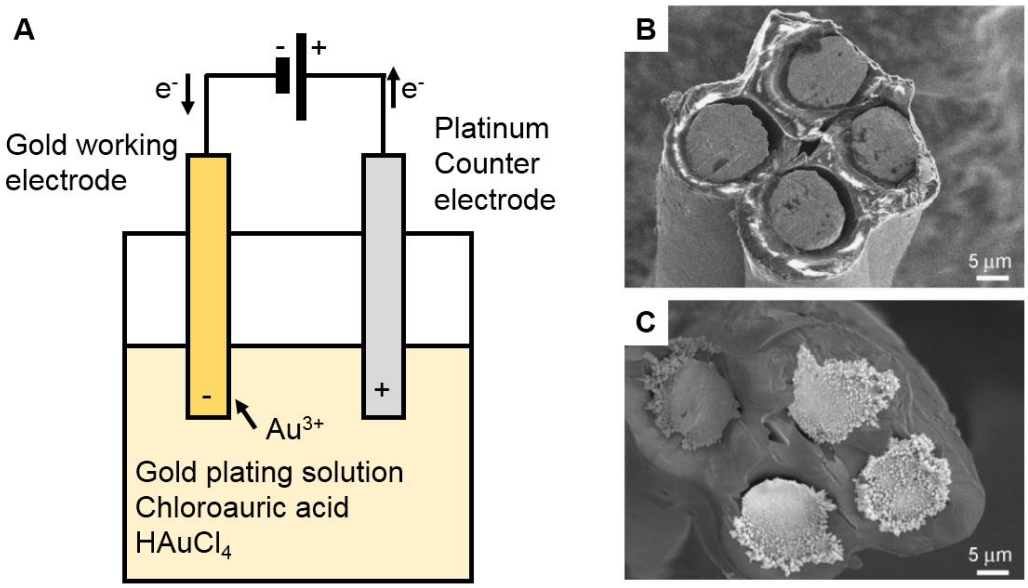

Figure 4.10 A) Gold electroplating setup, B) scanning electron microscope image of electrodes before gold electroplating, C) after gold plating. From [114].

4.4.2 Electrochemical polymerisation

This technique is similar to electroplating in that a current is used to coat the working electrodes but with this technique a thin film of conductive polymer is deposited instead. This was first demonstrated by Cui *et al* [112] who deposited conductive polymer films onto the surface of metal neural electrodes and measured a reduction in impedance. This was done by electrochemically oxidising the monomer in the presence of an electrolyte solution which leads to polymerisation at the electrode surface and deposition of a polymer film onto the electrode.

The polymer chosen for this work is Poly(3,4-ehtylenedioxthiophene), shortened to PEDOT with a counter ion of Polystyrene sulfonate (PSS). This was chosen for its properties of high conductivity, biocompatibility and stability as well as its previous use in similar applications of lowering the impedance in neural probe electrodes [112, 113, 115, 116]. Typical PEDOT:PSS conductivities range from 0.1 to 1 S/m [117]. The process was performed using a constant current applied for a fixed time to the working electrode and counter electrode which

were placed in a solution containing PEDOT:PSS and EDOT in a similar method to that used by Nyberg [116]. More details are given in chapter 8.

4.5 Impedance spectroscopy

One of the main ways to characterise the electrode-electrolyte interface is to use electrochemical impedance spectroscopy (EIS). EIS can be used to measure the magnitude of the impedance along with the phase angle when the electrode is stimulated with a sinusoidal current or voltage. An impedance spectrum can be found by varying this signal over a wide range of frequencies which are typically in the range of biological signals (1-10 MHz). A small voltage of less than 50 mV is used as to not damage the electrodes [118].

Many different types of electrodes have been characterised using EIS that can be used as a comparison to any novel devices that have been created. EIS was used in this work to assess the microfabricated zebrafish probes, along with the methods to reduce their impedance.

A network analyser (HP 9424, Hewlett Packard) was used to perform the impedance measurements with a two electrode setup in a saline solution (Figure 4.11). The saline solution was chosen as it is similar to the salty E3 medium that larval zebrafish are maintained in. The solution was made by mixing 8.6 g of sodium chloride with one litre of deionised water. The first electrode was the microfabricated zebrafish electrode and the second was a platinum counter electrode (0.4 cm radius). The counter electrode was very large compared to the electrode under test so had a negligible impedance in comparison. The impedance magnitude and phase were measured for a range of frequencies between 40 Hz and 0.1 MHz using a sinusoidal 40 mV signal. A custom LabView (National Instruments) program made by Andreas Frommhold was used to control the network analyser and export results. More details of these experiments are given in chapter 8.

The impedance analyser uses an auto-balancing bridge method (Figure 4.11). The voltmeter and ammeter (for magnitude and phase) can be used to measure the complex impedance of the device under test (DUT) in response to a generated signal. The test signal current (I_x) flows through both the DUT and through a 'range' resistor (R_r) so that the potential is maintained at zero at the 'low' terminal. A feedback loop controlled by an IV converter amplifier is used to maintain this. The DUT impedance is then determined from the voltage at the high terminal (V_x) and the range resistor (V_r, which is known) in the following way:

$$Z_x = \frac{V_x}{I_x} = R_r \frac{V_x}{I_r} \tag{4.16}$$

This system offers a highly accurate (0.08% of measured impedance) measurement over a large frequency range (40-110 MHz), with signal levels ranging from 5 mV to 1 V_{rms}. Impedances can be measured in the range of 3 mΩ to 500 MΩ with phases between 0° and -90° [119].

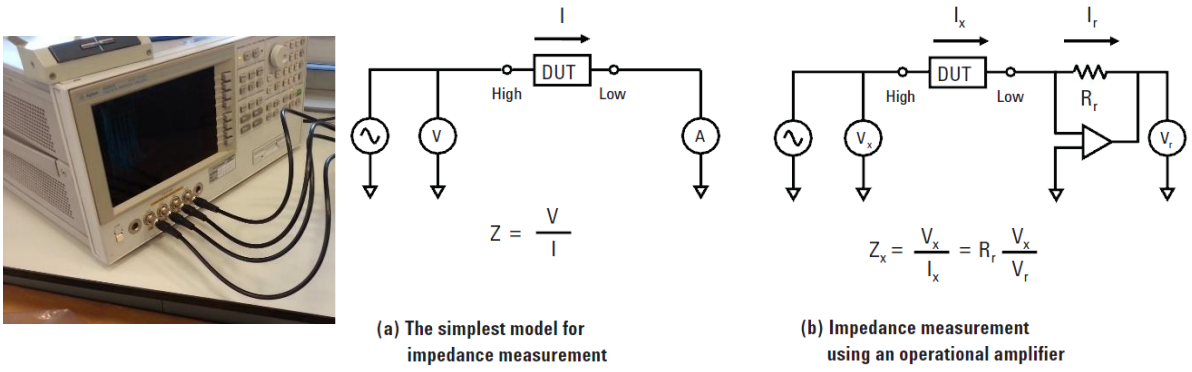

Figure 4.11 HP 9424 network analyser (left) and auto balancing bridge method principle (right) [119].

4.6 Zebrafish electrodes previous work

This section describes the previous work performed by Richard Barrett and Rhiannon Hurst towards the development of a zebrafish HTS system to give context to the work presented in chapter 8. This sections starts with an overview of the work followed by an outline of the microfabrication process.

4.6.1 Overview

Richard Barrett designed and developed a process for fabricating two sets of electrode designs (Appendix A1 and A2). Each set contains a number of different device shapes and styles and for each set there are three photo masks (M1, M2, M3). One mask is used for the substrate layer (M1), one for the photoresist (for patterning the metallisation, M2) and one for the insulation (M3). Each device is therefore based on a sandwich structure as shown in Figure 4.12 (numbers refer to the steps outlined previously). With electrode sites either located at the bottom of a PSPI well (left step 9) or at the end of the device (right step 9). This figure shows the build-up of each layer and how the layers are patterned to leave exposed gold areas for the electrodes and connection pads. The thickness of the metal layers has been largely exaggerated.

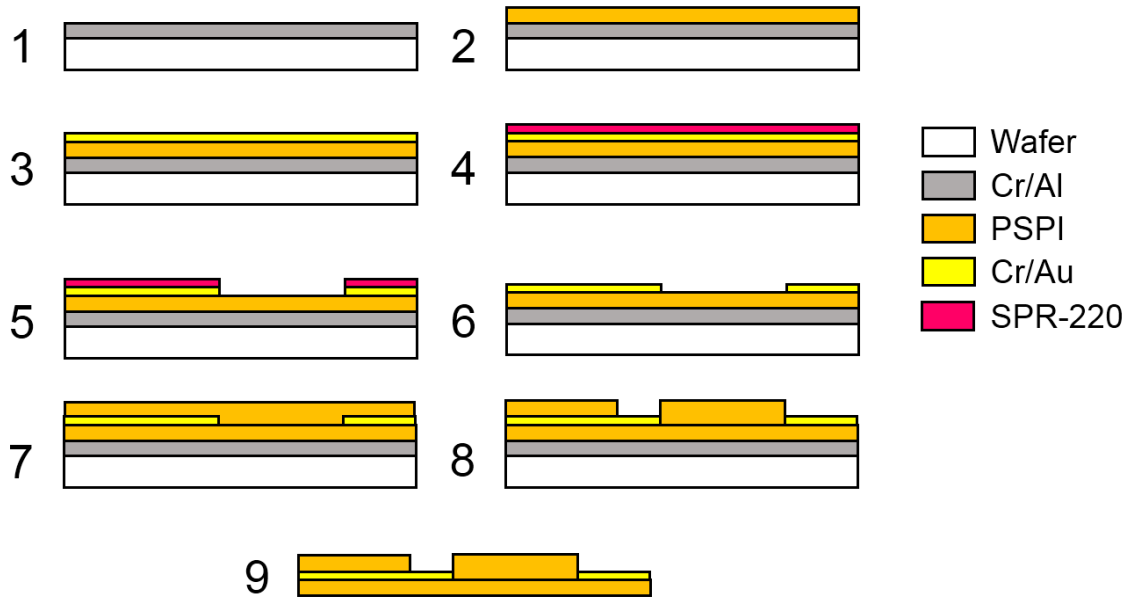

Figure 4.12 Zebrafish electrode device process flow.

Each type of electrode (well) and edge is shown in Figure 4.13 for a two channel device from set 1 and a four channel device from set 2. Both of these devices are designed to be probes for using on the zebrafish in a similar way in which a micropipette electrode is used, by moving them in to contact with the zebrafish which requires a large amount of positioning. Use of the

two channel device to test the impedance reduction methods is described in chapter 8. There are also other designs on each set of masks including 8 channel probes, and two styles of 20 channel arrays. The 20 channel arrays are designed to surround the zebrafish with electrodes (in a ring) and were thought to be the most likely design to be compatible with a high throughput system. Use of these is explained more in chapter 8.

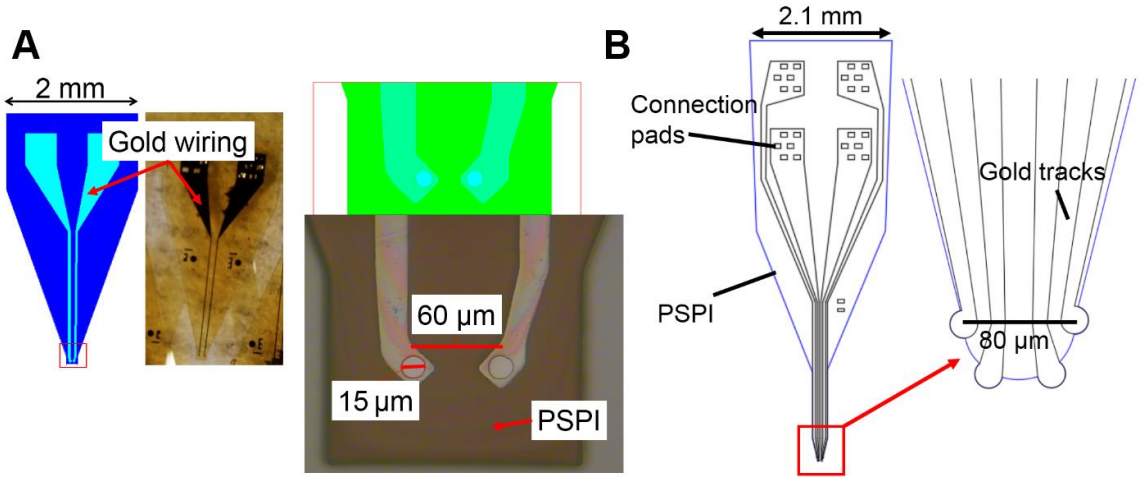

Figure 4.13 A) Two channel 'well' electrodes, B) four channel edge electrodes.

Connection of the majority of devices (with another method explained in chapter 8) was made possible with the use of Microflex technology [120]. This technique involves using a ball bonder (Kulicke and Soffa) (Figure 4.14) that is used to micro rivet released devices to a custom designed printed circuit board (PCB Appendix A6) at the connection pad holes of the devices. A review of how to implement this technology is given in [97]. This process mechanically and electrically connects each electrode (channel) on the device to the PCB. Wires are soldered to the PCB which lead to a 24 pin plug which was adapted to connect to an Intan recording system for zebrafish ECG measurements. This system consists of a head stage (64 Channel Amplifier Board RHD2164, Intan Technologies LLC) and pre amplifier (RHD2000 USB Interface Board, Intan Technologies LLC). ECG measurements were recorded relative to a chloridised silver reference electrode.

A

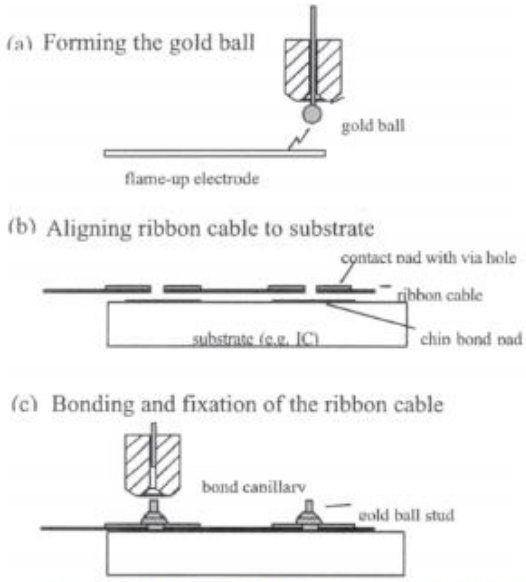

B

C

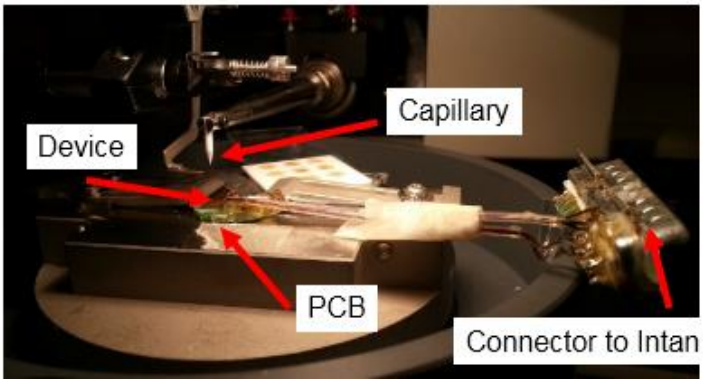

Figure 4.14 A) Diagram to show how micro rivets are performed [120], B) ball bonder, C) close up of sample stage showing device, PCB (Appendix A6) and 24 pin connector.

The main result of this work which took place after some of the results presented in chapter 8 but before the final results presented there, is that an ECG was able to be measured from one of the 4 channels of a 4 channel device. The electrodes on this device were coated with PEDOT as a result of the work described in chapter 8. This recording is shown in Figure 4.15 and as well as measuring the normal ECG signal (C) a change in QT length was measured after the administration of a QT prolonging drug (Terfenadine). This showed that microfabricated electrodes were capable of measuring the ECG but this style of device is no better than a micropipette for positioning making it incompatible with a high throughput application. Therefore, one of the aims of the continuation of the work was to measure a signal with one of the 20 channel devices. In addition, Figure 4.15 A and B are unrepresentative of the position required to measure the signal as quite a large amount of pressure needed to be applied.

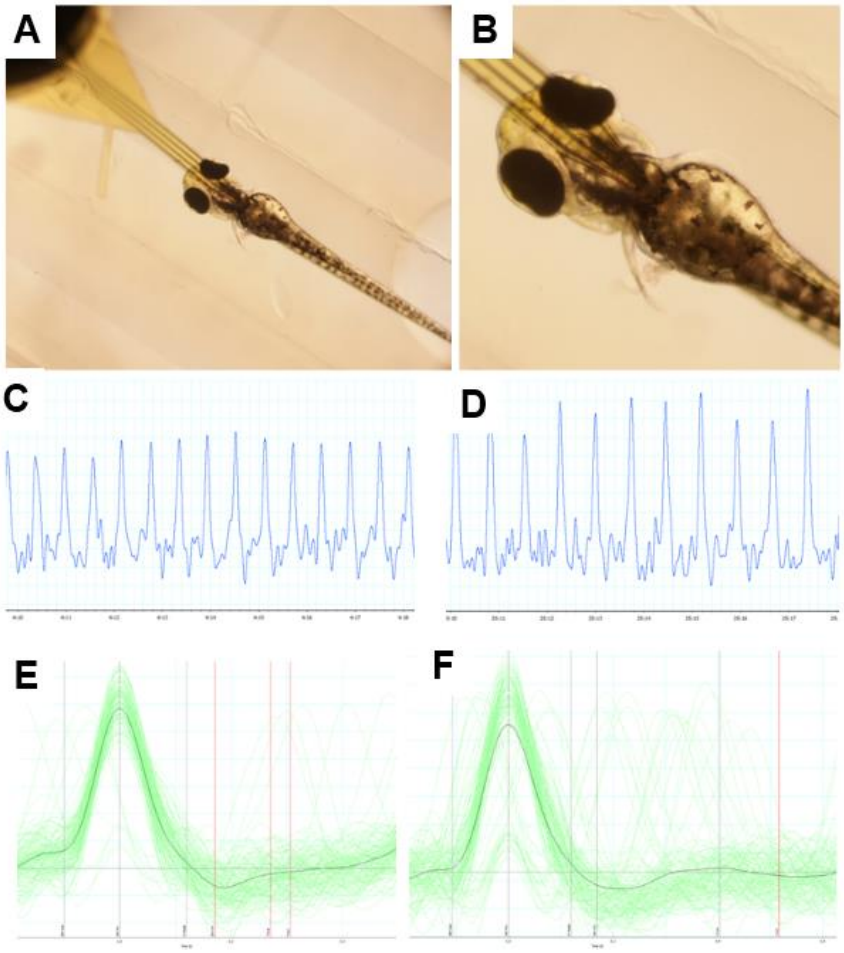

Figure 4.15 A) Four channel electrode positioned on zebrafish, B) close up, C) ECG signal from one channel pre drug treatment. Band pass filtered low (1 Hz) and high (10 Hz), D) ECG measurement post drug treatment, E) close up overlay before treatment, F) close up overlay after treatment. Provided by Rhiannon Hurst/Oliver Morgan.

5. HEART MODEL DEVELOPMENT

The aim of the zebrafish heart modelling was to create a model that could be used in the design of electrode arrays for measuring the larval zebrafish ECG by determining ideal electrode placement. It was thought this could be achieved by creating models that simulate the electrical activity of the larval zebrafish heart and hence the ECG. This chapter describes the early stages of the development of the larval zebrafish heart model that were progressively improved resulting in the bidomain heart model described in chapter 6. Early models of the human heart were created using a variety of equivalent sources described in chapter 3 [65] and so it was thought that a good starting point would be to apply the same techniques to the zebrafish. This started with simple stationary equivalent source models that were created using a variety of different dipole sources with simple geometry. A model was then developed of a more complex time dependent model using Fitzhugh-Nagumo equations. Firstly, the creation of the model zebrafish body is described which was used for all dipole models, along with the planes the body was sectioned into in order to analyse the results of each model. A model that uses the simplest source that can be used to represent the hearts electrical activation is then described, which is a point dipole. This source is then replaced by a slightly more complex source which is a hemisphere dipole, a third source is also described which uses dipole surfaces. The results and conclusions which can be derived from such models are discussed along with how the results of the three models (voltage distributions and ECGs) differ. The models are also compared to measured ECGs. Finally, a Fitzhugh-Nagumo equations model is introduced and a summary of the findings of this chapter is given.

5.1 Model body

All models described in this chapter use a simplified 3D geometry created in COMSOL where the larval zebrafish body is represented by an ellipsoid. The heart geometry varies between models which is explained in each subsection. The dimensions of the ellipsoid were determined by fitting ellipses to images of a 3 dpf zebrafish [51]. This resulted in a 1000x450x400 micron ellipsoid that was used to approximate the 3 dpf zebrafish body (excluding tail) based on measurements from the images as shown in Figure 5.1.

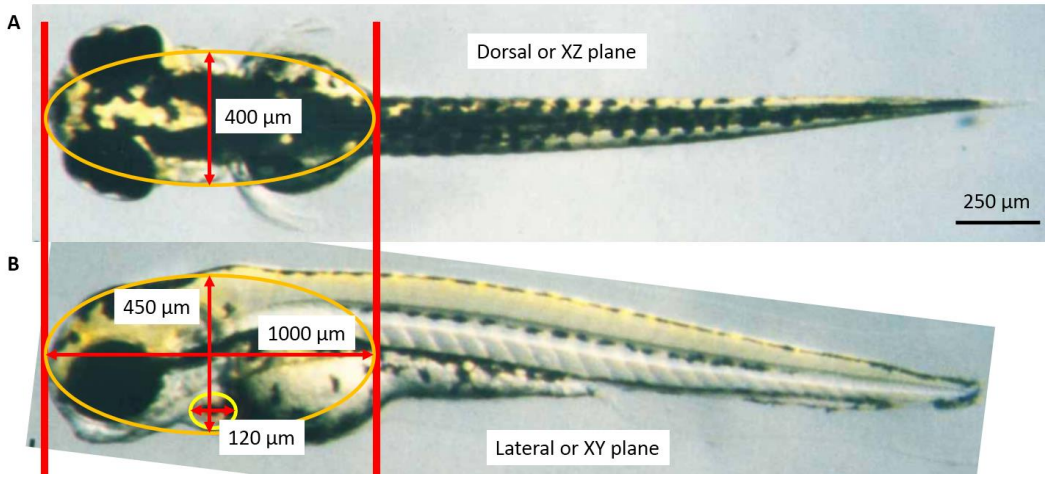

Figure 5.1 The fitting of an ellipse (orange) as an approximation of the zebrafish body shape. The heart and its approximate size is also marked with a second ellipse (yellow), A) dorsal view or the XZ plane, B) lateral view or the XY plane. Images from [51].

From these measurements a 3D ellipsoid was created within COMSOL (Figure 5.1). The geometry was divided into sections so that the voltage distribution could be investigated in 3 dimensions via the use of the XY, ZX and YZ planes.

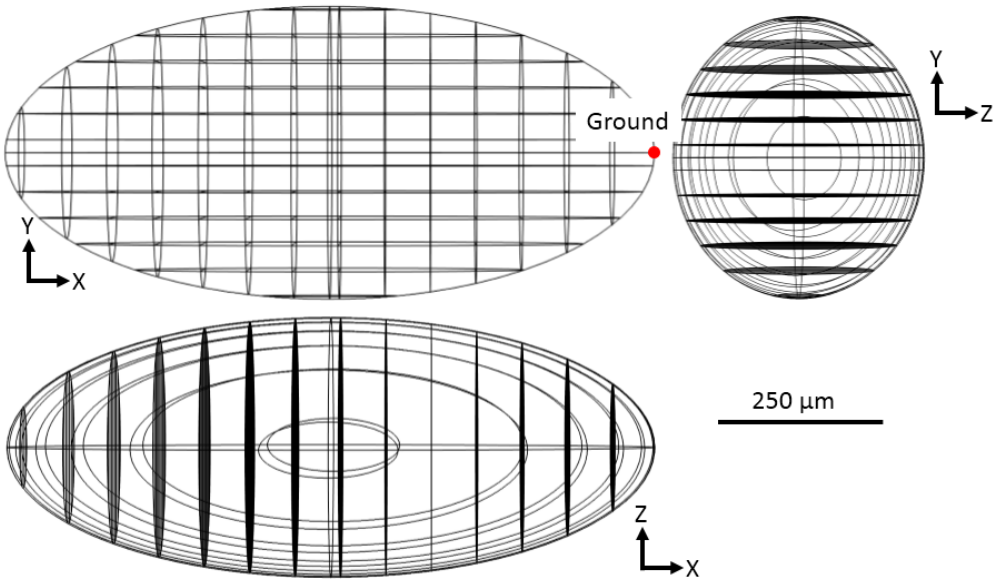

Figure 5.2 3D ellipsoid body geometry in COMSOL. With the ground point marked on the XY plane image.

The body was taken to be a homogenous volume conductor which means that the voltage distribution within it (due to a current source) could be determined using Laplace's equation:

$$\nabla \cdot \sigma \nabla \varphi = 0 \tag{5.1}$$

Where σ is the electrical conductivity in S/m and φ is the electric potential (V). The only parameter that is needed to describe the body is then the conductivity. This was taken to be 0.2 S/m which was chosen to fit with other heart models [80], in reality, the body conductivity varies due to the presence of other objects which were not modelled such as organs and blood. This value is typical of human models and so is unlikely to be correct for the larval zebrafish, but there are no zebrafish body conductivity measurements in the literature to compare it to. The body conductivity was found to only effect the magnitude of simulated ECGs and not the time course. Therefore, as the morphology of the voltage distribution is unaffected by changes in conductivity, this value of conductivity was acceptable to use. This is because investigation

of ECG morphology was the aim of the heart models rather than investigation of absolute magnitudes. The outer boundary of the ellipsoid was assumed to be insulating with a ground point at one side of the body. Using this condition, the voltage distribution within the body and at the surface could be investigated.

For ECG measurements it is the voltage on the surface body that is of interest so it is these voltages that were investigated. To investigate this, the sectioned rings around the edge of the ellipsoid were selected in three different planes (XY, ZY, XZ) from which the voltage could be plotted within COMSOL and exported for further analysis. As shown previously, the voltage produced by a dipole is largest close to the source and then falls away with distance as a function of $1/\text{distance}^2$. This means that the voltage on surface of the body closest to the dipole should be the largest and then the voltage should reduce away from the dipole. Therefore, the main areas of investigation were the regions closest to the current sources. The body was sectioned in such a way to give planes either side of the heart and across the middle in both the X and Y directions (Figure 5.3). The key planes are numbered in the figure and also correspond to what would be multiple recording positions from either side of the heart and centrally as well as above, below and centrally from the Y direction. The planes are referred to by their orientation and number e.g. YZ1, YZ3, XZ1, XY1 etc.

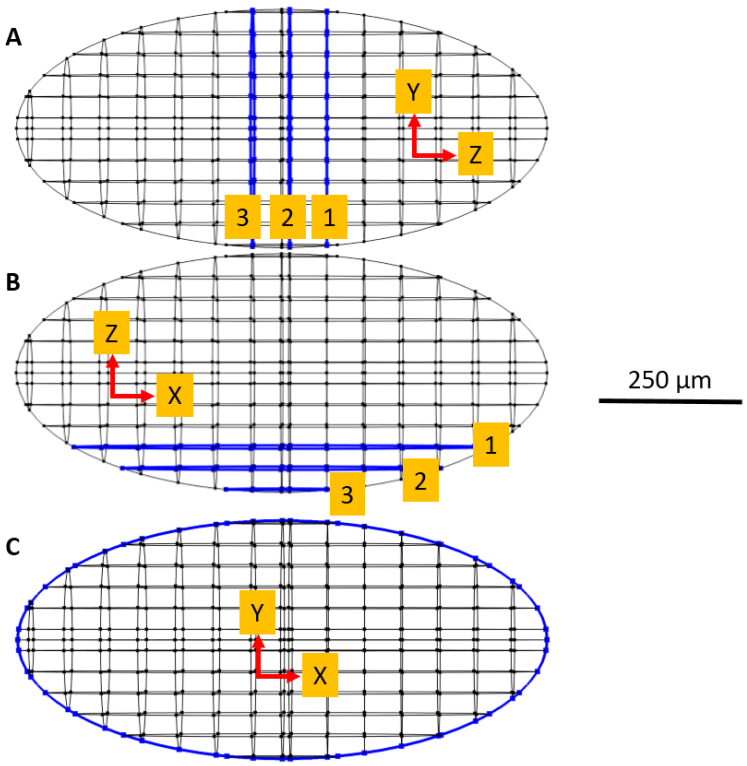

Figure 5.3 XY plane view of selected rings. A) Highlighted edges for three YZ planes, 1 is located to the right of where the atrium would be, 2 is located centrally on the heart and 3 is located to the left of where the ventricle would be. B) Highlighted edges for three XZ planes. 1 is below the heart/current source, 2 is positioned centrally and 3 is above the heart. C) Highlighted edges for a single XY plane positioned centrally.

5.2 Dipole models

5.2.1 Point dipole

The first heart model that was made used the simplest current source that is able to represent the depolarisation and repolarisation waves within the heart, a dipole. This 3D model consisted of the body ellipsoid with a dipole placed in the approximate location of the middle of the zebrafish heart. A dipole was created using two point current sources (one positive and one negative) separated by one micron with its fixed position, orientation and magnitude representing one stage in the heart's cycle. An arbitrary current magnitude of 2857.1 A was chosen to give voltages on the surface of the body in the 10's of mV range (not fitted, see Figure 2.7) to match what is measured (after amplification and processing). This value was not taken

from the literature but selected by fitting previous model voltages (not shown here) to ECG measurements from [11] which resulted in this value which is arbitrary. It was then carried over to the models presented here. Another arbitrary value could have been used such as 3000 A but 2857.1 A was chosen for consistency with previous models. This arbitrary value was acceptable as long as it was kept consistent between models because as explained previously ECG morphology was of interest rather than absolute magnitudes. As described previously in chapter 2 (Figure 2.5), different orientations and magnitudes of the dipole can be used to represent different stages of activation. Initially, the dipole orientation was chosen to replicate the first stage in the heart's activation cycle, that of depolarisation. As the zebrafish heart is essentially a tube with activation spreading from atrium to ventricle (tail to head of the body) the dipole was initially orientated so that the direction of the dipole (positive side) pointed from the atrium to the ventricle (towards the head of the zebrafish). In Figure 5.4 A, a simplified heart geometry is shown which shows what the chosen dipole direction within the model is attempting to replicate (Figure 5.4 B). The standard extremely fine mesh setting in COMSOL was used for all variations of dipole model.

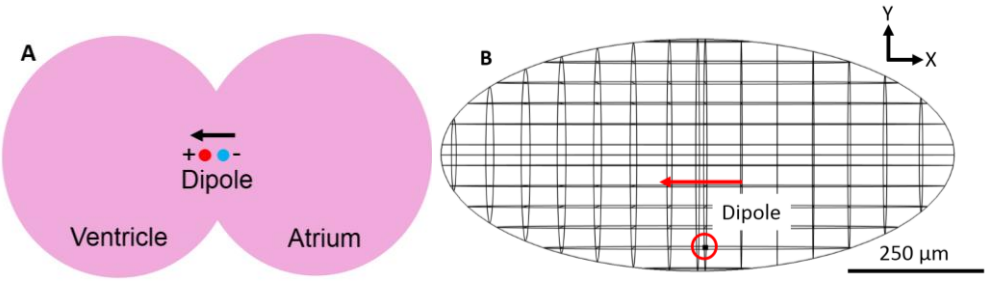

Figure 5.4 A) A simplified zebrafish heart showing the direction of the depolarisation wave and how the dipole relates to it. B) XY view of the dipole highlighted by the red circle in the ellipsoid body. The red arrow shows the orientation of the dipole.

The voltage distribution generated by the dipole is shown in Figure 5.5, different colours correspond to different voltages and are plotted on the geometry as a surface plot. Figure 5.5 A uses a wide voltage scale that shows the entire range of voltages produced by the dipole but as

the voltage is much higher very close to the current sources, the rest of the body appears to be at an equipotential of around zero on this scale. By using a narrower scale as in B, C and D the voltage distribution can be more easily observed, the regions closest to the source saturate to the maximum value of the scale but the differences in potential throughout the body can be more easily distinguished. Therefore, this narrower scale is used throughout this section and for the other models in this chapter. It can be seen that there are positive and negative voltages close to each pole of the dipole with a reduction away from either side to approximately zero.

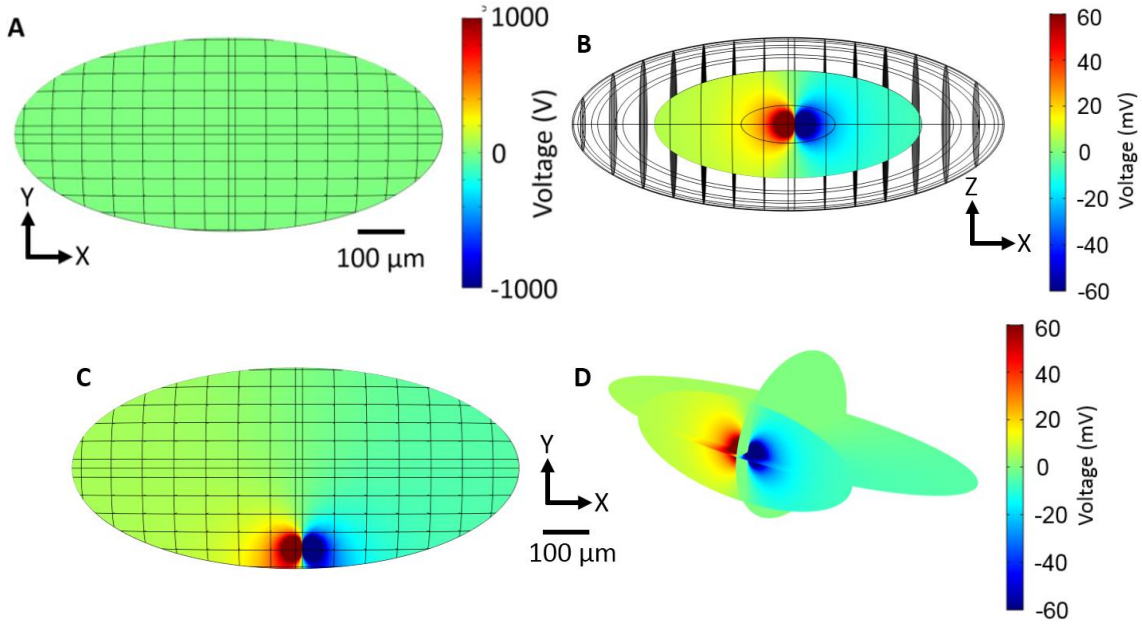

Figure 5.5 Surface plots A) The voltage distribution produced by the dipole with a wide voltage scale. B) XZ plane narrow voltage scale, C) XY plane narrow voltage scale, D) multiple plane (XZ,XZ,YZ) narrow voltage scale (no size scale).

The voltages for the planes ZY1, ZY2 and ZY3 are shown in Figure 5.6 A. For the ZY1 plane that is located on the negative side of the dipole (atrium side), the potential is largely negative close to the source then increases to zero. The reverse is true for the ZY3 plane which is on the positive (ventricle side) of the dipole the potential is large and positive close to the source and then decreases towards zero. The ZY2 plane is located in the middle of the dipole which means it is at an equipotential of zero. These results agree with

what is expected of measurement of a depolarisation wave within the heart i.e. positive when the wave travels towards the recording electrode and negative when the wave is moving away.

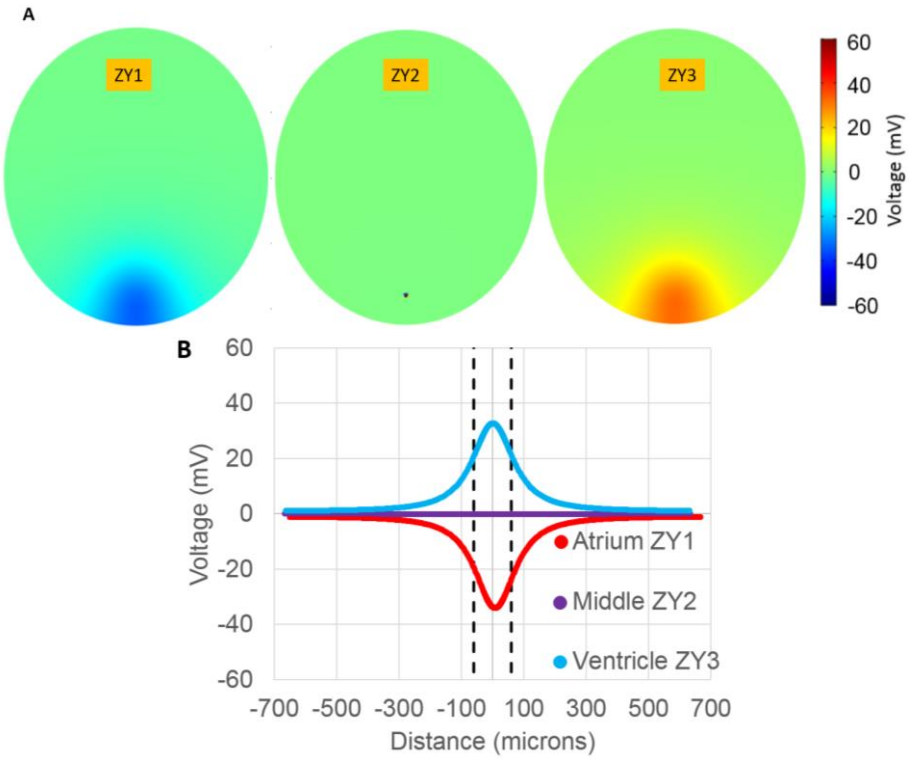

Figure 5.6 A) Voltage distribution in ZY planes, B) voltage on the edge of each plane. The distance refers to the distance around the edge of the plane from the point on the plane closest to current source. The black bars indicate the approximate size of zebrafish heart (120 µm).

Figure 5.6 B shows the variation of the voltage in the form of a graph as a function of distance away from the projection of the dipole on the edge of each plane. As seen in the plane surface plot for ZY1 the voltage is at a maximum at this point as it is the closest point to the dipole, the voltage then falls away sharply reaching nearly zero. The inverse is true for ZY3 and it can be seen that ZY2 is an equipotential of zero in the centre of the dipole. The black bars indicate the approximate size of the zebrafish heart which shows that the maximum voltage is measured close to the heart and electrodes would ideally be placed within this region. Similar surface plots and graphs were genereated for the XZ planes (Figure 5.7).

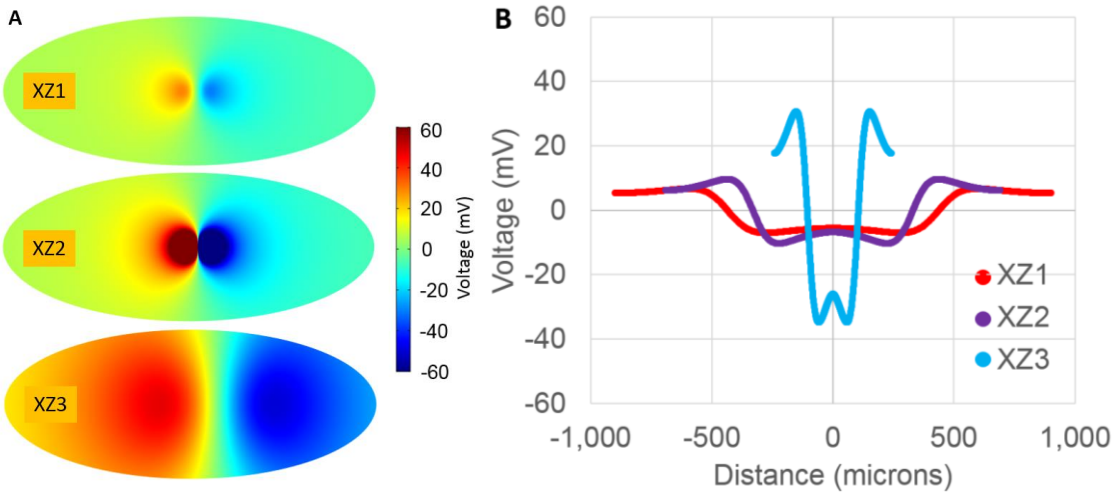

Figure 5.7 A) Voltage distribution in XZ planes. Plots were scaled to the same size. B) Plots of voltage on the edges of each plane. The zero point is the point on the far right of each plane.

The distribution in the XZ plane contains both positive and negative regions instead of one polarity like the ZY plane. The edge plots look more complex due to this but all three show a similar distribution. The graphs zero position is on the far right of the surface plots, from this position moving left or right it can be seen that the voltage initially decreases to a negative peak as the distance to the current source is reduced. This is followed by a sharp increase in voltage from positive to negative as the dipole is crossed to a positive peak followed by a decrease in potential as the distance to the source is increased. Again the maximum potential is closest to the heart and the distribution is symmetrical. Similar plots were also generated for the XY plane (Figure 5.8).

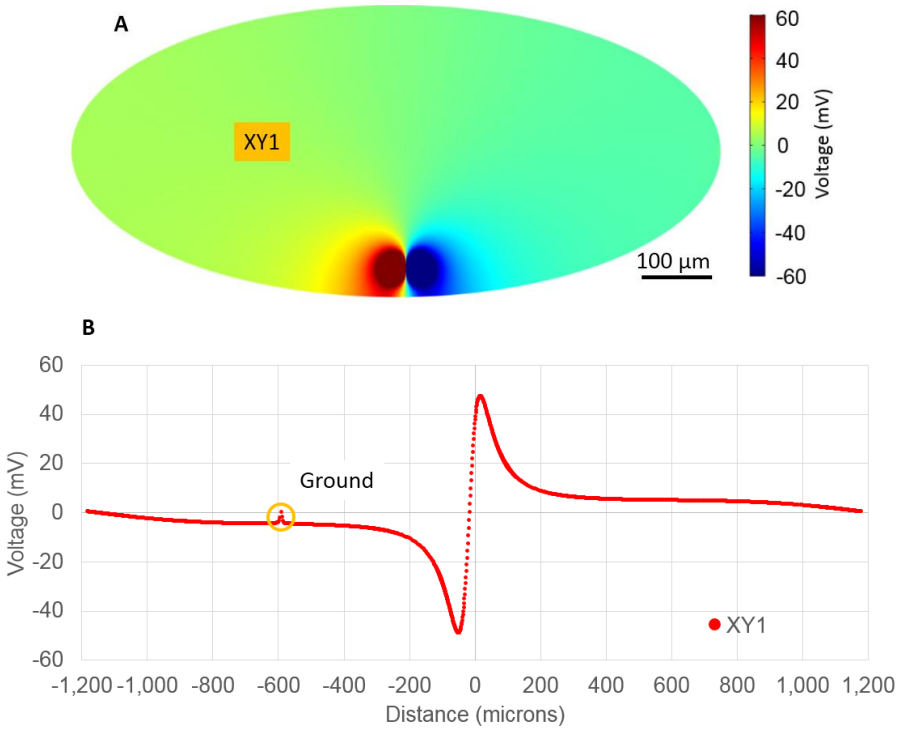

Figure 5.8 A) Surface plot of voltage distribution in the XY plane. B) Plot of voltage on the edge of XY1. The zero position is the point closest to the centre of the dipole. The position of the ground point is also in this plane and its position is marked.

The XY plane is the plane the dipole is in and the distribution reflects this. There are both postive and negative regions with a sharp change between the two and then a fall off in voltage with distance away from the source. Again the largest voltages are closest to the current source.

This model was then extended to replicate other stages of the hearts activation cycle. By reversing the polarity of the dipole, repolarisation was simulated and by changing the dipoles fixed position, the path of the depolarisation and repolarisation waves was also replicated. The dipole was moved using a series of six static simulations by solving for the dipole in one position/polarity, changing the position/polarity and then solving again. Figure 5.9 A shows the six stages that the COMSOL model is intended to simulate, with the intital stage that has already been described (central dipole) being stage 2 (Figure 5.9 B).

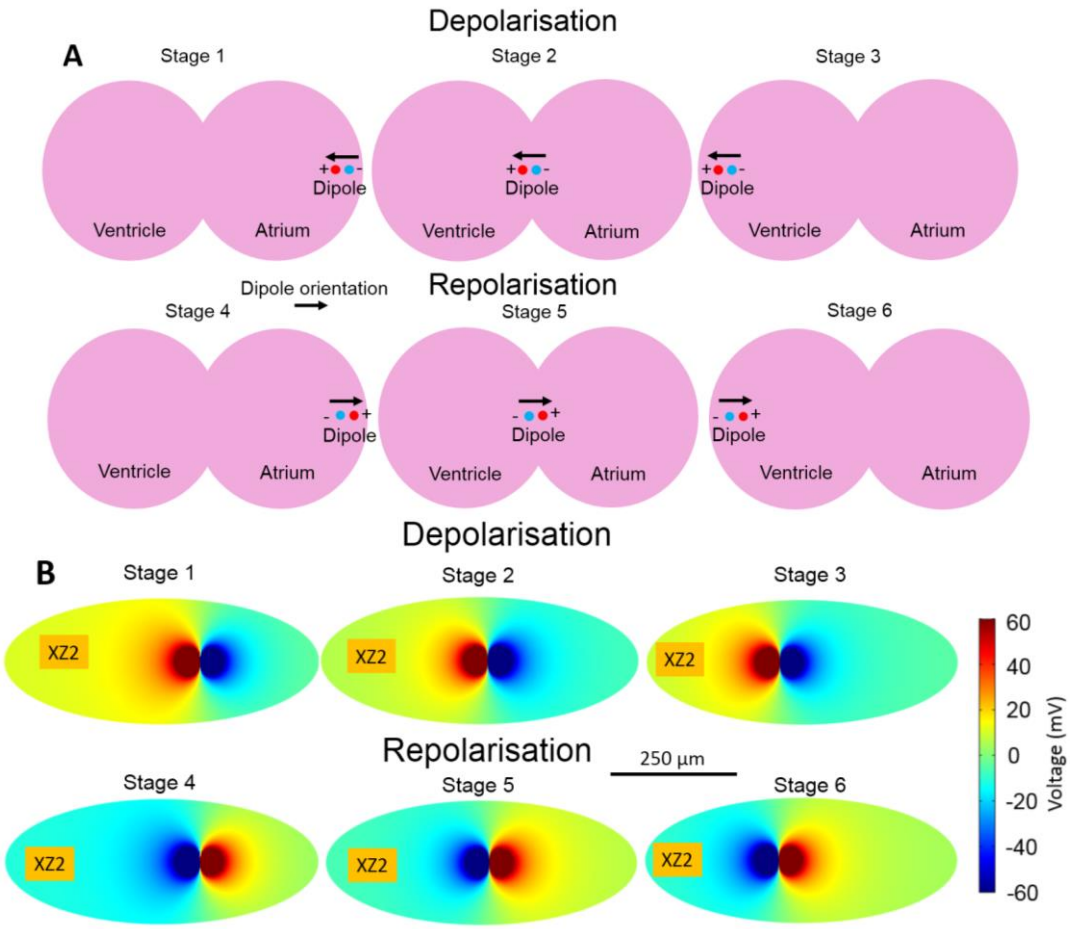

Figure 5.9 A) Simplifed heart with the hearts electrical activity split into six stages. Three for depolarisation and three for repolarisaiton. B) COMSOL model surface plot with the same stages, dipole position moved for stages 1 to 3 and then the same for stages 4-6 with a reversed polarity.

The inverted dipole results in the same shape distribution but with the reverse polarity (Figure 5.10). Postive voltages are towards the atrium side and negative towards the ventricle side, this was to be expected and agrees with the behaviour of repolarisation waves which move in the same direciton as depolarisation waves but with the opposite polarity and lead to inverted measured voltages in comparison to depolarisation waves. From the ZY1 (atrial) position a negative voltage would be expected to be measured when the depolarisation wave moves away from the recording position and a postive voltage when the repolarisation travels in the same direction.

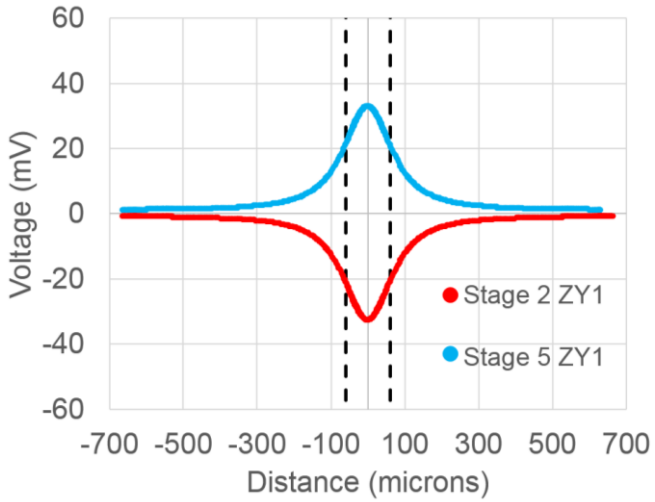

Figure 5.10 ZY plane edge. Stage 2 and stage 5 from ZY1 (atrial position).

The movement of the dipoles fixed position leads to changes in magnitudes and polarities of the voltage on the surface of the body ellipsoid for the different planes. These differences are displayed using the ZY plane edge voltages in Figure 5.11. The plot of each stage contains the voltage from the three planes chosen earlier with stage 2 being the same plot as shown in Figure 5.6. Starting with the atrium position (ZY1) the voltage is initally negative in stage 1 then increases slightly due to a small reduction in distance and widens as the plane is directly over the dipole in stage 2. The distance to the dipole from ZY1 is increased in stage 3 which reduces the potential but it is still negative. Stage 4 is the start of repolarisation and so the polarity of the dipole is reversed, so a positive potential is seen followed by the same changes for stage 5 as between stages 1 and 2. There is a then reduction in potential in stage 6 due to the increased distance. For the middle position (ZY2) the plane is on the positive side of the dipole, at stage 2 the plane is located centrally on the dipole so there is an equipotential and stage 3 shows a change in polarity as the plane is on the negative side of the dipole. Stages 4-6 are the reverse of stages 1-3, starting negative, zero, then becoming positive. Finally, the ZY3 plane voltage

starts low as the dipole is at its furthest point away from the plane, then the voltage increases for stages 2 and 3. Stages 4-6 are the same with the opposite polarity.

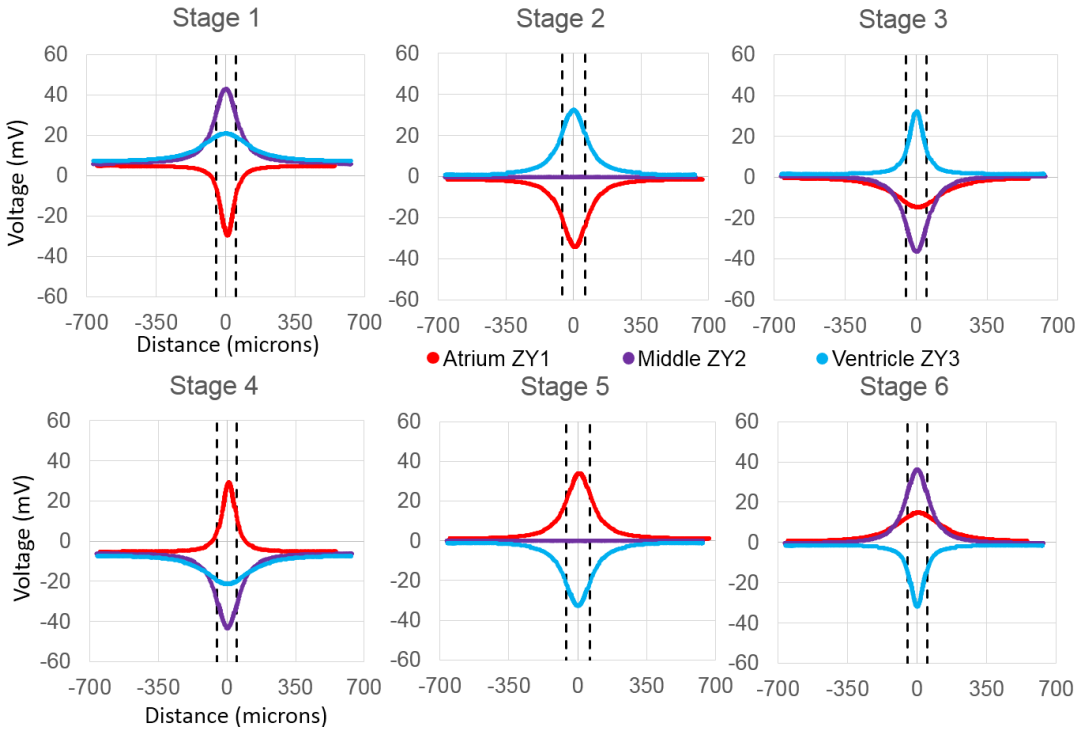

Figure 5.11 ZY plane edge voltages. All six stages and all three planes ZY1 (atrium), ZX2 (middle) and ZY3 (ventricle). The size of the heart is again marked by the black bars.

An approximation of the ECG was then constructed from the peaks of each of these graphs for each position to show what ECG could be expected to be observed at each position (Figure 5.12). These plots show that it was possible to determine a simplified ECG from a simple model of the zebrafish heart. It can be seen that the expected features of the ECG are present (P wave/R wave/T wave) but the time resolution is poor. The time resolution is poor due to the small number of static positions that were simulated. For the ZY1 plane, there is no clear distinction between the P wave and the R wave but they are negative as expected from a recording position where the depolarisation/dipole is moving away. The T wave is also positive as expected. The relative magnitudes of the features are unrealistic as the R wave is generally the largest feature in the real ECG. A clear distinction can be seen between the P wave, R wave

and the T wave in the ZY2 ECG because of the change in polarity from moving the dipole. Each feature also has the expected polarity. The ZY3 ECG is essentially an inverted ZY1 ECG with positive P/R waves and negative T wave with no distinction between P and R. In the real heart, atrial repolarisation occurs at the same time as ventricular depolarisation which was not part of the model and could give a clearer R wave for ZY1 and ZY3 if implemented.

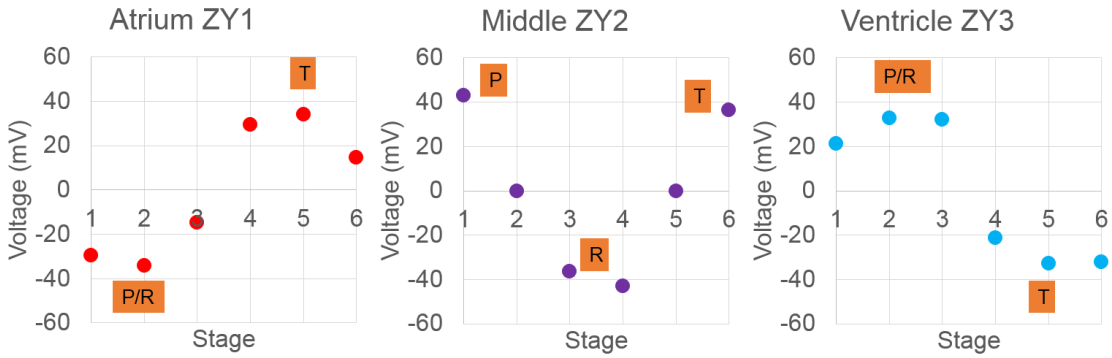

Figure 5.12 ZY plane ECG approximation. One graph for each plane was generated using the peak values of the ZY plane edge graphs. Common ECG features are marked (P wave/R wave/T wave).

This simple dipole model could then be developed and improved further by repositioning the dipole and changing its orientation to more realistically follow the activation in the zebrafish heart instead of just a linear path as presented here. More stages could also be added to improve time resolution and the magnitude of each stage could be scaled to reflect the difference in magnitudes that are observed in the measured ECG (large R wave etc.). Adding multiple dipoles or multipoles are another improvement that could be made. However, rather than implementing these changes it was decided that the realism of the current source should be increased instead, starting with a hemisphere dipole.

5.2.2 Hemisphere dipole

The hemisphere dipole consisted of a sphere split in half with a positive current source applied to one side (2857.1 A/m^2) and a negative current source (-2857.1 A/m^2) applied to the other (Figure 5.13 A). The sphere size was chosen to be approximately half the size of the zebrafish

heart with a radius of 25 microns. This sphere was then positioned in the same position as the point dipole. It was then moved into the same three positions with the same changes in polarity to reproduce the six stages of heart activation as with the point dipole model. The standard extremely fine mesh setting in COMSOL was used for all variations of hemisphere dipole model.

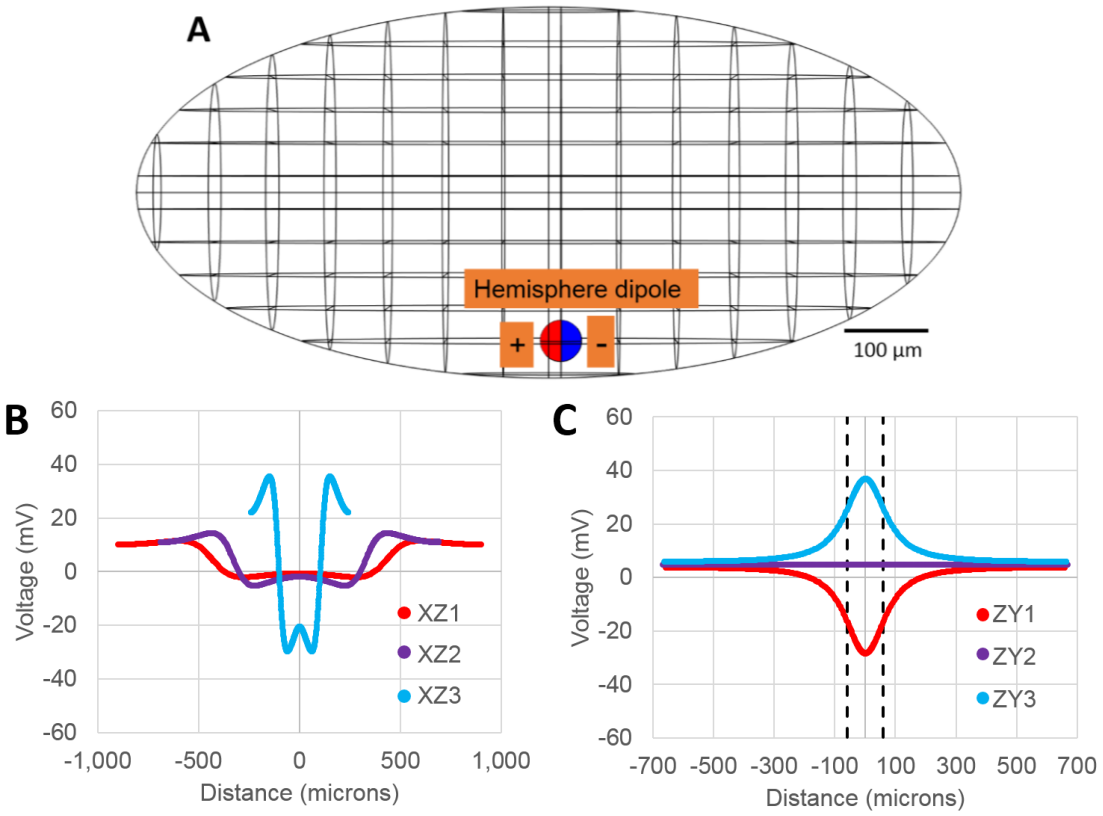

Figure 5.13 A) Hemisphere dipole position in ellipsoid body at stage 2 with positive and negative sides. B) Stage 2 XZ edge plot, C) stage 2 ZY edge plot. Black bars mark approximate size of the real heart (100 µm).

The edge plots of the XZ and ZY planes are largely similar to those from the point dipole as shown in Figure 5.13 B and C. The voltage is largest close to the source and then reduces with distance. Negative voltages are seen on the negative side (ZY1), an equipotential in the middle (ZY2) and positive voltages on the positive side (ZY3). The rest of the six stages are also similar for both surface plots and edge plots Figure 5.14. This means that the the ECGs

generated from this model were also similar. A comparison between the ECGs produced by both models is given later.

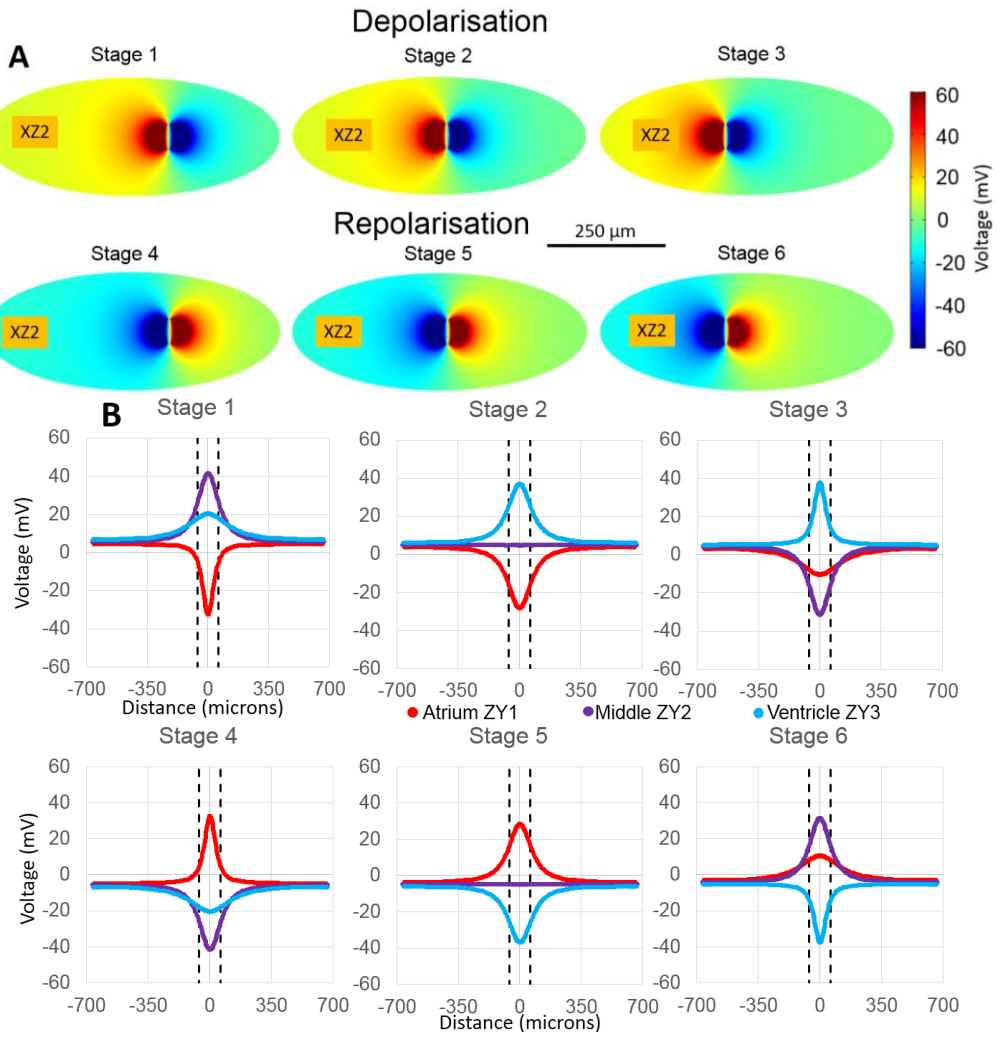

Figure 5.14 A) Surface plots of six stages XZ plane B) ZY Edge plots of six stages.

From here, the same improvements could be made as for the point dipole but instead of doing this, the current source was again improved by using surface dipoles.

5.2.3 Surface dipole

It was thought that the zebrafish heart's electrical activity could be more realistically simulated by using a surface dipole. This model used a simple two chambered 3D heart in place of the point dipole and hemisphere dipole used previously that was based on an image of the 2 dpf

zebrafish heart (Figure 5.15 A). At this stage the zebrafish heart is more tubular than at 3 dpf, which simplifies the geometry. The geometry was created using spheres, blocks and the Boolean operations available within COMSOL, with dimensions chosen to reflect the real size of the zebrafish heart (100-120 µm) (Figure 5.15 B and C). The five main regions of the heart were also incorporated into the geometry (sinoatrial node, atrium muscle, atrioventricular band, ventricle muscle and the two chambers). The standard extra fine mesh setting in COMSOL was used for the heart geometry in this surface dipole model and the finer setting was used for the body geometry.

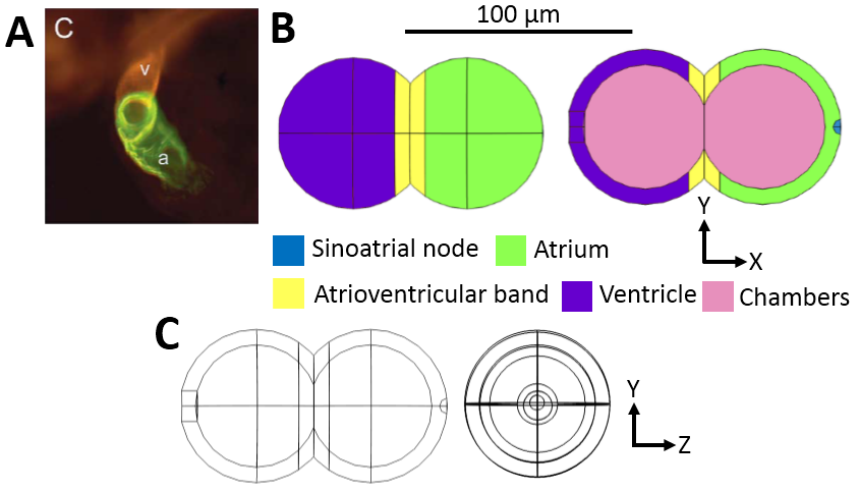

Figure 5.15 A) 2 dpf zebrafish heart from [121] (no scale is given but the approximate size was derived from other sources [50]). B) Simplified heart geometry coloured XY view and cut through showing the distinct regions. C) Wireframe XY and ZY view.

This geometry was then split into sections which created surfaces at fixed intervals through the geometry (Figure 5.16 A and B), where both positive and negative current sources could be applied to form a dipole. A current magnitude of 2857.1 A/m^2 was again used on the first boundary, as the boundaries are of different sizes the currents applied to the other boundaries were scaled according to their areas in relation to the first boundary. Nine of these surfaces were created and pairs were activated in turn to simulate the different stages of the hearts activity cycle. For example, for stage 1, to replicate the initial stages of atrial depolarisation a

positive boundary current source was applied to the second surface and a negative source was applied to the first surface as shown in Figure 5.16 C. This created a dipole that was orientated in the same way as the previous models. Movement of the depolarisation wave through the atrium was simulated in a similar way in stage 2 where a positive source was applied to surface 3 and a negative source was applied to surface 2.

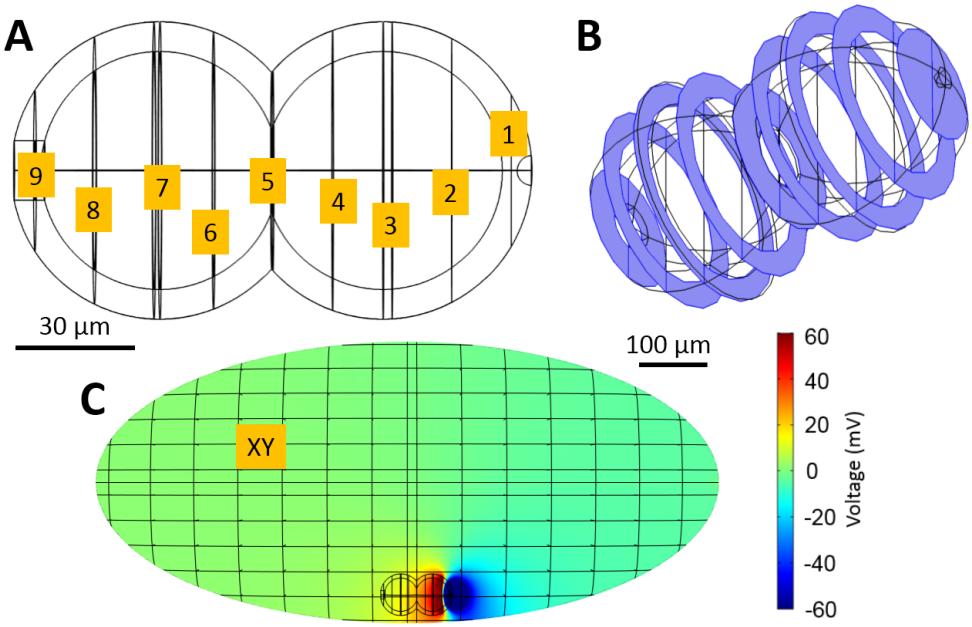

Figure 5.16 A) Sectioned heart geometry, the nine separate surfaces are numbered. B) Highlighted surfaces, C) heart in body with the first (negative) and second (positive) surfaces activated.

This process was continued for each pair of surfaces as shown in (Figure 5.17 A and B) until stage 5. At stage 5, atrial depolarisation ends and ventricular depolarisation begins. Atrial repolarisation occurs at the same time as ventricular depolarisation in the real zebrafish heart (as can be seen in the ECG, chapter 2). This was replicated in the model by applying a positive current source to surface 1 and a negative source to surface 2 (opposite polarity to stage 1) to simulate repolarisation (as with the previous models) in addition to surfaces 5 and 6 which were activated to simulate the start of ventricular depolarisation. Four surfaces were then activated at once in two pairs until stage 8 where the end of the heart geometry was reached. Then a

single pair of surfaces was used to simulate the remainder of the repolarisation for stages 9 to 12.

A

Boundary	Stage 1	2	3	4	5	6	7	8	9	10	11	12
1	-	0	0	0	+	0	0	0	0	0	0	0
2	+	-	0	0	-	+	0	0	0	0	0	0
3	0	+	-	0	0	-	+	0	0	0	0	0
4	0	0	+	-	0	0	-	+	0	0	0	0
5	0	0	0	+	-	0	0	-	+	0	0	0
6	0	0	0	0	+	-	0	0	-	+	0	0
7	0	0	0	0	0	+	-	0	0	-	+	0
8	0	0	0	0	0	0	+	-	0	0	-	+
9	0	0	0	0	0	0	0	+	0	0	0	-

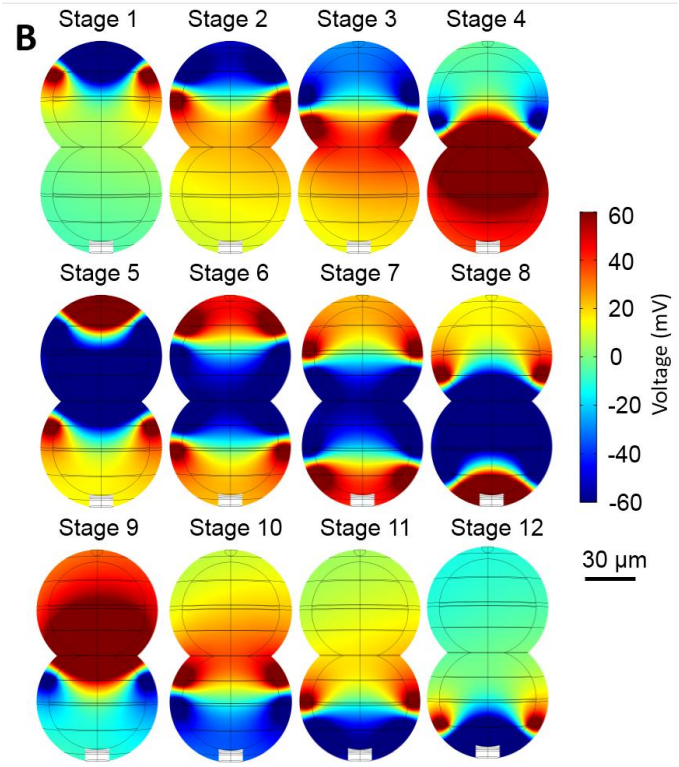

Figure 5.17 A) Table showing surface activation order B) Surface plot of all 12 stages.

As before, the voltage distribution on the surface produced by this model was plotted along the edge of the XZ and ZY planes (Figure 5.18 A and B). These plots largely resemble those from the previous models in shape with a peak followed by a reduction in voltage. For the XZ plane there is a larger spread of voltages but they all have a similar shape with a negative peak closest to the source on the negative side followed by a transition to a positive peak. Positive and negative peaks (minimums and maximums) are not always actually positive or negative voltages due an offset (from zero) that is a consequence of the more complex source. For the ZY plane (Figure 5.18 B), the distributions are also similar with a larger range of voltages but

with the same polarity peaks for the different stages and positions. E.g. Atrial depolarisation (stage 1), negative peak for ZY1 (atrium) and positive for ZY2 (middle) and ZY3 (ventricle).

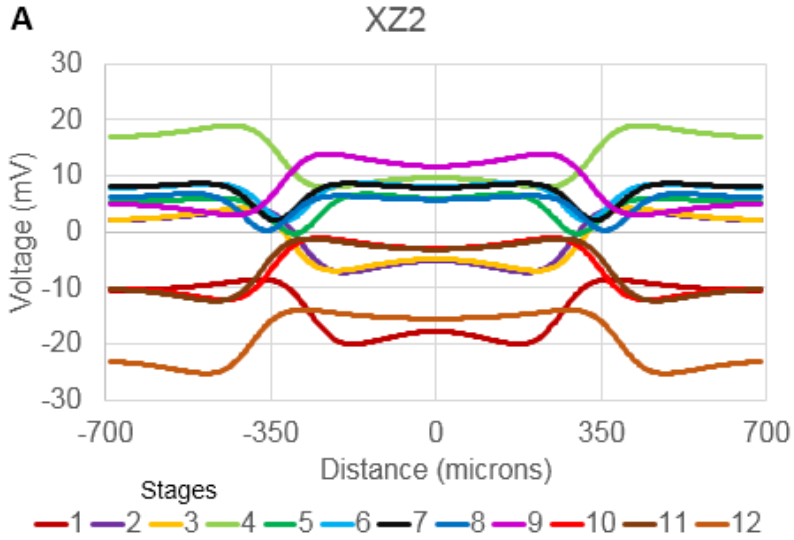

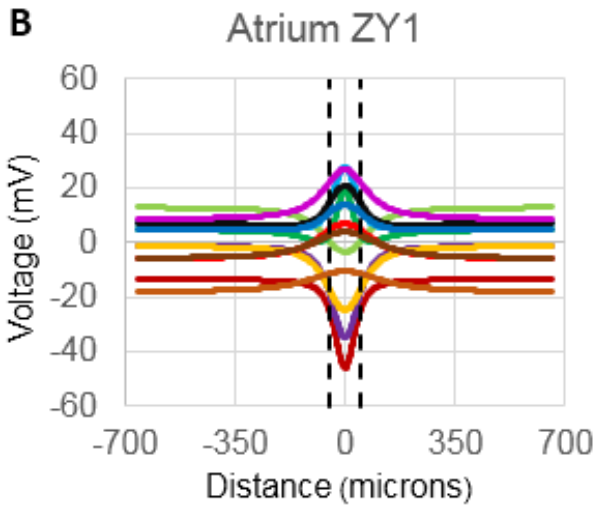

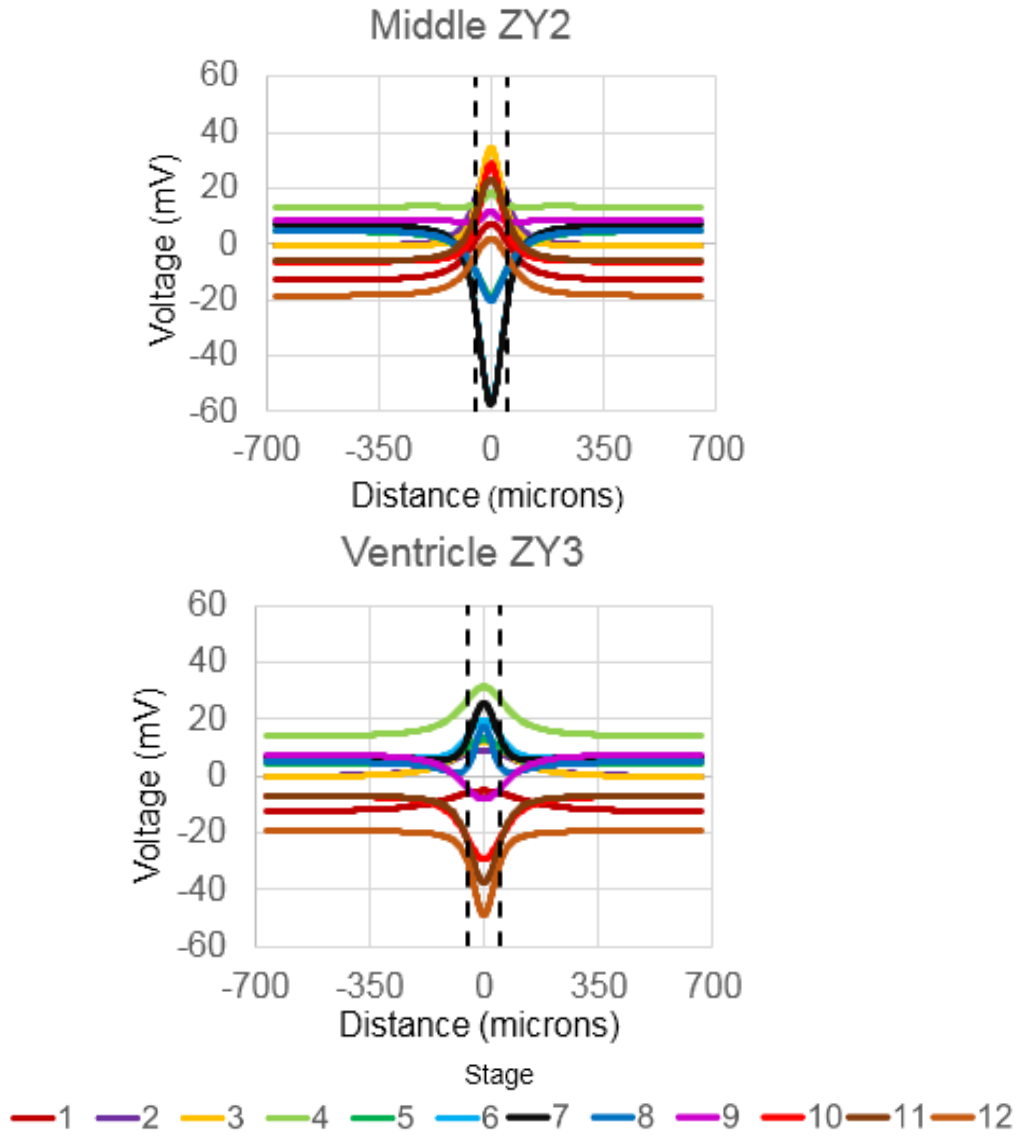

Figure 5.18 A) XZ2 voltage edge plot, B) ZY1, ZY2, ZY3 voltage edge plots. Black bars mark approximate size of real heart.

ECGs were constructed from each peak of the ZY edge plots (as before) as shown in Figure 5.19. It can be seen that these ECGs as with those from the previous models contain the main features of the ECG that are typically measured (P wave, R wave, T wave).

For the atrium position ECG there is a negative P wave as the dipole is orientated away from this position followed by a positive R wave. This is different to the previous models and is a consequence of initiating atrial repolarisation with the second inverted polarity dipole at

stage 5 which gives a positive voltage at ZY1 (atrium side). In reality, the signal received from the ventricle (which is negative) is much larger than that of the positive signal from the atrium [11], so the signal received from this position would be negative overall. But, due to the magnitude of the current sources used in the model, a positive voltage is seen. At stage 9 there is a small rise in voltage which is due to the model being reduced back to a single dipole after the end of depolarisaiton. A negative T wave is then seen which is consistent with the other models.

The ZY2 ECG for the middle position has a positive P wave from being on the postive side of the dipole. A negative R wave is present by stage 5 as this position is on the negative side of both dipoles. This is followed by a positve T wave, as this position is on the positive side of the repolarisation dipole from stage 9.

The ZY3 ventricle ECG is an inverse of the atrium ECG. With positive P and R waves and a negative T wave. There is a peak of voltage at stage 4 which then falls by stage 5 as the second dipole reduces the voltage at this position. The R wave is small due to the repolarisation dipole. The T wave is large and negative as this position is on the negative side.

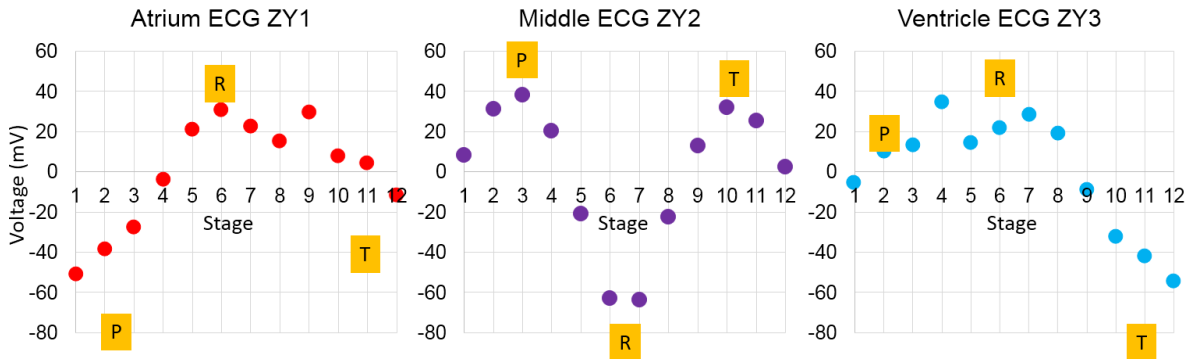

Figure 5.19 ZY edge plot ECGs for each plane ZY1 ZY2 ZY3.

This model could have been improved by varying the magnitude of the current sources for each stage, adding more surfaces and improving the geometry of the both the body and heart.

However, it was thought that a more realistic time dependent model of the heart would lead to a model was that was superior to an improved surface dipole model.

5.2.4 Dipole model comparison

A comparison is made in this section of the three types of dipole model. Figure 5.20 shows a comparison of the voltage distribution in the ZY planes between each model for stage 1 (atrial depolarisation). Unadjusted, the voltages for the point and hemisphere dipoles are very close to each other with the surfaces model slightly offset but with a similar distribution. A slightly different effective current magnitude is used for each model due to the differing surface areas vs a point. By scaling the voltage and changing the offset, these voltages all transform on to one another for stage 1 in all three of the positions (Figure 5.20 B). The same is true for all three positions at stage 6 for point and hemisphere models and the equivalent stage 12 for the surfaces model as shown in Figure 5.20 C. So it can be seen that each of the models produces the same voltage distribution within the body.

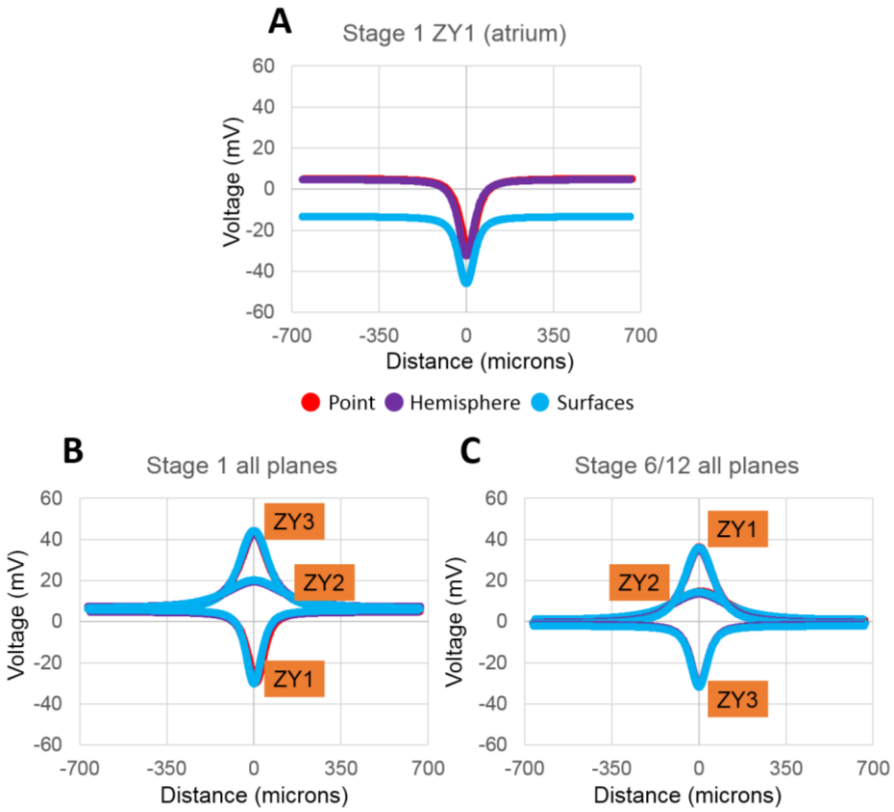

Figure 5.20 Comparison of ZY edge plots for each model. A) Stage 1 from each model ZY1 unadjusted voltages, B) adjusted voltages for stage 1 all planes, C) adjusted voltages for stage 6 (point and hemisphere) and stage 12 (surface).

A comparison of the ECGs from each model was then made as shown in Figure 5.21. The point and hemisphere models have half the amount of stages as the surfaces model so the spacing between each stage was doubled. This makes stage 1 of the point model stage 2 in this comparison followed by stage 2 in the point model being stage 4 in the comparison and so on. The ECGs from the point and hemisphere models are essentially the same which was to be expected as they simulate the same stages. The surfaces model added more complexity with two dipoles and more stages which resulted in slightly different ECGs. The atrium ECG has a negative P wave and R wave for the point but a positive R wave for the surfaces. This (as mentioned) is due to the second dipole in the surfaces model. The signal from the ventricle is much larger in reality due to the increased muscle mass which would make the R wave negative

from this position. The T waves are all positive. The middle position ECGs are similar with the same polarity for each feature and the surface model has more detail on the peaks. This detail is due to the variation in area of the current sources used which is an effect of the geometry as the dimensions of the spherical heart regions reduce at the extremes of the heart. The ventricle ECG shows a similar trend for the point/hemisphere and the surfaces model.

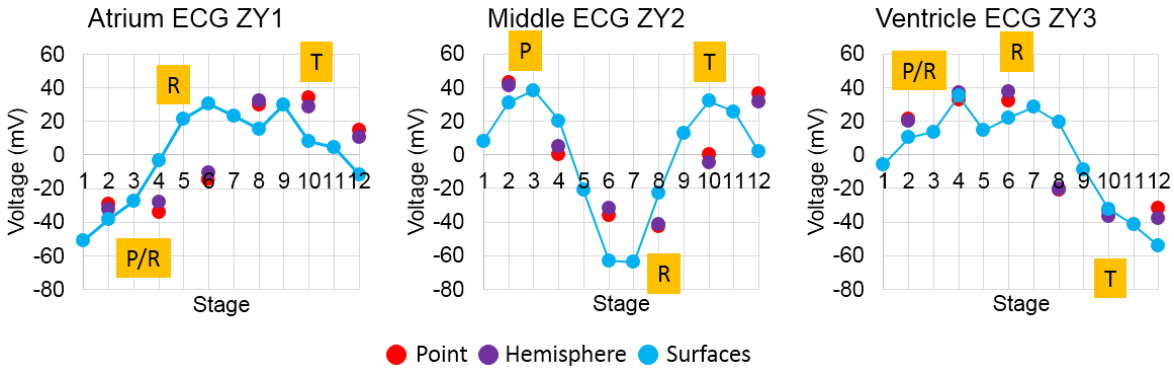

Figure 5.21 ECG comparison for each ZY plane.

The ECGs were then compared to typical recordings from the surface of the zebrafish at three similar positions to those used in the model (Figure 5.22). It can can be seen that the polarity of each peak for the models generally agrees with what is seen in the measurements. There is one exception, which is the R wave of the surfaces model in the atrial position which is positive in the model and negative in the recording.

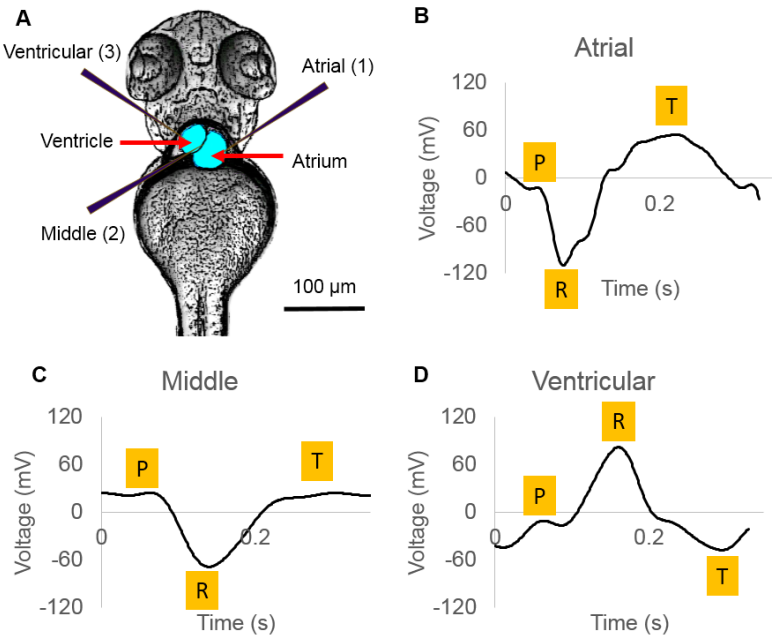

Figure 5.22 Typical ECG recordings from different positions. A) Location of recording positions, B) atrial, C) middle, D) Ventricular. These ECG recordings were provided by Sundeep Dhillon.

In summary, the dipole models are equivalent to each other, they produce the same voltage distribution in the model body and similar ECGs. There is some variation in the surface model due to the increased number of stages, two dipoles and the added heart geometry. The surface model has a higher time resolution due to the increased number of stages but the dipole models could achive the same by adding more stages and by adding an extra dipole as in the surfaces model. All three models could be improved by adjusting the current magnitudes of each stage in correspondence to the amount of muscle mass in each region, adding more stages to improve time resolution, improving the geometry and more realistcally replicating the path of the wave with each dipole.

5.3 Fitzhugh-Nagumo model

The previous models were adequate as a starting point to become familiar with COMSOL and gain an appreciation of the problem. But they were not very realistic and did not replicate some

of the key aspects of a real hearts electrical activity such as action potentials and wave propagation. An improved model was therefore developed by using the FHN equations as a current source in an effort to improve on this realism and produce more accurate results. Rather than using the original form of the FHN equations, the Rogers-McCulloch form of the FHN equations [74] were chosen due to their ability to better replicate the shape of cardiac APs without the negative recovery phase as described in chapter 3.

Firstly, the Rogers-McCulloch form of the FHN equations were used with a variety of simple isolated heart geometries to investigate their properties. The same 3D heart geometry was used as for the surface dipole model (before sectioning) as shown in Figure 5.15. This was used as an isolated heart. The equations as described in chapter 3 are [74]:

$$\frac{\partial u}{\partial t} = \nabla \cdot D\nabla u + c_1 u(u-a)(1-u) - c_2 uv \tag{5.2}$$

$$\frac{\partial v}{\partial t} = b(u - dv) \tag{5.3}$$

Where u is again analogous to the membrane potential and v is a recovering variable. a, b, c_1, c_2 and d are parameters that effect the shape of the AP and D is the diffusion coefficient which effects the waves propagation velocity. The parameters used were those given in [122] and are shown in (Table 5.1). The values of each of these parameters were fixed for all regions of the model heart.

Table 5.1 – Parameter values for the Rogers FHN equations [122].

Parameter	**Value**
a	0.1
b	0.024
c_1	10
c_2	10
d	1
D	5

The model was solved for t = 0 to t = 60 in steps of 0.1. Wave propagation was initiated by raising the potential of the sinoatrial region to 1, from an initial value of 0. This raised potential was applied between t = 2 and t = 5 which was above the threshold for activation, this triggered an AP which travelled through the heart geometry. The AP produced by the activation is shown in Figure 5.23 B. As the same parameters were used for all regions of the heart the APs from each region look the same which is not realistic as shown by Figure 5.23 A, where the duration of the ventricle AP is longer than that of the atrium AP. As mentioned previously, the units of the FHN equations are arbitrary space/time/voltage units and so to convert to real units, comparisons were made with the measured APs, as was done in [74]. The model voltage units range from 0 to 1. As the measured atrium and ventricle APs are different durations, comparing against each AP would give a different result. As the model contains only a single AP, it was decided just to scale the units of the model against the atrium AP. It was found that:

- 1 time unit = 0.00333 s
- 1 voltage unit = 0.104264 V

The space units could not be determined from measurements but the model was scaled so that one space unit was equal to one micron. The standard extra fine mesh setting in COMSOL was used for the heart geometry in this FHN model and the finer setting was used for the body geometry.

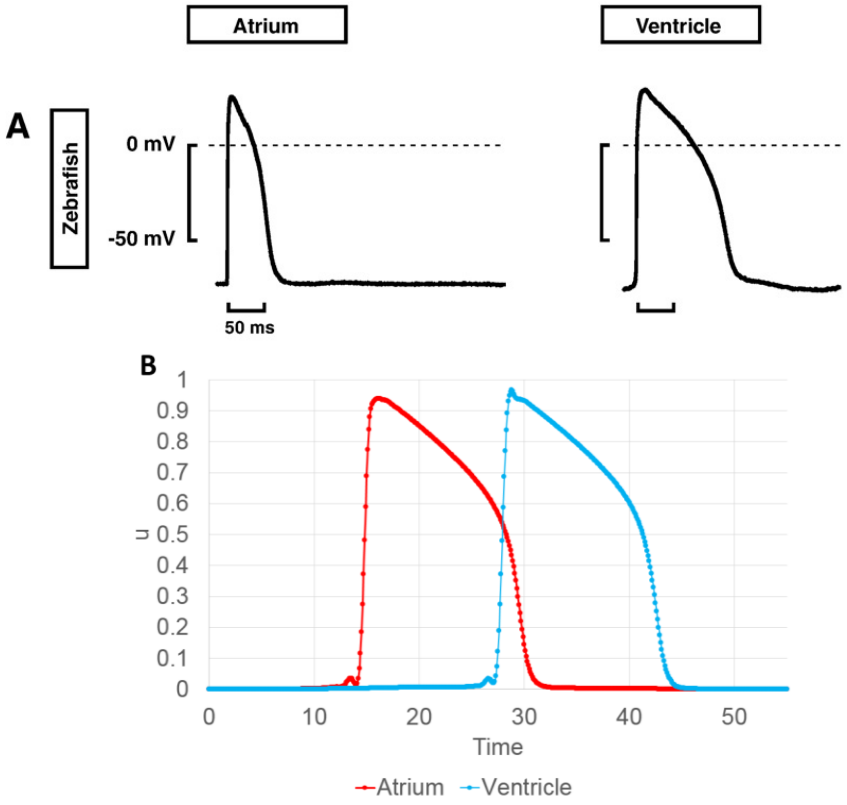

Figure 5.23 A) Measured action potentials from adult zebrafish [13], B) model action potentials plotted from points midway through the atrium and ventricle (arbitary units).

The progress of the AP through the model heart is shown in Figure 5.24. The wave is initiated at the sinoatrial node (top of the heart) and precedes through the atrium, through the atrioventricular band and in to the ventricle. It can be seen that the progression is much smoother than that of the surface dipole model with a much higher time resolution. This model uses a more realistic source but has some limitations, principally in simulating the ECG. The voltage that is determined with this model is the transmembrane voltage ($V_i - V_e$). The ECG is determined by the value of the voltages on the surface of the heart which are the extracellular voltages, which are simulated by the dipole models but not by the FHN equations. That is, unless, they are used in conjunction with the bidomain model (although other methods have been used [77]).

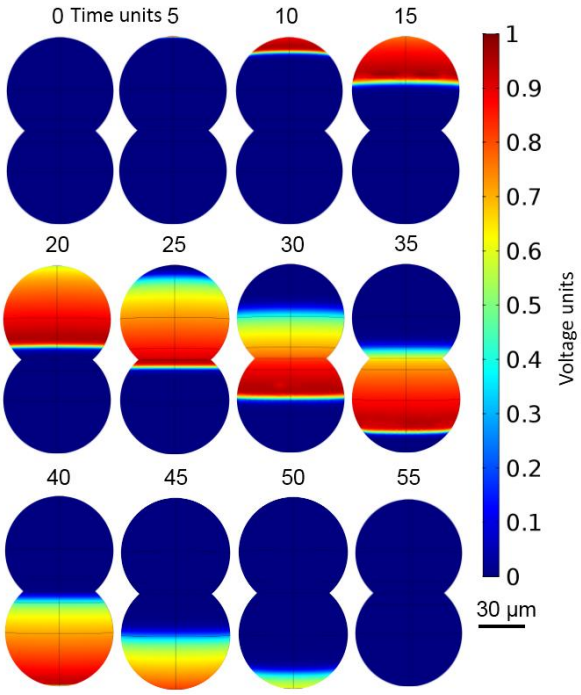

Figure 5.24 Action potential propagation through model heart at different time points (arbitary units).

5.4 Summary of this chapter

This chapter has described a series of models which were created in the development of a model of the larval zebrafish heart. The dipole models showed that they could produce a simple yet recognisable ECG. The same voltage distribution was generated in the body by each variation of dipole, with a high positive or negative voltage close to the current source/heart which then reduced with distance. This meant that similar ECGs were produced for each model. These models had the advantage in that they were simple and so could be solved in a small amount of time and improved easily. The geometry of the models is simple for both the body and heart. The surface model added more realistic heart geometry and a second surface dipole to simulate repolarisation occurring at the same time as ventricular depolarisation as is seen in the measured ECGs (Figure 5.22). This simplicity is also a limitation as they are not realistic models, no AP or propagating wave is simulated and their time resolution is poor.

Instead of improving the dipole models, a time dependent more realistic model was developed that incorporated the main features they were missing (AP and wave propagation), which was the FHN model. This model successfully simulated an AP that was of similar shape to those measured from the zebrafish. By comparing the model output to the measured values it was also possible to determine the magnitude of voltages in the model from the arbitrary units of the equations. Propagation of the AP through the same 3D heart geometry was also simulated with a high time resolution. In the real zebrafish heart, each region has different properties which leads to differing propagation speeds and AP shapes which both have an effect on the resultant ECG, whereas, the FHN model presented here used a single AP for the entire heart. This could be improved by varying the parameters of the equations for each region.

A disadvantage to using a more complex model is the increase in solution time when compared to the dipole models but it was thought that the added realism was worth the trade-off. The solution time is proportional to the number of elements in the mesh. A simpler geometry requires less elements to represent it. Therefore, the simplified two chamber heart geometry was useful in development of the model as less time was needed to solve to it but improvements in geometry realism would of course add to this time.

The main problem with the FHN model became apparent when attempting to model the ECG. The voltage that is determined with this model is the transmembrane voltage ($V_i - V_e$). The ECG is determined by the value of the voltages on the surface of the heart which are the extracellular voltages, which are effectively simulated by the dipole models but not the FHN equations by themselves. The FHN equations are commonly used to solely model wave propagation and arrhythmias within an isolated heart and not the ECG so this limitation is not generally an issue. They have been used to model the ECG before [77] by calculating the values

of dipoles as proportional to the gradient of u but the more common method (as described in chapter 3) is to use the FHN equations or other more complex variants as the ionic model in the bidomain equations [37]. This is the method that was chosen for expanding on the FHN model. It is explained in the next chapter and improves on all the problems with the models in this chapter with improved geometry, variation in APs between regions and predicts the ECG.

6. BIDOMAIN HEART MODEL

The previous chapter described various heart models that were created to simulate the ECG with their main disadvantage being their simplicity. The aim of the work described in this chapter was to expand on the previous models and create a more realistic model that was able to make more realistic predictions of the larval zebrafish ECG. This was achieved using a bidomain model of the zebrafish larval heart that uses the FHN equations as the ionic model. The model simulates APs, wave propagation and the resulting ECG. The electrical model used is described first along with the appropriate boundary conditions. Then the geometry of the model is explained for both the heart and body. This is followed by a section on the selection of the model parameters for generating realistic APs and conduction velocities with comparison to both measured APs and an activation map. Model ECGs are then compared to the observed ECGs and finally there is a summary and discussion of the results of this chapter. A paper has been published in PLOS One based on the work in this chapter.

6.1 Electrical model

The electrical activity of the zebrafish heart was simulated using a combination of Laplace's equation and the bidomain equations. The model body is again treated as a homogenous volume conductor described by the Laplace equation:

$$\nabla \cdot (-\sigma_b \nabla V) = 0 \tag{6.1}$$

Where V is the voltage in the body and σ_b is the body conductivity which was 0.2 S/m as used previously.

The cardiac electrical activity was simulated using the bidomain equations that as explained previously, have been widely used to model the human heart [35, 37, 40]. The heart is treated as a region consisting of two interpenetrating domains representing the intracellular and extracellular spaces. A derivation of the equations was given in in chapter 3. The following equations were inputted into COMSOL:

$$\frac{\partial V_e}{\partial t} - \frac{\partial V_i}{\partial t} = \frac{1}{C_m A_m}(-\nabla \cdot (-\sigma_e \nabla V_e) + A_m i_{ion}) \tag{6.2}$$

$$\frac{\partial V_i}{\partial t} - \frac{\partial V_e}{\partial t} = \frac{1}{C_m A_m}(\nabla \cdot (-\sigma_i \nabla V_i) - A_m i_{ion}) \tag{6.3}$$

Where V_e is the extracellular voltage (V), V_i is the intracellular voltage (V), σ_e is the extracellular conductivity (S/m), σ_i is the intracellular conductivity (S/m), i_{ion} is the ionic current, A_m is the surface-to-volume ratio (1/m) and C_m (F/m) is the membrane capacitance per unit area.

The Rogers-McCulloch version of the FHN equations [74] were again used for the models in this chapter as the ionic model. Again, despite being a phenomenological in origin, these equations were chosen as they reproduce the main properties of cardiac tissue (APs, wave propagation and threshold) and are capable of simulating the ECG in conjunction with the bidomain model [80], whilst still being relatively computationally inexpensive. They also do not require measurements of individual ion channels from the zebrafish heart (which were not available in the literature or elsewhere). i_{ion} in its self-excitatory form is given by:

$$i_{ion} = kc_1(V_m - B)\left[a - \frac{(V_m - B)}{A}\right]\left[1 - \frac{(V_m - B)}{A}\right] + kc_2 u \tag{6.4}$$

in the sinoatrial region and by:

$$i_{ion} = kc_1(V_m - B)\left[a - \frac{(V_m - B)}{A}\right]\left[1 - \frac{(V_m - B)}{A}\right] + kc_2u(V_m - B) \quad (6.5)$$

in the rest of the heart. As before, Vm is the transmembrane potential given by:

$$V_m = V_i - V_e \quad (6.6)$$

Where V_i is the intracellular voltage and V_e is the extracellular voltage. *u* is a recovery variable given by:

$$\frac{\partial u}{\partial t} = ke\left[\frac{(V_m - B)}{A} - du - b\right] \quad (6.7)$$

k, c1, c2, A, B, a b, d and e, are parameters that effect the shape of the AP. Each parameter has a major effect on the AP shape as well as minor effects with some overlap between parameters. The effects of these parameters are explained in the next sections.

6.1.1 Boundary Conditions

As with other models in previous work [37], a reasonable assumption is that the exterior faces of the body are insulated. A reference ground point was also located on this boundary as with the previous models. The boundaries between the body and heart have the condition:

$$V = V_e \quad (6.8)$$

All boundaries between the heart (excitable tissue) and the body/chambers (volume conductor) have a zero flux condition for V_i:

$$-\boldsymbol{n} \cdot \sigma_i \nabla V_i = 0 \quad (6.9)$$

where n is the unit vector normal from the boundary. For V_e, the inward flux is equal to the outward current density (**J**) from the body:

$$-\boldsymbol{n} \cdot \sigma_e \nabla V_e = \boldsymbol{n} \cdot \boldsymbol{J} \quad (6.10)$$

6.2 Geometry

In the development of the model a variety of simple geometries were used, such as 1D lines, 2D blocks with one block representing each region of the heart, 2D top down cross sections (Figure 6.1 C) and the same simplified 3D model as used in the FHN model from the previous chapter. But as the main objective of the model was to be useful in the design of ECG experiments a realistic geometry model was also developed. This was based on 3 dpf zebrafish as this is the stage generally used for ECG because the heart is functioning normally and positioning of the zebrafish is easier due to the lack of a swim bladder.

The realistic zebrafish body geometry was initially based on an image stack generated using Optical Projection Tomography (OPT) [123, 124] which was visualised by importing it into Slicer [125, 126] as shown in Figure 6.1 A-B. The main shape of the zebrafish body was extracted from this using thresholding and exported into Blender (Blender Foundation [12]). To start with the geometry was rough and progressive improvements were made. The tail section wasn’t needed so that was removed to reduce the number of elements required to represent the geometry.

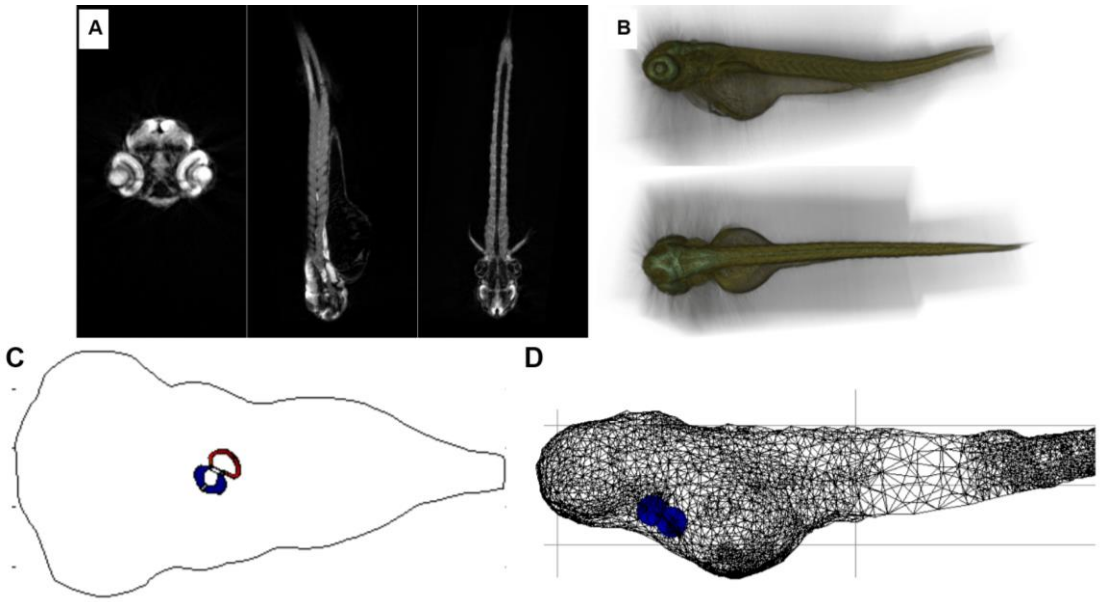

Figure 6.1. A) Slicer three plane projection, B) slicer visualisation, C) 2D topdown model geometry for testing, D) early 3D geometry using simiplifed heart geometry.

The rough outline was shaped to match bright field microscopy images provided by Sundeep Dhillon to arrive at the final geometry. The heart geometry was created using reference images from the literature [48, 52, 127-137] such as the image shown in Figure 6.2 A. Generally, heart images in the literature only show a clear view of the heart from a single plane, some sources show one plane and others another. Therefore, to create the 3D geometry the heart shape was approximated in other planes based on less clear images using ellipses as shown in Figure 6.2 B.

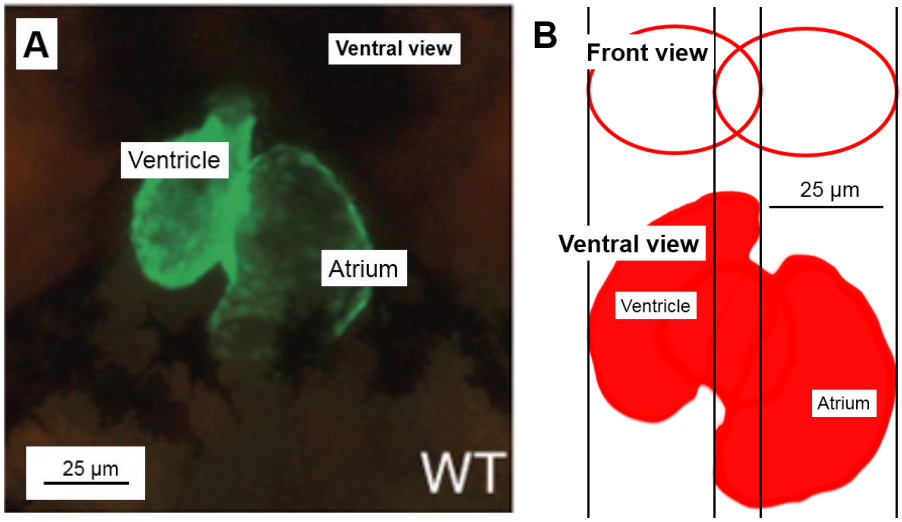

Figure 6.2. A) Fluorescent heart image which was used as the basis for the 3D heart goemetry from [52] B) Schematic heart images that were used to shape the heart geometry

Both the body and heart geometries were positioned and finalised in Blender, they were then imported into FreeCAD [138] to convert to a CAD file and then finally imported into COMSOL for the electrical simulation using the CAD import module (Figure 6.3). It can be seen that the model is an accurate representation of the larval zebrafish (Figure 6.3 A, B, C) when compared to the model geometry (Figure 6.3 D, E, F). The heart is located very close to the surface and it is visible through the skin from a lateral position, and also from above in a ventral position, as replicated within the model.

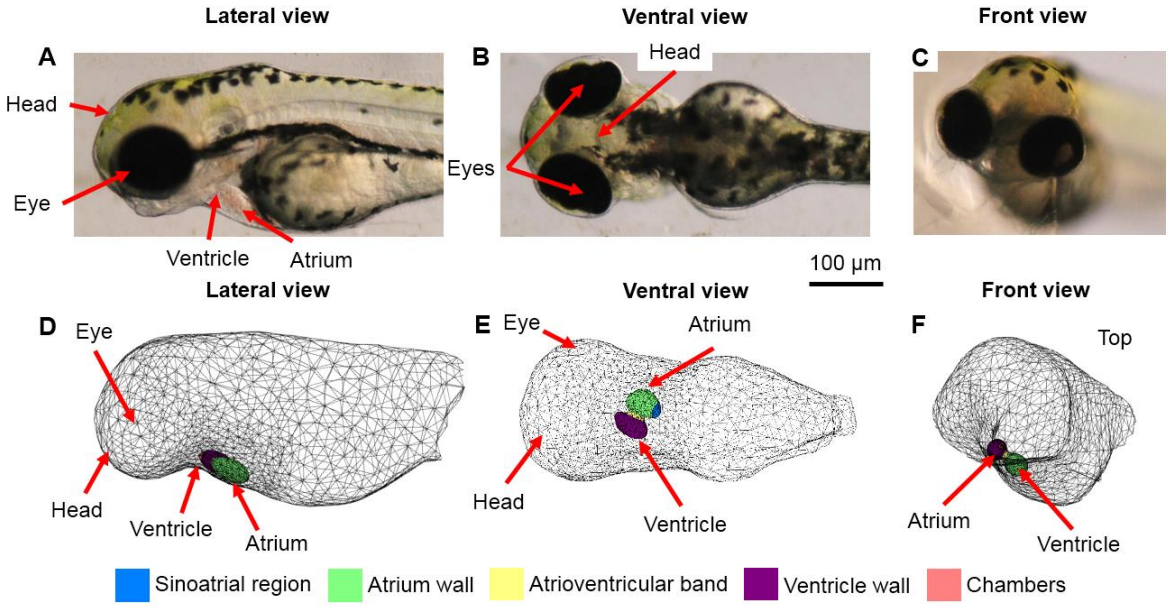

Figure 6.3. Comparison of 3D model geometry to 3 dpf zebrafish anatomy. A) lateral, B) ventral, C) front brightfield views; D) lateral, E) ventral, F) front view of model. The different coloured regions highlight the distinct heart regions within the model. Microscopy images were provided by Sundeep Dhillon.

The heart geometry was split into five distinct regions, as with the simpler heart geometry used in the FHN model, which were based on the different sections of the zebrafish heart: the sinoatrial region, atrium wall, atrioventricular band, ventricle wall and the heart chambers (Figure 6.4). This resulted in a model heart that is approximately 100 µm in size with ~7 µm walls.

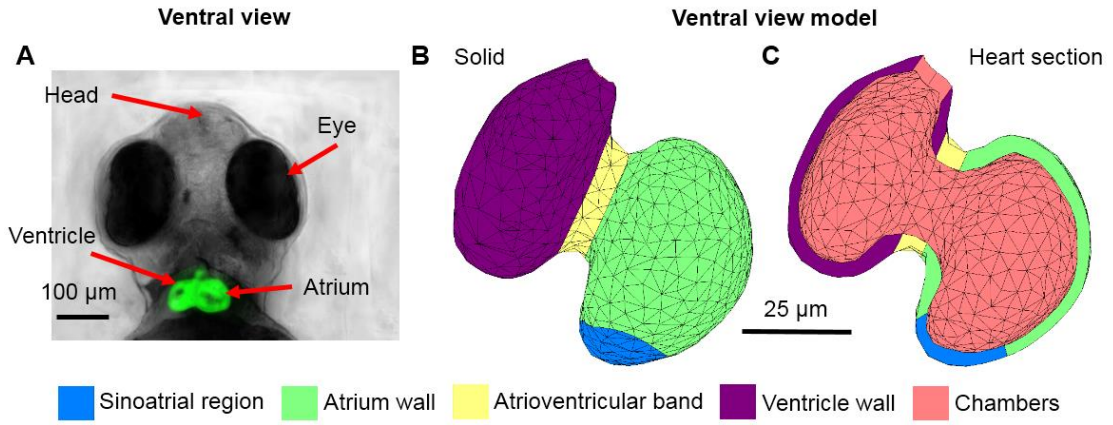

Figure 6.4. Image of 3 dpf zebrafish heart compared to model heart geometry. All images are from a ventral view. A) depiction of a 3 dpf *Tg(fli-1:EGFP)* zebrafish with a fluorescing heart, B) solid view of heart geometry, C) model heart geometry cut through showing the distinct regions. Microscopy images were provided by Sundeep Dhillon.

6.3 Model parameters

This section is split into three sections. The first describes the difference in the units of the bidomain model and the FHN model from the previous chapter. The selection of parameters that determine AP properties are described followed by those that determine the AP/wave propagation velocity.

6.3.1 Units

The version of the FHN equations used in this chapter are slightly different to those used in the previous chapter. The extra parameters (A, k, B etc.) in this version are there to scale the units and increase the adaptability of the equations. The units of the model are scaled directly rather than the original FHN equations which used arbitrary space, time and voltage units that needed to be scaled afterwards as in the previous chapter. Therefore, 1 voltage unit in the model is equal to 1 V, 1 time unit is equal to 1 s and 1 space unit is equal to 1 micron.

6.3.2 Action potential shape

The bidomain model was initially investigated using the parameters given in [80] that were chosen to produce human like APs and wave speeds. In this human heart model, the distinct

regions of the real human heart were replicated by using different parameters for each region to give APs with different shapes. A similar approach was taken to model the zebrafish heart by selecting the parameters of the equations in each region so that that they reproduced the shape of the atrial, atrioventricular band and ventricular APs as measured *in situ* from the zebrafish heart [49]. The *in situ* measurements are shown in Figure 6.5. This figure was created by extracting data points from Figure 3 in [49]. There was no available measurement of the AP from the SAR region but there are measurements from the rest of the main heart regions (atrium, atrioventricular band and ventricle). Each heart region has a distinct AP which was replicated in the model.

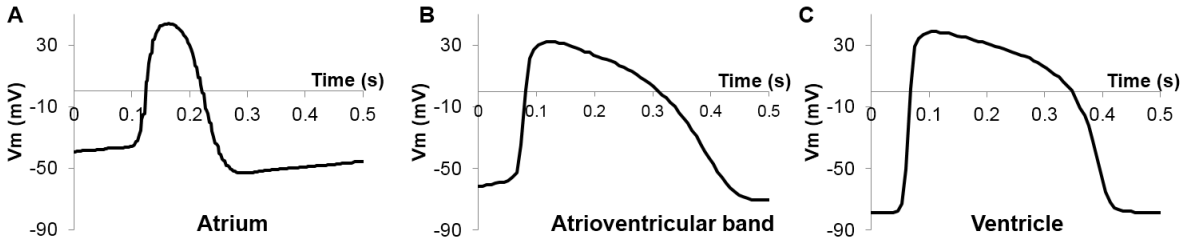

Figure 6.5 2 dpf zebrafish action potentials recorded *in situ* reproduced from [49]. A) Atrial muscle B) AV band, C) ventricular muscle.

Starting with the parameter values given in [80], a, b, c1, c2, e, k, A and B were changed systematically. Firstly, each parameter in the equations was investigated individually to judge their effects, then final values were selected that gave results that best matched the measured APs. A range of each parameter was used to determine its effect on the shape of the AP then the value that was found to give the closest match to the *in situ* recordings [49] was chosen as the final value. The closest match was determined by comparisons between the model output and the experimental recordings for the key parameters APD, magnitude, upstroke gradient and downstroke gradient. Each parameter has a major effect on the shape of the AP along with other minor effects, so parameters were adjusted for the major effect then the minor deviations were

accounted for by compensating in the preceding parameters. These parameter adjustments were carried out by hand and no fitting tool was used.

The most important part of the APs that the model needed to replicate was the APD of each AP as this feature has the largest effect on the morphology of the resulting ECGs. This is because the APD determines the time delay between ECG peaks associated with depolarisation and repolarisation. The fitted APs did not have to exactly match the measured APs because minor differences in AP shape (as there is between the fit used and the measured APs) were found to have a minimal effect on the ECG morphology. In addition, there are factors that have a larger effect on ECG morphology than minor differences in AP shape. There is a difference in temperature between the AP measurements and the ECG measurements (explained later) and there was also no indication of variability in measured AP morphology given in [49], so the model fit could well be within measured ranges. There are also other factors such as the choice ionic model, the geometry and the lack of heart movement. Therefore, a less than ideal overall fit that replicated the main feature (APD) of the AP as well as approximate fits of other key AP parameters is sufficient to simulate the ECG due to the minor effects of any other differences given the larger effect other factors have. This is shown by the comparisons to measurements in section 6.4.3.

Parameter sweeps were performed using a combination of 1D MATLAB simulations and simple 2D geometries in COMSOL. As there was no measurement for the SAR region the other three APs were fitted for first by triggering an AP using a stimulus current as with the FHN model from the previous chapter. The parameters of the SAR region were then selected using the atrium parameters as a starting point but with the alternate self-excitatory equation. The values were adjusted until an AP was triggered in the adjacent atrium region.

The results of these sweeps showed that for the non-excitatory equation the major effects are that ‘k’ affects the time scale/duration, ‘A’ the AP magnitude, ‘B’ offsets the voltage to set the resting potential, ‘c1’ and ‘c2’ effect the upstroke/downstroke and both ‘a’ and ‘e’ affect the APD.

Figure 6.6 A-D shows the effect of changing ‘k’ on the key parameters of the ventricle AP shape. The range of values used are around the final value chosen and all the other parameters are set to the final values (Table 6.1). The percentage change graphs show the percentage change for each parameter (magnitude, duration, upstroke/downstroke gradient) from that of the final value. ‘k’ can be seen to have little effect on the AP magnitude but much larger effects on the duration and gradients of the upstroke and downstroke. A value of 1000 was chosen as the final value (as in [80]) as this reduces the APD to approximately realistic values and then smaller adjustments were made using ‘e’ as in [80] rather using ‘a’. The effects of ‘e’ are shown in Figure 6.6 E-H, there is little effect on the magnitude/upstroke/downstroke with a much larger effect on the APD.

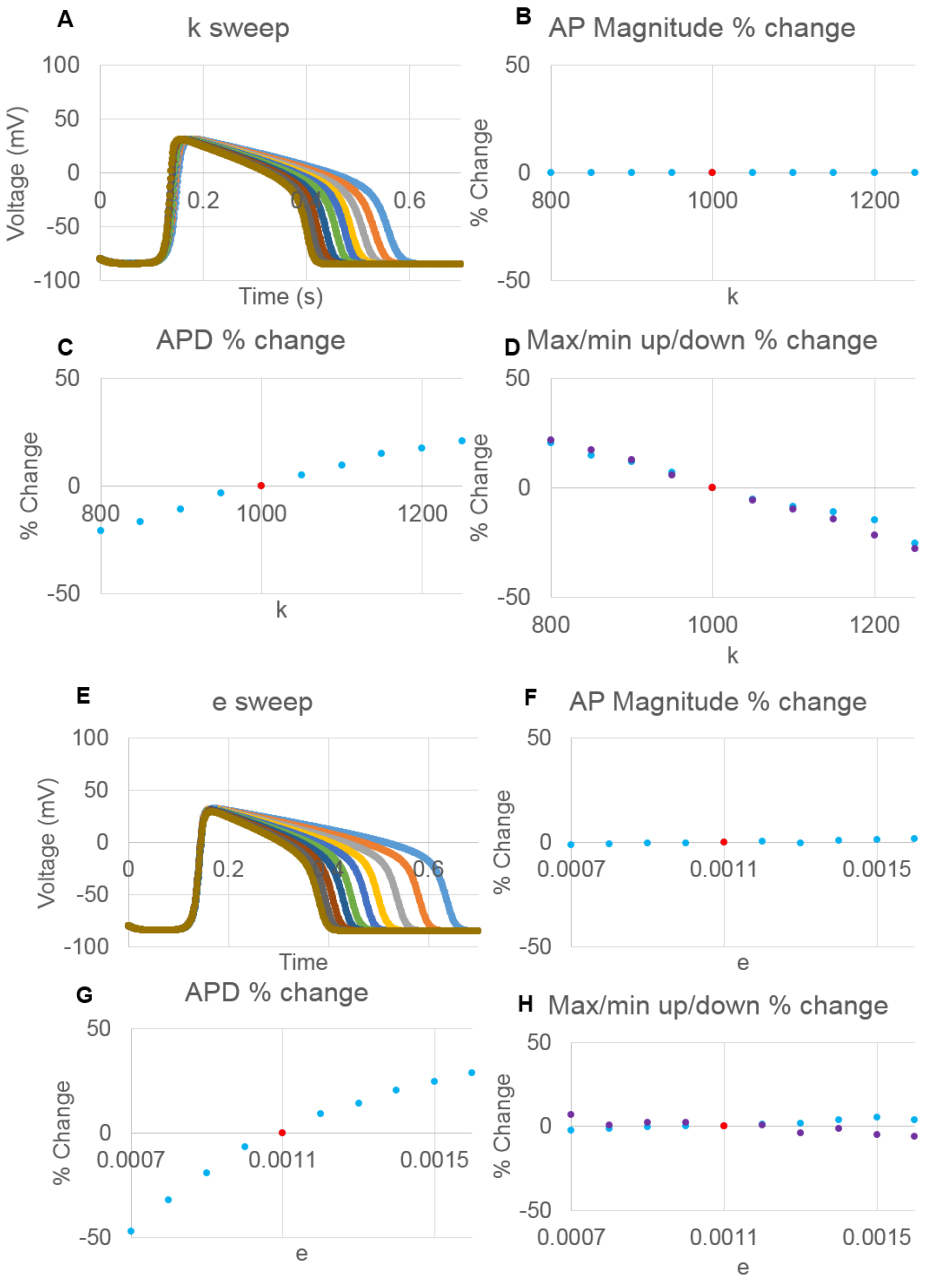

Figure 6.6 A) Ventricle action potential shape for different 'k' values, B) effect of 'k' on AP magnitude as a percentage change from magnitude using the final value (1000) marked by the red point. C) Effect of 'k' on the action potential duration. D) Effect of 'k' on the maximum upstroke and minimum downstroke gradients. E) Ventricle AP shape for different 'e' values. F) Effect of 'e' on magnitude. G) Effect of 'e' on APD. H) Effect of 'e' on upstroke/downstroke gradient.

'A' was found to be similar to 'k' in that it's major desired effect was scaling the magnitude of the AP and it also had the side effect of changing the gradient of the AP but there was little effect on the APD. To find the final parameters 'k' was fixed at 1000 with 'B' set to

the value directly from the measurements, then ‘e’ was changed to fit the APD followed by ‘A’ to set the magnitude. Finally, ‘c1’ and ‘c2’ were changed to try and replicate the measured gradients with some back and forth adjustments made to ‘e’ and ‘A’. The initial values of V_i were chosen directly from the measurements as with ‘B’. After this, a similar process was used to determine the SAR AP parameters but these adjustments were based on whether activation was triggered in the atrium rather than measurement values.

The end result of this process is shown in Table 6.1 where the final parameter values are listed along with the initial values.

Table 6.1 – Final parameter values for the bidomain model.

Parameter	**SAR**	**Atrium**	**AV Band**	**Ventricle**
a	-0.5	0.13	0.13	0.13
b	0.4	0	0	0
c1 ($A \cdot s \cdot V^{-1} \cdot m^{-3}$)	0.182	0.572	0.234	0.572
c2 ($A \cdot s \cdot V^{-1} \cdot m^{-3}$)	1	0.5	0.7	0.5
d	1	1	1	1
e	0.0001	0.004	0.00032	0.0011
A (V)	0.2	0.1088	0.1085	0.1205
B (V)	-0.135	-0.053	-0.07	-0.075
k (s^{-1})	1000	1000	1000	1000
Vi initial (V)	-0.0500	-0.0530	-0.0585	-0.0750
Ve initial (V)	0	0	0	0
u initial	0	0	0	0

Key: SAR =sinoatrial region; Atrium = atrial wall muscle; AV band = atrioventricular band muscle; Ventricle = ventricle wall muscle

A comparison between the *in situ* recordings and model APs is given in Figure 6.7, including the SAR AP which has no measured comparison.

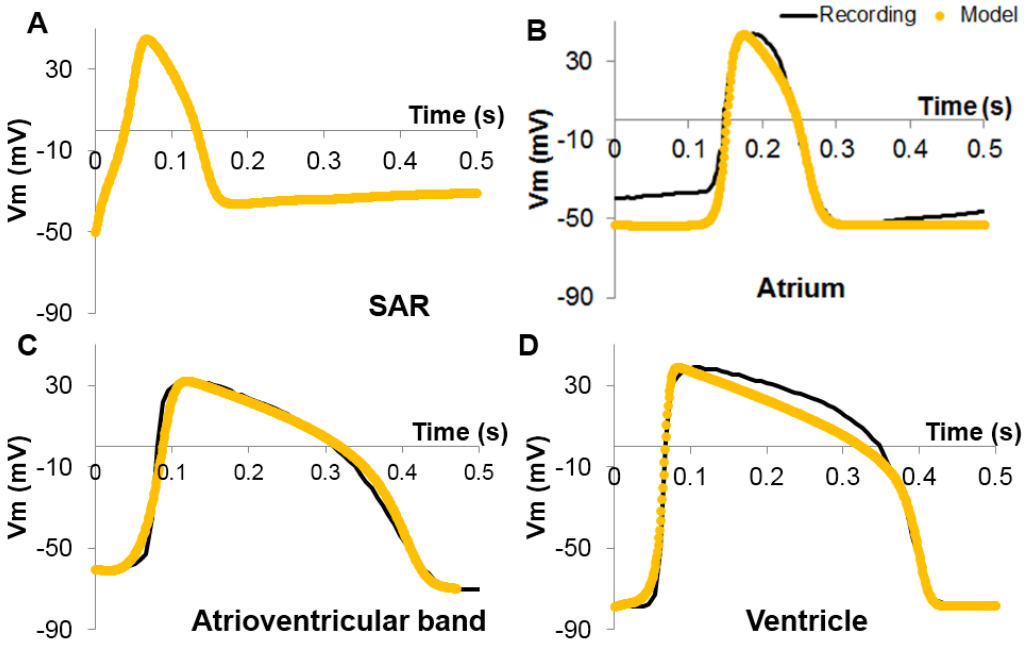

Figure 6.7 A comparison between model action potentials [49] from a 2 dpf heart and measured action potentials which were measured using patch pipettes and current clamp techniques, A) SAR (no comparison), B) atrium, C) atrioventricular band, D) ventricle.

The key parameters that define the AP (APD, magnitude, duration, gradients) for both recording and model are shown in Table 6.2. The APD and magnitude are in good agreement with the measured values as they were the simplest properties to change in the model. This is because they were controlled mainly by a single parameter for each (e for the duration and A for the magnitude). The upstroke and downstroke values showed less agreement, especially for the downstroke of the atrium and upstroke of the AV band, where the model APs were half as steep as the recorded values. The gradients of the upstroke and downstroke could not be finely controlled by the model parameters, but for the ventricle, which was within 20%. Combined with the APD and magnitude similarities, this shows that the model ventricle AP had the best fit, followed by the atrioventricular band AP.

Table 6.2 – Comparison between model and recorded action potential properties.

Region	Source	APD (ms)	Magnitude (mV)	Max upstroke (mV/ms)	Max down stroke (mV/ms)
Atrium	Recording	102	80.1	8.38	-3.99
	Model	108	96.8	4.59	-1.81
AV band	Recording	301	102.3	4.81	-0.65
	Model	316	103.4	2.28	-0.71
Ventricle	Recording	324	117.6	7.15	-1.69
	Model	329	116.4	4.16	-1.70

The value of each variable is given for both model and recorded action potential.
Key: SAR =sinoatrial region; Atrium = atrial wall muscle; AV band = atrioventricular band; Ventricle = ventricle wall muscle

6.3.3 Conduction velocity

The other main property that needed to be replicated within the model is the conduction velocity (CV) of the AP. The key parameters that determine the CV are the rate of depolarisation (AP upstroke), resistance (conductivity) within the cell and gap junctions as well as the cellular membrane capacitance. In the model, the key parameters are also the conductivity, AP upstroke and capacitance and there is also the added factors of the mesh size and surface to volume ratio but gap junctions are not included. The mesh size was fixed using a fine enough mesh to fully represent the geometry and upstrokes of the APs (the finest part of the AP). The AP upstrokes were also fixed by the constant parameters for each region, as was the surface to volume ratio. Therefore, the variable used to control the conduction velocity within the model was the conductivity. Figure 6.8 shows the measurements that were used to determine the model conductivity values. Activation maps display the progression of the hearts activation over time, including the path. The black lines indicate the activation front at 5 ms intervals, with the colour scale indicating the order of activation (blue to red). At 1 dpf (Figure 6.8 A) the activation is slow (tightly compacted lines). The speed increases by 3 dpf (Figure 6.8 B), with increased space between lines and significantly shorter time intervals. The activation path also becomes

more complex with different velocities for the inner and outer curvatures (anisotropy). The measured velocities are much lower than those from the adult human heart so the conductivity in the model needed to be reduced from the values in [80] to achieve these velocities.

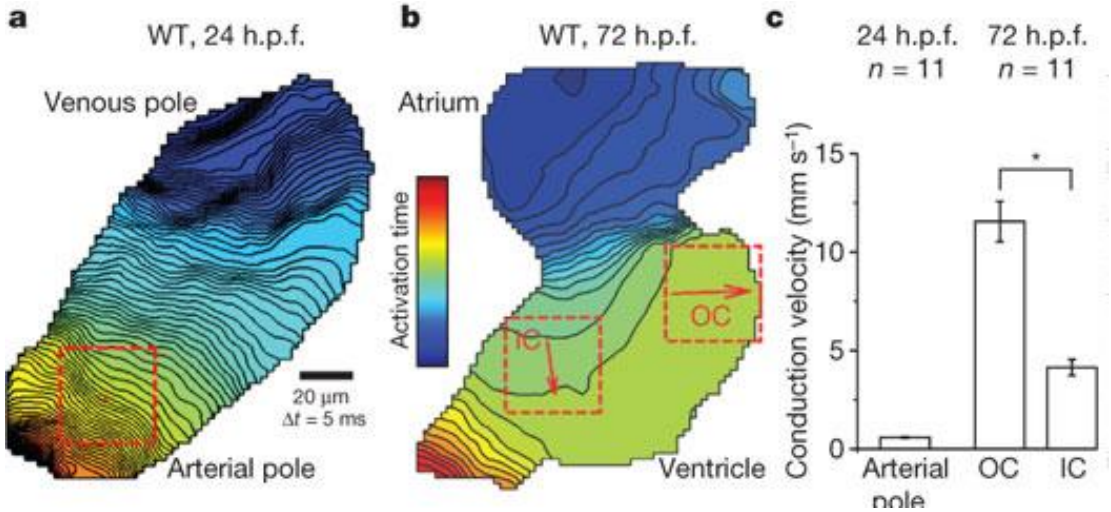

Figure 6.8 Activation map for A) 1 dpf zebrafish heart and B) 3 dpf zebrafish heart, C) Conduction velocity as measured from the activation map [59].

In order to reduce the velocity of the APs, a scaling factor needed to be introduced to reduce the conductivity (increase resistivity) of each heart region in the range of a 10^{-2} decrease from the values used in [80] (human model). This is a large decrease but it was needed to account for the difference in observed velocities between the adult human heart and the larval zebrafish heart (see Table 6.3). This is discussed later in this section

Table 6.3 – Activation wave conduction velocities in an adult human and a 3 dpf zebrafish heart.

	Human	**Zebrafish larvae (3dpf)**	**Model**
Atrium (mm/s)	800->1000	1.3-2*	1.5
AV Band (mm/s)	20->50	0.1-0.3*	0.1
Ventricle (mm/s)	300->800	4->12	6.6

Measurements obtained from [38] (human) and [59] (zebrafish larvae). The range of values are associated with anisotropy in the tissue. *approximation taken from activation map image.

The value of model conductivity needed to scale the model conduction velocity to the measured results was found by comparison with the activation map (Figure 6.8 B). This was

achieved by comparing activation times for each region, which was taken to be the time interval between the wave front entering the region and leaving the region. This was found to be ~32.5 ± 5 ms for the atrium, ~27.5 ± 5 ms for the AV band and ~10 ± 5 ms for the ventricle. An isotropic conductivity was used and scaled so that the activation times for each region within the model agreed with the activation map. This method was used along with estimated velocity equalisation (with Figure 6.8 C) due to the lack of direct conduction velocity measurements in the atrium and AV band regions of the zebrafish heart. This resulted in the conduction velocities shown in Table 6.3 which are within the measured ranges.

The relationship between conductivity and conduction velocity can be illustrated using a 3D block model consisting of three blocks, one for the sinoatrial region, one for the atrium and one for the body. The finer mesh setting within COMSOL was used with this model. Using this geometry, the wave velocity can be determined from a known distance. Activation was initiated at the sinoatrial block then the conduction velocity of the propagated wave was determined between two points in the centre of the block. A range of conductivity values were then used with the wave velocity calculated for each, as can be seen in Figure 6.9. It can be seen that the range of conductivity values needed to reduce the waves velocity to zebrafish levels is very low. The range of conductivity values used within human heart models varies, a typical range is 0.0005 S/m to 0.6 S/m [80, 139]. These values are either chosen by using a conductivity that gives the desired conduction velocity as is the method used in this work or from measurements which produce different results depending on the method used [140]. The upper range of conductivity values in the sweep (Figure 6.9) are similar to the lowest values used in human models (~0.0005 S/m) [80] which are used in models of the AV node.

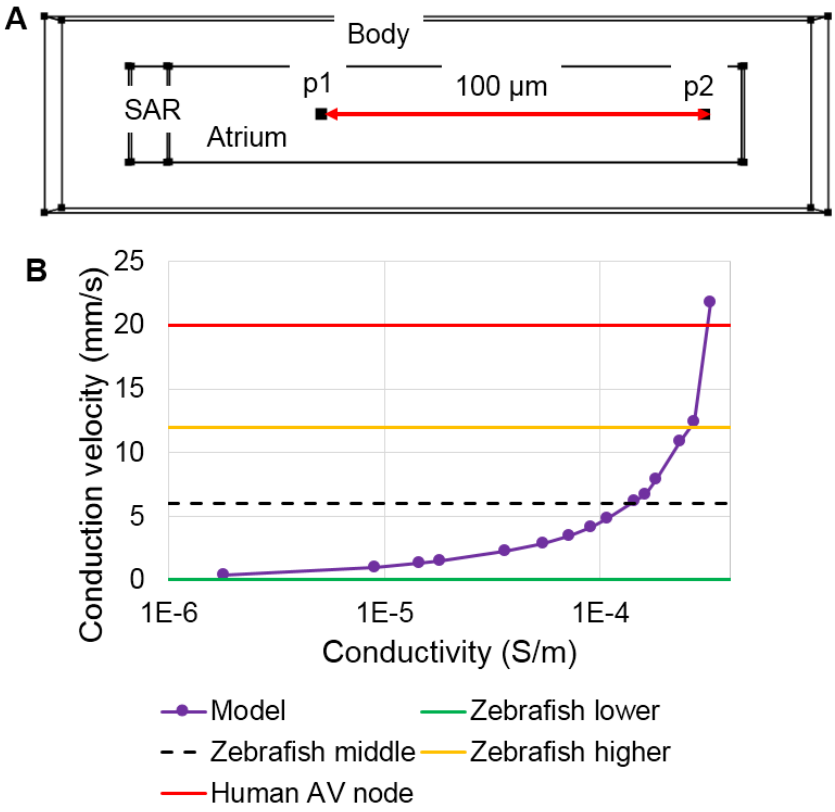

Figure 6.9 Conduction velocity and conductivity relation. A) 3D block model. 3 regions consisting of body, sinoatrial and atrium. Points 1 and 2 were used to determine the conduction velocity. B) The relationship between sigma and the resulting conduction velocity of the wave. The first horizontal line shows the slowest velocity that occurs in the human heart in the AV region and the bottom limits show the measured velocities from a 3 dpf zebrafish ventricle [38, 59].

Figure 6.9 shows the conduction velocity variation with conductivity in a 3D block model and Table 6.4 shows the final model values that were determined by performing similar sweeps with the 3D anatomical geometry. It can be seen that similar values are present in Figure 6.9 and Table 6.4.

Table 6.4 Conductivity values used within the model for each heart region.

Parameter	SAR	Atrium	AV Band	Ventricle	Body	Chambers
σe (Sm^{-1})	1.81E-05	1.81E-05	2.43E-06	1.55E-05	-	-
σi (Sm^{-1})	1.81E-05	1.81E-05	2.43E-06	1.55E-05	-	-
σb (Sm^{-1})	-	-	-	-	0.2	-
σc (Sm^{-1})	-	-	-	-	-	0.7

Key: SAR =sinoatrial region; Atrium = atrial wall muscle; AV band = atrioventricular band; Ventricle = ventricle wall muscle; σ_b = body conductivity; σ_c = chamber conductivity

Propagation of the AP through the model heart (Figure 6.10) begins in the sinoatrial region then moves into the atrium where it spreads; from here it travels through the atrioventricular band into the ventricle.

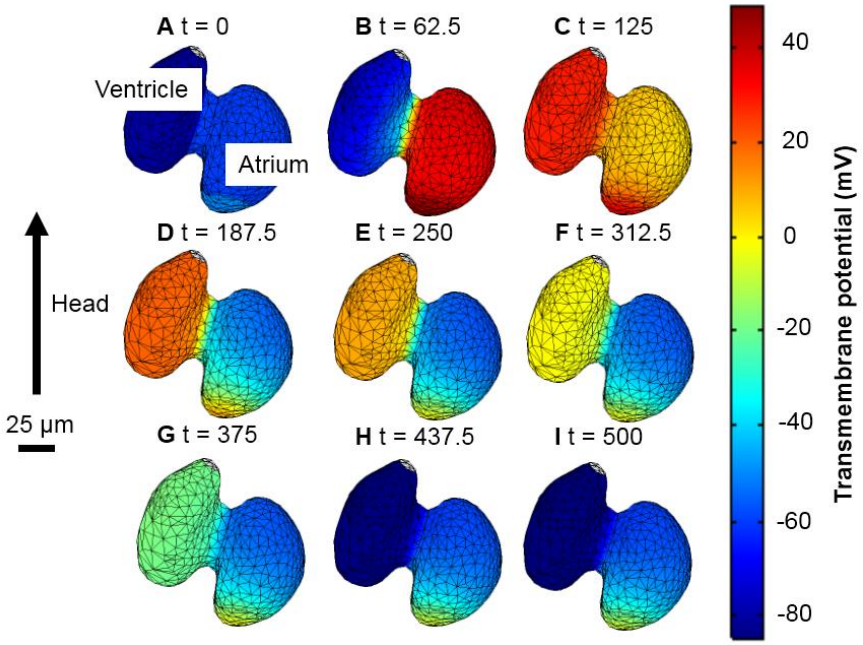

Figure 6.10. Temporal sequence of transmembrane potential (V_m). The propagation of an action potential through the heart is shown at different times (ms). Nine time steps were chosen to show the progression of the action potentials through all stages of the cardiac cycle. A) the heart at rest, B) atrial depolarisation, C) ventricular depolarisation, D) the end of atrial repolarisation and ventricular plateau stage E, F, G, H) ventricular repolarisation, I) returning to the rest state. The wave originates at the sinoatrial region then it progresses across the atrium, through the atrioventricular band and into the ventricle.

The need for such a large reduction in conductivity is a flaw of the bidomain model when used in this way. The bidomain model treats the heart as a single object approximating the discontinuous cellular structure as a continuum where the behaviour of individual cells averages out [35, 38]. This is the approach that is commonly taken when modelling the adult human heart as it contains a very large number of cells with complex geometry that is difficult to accurately reproduce. This approximation works well due to the large ratio between the size of each cell and the whole heart. But for the developing zebrafish heart, which is much smaller, the cellular structure becomes more pronounced. A discrete model of the zebrafish larval heart

is therefore desirable. Such a model would include each gap junction and cell within the heart. The propagation of activation through gap junctions is much slower than through the myocytes, this would have the effect of significantly reducing the conduction velocity without the need for decreasing the conductivity by such a large amount. This was unfortunately not feasible due to the difficulty in determining cell positions/gap junction distributions and the computational load that would be required.

In addition to this, bidomain models are generally applied to the adult human heart or sections of tissue and the values used for both intracellular and extracellular conductivity are three sets of measurements [141-143] that show significant disagreement. The range of values measured is due to the difficulty in measuring these values, the difference in measurement methods and the variability in the composition of cardiac tissue [144, 145]. The activation waves produced using these parameters have conduction velocities that fall within the measured ranges [38] for bulk human tissue. However, if the size of the tissue is reduced to just a few cells or a single chain of cells the measured velocity decreases [53], which is due to the increased effect of gap junctions at the microscopic level. If an attempt is then made to model this system with the same conductivity parameters as in the larger case, the conduction velocity of the resulting waves will have the same value as for the larger case and will not agree with measurements. This is a limitation of the continuum approximation as the measured conductivities are mean values, with the intracellular conductivity encompassing the conductance of the gap junctions [140], but they do not account for the structural change that occurs with small amounts of cells. Therefore, to effectively model this situation either gap junctions need to be introduced or the conductivity parameters need to be changed, as was done in the model presented here.

In addition to the continuum approximation limitations, the reason for reducing the conductivity by such a large amount, compared to a human heart model, is due to the large difference in conduction velocity between the human and zebrafish hearts. Modelling a small section of human heart tissue would not require such a large reduction as the intrinsic velocity is higher to start with [146]. Conduction in developing hearts is slow as the faster conducting pathways and tissue require maturation. The larval zebrafish heart does not develop a conduction system until after 3 dpf so propagation is initially slow, e.g. the adult zebrafish heart conduction velocity is over 100 mm/s [147] whereas in the larval heart it is around 10 mm/s [59]. There are no available measurements of the conductivity of zebrafish larval hearts in the literature but if there were such measurements available they would likely be much lower than that of the adult human heart. The assumption being that provided the overall morphology of the heart and body is realistic and activation of the heart can be approximated as an excitation wave, then scaling conductivity to alter the conduction velocity of the wave is a valid approach. This was thought to be valid as attempts were not made to model the finer details of cardiac conduction but the larger scale ECG which can be determined from depolarisation and repolarisation wave progression.

6.3.4 Surface to volume ratio and capacitance

The surface to volume ratio (A_m) was calculated from results given in [50] for the average myocyte surface area (300 μm^2) and the total myocardial volume ($1x10^6$ μm^3) of a 54 hpf zebrafish heart as well as the approximate number of cells in a 3 dpf zebrafish heart (300) [48]. Which resulted in a value of 90000 m^{-1}. The value of the membrane capacitance (C_m) was chosen in line with previous studies (human models) [148] which was 0.01 Fm^{-2}. As stated previously the surface-to-volume-ratio and membrane capacitance also have an effect on the

conduction velocity. The size of the zebrafish heart and cells mean that the surface-to-volume ratio is much higher than for human cells which leads to a lower conduction velocity. An estimate of surface-to-volume ratio was made based on measured values of area and volume [50] but any change in this value would result in a different value of conductivity to achieve the same conduction velocities. The same is true for capacitance, the small cell size likely results in a smaller capacitance than the value used in this work.

6.4 Model comparison to ECG measurements

In this section, the ECGs produced by the model are compared to the measured ECGs from 3 dpf zebrafish in three recording positions. The results of a mesh sensitivity analysis are given before the model results. Models were solved from 0 to 0.5 seconds to simulate one cardiac cycle. Further cycles were not necessary as the ability of the SAR pacemaker AP to initiate activation at a realistic frequency was not required. This reduced solution times to 20 minutes per simulation. Results were displayed at 1 ms intervals using the back differentiation formula (BDF) algorithm within COMSOL. The model consisted of 85,255 tetrahedral elements with 152,630 degrees of freedom. Each simulation took approximately 20 minutes to complete on a PC with an i7 processer and 16 GB of RAM.

6.4.1 ECG measurement

The ECG measurements were performed and the results were provided by Sundeep Dhillon and Rhiannon Hurst. Wild-type Tübingen strain zebrafish were used for all experiments. The recording procedure was as follows.

For all experiments, 3 dpf zebrafish larvae were used. They were first anaesthetised in ethyl-3-aminobenzoate methanesulfonate (0.3 mg/ml; Sigma-Aldrich) for 5–10 minutes before being transferred into 3 mL of E3 embryo medium in the plate used for subsequent

measurements. Once anaesthetised, individual zebrafish larvae were then transferred to the ECG recording plate (mini Petri dish containing a 2% agarose layer with grooves). The larva was positioned ventrally within an agarose groove and the tip (2 µm diameter) of a borosilicate glass micropipette (P84, World Precision Instruments) was positioned on the skin surface above the ventricle, the atrium, or above the atrioventricular band (avoiding penetration) using micromanipulators (Narishige) and Inchworm step motors (Burleigh), viewed under a Nikon microscope (SMZ600). The micropipettes were filled with 3M potassium acetate solution (Sigma-Aldrich) using MicroFil (P85, World Precision Instruments, USA), and a chloridised silver wire was inserted to carry electrical signal to the amplifier. A second reference electrode was placed in the surrounding medium during recordings. The differential amplifier (NPI electronics, Germany) used for recording was operated in DC mode with the high pass filter set at 0.1 Hz. The raw ECG signals were digitised (PowerLab; ADI Instruments) and viewed using LabChart 7 (ADI Instruments).

All of the recording equipment was housed on an air table within a grounded Faraday cage to minimise background noise. Experiments were performed at 28ºC and the temperature was controlled using a sensor placed in the recording plate and a homemade heating element (Cryocon 24 temperature controller, USA).

The three electrode positions chosen were over the atrium (1), atrioventricular band (2) and ventricle (3) as shown in Figure 6.11. These measured waveforms are the same as those from the previous chapter (Figure 5.22). As described before, the position of the recording electrode has a large effect on the shape of the observed ECG. By using different positions, more detail can be seen in the ECG which can be used to assess the differing effects of drug treatments. The signals from positions 1 and 3 were measured at the same time on the same

zebrafish, the signal from position 2 was measured on a different animal and hence no voltage scale is shown.

There is some variability in the measured ECGs due to the uncertainty in determining and replicating recording positions between measurements. Once an electrode has been positioned on the zebrafish, the waveforms measured are consistent but it is difficult to position another electrode in the exact same position in another experiment. This is one of the reasons why the models were created, to help determine the best position for electrode placement which is achieved by predicting what ECG should be expected in each position. As a result of this variability, the models in this thesis are compared to single typical recordings that are representative of what is measured from each of the three positions in comparison to similar model position ECGs. This is because clear data on the variability of ECG measurements was not available which would have ideally been used to compare the model to. This could be seen as creating a model to fit the ECG's that are shown. However, this is not the case as the model was constructed based on how activation of the larval zebrafish heart is known to occur and how the ECG is generated i.e. how the activation wave is known to spread through the zebrafish heart, the morphology of measured APs and the zebrafish geometry. This information in the literature was used to construct the model and the measured ECGs were only used as a comparison to the model results. This means that other measured ECGs may not show the same level of agreement with the modelled ECGs as those that have been used for comparison which could then be due to differences in position or the other reasons highlighted throughout this chapter.

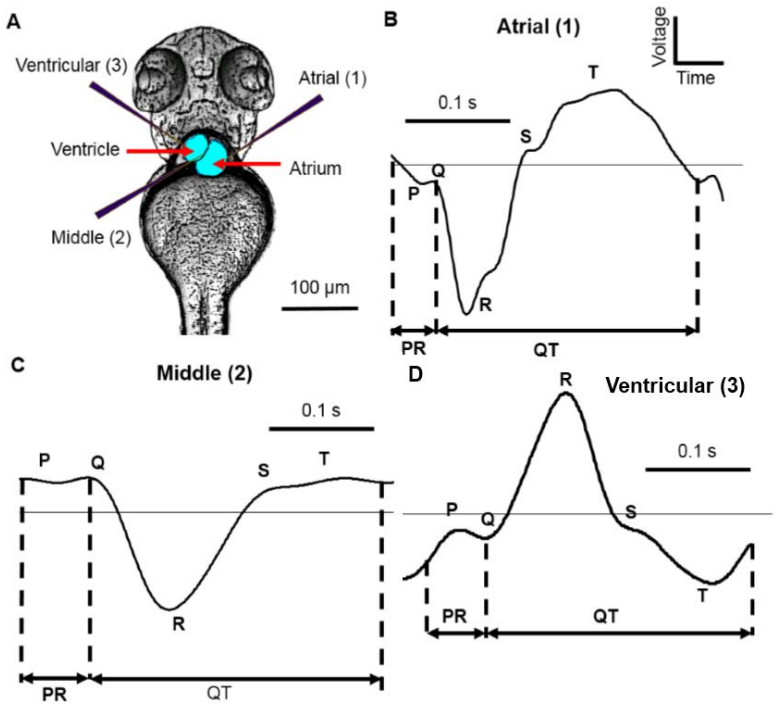

Figure 6.11. Electrode positions used for electrocardiogram recordings on a 3 dpf zebrafish. A) Processed image in ventral view showing electrodes in different recording positions. Electrode 1 is positioned over the atrium, electrode 2 over the atrioventricular band and electrode 3 over the ventricle, B) a representative atrial recording showing the key ECG features: P wave, QRS complex, T wave, PR interval and QT interval, C) a representative middle recording, D) a representative ventricular recording.

6.4.1 Mesh sensitivity analysis

A mesh sensitivity analysis was performed using the parameters described in the previous sections to ensure that a sufficiently fine mesh was used with this model. This was done to show that the simulations are converging and that the solutions presented in the following sections are valid. This analysis was performed using a 3D block geometry which is the same as the model used to illustrate the effect of conductivity on wave velocity that was described earlier in this chapter (Figure 6.9). This model uses the same tetrahedral elements that the anatomical model uses (Figure 6.12 A). The 3D block geometry consists of three regions, the body, the SAR and the atrium. The SAR and atrium regions use the same AP and conductivity parameters shown in Table 6.1 and Table 6.4 and the body conductivity is 0.2 S/m as used before. AP

propagation through the atrium region is initiated by the SAR and the wave then travels along the length of this region. To perform the analysis, the mesh density was increased from a very coarse mesh to a very fine mesh (using maximum element size) and the velocity of the propagating wave was investigated. This was determined from the time taken for the wave to move between p1 and p2 which are separated by 100 μm. The mesh density was used rather than a number of elements so that the results also corresponded to the anatomical model which is a different volume and therefore a single number of elements cannot be used for both models. It can be seen from Figure 6.12 B that the wave velocity converges with increased mesh density from (~1.9 mm/s to ~1.5 mm/s) and plateaus just after a density of 10^{-2} elements/μm^3. The dashed red line on this plot marks the mesh density used in the anatomical model. This was found by determining the number of elements which is 34255 (only heart regions) divided by the volume (1.84×10^4 μm^3). This gives a density of 1.86 elements/μm^3. Therefore, it can be seen that a sufficiently fine mesh was used in the anatomical model to give valid solutions.

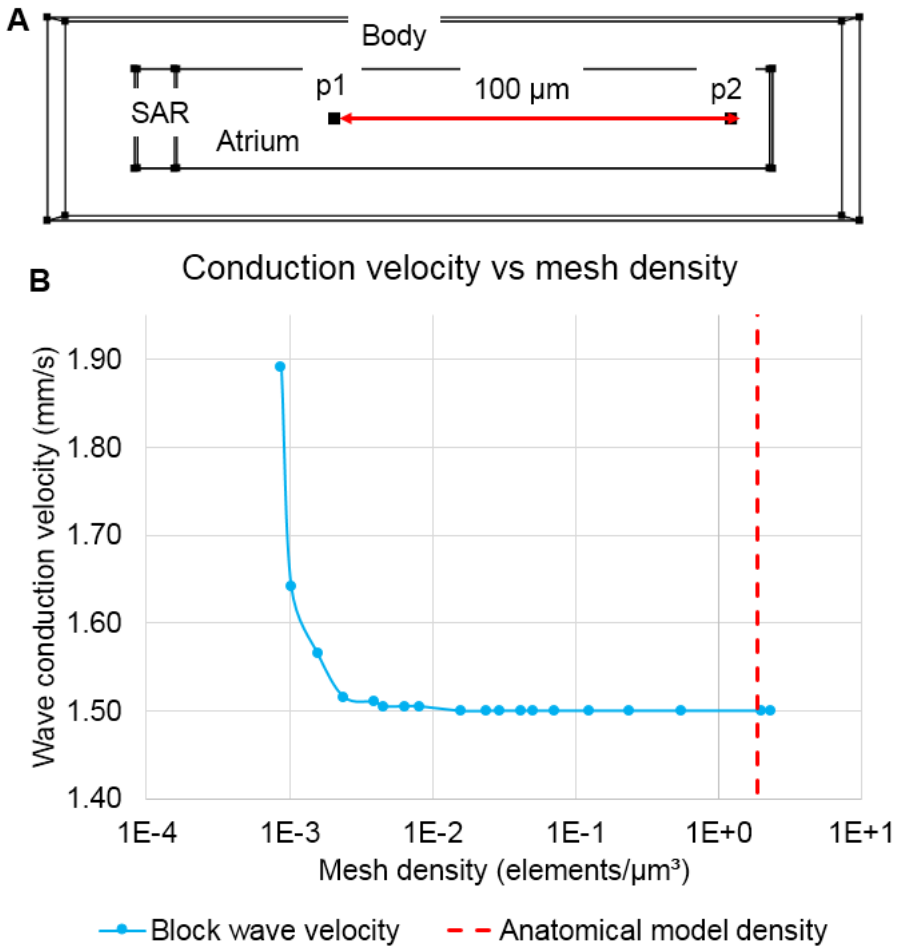

Figure 6.12. Mesh sensitivity analysis. A) 3D block geometry, B) wave conduction velocity vs mesh density for varying mesh densities. Anatomical model mesh density is marked.

6.4.2 Model Electrocardiograms

In order to investigate whether the model could replicate the measured changes in morphology, three points on the surface of the model body were chosen that corresponded to the electrode recording positions (Figure 6.13). The model ECG for each position is simply the voltage on the surface of the body at that specific point.

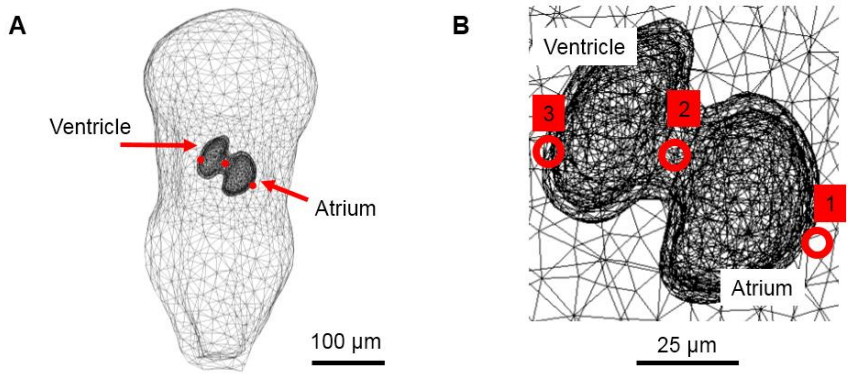

Figure 6.13. Model ECG positions. A) Expanded ventral view of equivalent electrode positions within the model, B) close-up ventral view of electrode positions over the heart.

Firstly, the model ECGs were investigated without a comparison to recordings to confirm which stage of activation the peaks seen in the model ECG corresponded to. Both upstrokes (depolarisation) and downstrokes (repolarisation) of APs were found to cause a peak in the ECG as expected. By overlaying the model APs, the origin of a peak could be identified by noting which AP upstroke or downstroke it coincided with (Figure 6.14). For example, to confirm which peak was the P wave (atrial depolarisation) the model atrium AP was overlaid onto the model ECG. The peak that occurred at the same time as the atrium upstroke was then taken as the P wave. The same process was used for the R and T waves confirming that all the major components expected to be found in an ECG signal from a zebrafish larva were present in the model. Other peaks were also seen corresponding to atrial repolarisation (marked as AR).

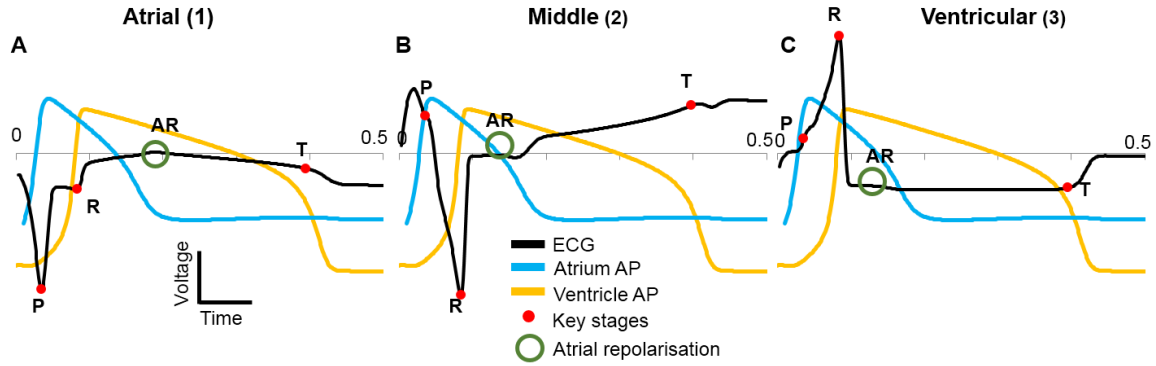

Figure 6.14. Model ECG at different positions with overlaid action potentials. A) atrial position, B) middle position, C) ventricular position. Red dots mark the key stages in each ECG (P, R and T waves). Atrial repolarisation is also marked (AR, green circle). No voltage scale is shown as the action potentials were scaled so that the ECG was visible on the same axes.

As expected, the model ECG shape was found to vary across the surface of the zebrafish body, with a larger P wave over the atrium and the R and T waves larger over the ventricle. The polarity of each ECG peak varied across the surface of the body over the heart; a positive peak refers to a maximum or positive deflection in the ECG and a negative peak refers to a minimum or negative deflection in the ECG whether the peak is situated above or below zero volts.

Movement of the depolarisation wave through the atrium, atrioventricular band and ventricle away from the atrial electrode position caused negative P and R waves; repolarisation had the opposite effect including a positive T wave. Similarly, the middle position showed a positive P wave, a negative R wave and a positive T wave. The ventricular position was positive P and R waves with a negative T wave. These results agree with how the ECG is generated as described in chapter 2 (Figure 2.5) based on the four cases of wave direction/polarity as was used to orientate the dipoles in chapter 5.

6.4.3 Comparisons to measurements

The model ECGs from the atrial, middle and ventricular positions were then compared to *in vivo* recordings from similar positions (Figure 6.16). Initially, the QT intervals of the model ECGs (Model 1) were much longer than the QT intervals of the recordings, which was likely

due to differences in temperature and the age of the fish as the QT interval is mainly dependent on the duration of the ventricle AP. The APs were recorded at room temperature with 2 dpf zebrafish [49] and the ECGs were recorded at a higher temperature of 28°C with 3 dpf zebrafish. APDs are temperature dependent in the adult zebrafish [149], with higher temperatures reducing APD but with no major change in AP shape. Therefore, it was assumed that if the APs were measured from a 3 dpf at the higher temperature, the ventricle APD would be shorter and match the QT length seen in the ECGs. To account for this difference in duration between model and recorded QT lengths, the model APD of all APs was reduced (using parameter 'e') by the same amount such that the APD of the ventricle AP was approximately equal to the QT length of the recorded ECGs (Model 2), thus giving the model ECGs similar QT lengths to the recordings. The model 2 APs with reduced APD are shown in Figure 6.15 with comparison to model 1 APs.

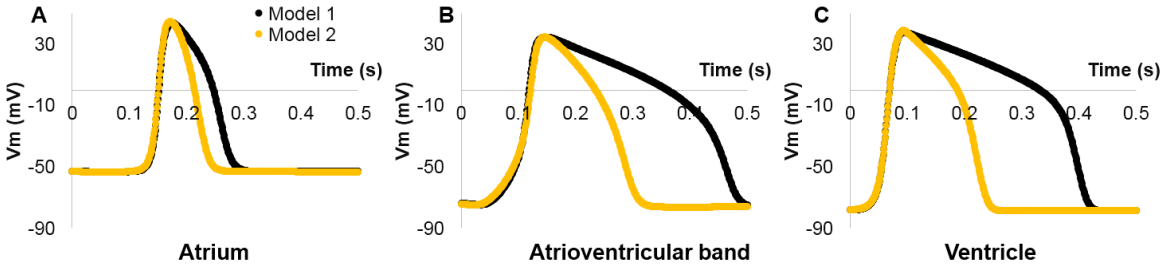

Figure 6.15. Model 1 and 2 APs. A) atrium, B) AV band, C) ventricle.

The voltage of the ECG recordings were scaled to the model magnitudes for comparison. Relative magnitudes between R and T are more relevant than absolute magnitudes due to the amplification of the measured signal, multiple recorded signals and the reduced voltage seen in the model because of the conductivity scaling factor (model ECGs peaks were in the $1x10^{-10}$ V range).

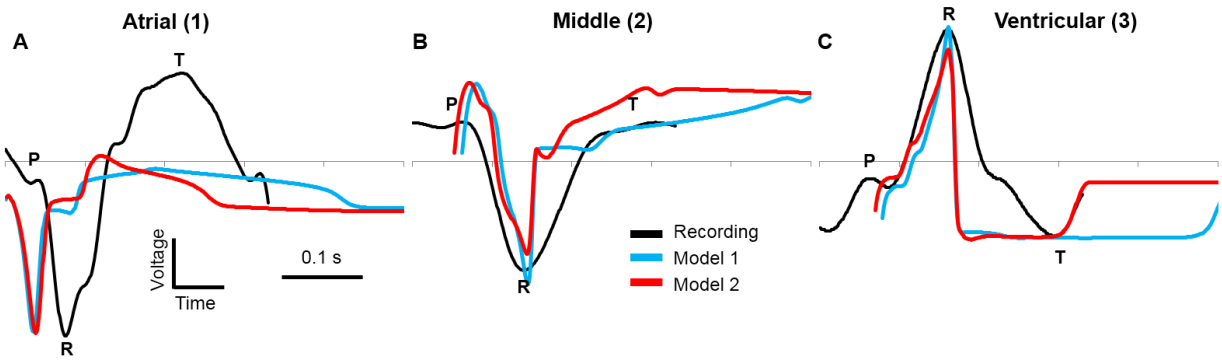

Figure 6.16. Comparison between ECG recordings and model ECG. The recorded ECG at three positions was compared to the model output. A) model comparison to atrial recording, B) model comparison to middle recording and C) model comparison to ventricular recording. Model 1 has fitted action potential durations, model 2 has a reduced action potential duration that gives a similar QT length to the recordings. No voltage scale is shown as the model ECG voltages are much smaller than the recordings.

The model showed good agreement with polarity of the recorded peaks. For the atrial position, both model and recording show negative P and R waves with a positive T wave; atrial repolarisation is also seen in the model. In the middle position, a positive P wave is seen for both model and recording, with a negative R wave and positive T wave for both. The ventricular position shows similar agreement with a positive P wave and negative R and T waves.

The model ECG from the atrial position (position 1) is quite different to the recorded shape, which showed a large amount of ventricular activity with little activity from the atrium; whereas the model showed equal amounts of atrial and ventricular repolarisation. This is most likely due to the difference in muscle mass between the thicker ventricular and thinner atrial walls within the zebrafish, which was not replicated within the model. The atrial signal is likely dominated by the signal strength from the ventricle in the recording. This is the case in humans, where atrial repolarisation is not normally seen in the ECG as ventricular depolarisation (R wave) occurs at the same time.

As mentioned in chapter 2, two of the common ECG parameters that are used to assess drug effects are the PR interval (measured from the start of the P wave to the start of the Q

wave) and the QT interval (from the start of the Q wave to the end of the T wave). A comparison between model ECG parameters and measured ECG parameters from the three positions showed variable agreement (Table 6.5). Position 2 shows the best agreement between model and recording for the P width with widths of 25 ms for the recording and 41 ms for the model. The T wave width is best replicated at position 2 with a width of 34 ms for the recording and 33 ms for the model. The QT interval is best replicated at position 3 with 232 ms for the recording and 204 ms for the model. Position 3 also shows the best agreement with the R wave width.

The PR interval was found to be shorter in the model for position 2 and position 3. Shorter PR intervals indicate that the delay caused by the atrioventricular band was not long enough, which could be accommodated by decreasing conduction velocity or extending the width of the atrioventricular band region. The increase in PR interval for position 1 was most likely due to the position of the Q wave being distorted by the increased atrial activity that was seen in the model ECGs; this created a peak which overwhelmed the QRS complex moving the position of the Q wave to an apparent later time and increasing the PR interval.

The width of the peaks showed less agreement with the measured values, with the model R waves being significantly narrower than the recording. The P wave duration was found to be closer to the measured value but still shorter, possibly due to the gradient of the model ventricle AP upstroke which affected the width of the ECG peaks in the model. The wide ECG peaks seen in the recordings could be due to decreased AP gradient at 3 dpf. In the model a steeper upstroke was found to result in a narrower ECG peak with a shallower upstroke resulting in a wider peak, although the model did not allow for fine control of the upstroke gradient to investigate this further. Another factor in the peak width difference is that the ECGs from the

model are from a point on the surface of the body which is effectively a perfect electrode with no area averaging effects (spatial filtering), noise, interface or electrode properties that could contribute to the disparity in peak widths.

Table 6.5 A comparison between model ECG (model 2) parameters and measured ECG parameters.

Region	**Source**	**P width (ms)**	**R width (ms)**	**T width (ms)**	**PR (ms)**	**QT (ms)**
Atrial (1)	Recording	27	91	147	27	250
	Model	49	38	41	49	193
Middle (2)	Recording	25	157	34	69	244
	Model	41	55	33	41	209
Ventricular (3)	Recording	40	117	76	55	232
	Model	20	53	47	20	204

The value of each variable is given for both model and recorded ECG.

The relative peak amplitudes at each position were also compared (Table 6.6) and were determined from the start of the simulation to the peak of the P wave and from the start of the Q wave to the peak of the R wave for the R wave. The relative peak heights for each recording position and the model were also compared. P to R was found to be best replicated in position 3 (8.4 measured and 3.7 model), R to T in position 3 (4.42 measured and 2.47 model) and P to T also in position 3 (0.53 measured and 0.67 model). Differences in these values could be explained by the distorted position of the Q wave, differences in AP shape, tissue volume or electrode position differences. As shown the placement of an electrode leads to a large difference in the resultant ECG so if the positions are not exactly like for like there will be differences in morphology.

Table 6.6. A comparison between model relative peak heights and measured relative peak heights.

Region	Source	P to R	R to T	P to T
Atrial (1)	Recording	10.83	2.29	0.21
	Model	0.01	0.33	37.33
Middle (2)	Recording	57.39	42.44	0.74
	Model	4.6	19.71	4.27
Ventricular (3)	Recording	8.40	4.42	0.53
	Model	3.70	2.47	0.67

The value of each variable is given for both model and recorded ECGs. P to R refers to the relative difference in magnitude between the P and R waves, and so on.

6.4.4 Maximum signal

As well as simulating the ECG, the model can be useful in optimising recording positions. The maximum value of the R wave was determined by selecting the time at which R occurs (0.84 s from the start of the simulation) in position 3 and then finding the maximum voltage on the surface of the body above the heart. This was found to be a point on the edge of the ventricle (Figure 6.17). Further investigation of the voltage distribution within the model revealed that the amplitude of the R wave decreased either side of point 5 (Figure 6.17 C, D) around the edge of the ventricle. If a recording electrode was placed at the furthest points from the maximum (point 1 and point 10) less than 20% of the maximum R wave amplitude could be recorded across approximately 75 μm in either direction. Similarly, a decrease in amplitude was seen experimentally by moving the recording electrode across the surface of the zebrafish and measuring a change in amplitude of the signal [11]. This suggests that the ideal place to position an electrode to measure the R wave is at the apex of the ventricle, directly in the path of the depolarisation wave.

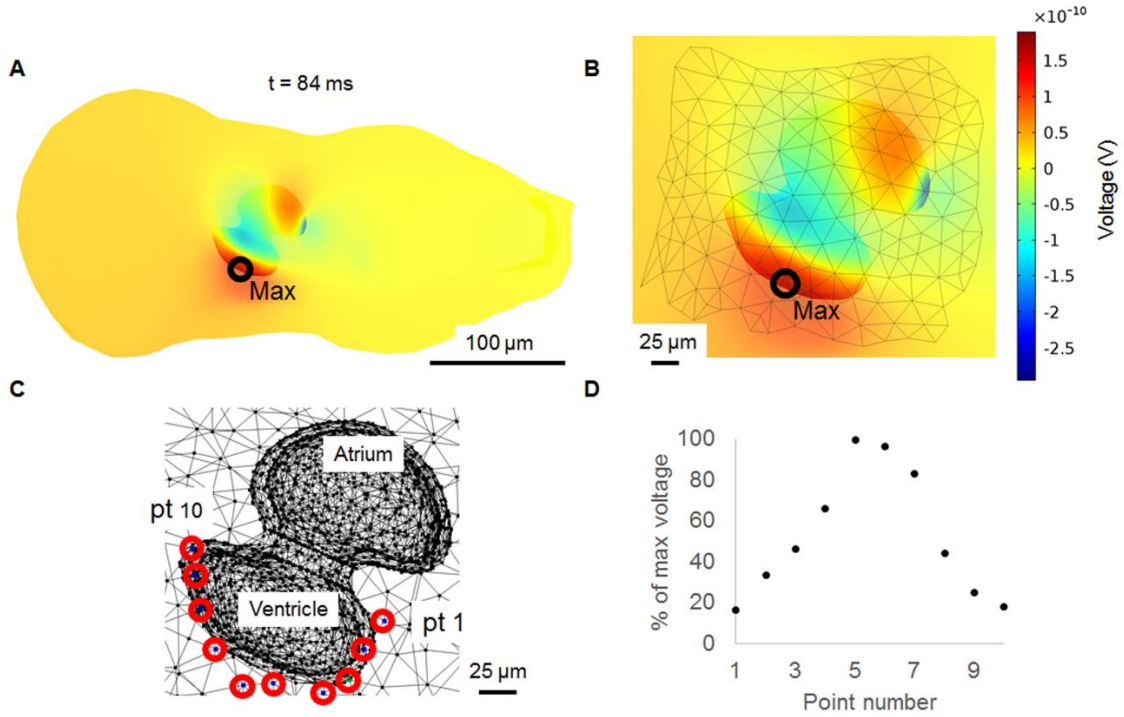

Figure 6.17. Maximum R wave voltage and R wave magnitude percentage change. The point at which the R wave is at its maximum is at 0.84 s from the start of the simulation. A) zoomed out ventral view of the model with the point of maximum voltage intensity labelled, B) close-up ventral view with the maximum point labelled, C) close-up ventral view showing ten different points distributed around the ventricle as seen on the surface of the body, D) percentage of the maximum R wave voltage at each point.

6.5 Summary

This chapter has presented a bidomain model of the larval zebrafish heart and body that was able to simulate and predict experimentally observed results. It is the first electrical model of the larval zebrafish heart. This model offered many improvements over the models presented in the previous chapter. The geometry was improved over previous models by using OPT/microscopy images and 3D modelling software to shape the geometry. The distinct regions of the zebrafish heart were replicated by using region specific parameters which were selected by comparisons to *in situ* recordings. Realistic wave propagation velocities were simulated by comparison to a heart activation map. ECGs were also simulated that showed a large resemblance to those that are observed at three positions across the zebrafish body. The

predictions the model can make (e.g. maximum value of the R wave) are useful for electrode positioning and design.

The accuracy of the geometry plays an important role in how useful the model can be. The shape of the heart determines the direction of activation and hence the ECG and the shape of the body has a similar effect on ECG determination from different positions. Therefore, it was important to replicate the real geometry of the zebrafish as closely as possible. The heart geometry was made to be as accurate as possible using images from the literature as well as those provided by Rhiannon Hurst and Sundeep Dhillon. It was difficult to get a clear image of the heart from even a ventral or lateral view where the heart is most visible due to it being translucent. The fluorescent images offered some improvement, however, the exact 3D shape was difficult to determine with images in the literature generally being captured from just a single plane. The heart geometry could be improved further by using more advanced imaging techniques to construct an even more realistic geometry such as OPT imaging or those used in [133]. The body geometry was much easier to produce due to the ease with which it could be captured using standard bright field microscopy which led to what is a more realistic shape than the heart geometry. Other features such as organs could also be incorporated in the future to improve realism. Another factor in the accuracy of the geometry is that the heart does not remain in a static position throughout activation. The heart geometry was based on a mid-point in the cycle where chambers sizes are similar in size and so the walls were given a similar thickness. However, the ventricular muscle has been shown to be thicker than the atrial muscle so this could also be implemented [50]. The movement of the heart could be added to the current model by simply expanding and contracting the hearts boundaries and solving multiple times or moving the boundaries through time. A more ideal solution would be to incorporate a

mechanical or electromechanical model alongside or instead of the current electrical model. A disadvantage of increased realism in the geometry and the addition of mechanical effects would be the increase needed in computational power as well as the increase the solution time. So much so that this could mean that a high performance computers (HPC) may have to be used or compromises made to the model.

The APs produced by the model were made as close to the realistic shape as possible. No range of values were given for the measured APs so it cannot be said whether they were within the range seen experimentally or not. It was explained earlier how the age of the zebrafish used for the AP measurements and ECG measurements was different, adult zebrafish APs do not differ much in shape to the larval APs so it is expected that there would not be much difference in shape between the two ages. The temperature was also different but this only effects the APD in the adult zebrafish so it was assumed that this was also the case for larval APs as well. To confirm this, experiments could be performed to measure the APs from the appropriately aged zebrafish under the same environmental conditions as the ECG recordings. The current model was able to replicate the AP and magnitude easily but not the gradients. To improve the accuracy of the model a more realistic ionic model could also be used or developed based on AP and ion channel measurements as has been done for human models in the literature [70]. This would also make the model more useful for assessing drug effects.

The propagation of APs through the heart was successfully simulated with activation times in agreement with the activation map. The path of activation is also the same, moving from SAR to atrium to AV band to ventricle. The key factor for the AP's conduction velocity as mentioned previously was the conductivity. An isotropic conductivity was used but this is unrealistic due to cardiac muscle being highly anisotropic. The activation map partially showed

this but there was not enough detail to implement it within the model. Regardless of this, a continuum model is not the ideal model in which to represent such a small number of cells and a discrete model would increase the realism. This would naturally include the anisotropy by including gap junctions and cell geometries. However, geometrically modelling each cell would be difficult as even the overall shape can be difficult to reproduce. In reality the assumption that activation propagates as a wave through the heart is likely flawed. Propagation through the larval heart is likely to not have a smooth wavefront due to the low cell number causing the activation front to be staggered, which in turn would have an effect on the ECG.

The results from the model and the measured ECGs were consistent with how the activation wave has been shown to travel through the zebrafish heart [59]. There is some debate in the literature regarding the presence of a ventricular conduction system. Such a system could result in apex-to-base [150] (edge of ventricle towards AV band) rather than base-to-apex [151] activation. The activation map [59] shows only base-to-apex activation and based on the model results, apex-to-base activation would invert the polarities of the R and T waves which wouldn't agree with the measured ECGs. Therefore, there is no evidence to suggest that a ventricular conduction system is present at 3 dpf but one could still develop at a later stage.

The results of the ECGs showed that the model was able to replicate the polarity of each of the peaks but not the width. This could possibly be due to the difference in AP gradients as well as the simple ionic model. The low ventricular activity in the atrial position could be increased by increasing the ventricular wall volume. Other geometric changes could also improve the accuracy of the simulated ECGs. There are other factors that could also have an effect such as comparing a perfect point electrode to an electrode with a physical size could be

the cause of some of the disparities. Heart movement has also been shown to affect the observed ECG in models [28] which would also add to the realism.

The model can predict the result APD prolongation has on the polarity of the T wave. The reduction of the APD for model 2 effectively means that the model 1 APD is prolonged. As can be seen from the ECG comparisons, both versions of the model give the same T wave polarity. This was to be expected as there is only one ventricle region within the model and repolarisation occurs in the same order as depolarisation (but with reversed polarity) for both models. Prolonging the APD therefore only has the effect of delaying the T wave in the model. This is not the case in the human ventricle as the inner muscle (endocardium) has a longer APD than the outer muscle (epicardium) [38] so changes in APD can affect the direction of the repolarisation and hence the T wave polarity. There is evidence that different tissues are present in the larval zebrafish ventricle [50] but there are no measurements of any differences in APD between the regions to determine if they differ similarly to how they do in the human heart. The polarity of the measured ECGs suggest that this is not the case (at least at 3 dpf), as the T wave polarity is consistent with inner to outer repolarisation as outer to inner repolarisation would result in the reverse T wave polarity.

The main aim of the model was to help with the measurement of the ECG for both standard micropipette electrode measurements and microfabricated electrode arrays. There are two parts to this system, the larval zebrafish heart and body and the electrodes used to perform the measurement. This model has successfully simulated the key features of larval zebrafish ECG and the next chapter covers modelling of the electrodes.

7. ELECTRODE MODELS

There are two parts to an ECG measurement, the first is the biological electrical activity and the second is the electrodes (with external electronics/signal processing) that are used to measure this activity. The previous two chapters have described models of the biological side and this chapter describes modelling of the electrodes. As discussed in chapter 4, the effects of electrode size and shape greatly affect the effectiveness and ability of electrodes to measure signals. This chapter explores this by describing and analysing the results of a series of stationary electrode models which were created within COMSOL. These were created with the aim of assisting the design process of the microfabricated metal electrodes by exploring the effects of shape and size on the electrode voltage. They are useful for investigating the effect of spatial filtering which affects electrode spatial resolution. This is accomplished by determining the ideal electrode shape and by showing that small electrodes are more sensitive than large electrodes. Firstly, a circular electrode is placed in a uniform field and its voltage and effect on the field is investigated for various positions and electrode areas. A comparison is then made with an analytic solution followed by placing more electrode shapes into the geometry. From this, assessments are made on relative electrode performance for the different shapes and areas. The uniform field is then replaced by a more realistic dipole field and the different electrode shapes and sizes are used in the same way with a similar analysis. A simple model of the zebrafish skin is then added to the model. Finally, the most effective electrodes from the previous models (square and circle) were added to the bidomain heart model to see the effect of using a finite electrode rather than a point. The chapter ends with a summary and a discussion of the results. All models in this chapter use the standard

extremely fine mesh setting in COMSOL apart from the electrode bidomain model (section 7.3) which uses the same mesh as described in the previous chapter.

7.1 Uniform field

The first set of models produced were created to investigate the effect of electrode shape and area on the measured voltage in a uniform electric field. All of the models presented here are stationary models and therefore are described by the equations of electrostatics. In this situation, as the electrodes are made from very good conductors the potential is uniform throughout the region.

7.1.1 COMSOL model

The first model created was used to investigate the effect of electrode geometry and size on the measured potential in a uniform electric field. This field was chosen as it is the simplest type of field and could be created in COMSOL using simple geometry similar to a parallel plate capacitor. This geometry was constructed in COMSOL using a 2D rectangle/region, the top and bottom edges are the positive and negative plates and the rest of the block is the separation between them. The two edges are designed to simulate the situation in an actual measurement experiment. The positive edge represents the signal that is being investigated and the negative edge represents the distant ground. A 2D model was chosen as such a model was sufficient to replicate a metal electrode probe without the added complexity of a third dimension. This region was given a conductivity of 0.7 S/m to replicate that of saline [100] which is similar to the E3 medium in which zebrafish ECG experiments are performed. The dimensions of the block were chosen to be large in comparison to the electrode dimensions to negate effects caused by being close to the boundary. This resulted in a block that was 300 μm (width) by 200 μm (height) that is shown in Figure 7.1. The voltage distributed was found by solving Laplace's equation as was

used with the zebrafish body's in the heart models. Figure 7.1 B shows a surface plot of the voltage distribution along with the electric field lines.

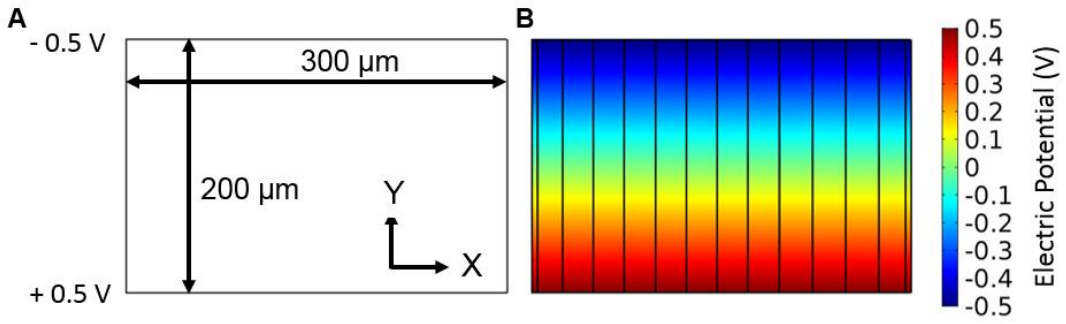

Figure 7.1 2D Parallel plate geometry in COMSOL. A) Empty block showing model dimensions, B) surface voltage plot and electric field lines (black lines).

Figure 7.2 shows the results from the model with a plot of the E field (A) along a central line from the positive plate to the negative plate along with the voltage (B) along the same line. The electric field is constant with a value of 5000 V/m; this is what is to be expected from a uniform field. As a consequence, the voltage linearly reduces from 0.5 to -0.5 over the separation distance. For a smaller separation distance, the voltage would reduce more quickly and the gradient of this graph would be steeper with the opposite true for a larger separation. Therefore, it is expected that the voltage on any electrode within the field should also reduce with distance in the same way unless the electrode causes some distortion to the field.

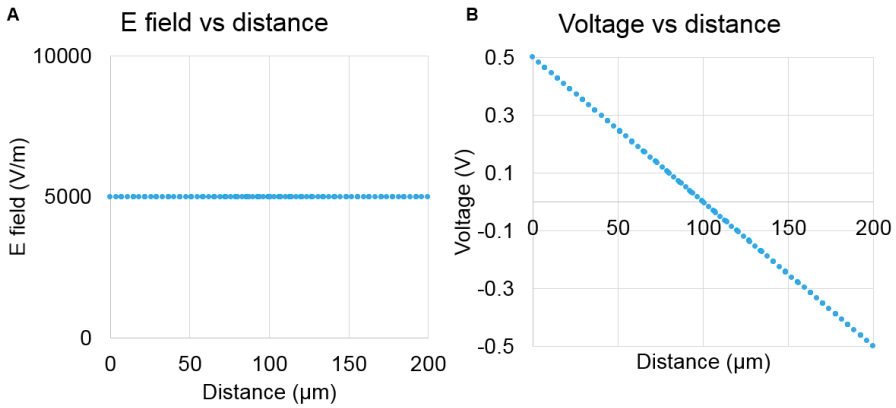

Figure 7.2 A) E field vs distance plot, B) voltage vs distance plot.

A circular gold electrode with a radius of 15 μm was then added to the centre of the geometry with a conductivity of 5.99×10^7 S/m [100]. This represents a microfabricated electrode with the dimensions chosen to reflect the largest electrode that would likely be of use due to the approximately 100 μm zebrafish heart. This shape and position were chosen first as the results can be found analytically, which is shown in the next section. The results from the model, with and without the electrode, are shown for the same line as previously in Figure 7.3. It can be seen that the electric field shows a large amount of distortion near the electrode with a large increase in magnitude that falls away to close to the empty value at the edges. The electric field is zero inside of the metal which means the electrode is at an equipotential as is expected in a stationary model of a metal electrode. The voltage distribution within the electrode is close to the empty voltage until near the edge of the electrode (flat region) where it distorts. The voltage on the electrode is 0 due to its positon within the region in that it is half way between each edge. The value of this equipotential is the key result that is of interest from these models as this is the potential that would be measured (ignoring impedance/noise).

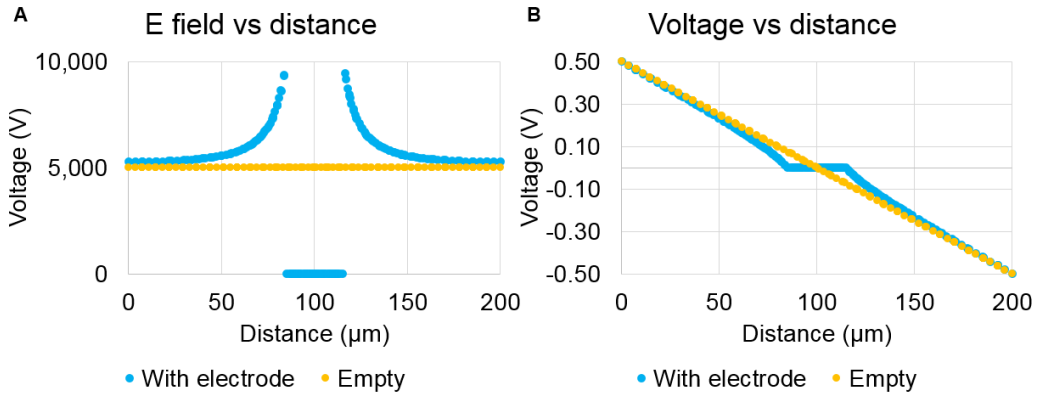

Figure 7.3 A) E field vs distance plot, B) voltage vs distance plot for empty electrode containing regions.

The aim of an electrode is to measure a voltage that is as close to the actual voltage as possible. If the positive edge of the volume is taken to be the source, then the electrode needs to be able to measure this potential as accurately as possible. Ideally, the voltage measured would be the same as that of the empty voltage shown in Figure 7.2 B, but due to the finite size of the electrode this is not possible. This voltage corresponds to the point of the electrode that is closest to the source. So, for the circle electrode shown, the empty voltage is 0.07 V whereas the electrode only measures 0 V (from Figure 7.3 B).

To explore this further, the electrode area was changed, this was achieved by reducing the area from the practical maximum area already described. A range of areas were used as shown in Table 7.1 and Figure 7.4 A. The sizes chosen reflect the sizes that are possible to fabricate with the methods used in this thesis. The smallest size is slightly under this limit, to be closer to a point electrode and offer a larger range for comparisons.

Table 7.1 – Circle electrode areas.

Area scale factor	Radius (μm)	Area (μm^2)
1.00	15.00	706.86
0.75	12.99	530.14
0.50	10.61	353.43
0.25	7.50	176.71
0.10	4.74	70.69

With reduced area, the radius of the circles is reduced, this is reflected in the voltage distribution through the centre of the volume from edge to edge with the width of the equipotential plateau being the same as the diameter of each electrode. A similar graph to Figure 7.3 B can be produced for each area as shown in Figure 7.4 B and C. Each electrode was fixed in the central position as with the largest electrode. The point on each electrode that is closest to the source is different for each area using the middle position which makes each model still symmetric. The voltage on each electrode is 0 V which suggests that this is due to the symmetry of the model. The distributions are all similar with the main difference being the width of the plateau which is the diameter of the circle. The different sizes also affect the voltages either side of the electrode, within the region. For the smallest electrode, the voltage gradient is shallower up to the edge of the electrode. The position at which the voltage is zero is further away from the bottom edge. For the largest electrode, the gradient is steeper with the zero voltage closer to the bottom edge.

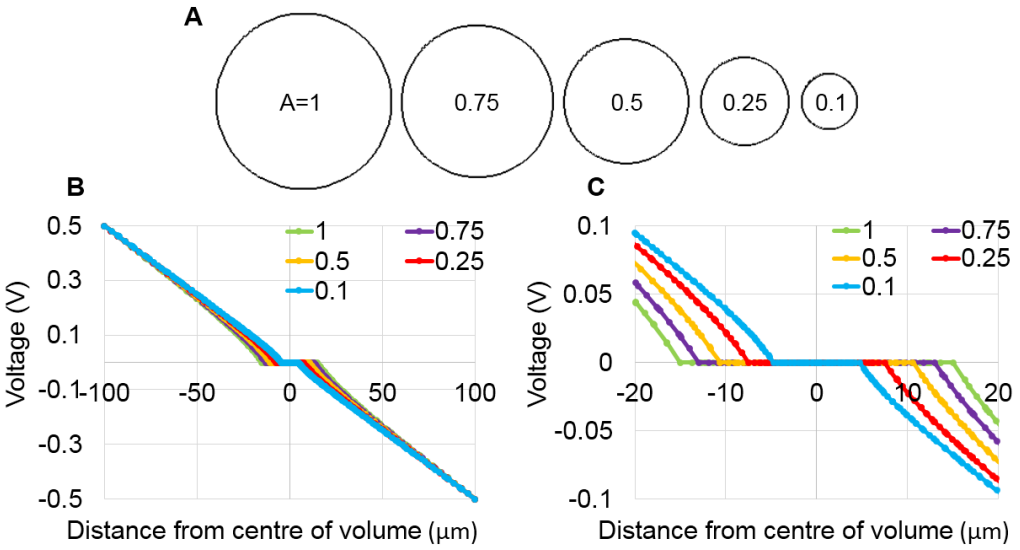

Figure 7.4 A) Range of circle sizes used with the area of each shown in relation to the largest, B) voltage vs distance through centre of volume (from positive to negative edges) for each area, C) enlarged view. Electrodes are located in the centre of the volume with the x axis of the graph referring to the distance from the centre of volume along a vertical line in the middle of the volume.

The electrodes were then moved along the Y axis in 10 μm intervals to different distances away from the source (from 10 μm to 130 μm), in order to replicate different recording positions (Figure 7.5 A, B). It was expected that each electrode should measure a linear reduction in voltage, the same as the true (empty/unaltered) voltage distribution. The electrode voltages are, again, compared to the empty voltage at the closest point of the electrode (y axis) to the source (Figure 7.5 C). This is because this is a 2D model of a probe electrode and the voltage at this point is the voltage that the electrode is being used to measure. The resulting voltages are shown in Figure 7.5 D, for the empty volume and the largest electrode. The voltage source was changed to 1 V at the bottom with a ground at the top to better replicate a measurement, the results are the same except the voltage values are shifted by 1. The electrode voltage decreases linearly like the empty voltage but it is significantly lower. This suggests that the size of the electrode is responsible for the reduction in measured voltage. This appears to be an averaging effect that results in the magnitude of the voltage on the electrode being

approximately equal to the average of the voltages it encompasses in the empty region. If the electrode was replaced by a number of equally spaced point electrodes, the whole electrode voltage would be approximately equal to the average of the point electrode voltages (provided the volume is large compared to the electrode). This has been previously described in the literature [91, 152]. For the middle position this results in an average of potentials that were higher than the middle voltage (0.5 V) on the source side of the electrode in combination with potentials that were lower than 0.5 V, resulting in an equipotential of 0.5 V for the whole electrode.

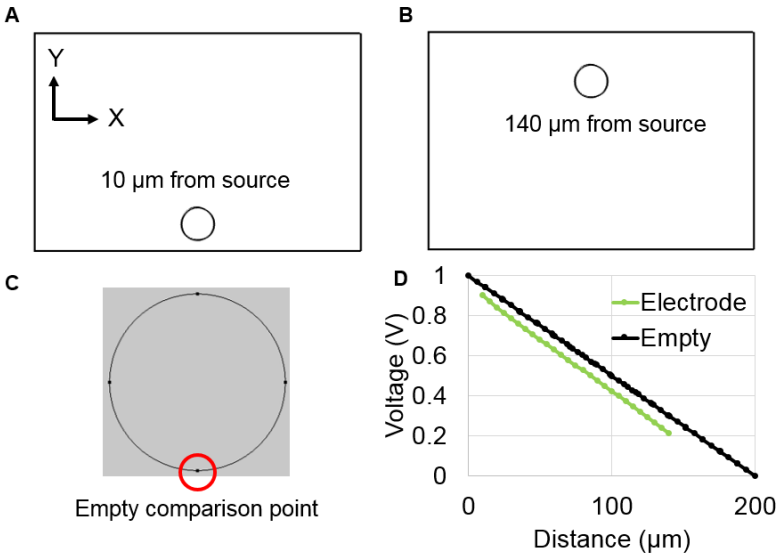

Figure 7.5 A) Electrode 10 µm from source, B) electrode 140 µm from source, C) point of comparison with empty voltage, D) empty voltage and electrode voltage vs distance.

Each electrode size was moved in the same way as the largest electrode and a similar graph to Figure 7.5 C was generated for each as shown in Figure 7.6. The full range of movement used is shown as well as an expanded view that better highlights the differences in voltage. The change in position of the lowest (in Y) point of the electrode with area was accounted for by scaling centrally on this point which positioned all sizes at the same level. The electrode voltage increases towards the empty voltage as the electrode area decreases. Which shows that smaller

electrodes have better spatial resolution, so ideally the smallest electrode possible would be used for experimental measurements. However, as mentioned previously electrode impedance is proportional to electrode area so the smallest electrode possible is not necessarily practical.

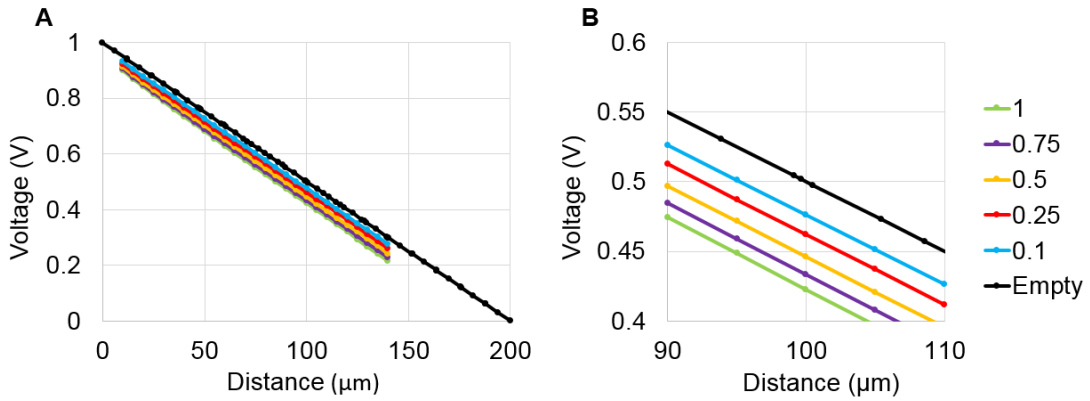

Figure 7.6 A) Electrode and empty voltage vs distance to source (bottom edge of region), B) expanded view.

The increase in voltage sensitivity for the smaller electrodes is explained by the averaging effect. The smaller electrodes average voltages over a smaller area which means over a smaller range of voltages that are closer to the source leading to higher measured voltages which are closer to the empty voltage. To illustrate the averaging effect, a second region was created containing a 'pseudo' electrode consisting of 5 points in an otherwise empty region shown in Figure 7.7 A. The shape of the circle electrode is included so the point voltages can be easily determined, but the high conductivity of the metal was not applied to the domain. The 5 points are shown in Figure 7.7 B along with a plot for each point in Figure 7.7 C. These plots show the variation in voltage at each point, the central point on its own gives a reasonable estimate of the electrode voltage. The other voltages at the other points are an equal amount higher or lower (depending on position). There are only three different voltages due to the nature of the field. These voltages were then averaged and compared to the previous results for the smallest and largest area electrodes (Figure 7.7 D). The averaged results are closer to the full electrode

model for the smaller electrode. For the larger electrode, the voltages are close in the central region and diverge slightly at the extremes of the electrode position. This could be due to the electrode position being close to the boundary which introduces edge effects that are larger for the larger electrode. For the smaller electrode the averaged results match the electrode model more closely. These results show that the electrode voltage is approximately the average of the voltage at the points contained within it and the voltage can be estimated with only a small number of points. It would be expected that a larger number of points would give a more accurate estimate. This averaging means that the electrode voltage is approximately the voltage at p3, which is at the centre of the circle.

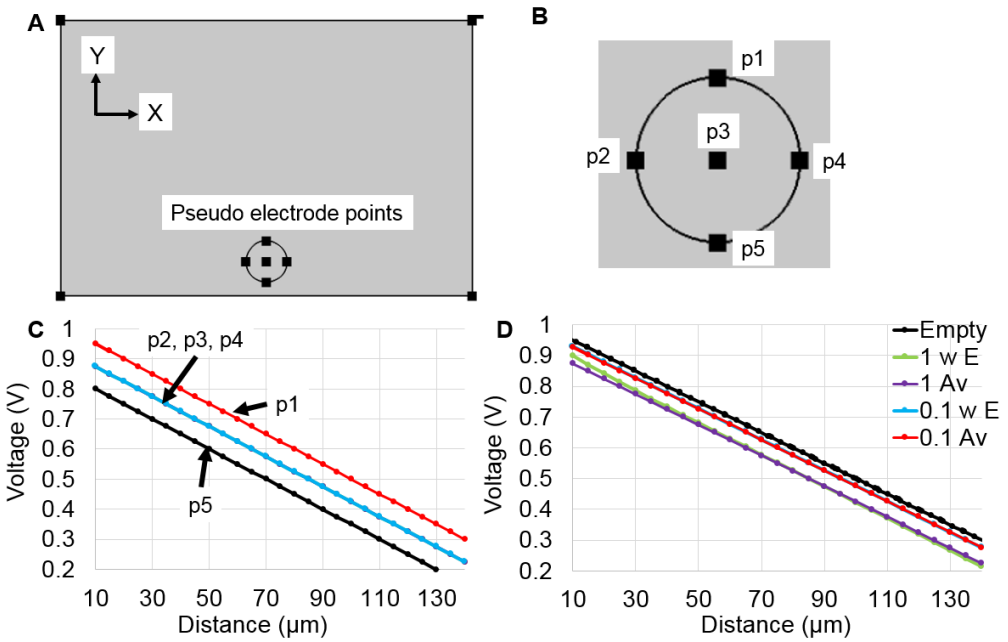

Figure 7.7 A) Pseudo electrode points in region, B) close up with labelled points, C) voltage at each point vs electrode position, D) voltage vs electrode position for the averaged points (of B), and the electrode model for the largest area (1) and the smallest (0.1). Av = average of points. w E = model with electrode.

7.1.2 Analytic Empty

The results from the COMSOL model can also be determined analytically. First the case of the uniform field is considered with no electrode present. A parallel plate geometry is shown in Figure 7.8.

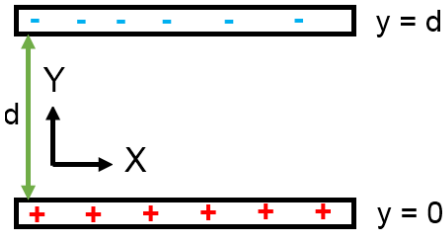

Figure 7.8 Parallel plates of charge seperated by a distance d

The magnitude of the electric field between the plates is given by:

$$E = \frac{\sigma}{\varepsilon_0} = \frac{V}{d} \tag{7.1}$$

Where σ is the charge density, $\varepsilon_0$is the permittivity of free space, V is the voltage between the plates and d is the plate separation. Laplace's equation can be used to determine the potential distribution as given by:

$$\sigma \nabla^2 V = 0 \tag{7.2}$$

Where V is the electric potential. For the geometry shown in Figure 7.8 there are no X and Z components so:

$$\frac{\partial^2 V}{\partial x^2} = \frac{\partial^2 V}{\partial z^2} = 0 \tag{7.3}$$

The Laplace equation then reduces to:

$$\frac{\partial^2 V}{\partial y^2} = 0 \tag{7.4}$$

This can be solved by integrating twice:

$$\frac{\partial V}{\partial y} = A$$
$$V = Ay + B \tag{7.5}$$

The constants of integration (A and B) can then be found using the following boundary conditions:

$$at\ y = 0, \quad V = 0, \quad so\ B = 0$$
$$at\ y = d, \quad V = V_0, \quad so\ A = \frac{V_0}{d} \tag{7.6}$$

Then by substitution:

$$V = \frac{V_0 y}{d} \tag{7.7}$$

However, for a truly uniform field d → ∞, the voltage is given by:

$$V = -Ay = -Ar\cos\theta \tag{7.8}$$

In Cartesian and polar coordinates.

7.1.3 Analytic with electrode

Suppose a spherical conducting metal electrode is added to the centre of the two plates as shown in Figure 7.9. The addition of an electrode complicates the field; such a problem can again be solved using Laplace's equation. The resulting field is a combination of the uniform field and the field from the metal due to the induced charge from the uniform field.

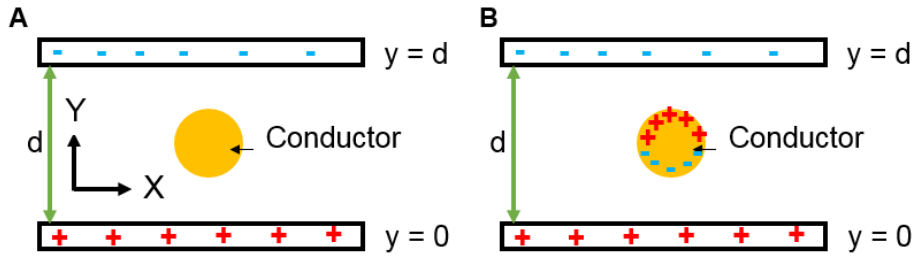

Figure 7.9 A) Conductor in uniform electric field (before charges redistribute), B) after charges redistribute due to applied field.

In the static case, when a metal is placed in an electric field it becomes polarised. All its free electrons will redistribute due to the influence of the field in such a way that cancels the effect of the applied field within the metal. This means that the field inside of the metal is zero, if it were not the electrons would be moving due to the field which would mean it was not the static case. This also means that the voltage inside of the metal is constant or at an equipotential. As there is no electric field within the metal, charges are only found on the edges/surface of the metal. The electrons in the metal are attracted to the positive plate, which leaves positive charges on the opposite edges as shown in Figure 7.9. Due to the symmetry, half the sphere becomes negatively charged and half positively charged.

This distribution of charge is similar to that of a dipole, so as a trial solution the solution to Laplace's equation for a dipole can be used which is given by:

$$V = C\frac{\cos\theta}{r^2} \tag{7.9}$$

The uniform field can be considered to be uniform far from the metal as $r \to \infty$ with a constant magnitude (E_0) and direction.

$$V(r \to \infty) = -E_0 r\cos\theta \tag{7.10}$$

The resulting field can then be found by combining the two fields to give the voltage outside of the metal:

$$V_{out} = C\frac{\cos\theta}{r^2} - E_0 r\cos\theta \tag{7.11}$$

The metal is located in the middle of the uniform field so by symmetry the value of the potential inside of it must be zero:

$$V_{in} = 0 \tag{7.12}$$

The constants can be found using appropriate boundary conditions. The potential at the surface of the metal must be continuous across the boundary and must therefore be zero.

$$at\ r = R, \qquad V = 0$$
$$C\frac{\cos\theta}{R^2} - E_0 R\cos\theta = 0 \tag{7.13}$$

From which C can be found to be equal to E_0a^3 which means the solution is:

$$V_{out} = E_0 a\frac{\cos\theta}{r^2} - E_0 r\cos\theta \tag{7.14}$$

This is the correct and only solution as it satisfies all the boundary conditions as the uniqueness theorem states.

7.1.4 Comparison

This section presents a comparison between the COMSOL model for the circle electrode in the middle position and the analytic solution. The simplest comparison that can be made is the magnitude of the electric fields in the empty volume. For the plate separation and plate voltages used in the COMSOL model the magnitude of the E field in the empty volume should be:

$$E = \frac{\Delta V}{d} = \frac{1}{200\mu m} = 5000\ V/m \tag{7.15}$$

Which as shown in Figure 7.2 is the same as what is generated by the COMSOL model. The voltage distributions can also be compared by plotting Equation (7.14 with θ = 0, E_0 = 5000 V/m and the same radii as the COMSOL models. This results in similar plots to those shown in Figure 7.4. These results are plotted with the corresponding COMSOL results in Figure 7.10. Plots are shown for the largest and smallest area electrodes used along with an expanded view to more clearly see the distribution around the electrodes. Both models show similar voltages for outside of the electrode with a closer match for the smaller electrode as shown by the percentage differences for both. For the large electrode there is a maximum difference of ~30%

and for the small electrode there is a maximum difference of ~25% close to each electrode. These differences then reduce towards zero with increasing distance from the electrode. The voltage inside the electrode is the same for both. The discrepancies for the outside voltages could be due to the limitations of the assumptions made in deriving the analytic solution. The COMSOL model uses a finite region where the size of the larger electrode is closer to the size of the region, so there are more boundary effects. A dipole like induced current density may also not be as valid for the larger electrode with the smaller electrode being much more dipole like due to its size.

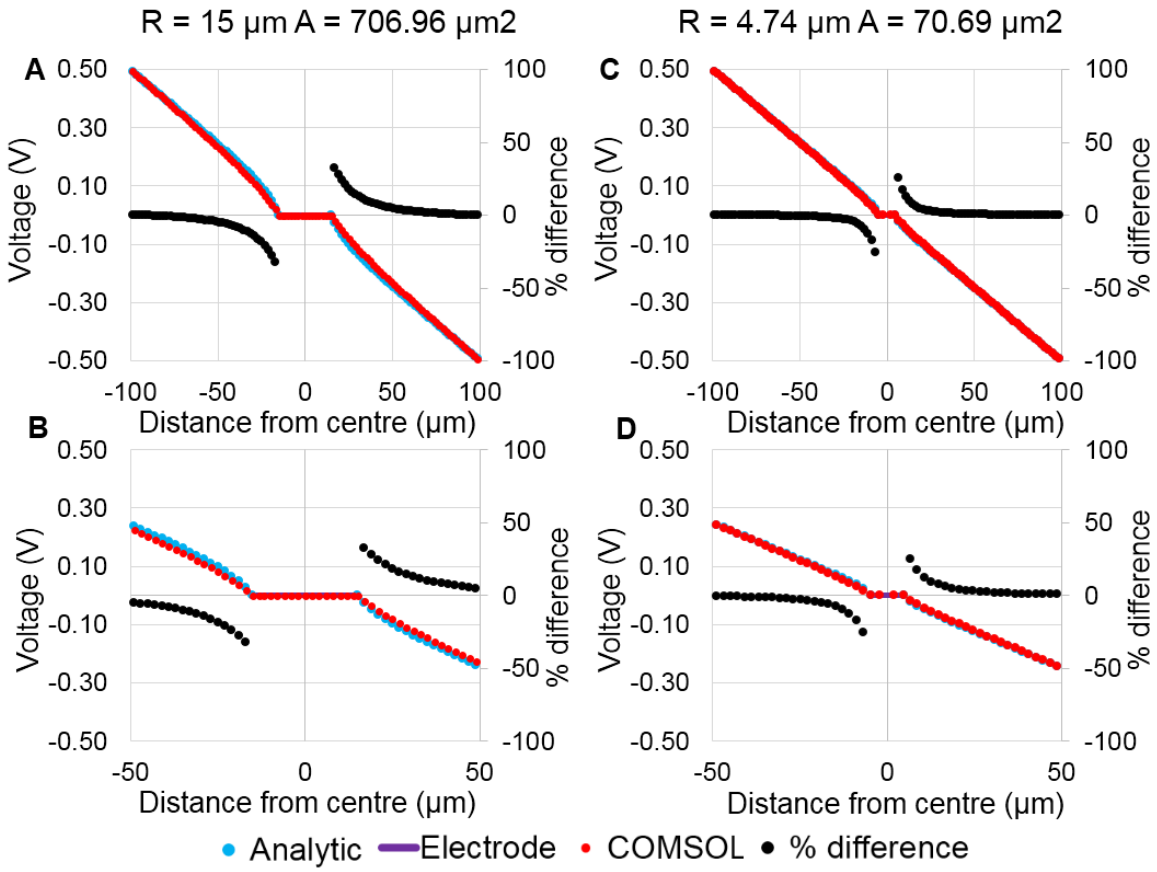

Figure 7.10 Voltage vs distance from source to top edge for COMSOL model and analytic solution. A) Largest electrode area (1A), B) expanded view, C) smallest electrode area (0.1A), D) Expanded view. The percentage difference between the analytic and COMSOL solution is also plotted on each graph using the secondary (right) y axis.

7.1.5 Other shapes

The COMSOL model was then expanded to include differently shaped electrodes in order to determine the best electrode shape. The following basic shapes were used as listed below (Figure 7.11):

1. Equilateral triangle point nearest source
2. Square
3. Horizontally aligned rectangle wrt source (3 to 1 side ratio)
4. Vertically aligned rectangle wrt source (3 to 1 side ratio)
5. Equilateral point away from source
6. Circle
7. Horizontally aligned ellipse wrt source (3 to 1 axis ratio)
8. Vertically aligned ellipse wrt source (3 to 1 axis ratio)
9. Diamond (square rotated 45 degrees)

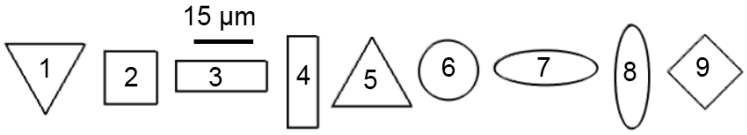

Figure 7.11 Electrode shapes.

The areas of each shape were all scaled to the same value as the largest circle electrode described earlier, their positions were adjusted so that the ‘lowest’ point (in Y) of each shape was at the same level. Each shape was then moved away from the source along the Y axis as before, away from the 1 V source. From this a plot of the electrode voltage vs distance from the source was generated for each electrode shape as shown in Figure 7.12. The voltage on each electrode reduces linearly with a similar gradient. Each electrode shape has a different voltage offset from the empty voltage with an approximately constant gradient. As described

previously, the ‘best’ shape is that where the electrode voltages are closest to the empty voltage and the worst is the opposite. The amount of offset in the voltages remains in a constant order of best to worst over the range of distances. The vertically aligned ellipse (8) is the worst and the horizontally aligned rectangle electrode (3) is the best.

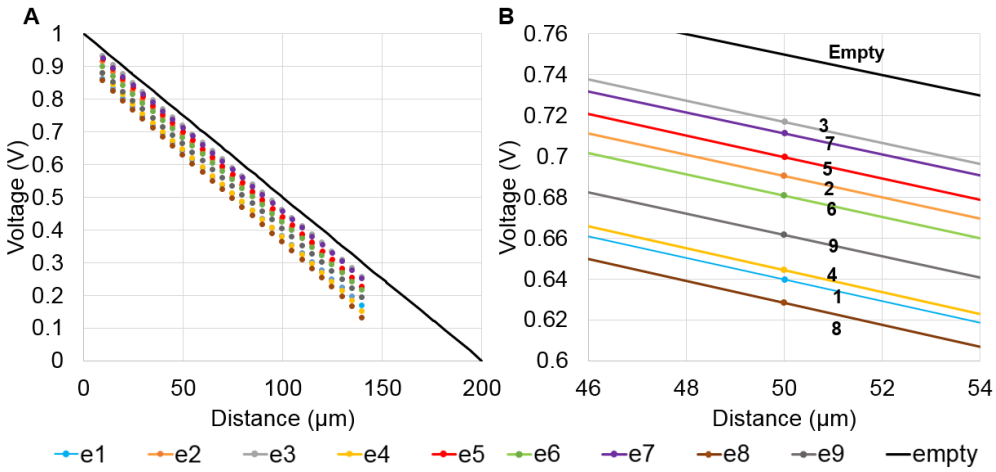

Figure 7.12 Electrode voltage with position. A) Full view, B) expanded view and then additionally equally scaled as before with the circle electrode. Numbered electrodes are the same as previously listed.

The ability of each electrode shape to measure the desired potential was investigated further by determining what percentage the electrode voltage was of the empty voltage 70 μm from the source. This was calculated for each shape with the results (Figure 7.13) presented as a ranking table. This table ranks the electrode shapes based on their ability to measure the empty voltage, therefore, a higher percentage is better. The order is the same as from the section of Figure 7.12. The voltage only varies in the Y direction in the uniform field so the horizontal rectangle (3) is the most effective (~94%) as its Y dimension is the smallest. Therefore, the averaging effect of the electrode is over the smallest range which is also closest to the source resulting in the closest value to the empty voltage. The Y dimension of the horizontal ellipse (7) is the next smallest so this results in the next best measure of the voltage (~93%). The point up triangle (5, ~91%) is slightly different as its Y dimension is larger than that of the square (2, ~90%) or circle (6,

~88%) but its voltage is closer to the empty voltage than either shape. The geometric centre of the shape is however lower (Y direction) due to the point facing up which results in a better voltage measurement. The effect of this can be seen by looking at the point down triangle (1, ~82%) which is exactly the same as the other triangle but orientated the opposite way. The voltage for this shape is much larger as its geometric centre now lies further away from the lowest point of the electrode. The square (2) and circle (6) are quite similar, the circle (6) is worse due to the extreme lower and upper points being separated by a greater distance than the lower and upper points of the square (2). This is also true for the diamond (9) where these points are separated by an even greater distance. The large Y dimension of the vertical ellipse (8) and rectangle (4) lead to poorer voltage measurements for each.

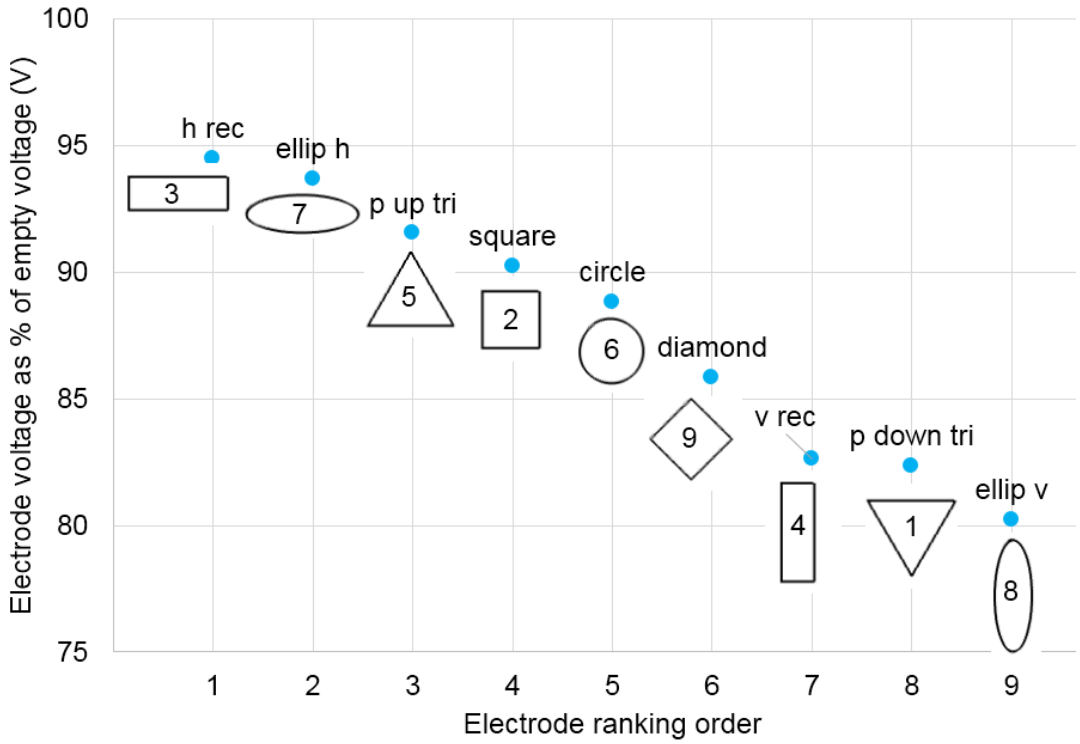

Figure 7.13 Electrode voltage as a percentage of the empty voltage for each shape (ranking order). Distance from source = 70 µm.

Addtionally, each electrode was then scaled in area as before down to 0.1A as shown in Table 7.2. The areas are the same for each electrode with the differences in axis lengths due to the nature of each shape.

Table 7.2 – Electrode dimensions and areas. All units are in µm for distance and µm^2 for area.

	Circle		Rectangles			Ellipses			Square		Triangle	
A Scale Factor	Radius	Area	s1	s2	A	a	b	A	s1	A	s1	A
1.00	15	707	15	46	707	9	26	707	27	707	40	707
0.75	13	530	13	40	530	8	23	530	23	530	35	530
0.50	11	353	11	33	353	6	18	353	19	353	29	353
0.25	8	177	8	23	177	4	13	177	13	177	20	177
0.10	5	71	5	15	71	3	8	71	8	71	13	71

Where A is Area, s1/2 = side 1/2. a and b are the ellipses semi axes

The result of this is similar to the circle electrode for every electrode, with the smaller electrodes measuring voltages closer to the empty value than the larger electrodes. The spread of the resulting voltages for each electrode is different however. For example, Figure 7.14 shows the difference in the spread of voltages for different electrode areas for the vertically aligned ellipse (A) and the horizontally alligned ellipse (B). This is due to the reduced area having a larger effect on the Y dimension of the vertical ellipse (8) than the horizontal ellipse (7).

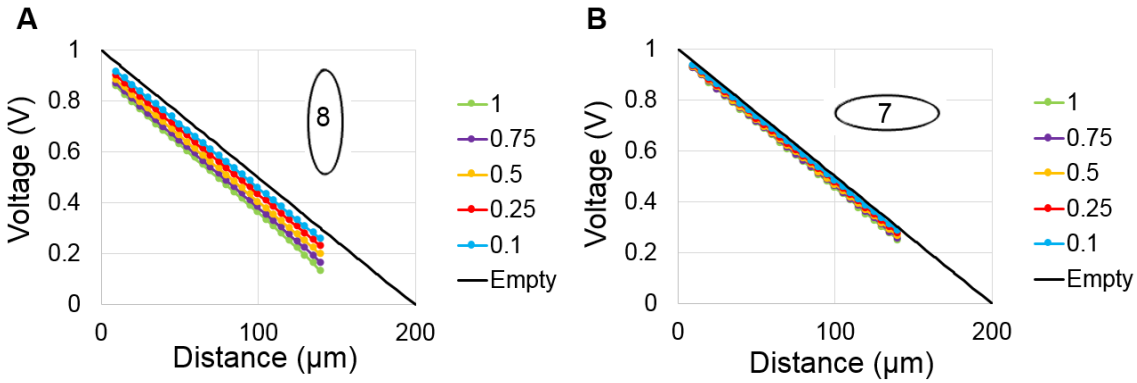

Figure 7.14 Electrode voltage vs distance from source. A) Vertical ellipse, B) Horizontal ellipse.

The spread of voltages for each electrode shape was calculated by subtracting the 1A electrode voltages from the 0.1A electrode voltages for each position and shape and then the average was

calculated of the result (Figure 7.15). The electrode order here is the same as for the differences to the empty voltage for each shape (Figure 7.13). The change in electrode area has the most effect on the shapes with the largest Y dimension. The difference to the empty voltage order also remains constant for each of the areas (not shown in figure).

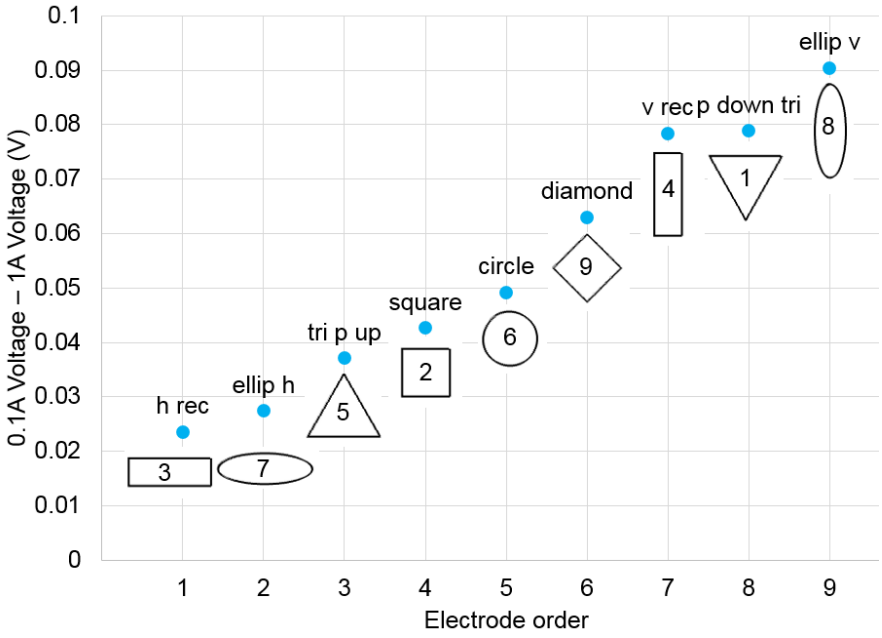

Figure 7.15 Effect of electrode area on electrode voltage.

In summary, it can be seen from these results that the horizontal rectangle and ellipse and the point up triangle are the most effective electrodes shapes. However, this is only for a uniform field, it is expected that for a field that varies in 2 or 3 dimensions the performance of these electrode shapes would be significantly reduced with the dimensions of the shapes being a key factor in the resulting electrode voltages. Due to this electrode shapes with a large Y dimension are more sensitive to changes in area as proportionally the extended Y dimension is reduced more than the X dimension.

7.2 Dipole

7.2.1 Source

In this section the uniform field is replaced by a more realistic dipole field. The models use the same region with a positive (2857.1 A) and negative point current source (-2857.1 A) creating the dipole as with the heart models. The positive source was placed 10 µm from the bottom edge of the region with the negative source positioned 1 µm directly below it. The same electrode shapes and areas from the uniform field model were then placed at varying distances directly above the dipole. Figure 7.16 shows the geometry of the model with the empty dipole region (A) and with the circle electrode (B). The electric field lines for the empty region show the expected distribution for a dipole. Placing the electrode within the geometry distorts the field as with the uniform model.

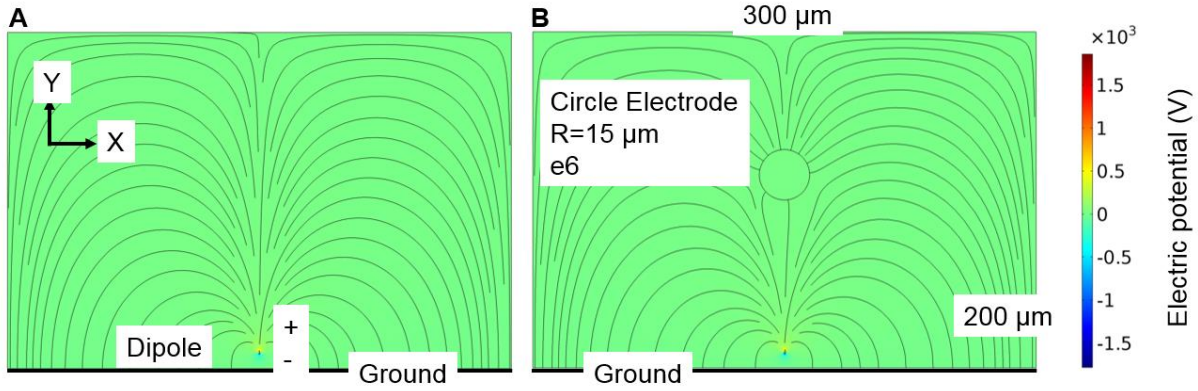

Figure 7.16 Surface plot of dipole region setup, with electric field lines. A) Empty region with dipole, B) Region containing circle electrode 100 µm from the source.

This model simulates voltages on the electrodes that are directly in the path of the depolarisation wave from the heart with the electrode facing the positive side of the dipole. The orientation of the dipole is such that voltages are expected to be positive and reduce from the source in the Y direction in a similar way to that which is described by the analytic dipole model described in chapter 3

$$\varphi_d = \frac{p \cos\theta}{4\pi\sigma r^2} \tag{7.16}$$

Where p is the dipole moment, θ is the angle, σ is the conductivity and r is the distance to the dipole. However, the distribution from the COMSOL model (when plotted) is proportional to $1/x^{-0.76}$ rather than $1/x^2$ (Figure 7.17 A), which was determined using a MATLAB curve fit. This is most likely due to the relatively large point separation in the COMSOL model and compression by the volume walls. This isn't a problem as the voltage still varies in two dimensions as shown in Figure 7.17 B. This is an extruded surface plot showing the voltage variance from the positive source within the model. The data scale and colour scale has been lowered to better show the shape of the distribution. There is a steep and narrow change in voltage close to the positive source that then widens and flattens with increasing distance.

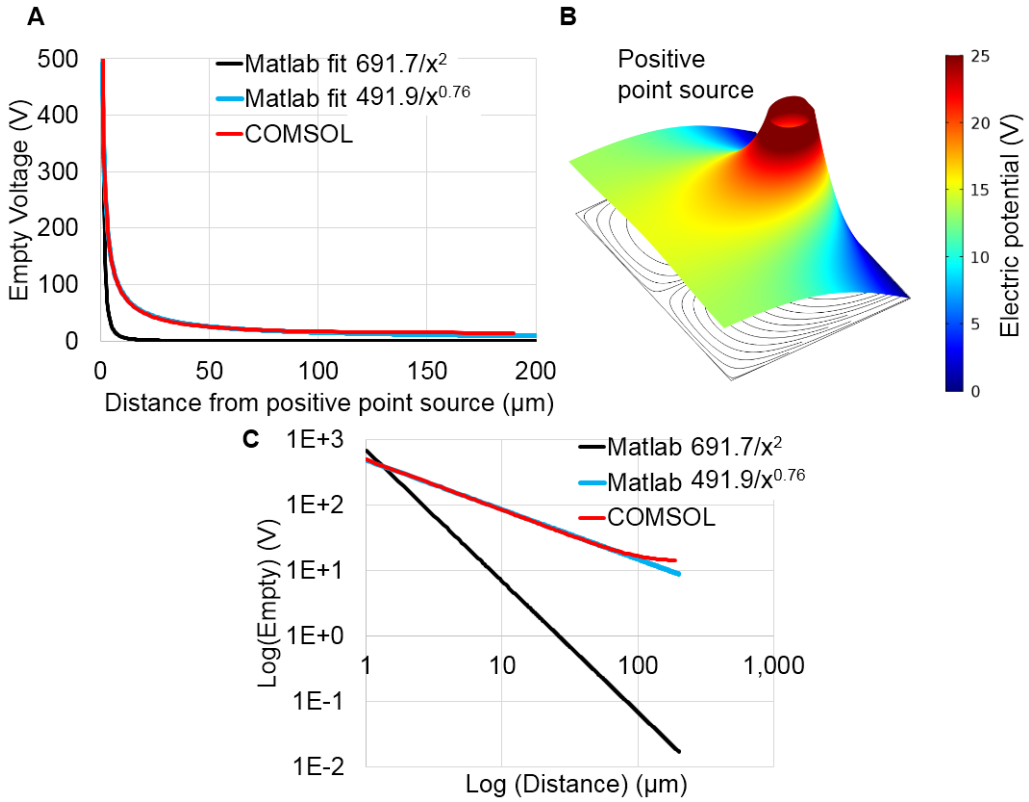

Figure 7.17 A) Empty region voltage centrally from postive source along Y axis with fitted voltage distributions, B) 3D extruded surface plot of empty region voltage, C) log-log plot of A.

When an electrode is placed in the geometry, the voltage distribution is distorted and there is a flat equipotential region for the electrode as with the uniform field (Figure 7.18). For the empty region (A) there is a smooth drop in voltage. The equipotential region is shown for a circle electrode placed at 20 µm (B) and at 50 µm (C) from the positive source.

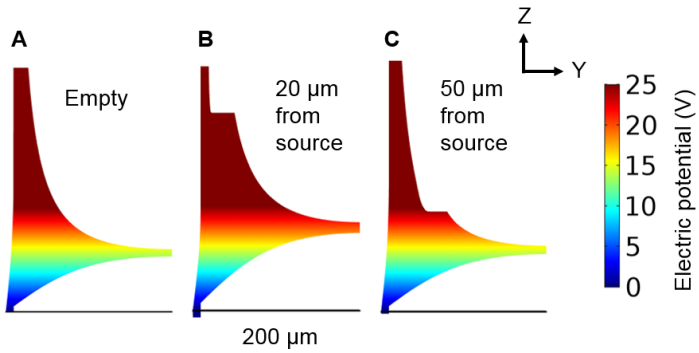

Figure 7.18 Extruded surface voltage plots. A) Empty region, B) circle electrode 20 µm from the source, C) circle electrode 50 µm from the source.

7.2.2 Electrode shape results

The same electrode shapes and areas (as with the uniform field model) were placed in the dipole field, each electrode was placed 5 µm from the source and then moved away at 2.5 µm intervals up to 130 µm. Figure 7.19 shows the result of this for all electrode shapes and the largest (1A) and smallest (0.1A) electrode areas. The electrode voltages are much less than the empty voltage close to the source but then move closer to the empty voltage with distance. This is because the voltage gradient close to the source is large so the averaging effect of the electrodes skew the electrode voltages lower. Further away from the source the gradient is much shallower so the averaged voltages are much closer to the empty voltage.

It can be seen that once again the smaller electrode voltages are closer to the empty voltage than the larger electrodes. There is also a smaller range of voltages for the smaller electrodes which suggests that the electrode shape has less of an effect on the resulting electrode

voltage when the electrode is small. In contrast to the uniform field, the relative performance of each electrode shape does not remain constant over the distance for both sizes. There is also a difference in the order of effectiveness between the two areas. This is due to the distribution of the dipole field, as shown in Figure 7.17 B the distribution starts steep and narrow and then reduces and widens which leads to different electrodes being more or less relatively effective at different positions.

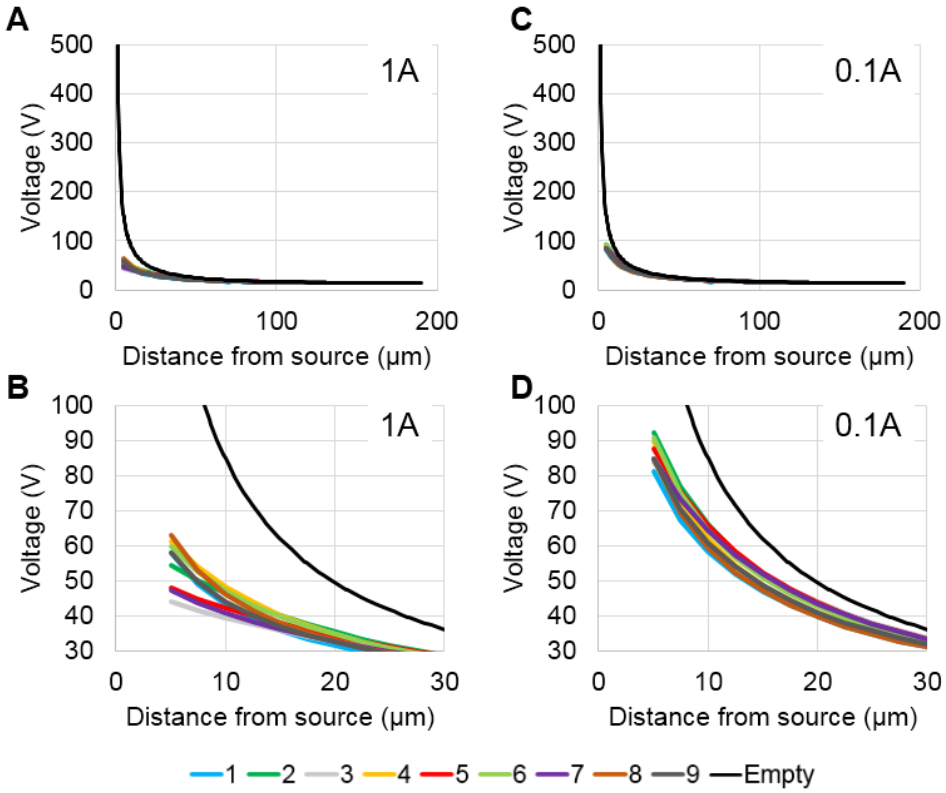

Figure 7.19 Electrode and empty voltages for varying electrode distances. A) 1A full view, B) expanded view, C) 0.1A full view, D) 0.1A expanded view.

Therefore, the relative performance of each electrode cannot simply be determined for the entire range with a comparison to the empty voltage as with the uniform field. Instead, this was determined for 5 µm to 55 µm at 5 µm intervals. The electrode voltage was subtracted from the empty voltage for each position then rankings were assigned as before, with the highest difference in voltage given a ranking of 9 (the worst) and the lowest a ranking of 1 (the best).

The results of this are shown in Figure 7.20. Colours were assigned to each electrode shape along with a number (C), for each distance the electrode ranking is given by each colour and number. This shows the change in ranking for the different positions and the differences between the two electrode areas.

For 1A (Figure 7.20 A) the ranking of each electrode is variable close to the source and then settles into a constant order by 45 μm. The vertical ellipse (8) and the vertical rectangle (4) start out as the most effective electrodes. This is because the voltage reduces less along the middle of the volume than the sides (Figure 7.20 D and E) and as these electrodes have a small X dimension they only measure the higher voltages. As the electrodes are moved away their relative effectiveness reduces as the middle voltage reduces relative to the voltages at the sides. Their long Y dimension is then a disadvantage. The opposite is true for the horizontal ellipse (7) and rectangle (3), their rankings start low and then increase with the change in distribution. The point down triangle (1) starts in the middle of the rankings then gets worse with the opposite true for the point up triangle (5). This is consistent with the other results with (1) having a high geometric centre like the vertically aligned electrodes and (2) the opposite, like the horizontally aligned shapes. The circle (6) and square (2) are quite similar as they were for the uniform field; their shape leads to initial poor performance where the electrode is wide enough to cover the greater voltage drop but this improves with distance where the compactness of the shape is beneficial.

For 0.1A (Figure 7.20 B) as shown in Figure 7.19 C and D the effect of the electrode shape is reduced. All the electrodes are more point like, this changes the ranking at each position. A stable ranking is established more quickly that is the same as that for the uniform field (Figure 7.13). The square (2) and circle (6) start out the best as they are the most point

like, then the shapes with smaller Y dimensions perform better, with the larger Y dimension shapes performing worse. This is due to the gradient of the voltages reducing and the distribution becoming more linear.

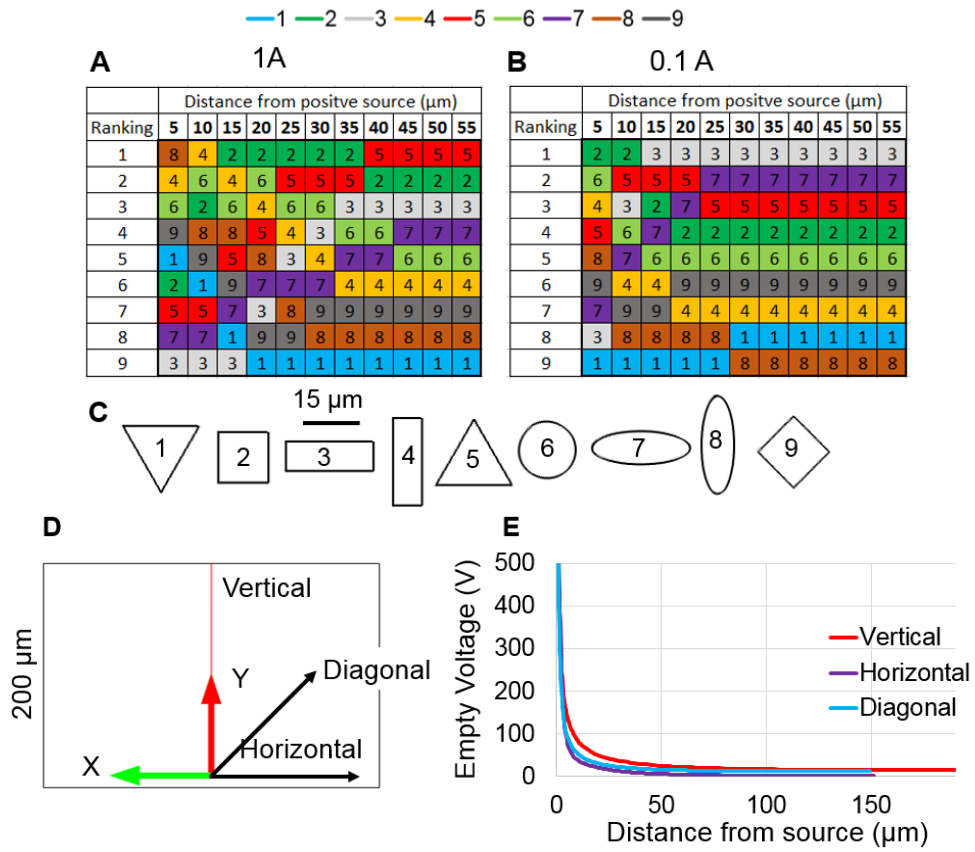

Figure 7.20 A) Electrode ranking for 1A electrodes, B) for 0.1A electrodes. Each electrode has a corresponding colour and number within the tables with changes in electrode ranking determined by their ability to measure the empty voltage at each distance. (1 = best, 9 = worst). C) Electrode shapes (1A) D) Empty volume plot directions, E) plot of empty voltage in each direction away from the source.

The overall result of these models can be seen by combining the rankings for each shape for each area at the 5 µm and 55 µm positions (Figure 7.21) with the lowest combined ranking being the most effective electrode shape (as 1 = best 9 = worst). This shows that the top three electrode shapes are the square (2) followed by the circle (3) and the point up triangle (5). The square and circle work best due to their symmetry and compactness which mean they average potentials over the smallest areas. They are effective at both sizes and at different distances with

the other shapes effectiveness varying more. The point up triangle also has a low geometric centre but is less compact than the square and circle.

	1A			0.1A			
Electrode	5 µm	55 µm	Combined	5 µm	55 µm	Combined	Total
1	5	9	14	9	8	17	31
2	6	2	8	1	4	5	13
3	9	3	12	8	1	9	21
4	2	6	8	3	7	10	18
5	7	1	8	4	3	7	15
6	3	5	8	2	5	7	15
7	8	4	12	7	2	9	21
8	1	8	9	5	9	14	23
9	4	7	11	6	6	12	23

Figure 7.21 Electrode ranking combined table. The ranking for each electrode shape at 5 µm and 55 µm is shown (for 1A and 0.1A areas) from Figure 7.2. The combined ranking is the sum of the rankings at 5 µm and 55 µm for each electrode shape (from the previous figure). The total is then the sum of the two combined rankings. The same colour scheme as Figure 7.2 is used for the electrode column and the colours in the total column highlight which electrodes have the best (lowest) total ranking.

7.2.3 Effect of area

As with the uniform field the effect of area on the electrode voltage was calculated. The spread of voltages is different for each area and shape as shown in Figure 7.22. The horizontal ellipse (7) has a larger spread of voltages compared to the vertical ellipse (8) this, as already explained, is due to the voltage gradient in the middle of the volume being higher than the outside gradients. As the size of the electrode is reduced, this effect is reduced and the voltages become similar.

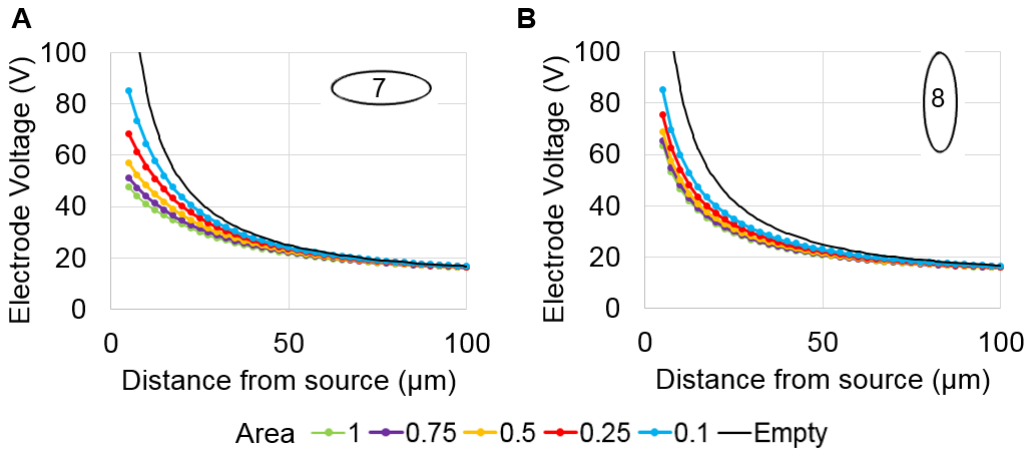

Figure 7.22 Electrode voltage vs distance from source for A) horizontal ellipse, B) vertical ellipse.

As with the shape results the electrode ranking varies between each area so the ranking was determined over the 5 – 65 µm in 5 µm steps (Figure 7.23 A). The ranking here, as with the uniform field, is given based on the range of voltages for each electrode area and shape at each position. 1 is the lowest change in voltage (least affected by area) and *vice versa*. Figure 7.23 B shows the combined rankings to see which electrodes are affected the most and least over the position range. The vertical electrodes are least effected by area as they are already small in X and cover the higher part of the voltage. The wider (in X) electrodes reduce in width and so improve in effectiveness. The 'best' performing electrode shapes (square (2), circle (6), point up triangle (5) from the previous results, vary in their ranking. The circle stays approximately the same but the square and point up triangle ranking changes largely with distance with a higher spread of voltages close to the source which reduces to a lower spread.

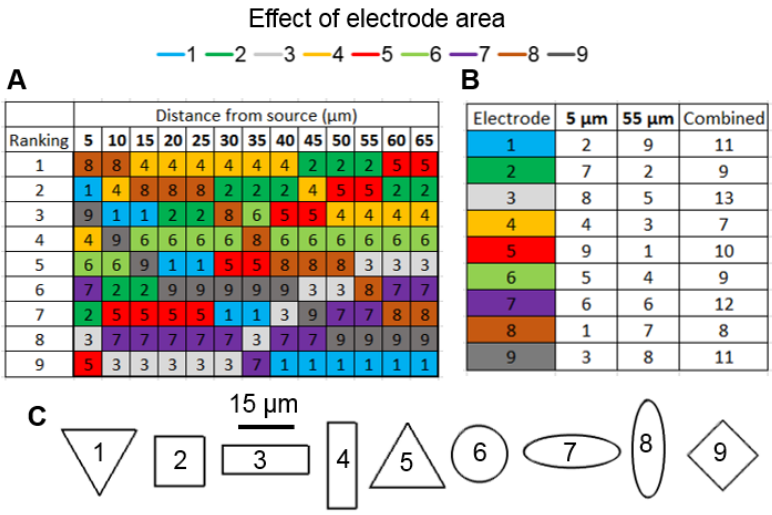

Figure 7.23 A) Electrode ranking table for multiple electrode positons, B) ranking combined table compiled in the same way as before, C) electrode shapes.

These results suggest that the circle is the best shape as it performs well against the other shapes and the effect of its area is similar relative to the other shapes in both a rapidly changing field and a smoother field.

7.2.4 Averaging

As with the uniform field, a pseudo circle electrode was created for the dipole field to confirm the averaging effect of the electrodes (Figure 7.24 (A and B)). The 5 circle points are plotted in (C) along with the average and circle electrode voltage in (D). The average voltage is quite close to the electrode voltage but there is a larger difference than with the uniform field. This shows that the electrode voltage is approximately equal to the average of all the voltages contained within the electrode area if there were no electrode.

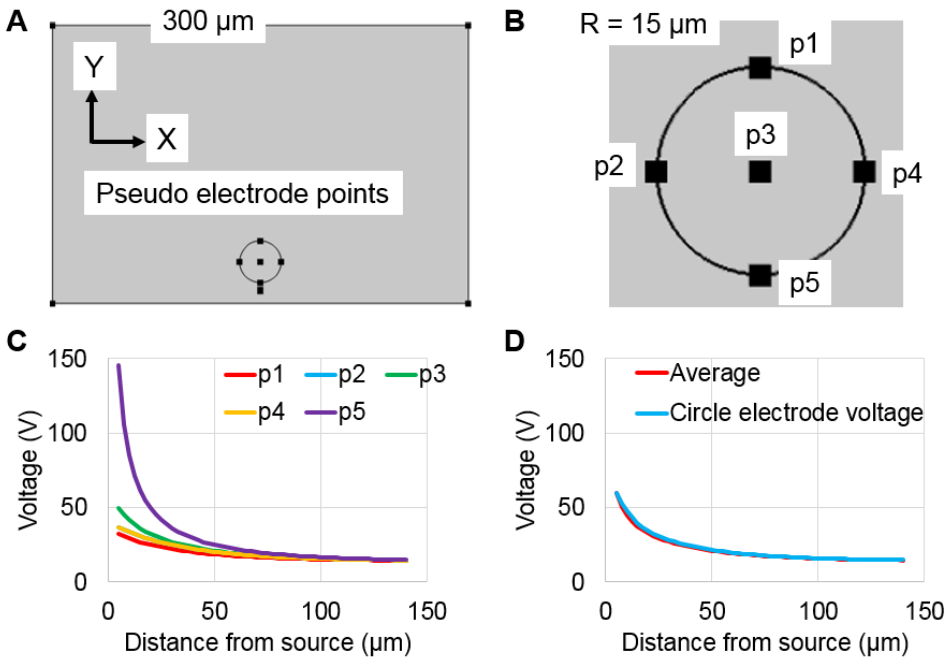

Figure 7.24 A) Pseudo electrode points in volume, B) close up and labelled points, C) voltage at each point over distance, D) comparison between average of 5 points and electrode voltage for a circle electrode.

7.2.5 Zebrafish skin

The previous models neglected an important factor in measuring the electrical activity of the zebrafish heart which is the zebrafish skin. This section introduces a high resistance region between the dipole source and the electrode to investigate its effect on the electrode voltage. A three region model was created with one region containing the dipole which represents the inside of the zebrafish (200x20 µm), one region with low conductivity (200x10 µm) which represents the skin and a third region (370x200 µm) which represents the surrounding electrolyte (Figure 7.25 A). Three of these geometries were created containing square and circle electrodes as well as a completely empty version. The electrodes were again moved away from the source with electrode voltages compared to the empty voltages (zero is the skin region rather than the positive source) (Figure 7.25 B and C). The skin was given two conductivities, 0.7 S/m (the same as the surrounding regions) and 1e-4 S/m (low conductivity to simulate high

resistivity skin [153-155]). The result is that the electrode voltages were significantly reduced, as were the empty voltages. This shows that it is hard to measure a signal even if the electrode is in good contact with the zebrafish as the signal is significantly reduced by the skin. This obviously reduces the signal for electrodes making partial or no contact compared to a low resistance skin.

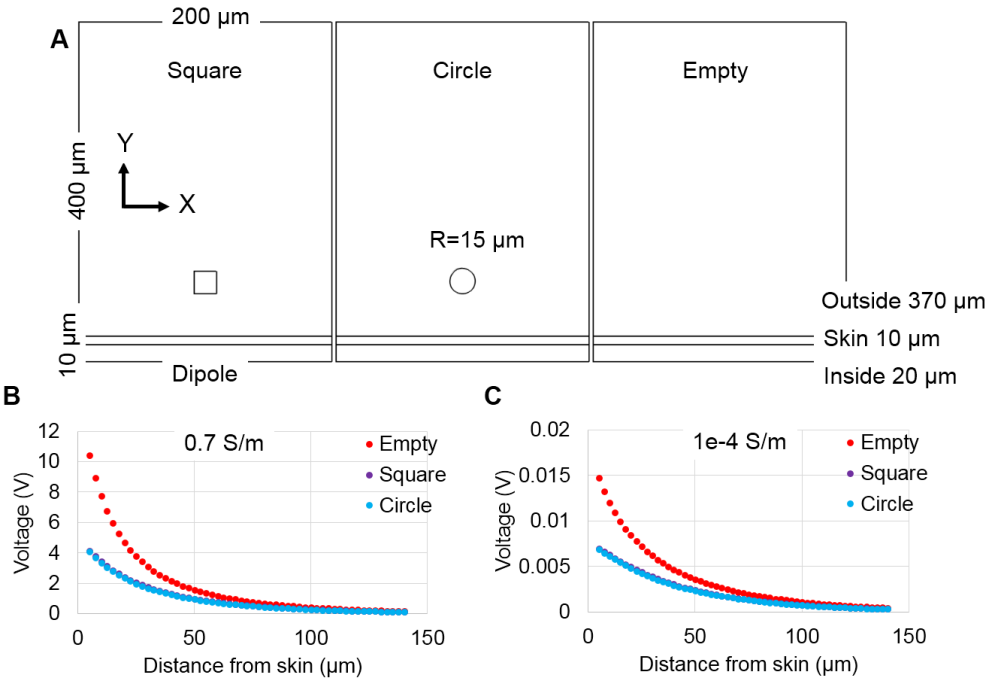

Figure 7.25 A) Volume geometry with added skin region, B) voltages measured from skin for 0.7 S/m conductivity, C) voltages for 1e-4 S/m.

7.3 Incorporating heart model

The square and circle electrodes were then incorporated into the bidomain heart model described in the previous chapter. The ventricular position (3) from the bidomain model (Figure 7.26 E) was chosen for comparison with the electrode voltages. The electrodes were added to the geometry by extruding a work plane centred on the ventricular position of the model body and then using Boolean operations to leave the electrode surface on the boundary (Figure 7.26 A, B, C and D). The largest (1A) and smallest (0.1A) areas for each electrode were used and

compared to the point voltage (Figure 7.26 F). The first thing to note is the size of the 1A electrodes in comparison to the heart, they are roughly 1/3 of the size of the heart and these models do not include the polyimide insulation or wiring. As described previously, the 0.1 A electrodes are too small to fabricate but show the effect of the electrode area more clearly due to the large difference in size. The point voltage represents the ideal electrode and it is the aim of the other electrodes to measure the voltage at this point. This is a 3D model and it simulates electrode arrays rather than probes where the electrode is placed on the surface (parallel contact) rather than the probe style perpendicular contact as with the previous models. The electrode voltages for the square and circle are similar for both shapes as they were for the 2D models at both sizes. The 0.1A electrodes are again more effective at measuring the desired voltage than the 1A electrodes. However, the ECG is still recognisable with the larger electrodes, the voltage magnitudes are just reduced slightly. The 1A electrodes cover a much larger area of the body which includes regions where the voltage is much lower, which reduces the overall electrode voltage. The creation of the electrode geometry assumed that all of the area of the electrode makes contact with the body leaving a curved surface over the body. This would not be the case in an experiment as the electrode would be unable to conform to the exact geometry and some part of the electrode would likely be exposed to the surrounding saline/E3 which could reduce the voltage further.

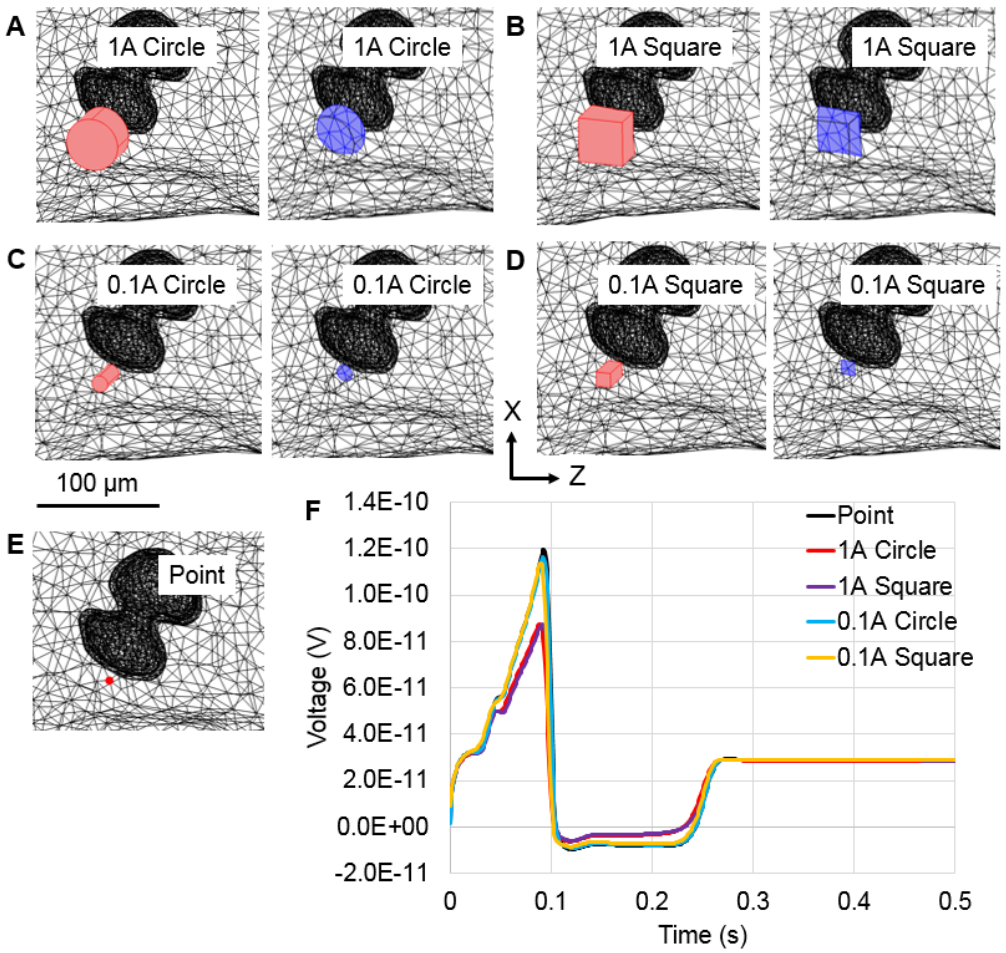

Figure 7.26 Electrodes in bidomain heart model. A) 1A circle electrode extrusion with electrode surface, B) 1A square, C) 0.1A circle, D) 0.1A square, E) point electrode position.

7.4 Summary

This chapter has presented a series of electrode models for use in the design of zebrafish electrode recording arrays. The starting point for the models was that electrode impedance is proportional to area but spatial resolution is inversely proportional to area so there needs to be a balance in creating electrodes that have a low impedance but also good voltage sensitivity. To do this a series of static 2D COMSOL models were created of differently shaped and sized electrodes. A simple uniform field was used as well as a dipole field before combining the electrode models with the bidomain heart model from the previous chapter.

The main result of these models is that small electrodes were confirmed to be more voltage sensitive than larger electrodes. This means electrodes should be made as small as possible. The electrode voltage is approximately the result of the average potentials contained within its area which explains why smaller electrodes are more voltage sensitive. Circle and square shaped electrodes were found to be the most effective electrode shapes due to their compact size and symmetry. They are essentially expanded points so this is not a surprising result. The two types of triangle showed that orientation is also important, as the square is not rotationally symmetric, this gives the edge to circular electrodes. Introducing the simple zebrafish skin model reduced the electrode voltage significantly which explains why it is difficult to measure a signal when not in contact with the skin. The results with the combined bidomain/electrode models were consistent with those from the 2D models, larger electrodes are also likely to not measure the finer details of the ECG. The reduced effectiveness of the larger electrodes relative to the smaller electrodes suggests that there needs to be a large amount of contact between the area of the electrode and the zebrafish otherwise the resulting electrode voltage would be even lower. An improvement would be to account for any capacitive effect of the skin as well as including the skin in the bidomain heart model along with a saline/E3 volume surrounding the body geometry.

A factor not considered in these models was the electrode-electrolyte interface. As described previously, the electrode-electrolyte interface is a complex combination of capacitance and resistance. For static models this can be reduced to a simple resistance which would just lower the voltage on any electrode with this boundary condition. This effect could have been added using the contact impedance boundary condition within COMSOL but all it would do is reduce the electrode voltage by an amount proportional to the value of the selected

resistance. Future models could incorporate a full model for the interface by using an equivalent circuit model and time varying signals.

The previous chapters have covered the majority of the modelling work in this thesis for the heart and the electrodes used to measure them. The next chapter focuses on the design and fabrication of the electrodes themselves.

8. ELECTRODE FABRICATION AND IMPEDANCE REDUCTION METHODS

This chapter continues the previous work (described in chapter 4) to develop electrode recording arrays for zebrafish ECG measurement including the design, fabrication and testing of the devices. The previous work had shown that an ECG signal could be measured using a probe style device and so the work described in this chapter is focussed on the use of the 20-channel array device that is more compatible with a high throughput application. The electrode models in the previous chapter showed that electrodes need to be made as small as possible to improve their spatial resolution, which has the side effect of high impedance. The importance of low electrode impedance was also highlighted in chapter 4. Therefore, this chapter describes the use of impedance reduction techniques to reduce the necessarily high electrode impedance of small microfabricated electrode arrays for larval zebrafish use. The techniques used (as described in chapter 4) are a combination of gold plating and PEDOT:PSS electropolymerisation which increase the surface area of the electrodes via roughing and means that electrode dimensions can remain small and still have a low impedance. The findings of the experiments are discussed along with comparison to the equivalent circuit model from chapter 4. The structure and use of the 20-channel device is then described followed by a redesign and further testing. The chapter ends with a summary.

8.1 Gold and PEDOT coating

This section describes the testing of gold and PEDOT:PSS coating that was performed on microfabricated zebrafish probe electrodes with the aim of reducing their impedance for ECG

measurements. A good target to aim for was thought to be the impedance of a micropipette electrode (which is able to measure a good signal) of ~1 MΩ [92] and as a metal electrodes impedance is frequency dependent this impedance needed to be achieved at ECG frequencies which are around 100 Hz. 1 MΩ was the maximum impedance that was being targeted. The aim of this work was to reduce the impedance of the electrodes by as much as possible. These devices were fabricated using the techniques described in chapter 4. Also, as described in chapter 4, the work of Richard Barrett was used as a starting point for this work, a number of zebrafish probe electrodes were supplied by him and used for the initial testing of the gold and PEDOT:PSS coatings.

8.1.1 Sample preparation

The procedure for each of the experiments was to use electrochemical impedance spectroscopy to assess the probes in their initial state which was followed by using a Keithley 2400 source meter to apply either a constant current or voltage. Another impedance test was then performed to judge the effect of the plating/coating. Therefore, the first consideration was interfacing the microfabricated probes with both the network analyser and the Keithley source meter. Both of these instruments are compatible with a simple 2.54 mm pin head connector, so two of these connectors were soldered to the end of small sections of copper board and the probes were then attached to the opposite end (Figure 8.1). For these tests two channel electrode probes were used, their design incorporates connection pads and holes to make them compatible with ball bonding, however, at the time of use there were no PCBs to connect them to. Therefore, they were secured and electrically connected to the copper board using a different method.

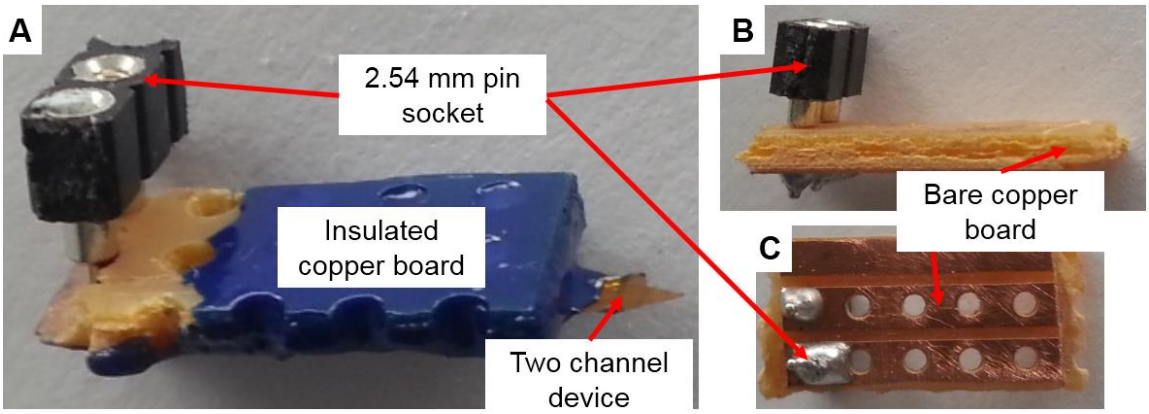

Figure 8.1 A) Two channel electrode secured to insulated section of copper board side view, B) bare copper board side view, C) bare copper board bottom view.

The surface of the board was cleaned then a small amount of nail varnish was applied to the surface of the board and then the probes were mechanically secured by placing them on to the nail varnish and leaving it to dry. The size of the probe was such that each connection pad was approximately in line with the tracks of the copper board. Each probe was then electrically connected to each track using conductive epoxy and insulated using nail varnish on the full length of the copper board. Each electrode on each probe could then be selected for impedance testing or plating by connecting to the associated pin head connector.

8.1.2 Gold plating

This section describes the gold plating method which was kept constant for all experiments unless otherwise stated. The gold plating solution was made by thoroughly mixing 13 µL of Chloroauric Acid (Sigma-Aldrich) with 10 mL of distilled water. This solution was then stored in a vial and could be reused for each experiment. For gold plating, the working electrode and a platinum counter electrode were submerged in the plating solution which was poured into a petri dish or similar. A Keithley 2400 source meter was then used to apply a constant voltage with the working electrode connected to the positive terminal and the counter electrode connected to the negative terminal. A +0.8 V voltage was then applied for 5 seconds to try and

remove any impurities from the working electrode followed by the application of a -1.6 V voltage for 30 seconds to actually plate the sample. The next electrode was then connected and the process was repeated until each electrode had been plated. These voltages were used as they were found to be effective in Richard Barrett's previous work and proved to also be effective in this work. The working electrode was then removed from the solution and washed gently using DI water and then dried, to remove any loose material and to prevent further reactions. The solution was then returned to the vial for storage and later reuse, or another sample was placed in the solution. This setup is shown in Figure 8.2 A during a later experiment with a 20-channel device connected to a PCB but the method was the same for the earlier experiments. The zebrafish devices could not be imaged and so Figure 8.2 B and C show the intended effects gold plating. A typical thickness of gold plating could not be obtained and is not available in the literature but from Figure 8.2 C an approximate value appears to be ~1 µm although this will vary depending on the amount of current applied and the duration it is applied for.

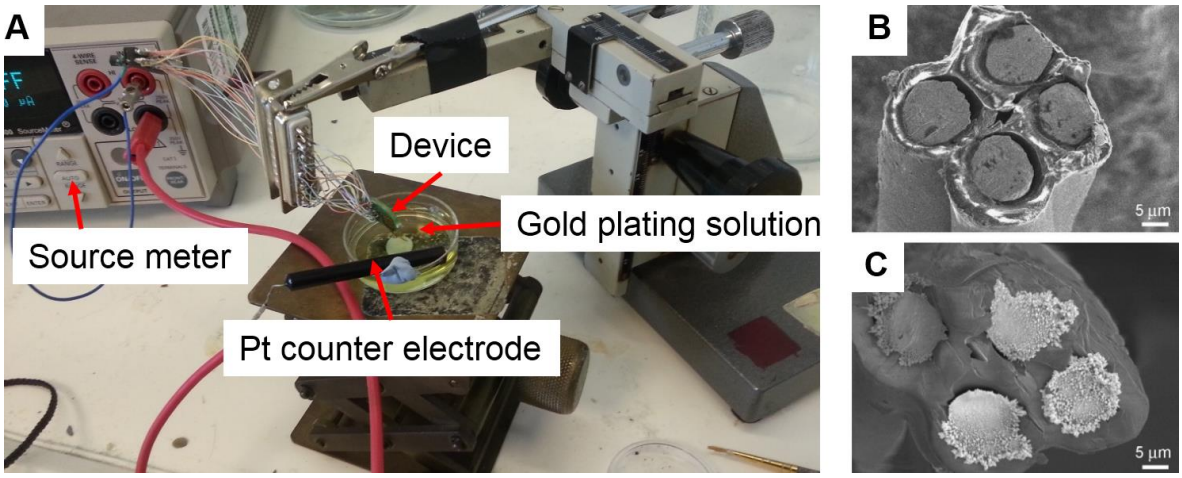

Figure 8.2 A) Gold plating of electrode setup (from a later experiment). B) SEM images of tetrode before gold plating, C) tetrode after gold plating from [114].

8.1.3 PEDOT:PSS coating

The method for PEDOT:PSS electrochemical polymerisation was similar to that used by Nyberg *et al* [116] who reported a large reduction in electrode impedance (~$10^8\,\Omega \rightarrow$ ~$10^5\,\Omega$ at

10 Hz) with good reliability. PEDOT:PSS (Clevios P, Heraeus) was used along with the EDOT (Sigma-Aldrich) monomer. The plating solution was prepared by mixing 10 mL of PEDOT:PSS with 10 µL of EDOT. The PEDOT:PSS solution contained 9.8 mL water. Both the working electrode (positive terminal) and the counter electrode (negative terminal) were then connected to the source meter and submerged in the PEDOT:PSS/EDOT solution as with the gold plating. A constant current was then applied to the working electrode for 2 minutes. The magnitude of the current used was varied as described in the next section but the time remained constant through all experiments unless otherwise stated. After this, the working electrode was removed from the solution and washed in DI water to remove loose material and then dried. The remaining solution could then be reused although its viscosity made it difficult to transfer between containers so it was stored in the same container in a fridge. The setup for this is shown in Figure 8.3 A. The high viscosity can be seen as the solution did not spread and fill the dish. SEM images of PEDOT:PSS coated electrodes are shown in Figure 8.3 B [113].

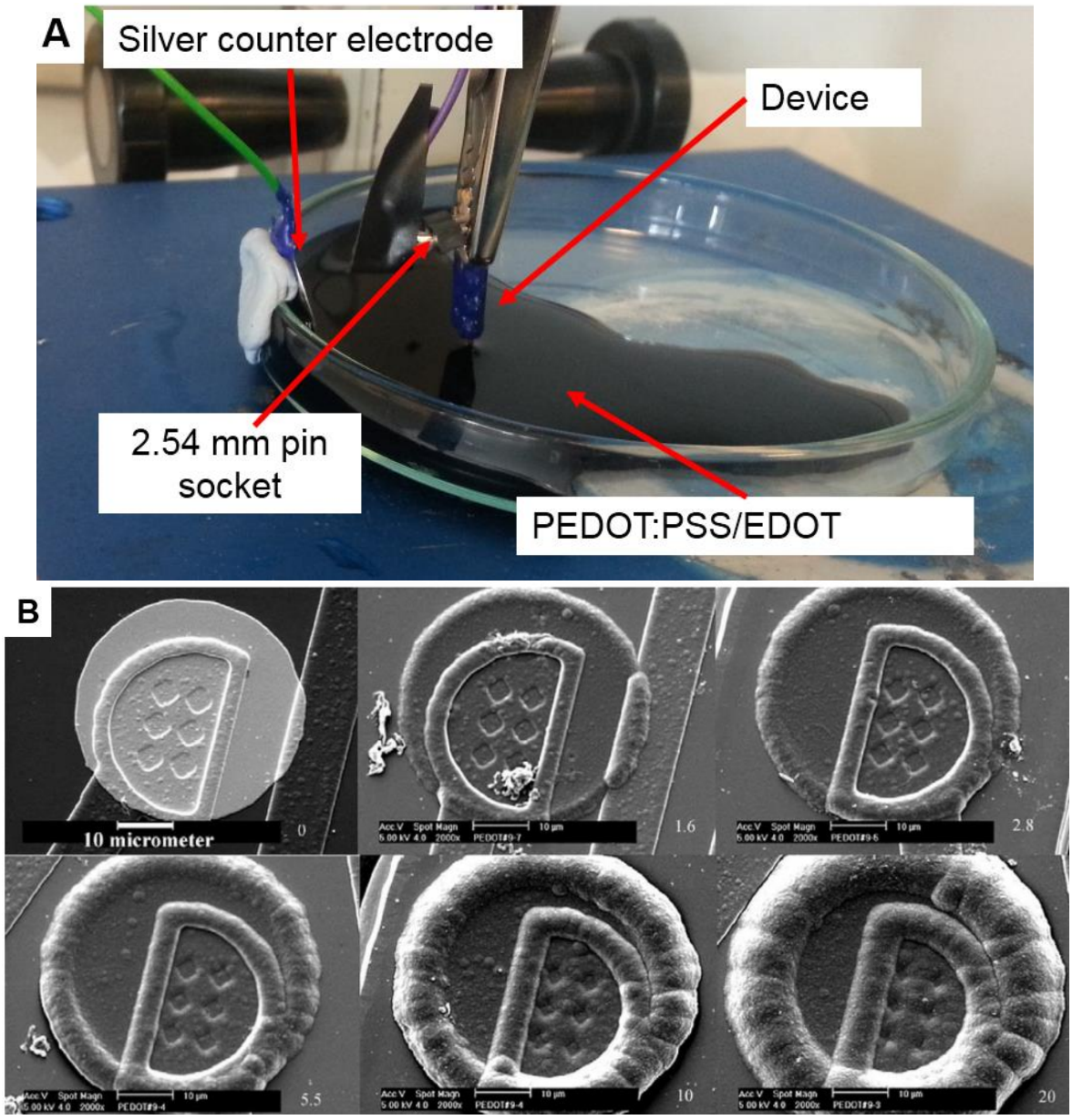

Figure 8.3 A) PEDOT:PSS coating setup. B) SEM images of galvanostatic growth of PEDOT:PSS on microelectrode sites, bottom right numbers indicate the charge on each site in µC. Same scale bar for each image (top left). From [113].

8.1.4 Overview of experiments

The samples tested consisted of probes with two circular electrodes per probe, each with a diameter of 15 µm as well as some with a diameter of 30 µm. As mentioned, an initial impedance test was conducted in a saline solution for each electrode prior to any coating, this was to determine if the electrodes were functioning and for later comparison after they had been

plated. The results from this showed that 8 out of 9 larger probes appeared to be functioning as expected.

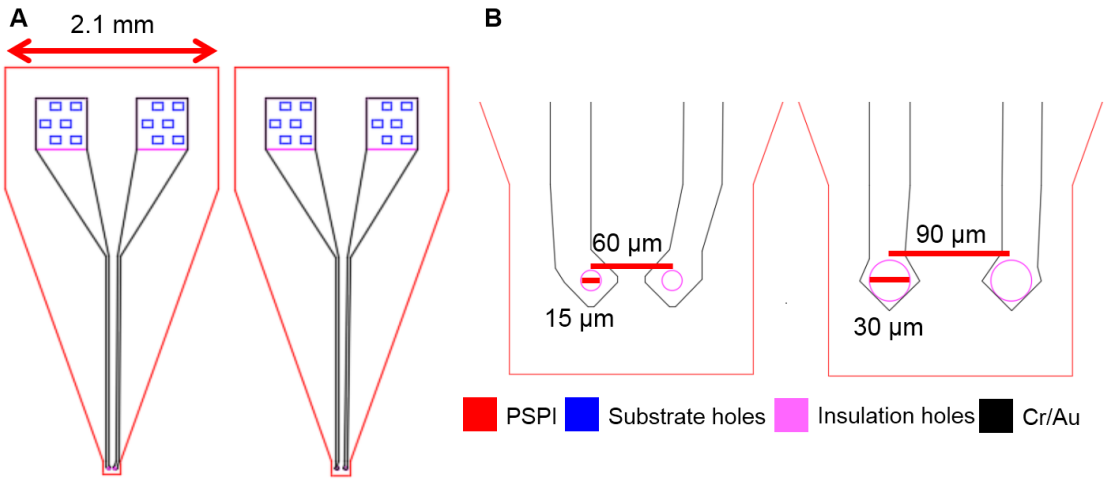

Figure 8.4 Two electrode probes with diameters of 15 µm and 30 µm.

It was thought that plating these larger electrodes (30 µm) would be more effective due to the possibility of more useable currents for the larger area, so these electrodes were used first. They were then split in the following way:

- 8 15-micron radius dual electrode probes (16 electrodes in total):
    - 2 Control devices (4 electrodes)
    - 1 gold plated + 5 nA PEDOT:PSS (2 electrodes)
    - 1 5 nA PEDOT:PSS (2 electrodes)
    - 1 gold plated + 50 nA PEDOT:PSS (2 electrodes)
    - 1 50 nA PEDOT:PSS (2 electrodes)
    - 1 gold plated + 500 nA PEDOT:PSS (2 electrodes)
    - 1 500 nA PEDOT:PSS (2 electrodes)

The experiments were performed in pairs with e.g. one device (both electrodes) being plated with gold followed by PEDOT:PSS and another device plated using only the PEDOT:PSS and so on. This was to confirm that as shown in previous work [156], the combination of gold and

PEDOT:PSS deposition results in lower impedances. Three pairs of devices were used to determine suitable current magnitudes for the PEDOT:PSS coating. To do this 5 nA, 50 nA and 500 nA were applied for 2 minutes to the samples listed previously. The actual applied currents were displayed by the source meter during deposition and were lower than the inputted values (~1 nA, ~47 nA, ~470 nA).

Impedance tests were performed on each sample after each stage in saline. The results of these tests showed that the gold plating was effective in reducing the impedance of all of the electrodes with the PEDOT:PSS only effective using the 1 nA current for both the gold plated and non-gold plated electrodes. The addition of the gold plating before the PEDOT:PSS did result in lower impedances than the PEDOT:PSS on its own as expected. Attempts were then made to use the 1 nA current on the devices that had already been plated with the higher current but this proved to have little effect on the impedance, which suggests the larger current either caused a blockage or damaged the electrodes.

As shown in the last chapter, smaller electrodes are preferable to larger electrodes so a similar coating test was then performed on one of the smaller 15 µm devices (for both electrodes). The electrodes were gold plated first as before, followed by the PEDOT:PSS coating with a 1 nA current for 2 minutes. This resulted in no reduction in impedance for either electrode. It was thought that this was due to the current magnitude/density being too high for the smaller electrode. 1 nA was the smallest current that the Keithley source meter could supply. Therefore, application of a constant voltage was tested instead, using 0.5V, then 1V, then 2V (for separate devices), with each voltage applied for 2 minutes. These tests all resulted in no reduction in electrode impedance when using the PEDOT:PSS. However, there was still a reduction due to the gold plating for each sample.

It was then thought that part of the problem could be due to the high viscosity (as seen in Figure 8.3) of the PEDOT:PSS/EDOT solution and that the number of reactants in the local area of the working electrode could become restricted during deposition. Therefore, to try and solve this problem two modified PEDOT:PSS/EDOT solutions were made. One with 10% (1 mL) of isopropyl alcohol (IPA, Sigma-Aldrich) added to the normal mixture of 10 mL PEDOT:PSS and 1 µL EDOT which is referred to as solution 2. And another with 1 mL IPA, 10 mL PEDOT:PSS and 10 µL of EDOT which is referred to as solution 3, where solution 1 is the normal mixture. More tests were then conducted with these new solutions on both sizes of electrodes.

A repeat of the previous tests with the 30 µm electrodes and solution 1 showed a similar reduction in impedance as before. The 30 µm electrodes were then tested with solution 2 and a reduction in impedance was again measured but only by the same amount as before, this was also true for solution 3. Solution 2 was then tested with the 15 µm electrodes and a reduction in impedance was measured, solution 3 was also tested which also resulted in a similar impedance reduction. This suggested that the introduction of the IPA increased the effectiveness of the solution for the 15 µm electrodes but had no added benefit for the 30 µm electrodes. The extra EDOT had no added effect. The key results are shown in the next section along with a comparison to the electrode-electrolyte interface model from chapter 4.

8.1.5 Results

The impedance and phase spectra measured after each stage of the processes using solution 1 (PEDOT:PSS/EDOT) with the 30 µm diameter electrodes is shown in Figure 8.5. The results from four electrodes are shown (2x 2 channel devices) along with results from the model described in chapter 4 with some fitting using the idealness (n) and surface area which was

scaled (Afac). The area was scaled as the plating methods reduce impedance by increasing surface area. The target is for the impedance (as described earlier) to be similar to micropipette electrode impedance which is ~1 MΩ at a target frequency for ECG measurements of 100 Hz.

The impedance spectra show that the impedance is reduced at each stage at the target frequency for each of the electrodes. There is some scattering on the initial impedance spectra at low frequencies which is likely due to the larger amount of noise associated with the higher impedance in this range, this can also be seen in the phase spectra. This is also suggested by the highest impedance electrode which has the highest amount of scattering. Each electrode has differing impedances which could be due to differences in electrode area or quality. The impedance reduces linearly with frequency but doesn't reach the solution resistance plateau which suggests the interface is dominated by the interfacial capacitance. This is reflected in the phase spectra where the phase angle does not fall towards 0°. The expected impedance from the model is much lower than that which was measured and appears to reach the solution resistance which is indicated by the phase which falls towards 0°. An approximate model fit can be produced by reducing the area by a factor of 0.1 and using n = 0.8. The need for the reduced area suggests that the quality of the electrodes was perhaps not high with contaminants possibly coating the electrode surface such as salt from the device release. The lowered idealness is due to the surface roughness. The corresponding phase appears to be a similar shape but with a larger resistive component (higher phase angle).

The gold plating was more effective for one device than the other (two electrodes each) but reduced the impedance similarly for the electrodes on the same device (the magnitude of the reduction is discussed next). The two lower impedance electrodes reduced to close to the target impedance with the other two slightly above. The two higher impedance electrodes

impedances reduce linearly and in combination with the phase it can be seen that the impedance is still dominated by the capacitance. The lower impedance electrodes start to plateau to the solution resistance at higher frequencies with the phase angle moving towards 0°. The model was fitted by increasing the area by 1.1 (from the initial fit) or by 11 from the initial model and by increasing idealness to 0.9 from 0.8. An increase in area is the expected effect of the gold plating and provides a suitable fit. The change in idealness that was required to fit the model could possibly be explained by the plating increasing the capacitance of the electrodes making it behave more like an ideal capacitor resulting in the change in the spectrum. The model phase spectrum shows a similar shape to the measured values with a capacitive plateau followed by an increase in the resistive component of the interface.

After the PEDOT:PSS coating there is again a range of impedances with a closer range for the linear region and a wider spread for the plateau. The impedance of all four electrodes was reduced significantly below the target impedance (more detail to follow). The linear region is much shorter for all the electrodes and plateaus just after 100 Hz, this is also seen in the phase spectra which suggests a large resistive component starts to dominate the capacitive component as the frequency is increased. The higher impedance gold plated electrodes reached the same impedance as the lower impedance electrodes when coated with PEDOT:PSS which suggests this is the limit to which the impedance can be reduced. As shown in the model example in chapter 4, larger electrodes reach the solution resistance more quickly. The model fit is quite poor for the plateau region as the plateau is reached much later in the model which is to be expected as the model is for a metal electrolyte interface. However, a reasonable fit can be made of the linear portion with an increase of area. The model phase spectrum is similarly shaped with the main difference being a delayed increase to 0°.

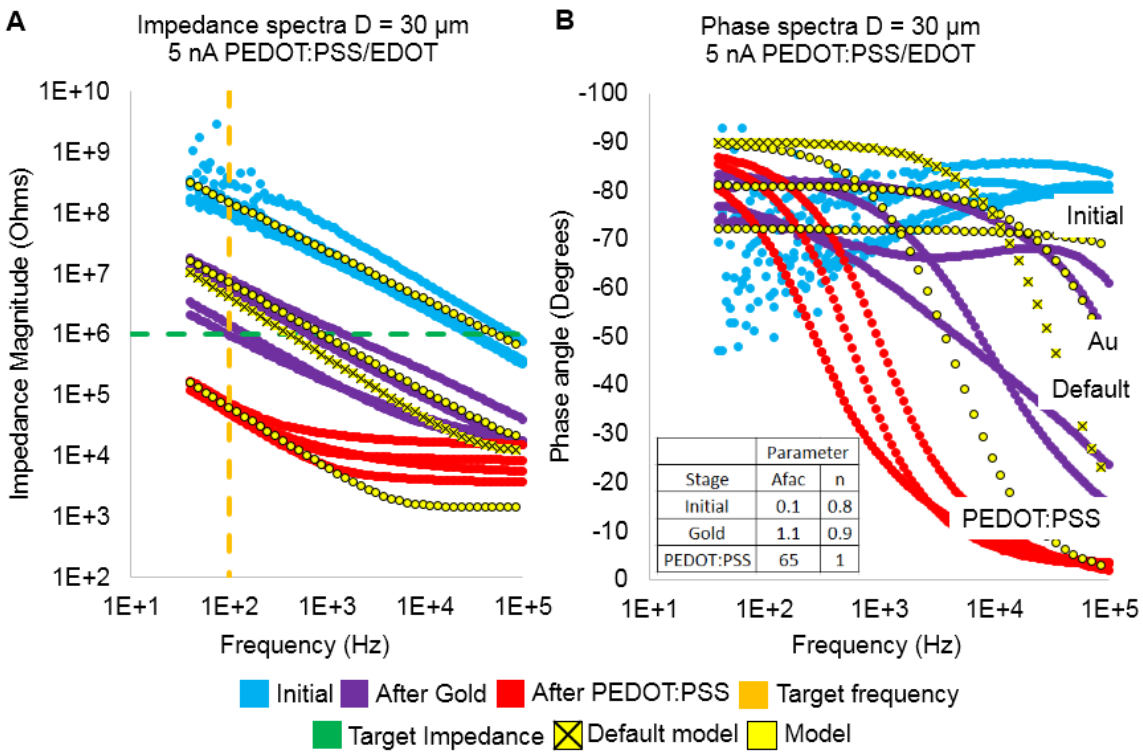

Figure 8.5 Impedance and phase spectras for plating/coating of 30 µm diameter (D) electrodes. A) Impedance magnitude for each stage of the process. Initial (before plating), after gold plating and after the PEDOT coating. The results from four probes are shown for each. The model (from chapter 4) results are fitted by changing the parameters shown in B along with the default model result for an electrode of this area. Target impedance is (1 MΩ) at the target frequency (100 Hz), B) phase spectra for the same results. Associated model results are labelled.

The impedance and phase at 100 Hz (target frequency) is shown in Figure 8.6 for each electrode and stage of the process. It can be seen that there is some variation in the initial impedance and the gold plated impedance. After the PEDOT:PSS coating it can be seen that the impedance of each electrode is reduced to similar values. The phase angle is similar throughout with the capacitive effects dominating at this frequency.

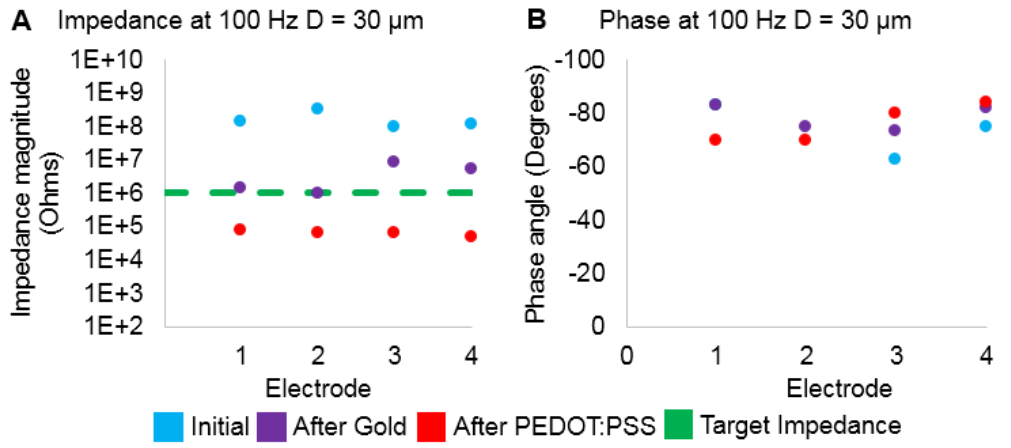

C

	Normal		Gold			PEDOT:PSS		
Electrode	Mag (MΩ)	Phase (°)	Mag (MΩ)	Decrease	Phase (°)	Mag (MΩ)	Decrease	Phase (°)
1	140	-83	1.43	98	-83	0.074	1884	-70
2	303	-104	0.97	313	-74	0.064	4709	-70
3	89	-62	7.95	11	-73	0.061	1467	-80
4	110	-74	5.29	21	-82	0.049	2266	-84

Figure 8.6 Impedance and phase angle at 100 Hz. A) Plot of impedance for each electrode at each stage, B) phase angle for each electrode at each stage, C) comparison table of impedance and phase angle at each stage for each electrode with the decrease (multiple) in impedance at each stage.

Similar plots for the impedance and phase spectra of the results from the initial test, gold plating and the 5 nA for 2 minutes with PEDOT:PSS/EDOT/IPA (solution 2) experiments are shown in Figure 8.7 for four electrodes across two devices. These were the only tests performed due to a limited number of devices, but additional tests were performed with the modified ring electrodes and details are given later in this chapter (section 8.3). Overall, the results are similar to the 30 µm electrodes with more similarity between electrodes. The impedance of these electrodes is similar to the 30 µm electrodes which is surprising as these electrodes would be expected to have a larger impedance due to their lower surface area. This could be due to the 30 µm electrodes being of poor quality as indicated by the model comparison. The impedance of the 15 µm electrodes is reduced by each plating/coating method, with the gold plating reduction close to the target impedance and the PEDOT:PSS coating significantly below it. One of the electrodes has an unusual impedance spectra and phase which could be caused by impurities/damage or a problem during measurement (movement of apparatus etc.).

For the modelled spectra, the default model for this electrode area is a much closer fit which suggests the electrodes were of better quality (than the 30 µm electrodes) initially and the fit was made by only reducing n. Then an increase in area (15x) was sufficient to fit the impedance spectra for the gold plating, with corresponding similar phase spectra. The fit is again poor for the PEDOT:PSS where the solution resistance is reached at a much lower frequency. But the linear portion can be fitted with an increase in area (x400) with n = 1.

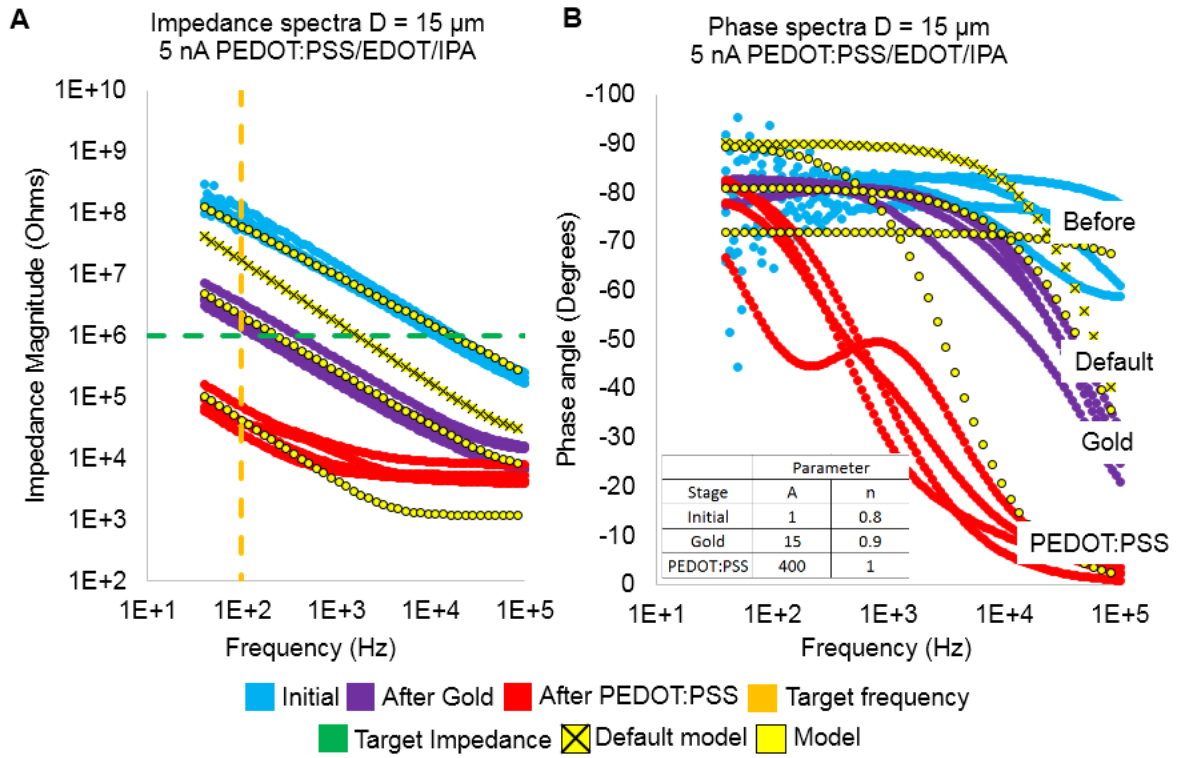

Figure 8.7 Impedance and phase spectras for plating/coating of 15 µm diameter (D) electrodes. A) Impedance magnitude for each stage of the process. Initial (before plating), after gold plating and after the PEDOT coating. The results from four probes are shown for each. The model (from chapter 4) results are fitted by changing parameters shown in B along with the default model result from an electrode of this area. Target impedance is (1 MΩ) at the target frequency (100 Hz), B) phase spectra for the same results. Associated model results are labelled.

A comparison of impedance and phase is shown in Figure 8.8. Similar reductions in impedance were achieved with the gold/PEDOT:PSS combination as for the larger electrodes in the 10^3 range. With all four electrodes below the target impedance and with the impedance being capacitive at this frequency.

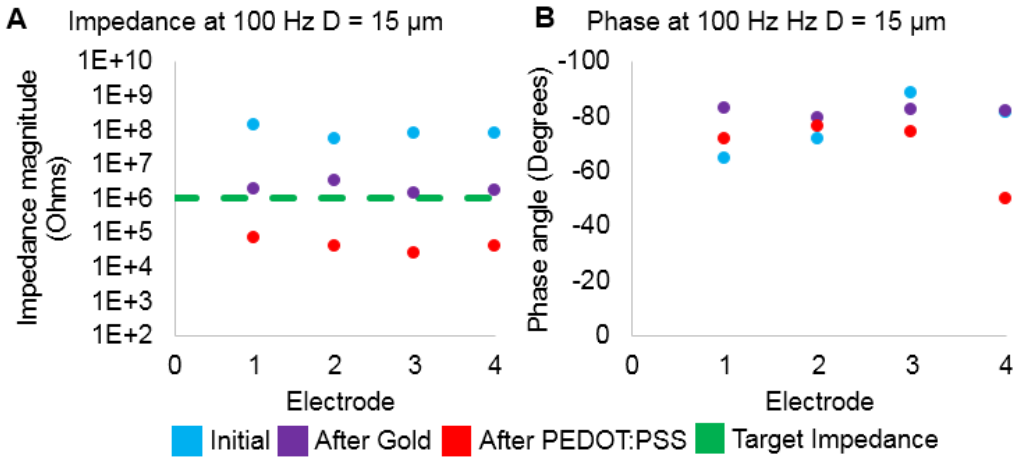

C

	Normal		Gold			PEDOT:PSS		
Electrode	Mag (MΩ)	Phase (°)	Mag (MΩ)	Decrease	Phase (°)	Mag (MΩ)	Decrease	Phase (°)
1	131	-65	1.75	75	-83	0.067	1956	-71
2	54	-72	3.24	17	-79	0.039	1412	-76
3	75	-88	1.30	57	-82	0.024	3068	-74
4	75	-81	1.62	46	-82	0.038	1976	-50

Figure 8.8 Impedance and phase angle at 100 Hz. A) Plot of impedance for each electrode at each stage, B) phase angle for each electrode at each stage, C) comparison table of impedance and phase angle at each stage for each electrode with the decrease (multiple) in impedance at each stage.

These results are consistent with those found in the literature. The PEDOT:PSS impedance and phase spectra are similar to those found in the literature where the low frequency is capacitive and the high frequency is resistive [157, 158]. The magnitude of the reduction (decrease in table) of the PEDOT:PSS coating (from initial bare gold) is also similar to that reported by Abidian *et al* [158] (~100 MΩ → ~0.1 MΩ ~x1000 reduction).

8.2 20 channel ring electrode device

The results of the PEDOT:PSS work in the previous section showed that it was possible to achieve low impedances for the small 15 µm electrodes. As described in a previous chapter, by using a similar method as described earlier, solution 2 was used to plate one of Richard Barrett's later 4 electrode probe designs and successfully measure the ECG of a 3 dpf zebrafish (chapter 4). This showed that microfabricated electrodes were capable of measuring the larval zebrafish

ECG. The probe design used was not suitable for a high throughput (HT) application due to the need for positioning. Therefore, the aim of this work was to try and use a differently designed electrode array that should be more suitable for a HT application, which was the 20-channel electrode array (Richard Barrett's design) or ring device. This was chosen as it was thought to be the most promising of the designs that had been previously tested and is shown in Figure 8.9.

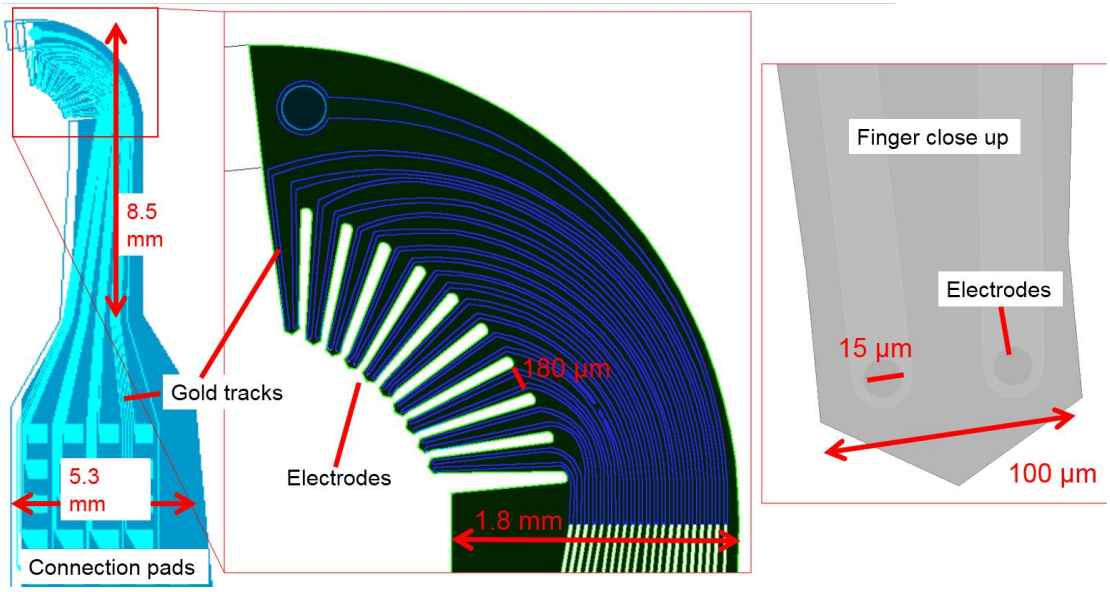

Figure 8.9 Ring electrode mask design. 10 fingers, two electrodes per finger. Each electrode is 15 µm in diameter.

The design is of a flattened cone which can be gently folded and rolled to form a cone shape that is designed to encase the larval zebrafish (Figure 8.10) with the electrodes positioned on the heart forming a ring around the zebrafish. These ring devices were carefully rolled using tweezers and fixed in place with nail varnish, it was difficult to roll ring devices to the same size each time due to the small size of the devices. Figure 8.10 A shows the fabricated design and it can be seen in (B) and (C) how this design transforms into a ring of electrodes when folded. It can also be seen that the design is able to encase the zebrafish and that the fingers can

be positioned in the approximate heart location. Various tests had been performed with this device (C) and it was the intention of this work to try and measure an ECG signal with it.

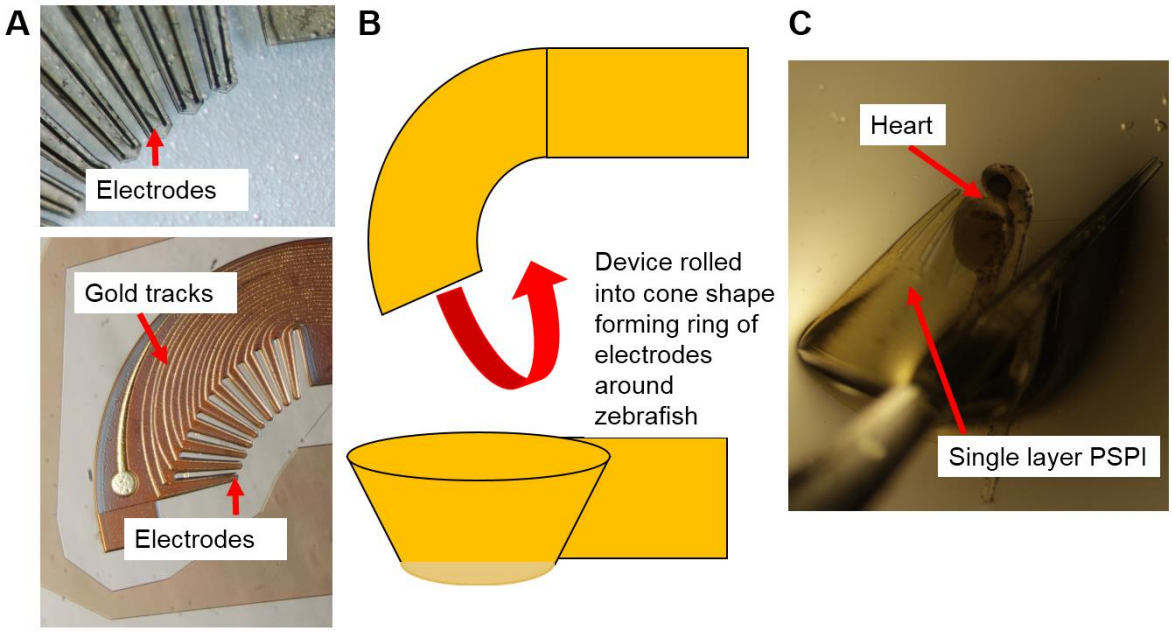

Figure 8.10 Ring electrode array design. A) Flat fabricated design on wafer, B) schematic of intentional use of ring, C) test of single PSPI layer with zebrafish. Photographs provided by Richard Barrett.

8.2.1 Fabrication

Previously, devices had been made with two PSPI layers of equal thickness. This meant that the devices were made as thin as possible in order to reduce the depth of the well or step down to the electrodes shown in Figure 8.11. This made them highly flexible which is not ideal for the probe style devices and also not ideal for the ring device as it was thought that the electrodes needed to make good contact and apply pressure to the zebrafish. Therefore, to have an electrode with a shallow well and stiffness, two thicknesses of the PSPI were used. A 10 µm layer (Durimide 7020) was used for the substrate with a 3 µm layer (Durimide 7505) used for the insulation. These thicknesses were chosen as the microfabrication process had worked well previously for these thicknesses and they were not at the extreme thickness ranges available, so there was room for adjustment later (max ~20 µm, min ~1 µm).

The reason for previously using PSPI layers of equal thickness was to ensure that the gold layer was located on the neutral plane. This was done to reduce the strain on the gold layer and prevent damage to it during use. A personal communication with James Churm revealed that he had performed tests with a similar PSPI based device to test if the gold layer would be more susceptible to damage when moved from the neutral plane. His results suggested that there was no negative effect associated with moving the gold layer from the neutral plane. A possible explanation to this could be that when a thin gold layer undergoes a breakage it is usually due to a localised strain within sub-sections of the layer that are caused by it not being completely homogeneous. A break or fracture in the layer can then occur when the localised strain concentrates stress at its source. It is then possible that the addition of a polymer substrate alleviates these concentrated areas of strain by supporting the gold and preventing fractures from forming [159]. Therefore, it was decided to use unequal thicknesses to maximise the electrode exposure. The successful impedance and artificial signal tests from later in this chapter show that moving the gold layer from the neutral plane did not affect the function of the devices.

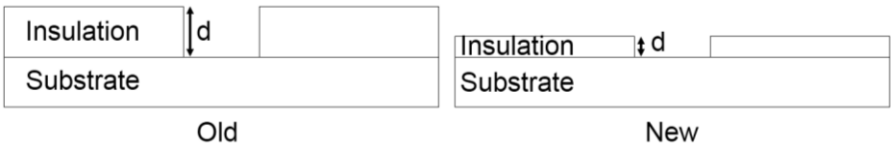

Figure 8.11 Well electrode design. The depth of the well (d) can be reduced by reducing the thickness of the insulation layer.

The method of fabrication was followed as given in chapter 4 with more details given in Appendix A5. The Polaron evaporator malfunctioned at this point so the Cressington system was used instead for the sacrificial layer. The fabrication processes worked as intended until the release of the devices. At this point the majority of devices failed to release with a few partial releases that were coated with a black precipitate which was thought to be Aluminium

Oxide (Al_2O_3). This was not a problem before previously and was thought to be related to the use of the different evaporator for the sacrificial layer. This caused a large reduction in the number of devices that could be fabricated and then tested. A few useable devices were eventually made and then tested on the zebrafish by adding a chrome layer on top of the aluminium during the sacrificial layer process. As described in chapter 3, a shutter was used with the chrome but not for the aluminium, when using the Cressington coating system. This release process was not repeatable for other samples but another workable solution was found which is described later.

Figure 8.12 Black precipitate on released devices, thought to be Al_2O_3. Test PSPI single layer.

The useable ring electrodes were rolled into the cone/ring shape and secured using a small amount of nail varnish with the electrodes on the inside of the ring. The ring was then ball bonded to the PCB connector. The electrodes were then plated using gold and coated with PEDOT using a nanoZ kit (NeuraLynx) rather than the method used before for ease of use. All the electrodes on the devices could be connected at once and plated in turn with the use of the nanoZ software. The impedance could also be measured so electrodes could be plated to a desired impedance which was 0.5 MΩ in the gold solution followed by a reduction to 0.1 MΩ with the solution 2 mixture described previously. After plating these electrodes were then ready to be used with the zebrafish.

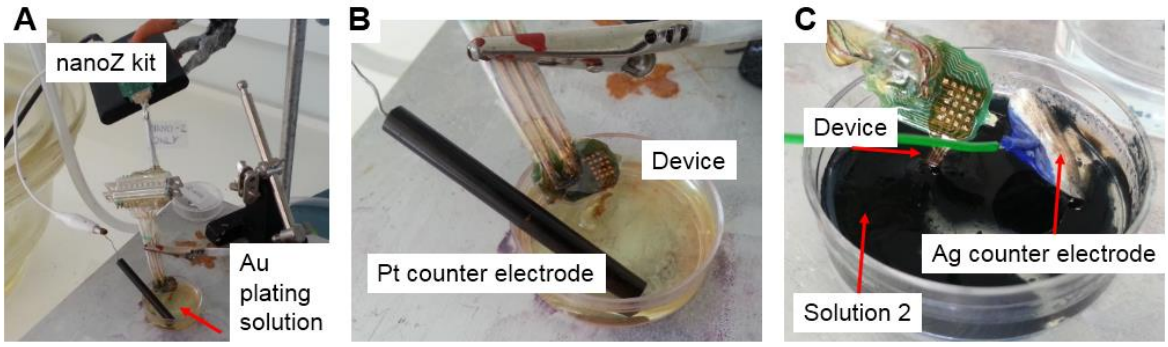

Figure 8.13 A) Plating setup using nanoZ kit, B) gold plating, C) solution 2 PEDOT:PSS coating.

Using the ring device on its own once again required significant positioning of the zebrafish but it was thought that a solution could be found to this problem after confirming the function of the device. A few positioning setups were trialled, but the one found to work the best was to tape the PCB/connector combination to the bottom of a petri dish lid and then fill the lid with agarose, being careful not to cover the electrodes. A groove was then created to allow the fish to be positioned into the ring (Figure 8.14). The zebrafish could then be manoeuvred by gently picking them up with micropipette suction and releasing them into the device. Additionally, the zebrafish were PTU treated to remove their pigment to improve visibility for electrode positioning. These experiments were performed in conjunction with Sundeep Dhillon who handled the zebrafish.

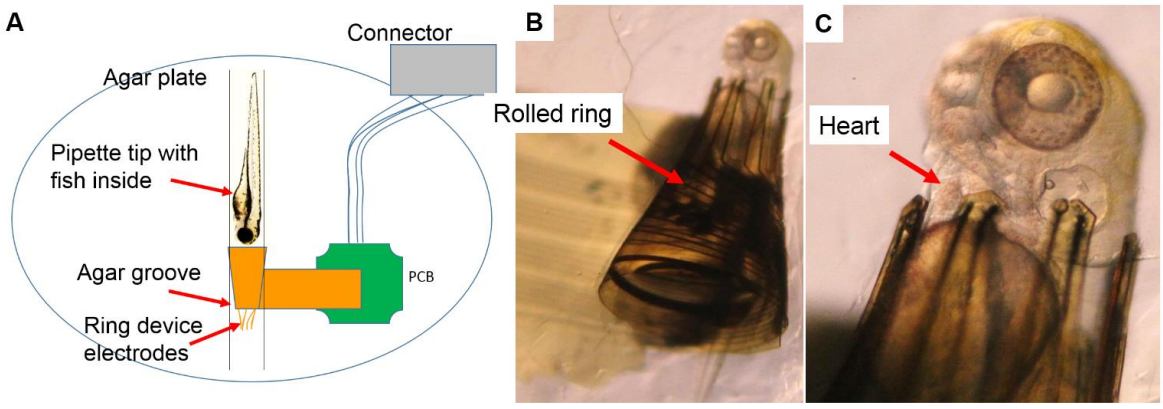

Figure 8.14 A) Schematic of zebrafish positioning, B) 3dpf zebrafish in ring, C) close up.

Unfortunately, no ECG signal was measured for a number of positions and zebrafish using the Intan recording system. Even though an artificial signal could be measured that was created in the solution using a twisted pair of wires and a sine wave current source. This was thought to be due to lack of electrode contact, as can be seen from Figure 8.14, it was difficult to see if contact was being made between the electrodes and the heart. In addition, not all electrodes were functioning on the tested devices, but the zebrafish was rotated to account for this. It was thought that even if contact was made, the drop down to the well style electrode may also prevent actual contact. It was expected that the plating/coating had filled some of the hole but it was impossible to see if this was complete based on standard microscope images. The location of the electrode is also ~18 µm from the edge of the finger which could also make contact more difficult. Therefore, it was decided that the electrodes should be redesigned to be similar to those from the 4-channel device (chapter 4) that was capable of measuring a signal.

8.3 Redesigned electrodes

The redesign involved changing each of the masks with the basic footprint of the ring device largely unchanged, the resulting masks are shown in Appendix A3. The connection pads remained the same to be compatible with the PCBs, as did the rest of the device up to the neck of the ring (Figure 8.15). Slots were added above the electrodes for interfacing with an additional positioning device and to ensure the rolled ring size could be reproduced for each ring. However, this wasn't used, as the goal was to ensure a signal could be measured before developing the positioning further.

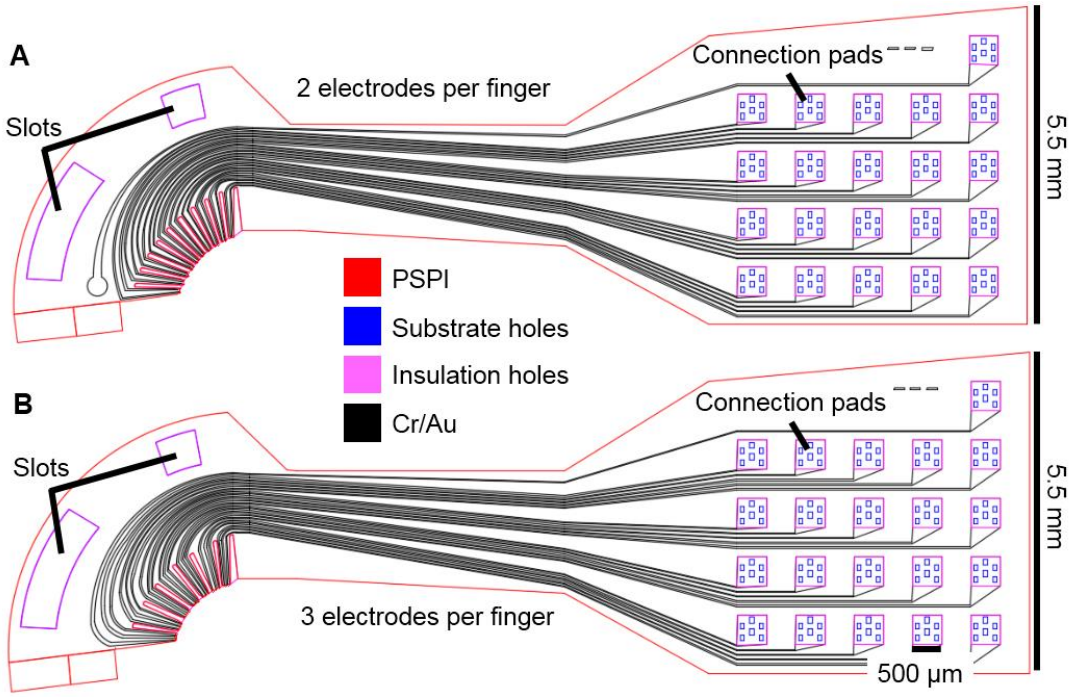

Figure 8.15 A) Mask design of modified ring device with 2 electrodes per finger and B) 3 electrodes per finger rings.

The other main difference is that the electrodes (as mentioned) were modified to replicate those of the 4-channel device (chapter 4) as shown in Figure 8.16. From the tests with the previous ring devices (Figure 8.14) it also became apparent that there was room to add a third electrode to each finger in order to increase the electrode density for three electrodes (Figure 8.16 B) as well as to apply more pressure to the zebrafish with the larger finger. This resulted in three electrodes that are separated by ~123 µm (centre to centre) rather than 193 µm for the two electrodes per finger (EPF) electrodes. There are seven fingers giving a total of 21 electrodes but only 20 were usually connected due to the connectors used. This has the disadvantage of a larger gap to the fourth electrode than the two EPF design. Both designs were included in case there were problems with the fingers spreading to allow the zebrafish through or other unforeseen problems. More electrodes per finger could have been added but this would have restricted their movement.

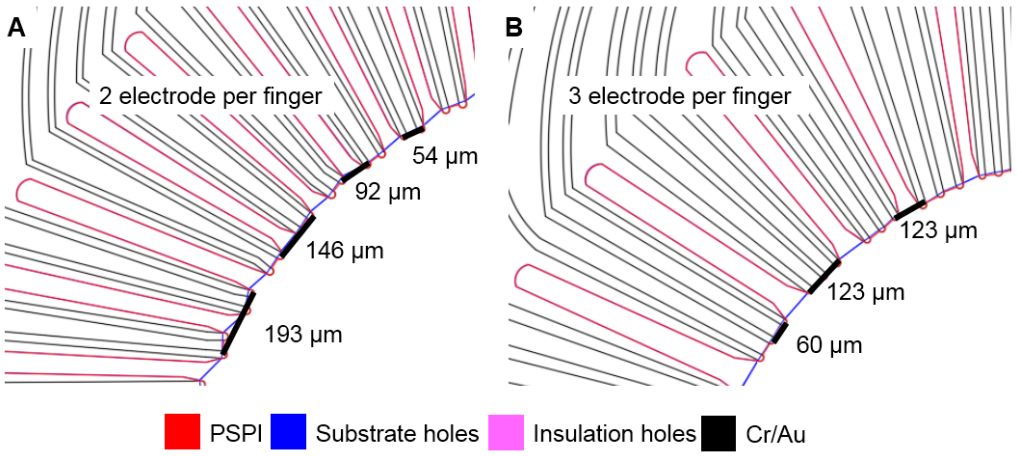

Figure 8.16 A) 2 electrodes per finger showing electrode spacing, B) 3 electrodes per finger.

The size and shape of the electrodes themselves were also considered, two sizes were chosen for the final designs (Figure 8.17). The aim was to maximise the distance that the electrodes pertruded from the insulation layer (x) to try and improve the chance of contact with the zebrafish. This is shown by the approximate curvature of the zebrafish body against the size of the electrodes. The selected electrodes sizes were chosen to minimise the effects of spatial filtering while still being viable for fabrication. Two electrode areas were chosen, 180.2 μm^2 (similar to the 15 µm diameter electrodes) and larger electrodes of 278.9 μm^2. The larger electrodes have a larger x value to increase the chance of contact with the zebrafish and their larger area means they were also more likely to survive fabrication.

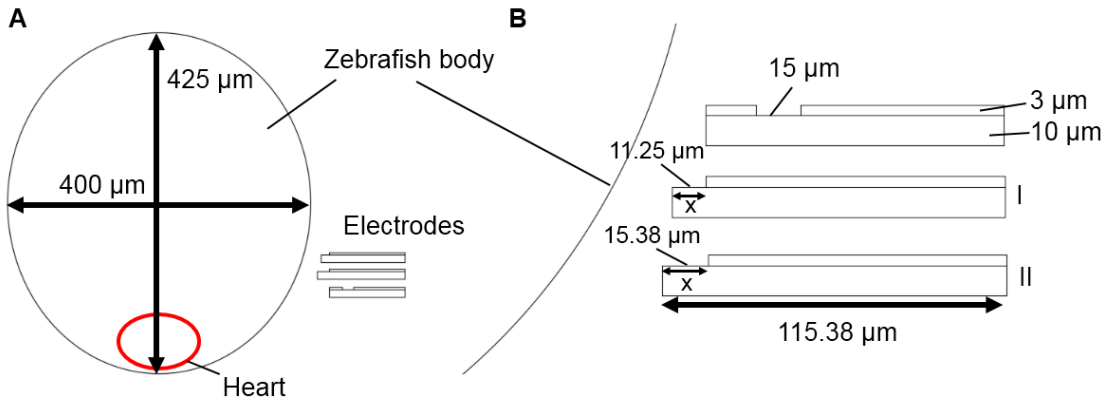

Figure 8.17 A) Zebrafish body size from chapter 5 compared to the electrodes, B) electrode well design and the two sizes of modified edge electrodes.

The electrodes of the 4 channel devices did not always survive the fabrication process due to the small width of the gold tracks leading to them. Therefore, the gold tracks in the new designs were made a minimum of 20 µm wide along the entire length of each track up to the start of the electrodes (Figure 8.18). Maximising x and keeping the shape compact for spatial resolution resulted in a cut ellipse shape for the electrodes. The completed designs were spread throughout the photomasks, the footprint of each device meant that 34 devices could be fitted onto the masks with slightly less able to be fabricated due to the shape of the wafer.

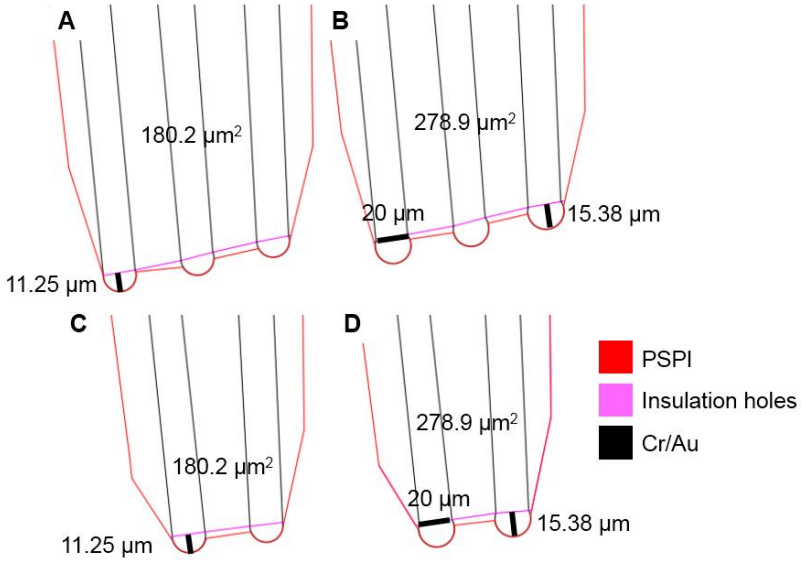

Figure 8.18 A) 180 µm² 3 EPF, B) 278.9 µm² 3 EPF, C) 180.2 µm² 2 EPF, D) 278.9 µm² 2 EPF.

8.3.1 Fabrication

Fabrication of these devices followed the same process as before with a 10 µm substrate layer and a 3 µm insulation layer. The problems with the device release also persisted up to this point. Various tests were performed based on similar process described in the literature [107, 108] by varying the thicknesses of both the aluminium and chrome layers. A workable solution was found which was effective enough to release some devices for further tests. The sacrificial layer was formed by using a 100 nm chrome layer (sputtered) followed by a 125 nm aluminium layer (evaporated) and then finally a third layer of 25 nm of chrome (sputtered). Again, as described in chapter 3, a shutter was used for the chrome but not for the aluminium, when using the Cressington coating system. To release the samples; the wafer was connected to the Keithley 2400 source used in the plating experiments and a 0.5 V potential was applied between the sample wafer and a gold electrode in 2M NaCl (Figure 8.19). This process then took 1 day → 1 week to remove the aluminium which resulted in released devices that floated in the solution. The maximum distance that the undercut etch had to achieve was at the connection pad end of the devices and measures 5.5 mm (width of the device). The released devices were then placed in chrome etchant to remove any chrome from the back of the devices.

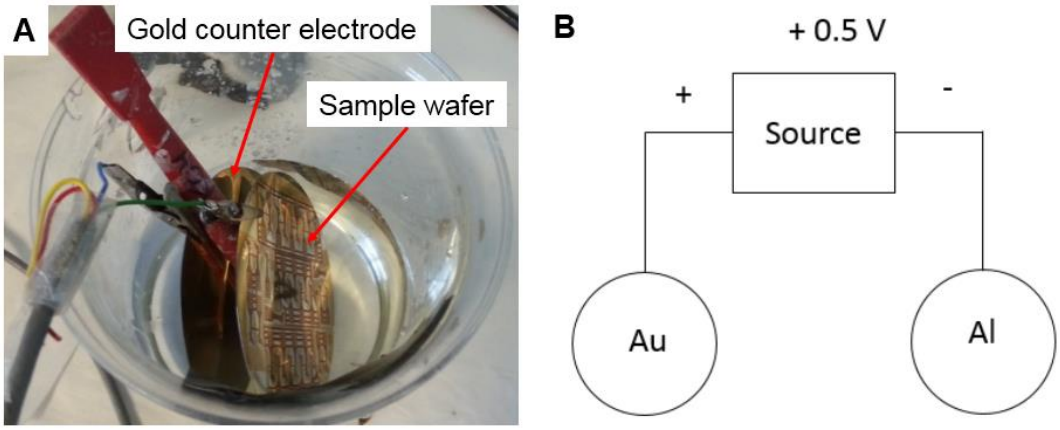

Figure 8.19 A) Release of samples from wafer, B) release circuit.

The rest of the fabrication process was successful with reasonable alignment between layers and successful substrate, metallisation and insulation. Some images from the process are shown in Figure 8.20. The released devices had a tendency to curl, so to acquire images they were secured flat to a microscope slide with some clear nail varnish (which can be seen in the background). Some precipitate can be seen that blocks some of the holes in the connection pads (Figure 8.20 F left and right) but this could usually be bonded through after multiple attempts. (H) shows the connector used to interface the microfabricated devices with external electronics.

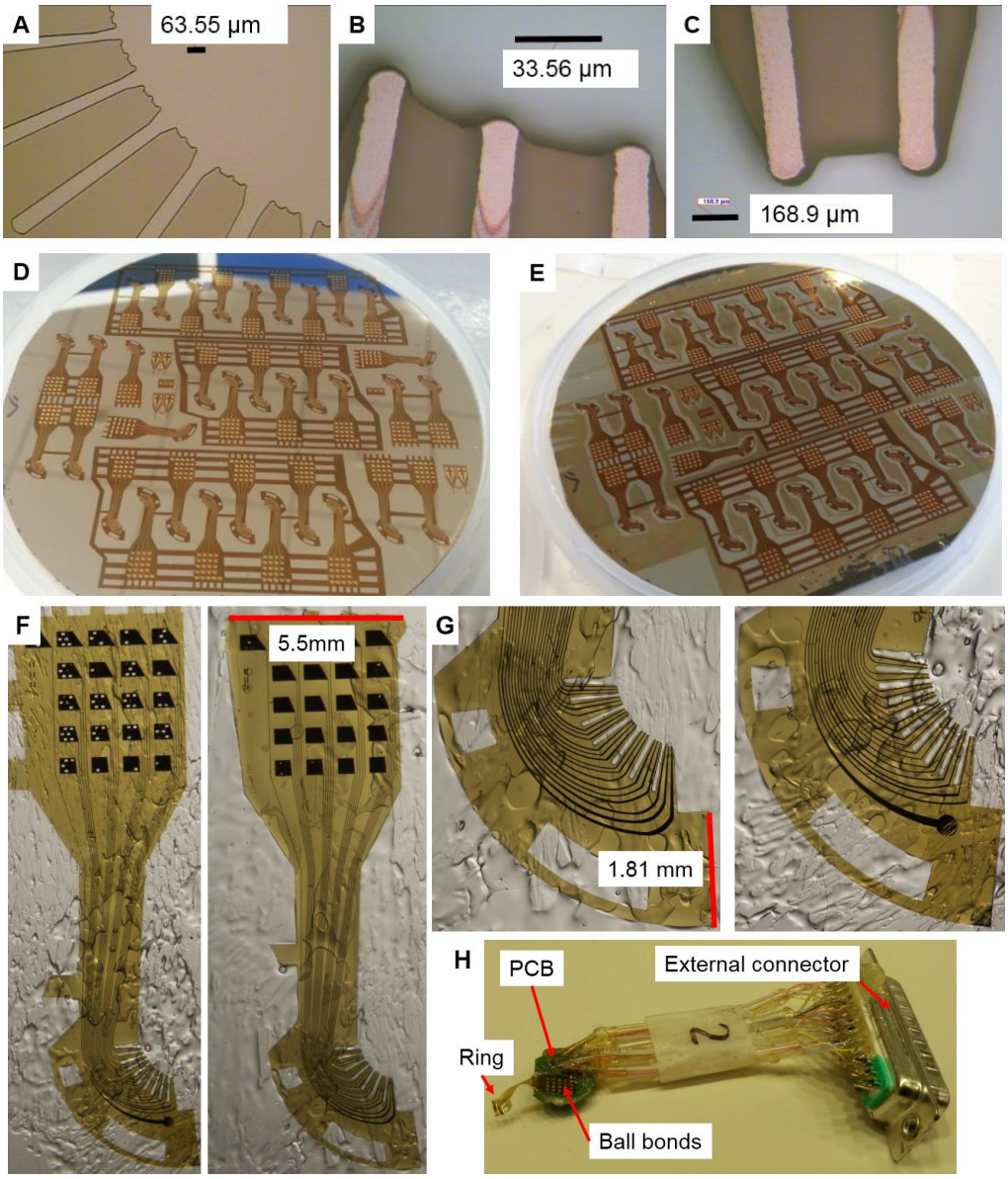

Figure 8.20 A) Substrate layer 3 EPF, B) electrode sites 3 EPF, C) electrode sites 2 EPF, D) whole wafer post plasma/UVO clean before insuation layer, E) after insulation layer before baking, F) whole released 3 EPF device (left) and 2 EPF device (right), G) close up on 3 EPF (left) and 2 EPF (right), H) device ball bonded to PCB with soldered wires to external connector.

8.3.2 Retesting impedance reduction methods

Coating experiments were performed on one device from the new designs before testing them on the zebrafish to confirm the previous results and assess the effectiveness of the methods with the new designs. These tests were performed in the same way as the previous experiments using the Keithley source meter rather than the nanoZ with impedance tests performed before and

after each stage. A 2.54 mm pin adapter was made for the PCB/plug combination to interface the device with the Keithley source meter and the network analyser. The setup for each step is shown in Figure 8.21.

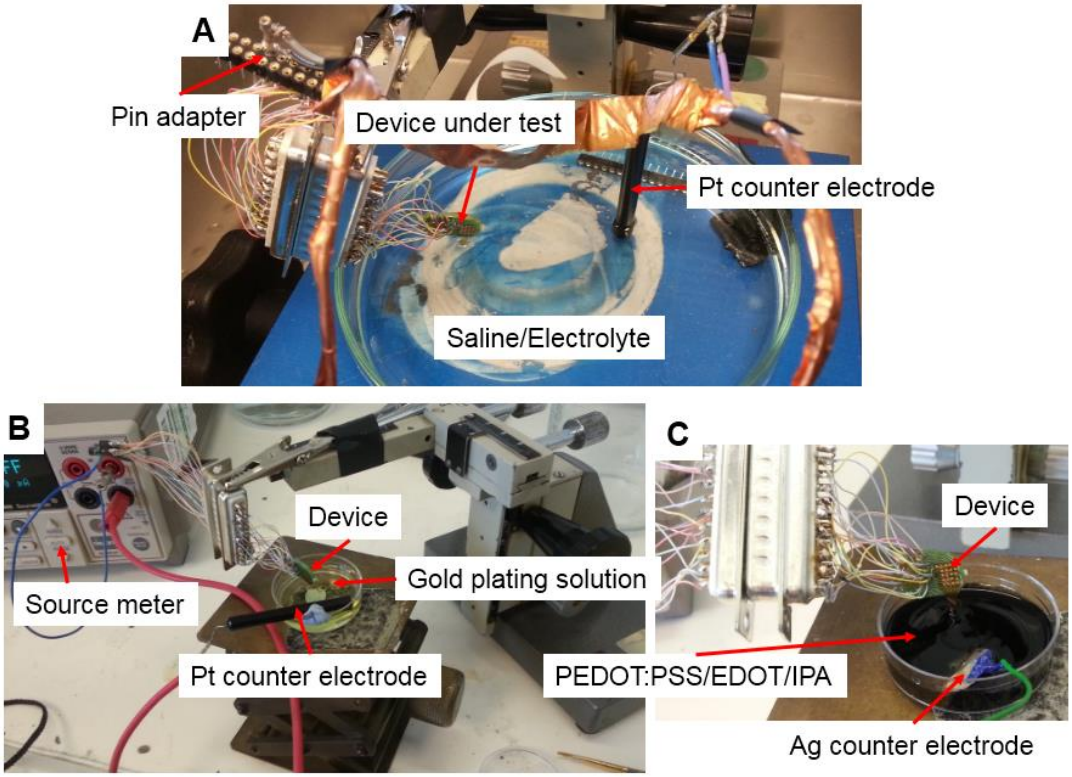

Figure 8.21 A) Impedance test, B) gold plating, C) PEDOT:PSS coating.

A three EPF unrolled ring device with the smaller electrodes (180.2 μm^2) was ball bonded to a PCB with a 24-pin plug. Firstly, the entire device (all 20 electrodes) was impedance tested to determine the function of each electrode. Then, out of those that were functioning, 9 electrodes were selected to be used in the test. They were all gold plated in the same way as previously described and then impedance tested again. The PEDOT:PSS coating was performed using solution 2 as before. Three different currents were used (5 nA, 10 nA, 20 nA) which resulted in actual applied currents of 1 nA, 6 nA and 16 nA. These currents were applied to three electrodes each spread over a total of nine electrodes as shown in Figure 8.22. Each current was applied for two minutes as before and then the impedance of each electrode was measured again.

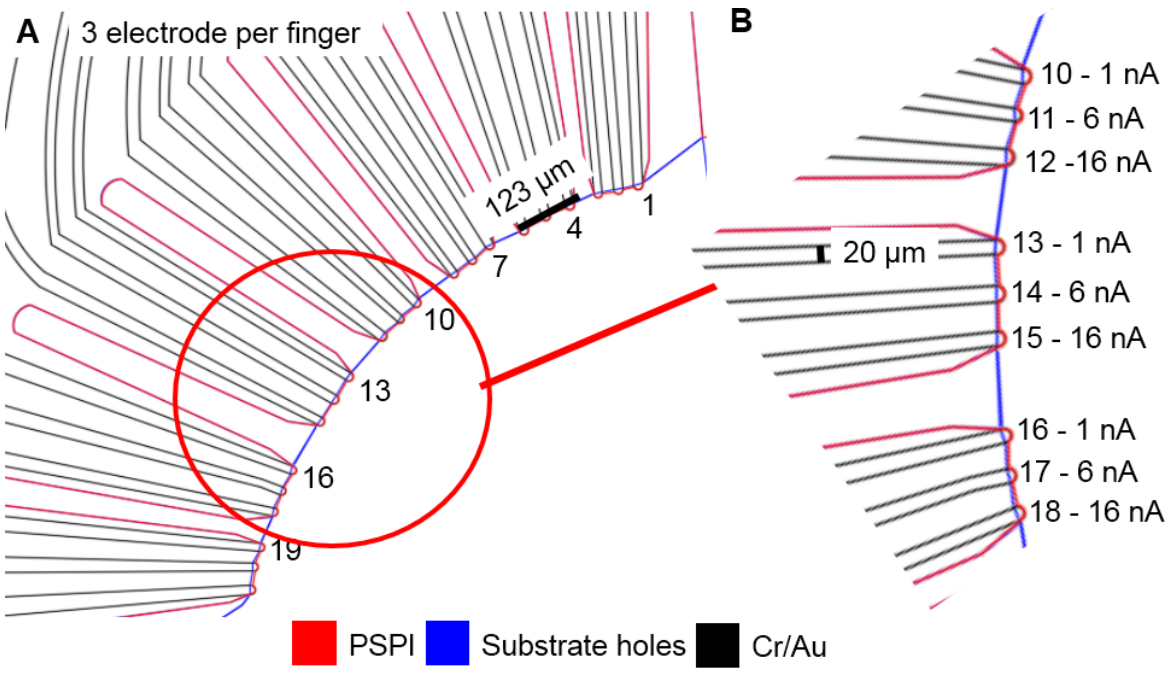

Figure 8.22 A) 3 EPF showing electrode numbers, B) expanded view of electrodes that were coated using solution 2 with the different currents for 2 minutes each.

The impedance and phase spectra for the 1 nA current electrodes are shown in Figure 8.23. The initial impedance is much lower than for the previous electrodes even though they have almost the same area as the 15 µm^2 diameter circular electrodes used in the previous tests. These impedances are also lower than the model values which were higher than the previous electrodes measured impedance. This could be due to the electrode area being higher than intended due to slight misalignment between layers or over development. Or it could be due to some unexpected reduction in impedance due to the different design, or some aspect of the microfabrication process such as reactions with the gold counter electrode during release. The previous electrodes could have also been worse in quality making these electrodes appear comparatively better. This means that there is comparatively less overall reduction in impedance but the impedance is still reduced below 1 MΩ at 100 Hz (target impedance and frequency). This was achieved by the gold plating only. The 1 nA proved to be ineffective at reducing the impedance any further than the gold plating with it actually increasing impedance.

This suggests that the electrodes were not successfully coated with PEDOT:PSS. The general behaviour of the electrodes is similar to that previously described with capacitive effects dominating at low frequency with impedance the falling to the solution resistance at higher frequencies after plating/coating.

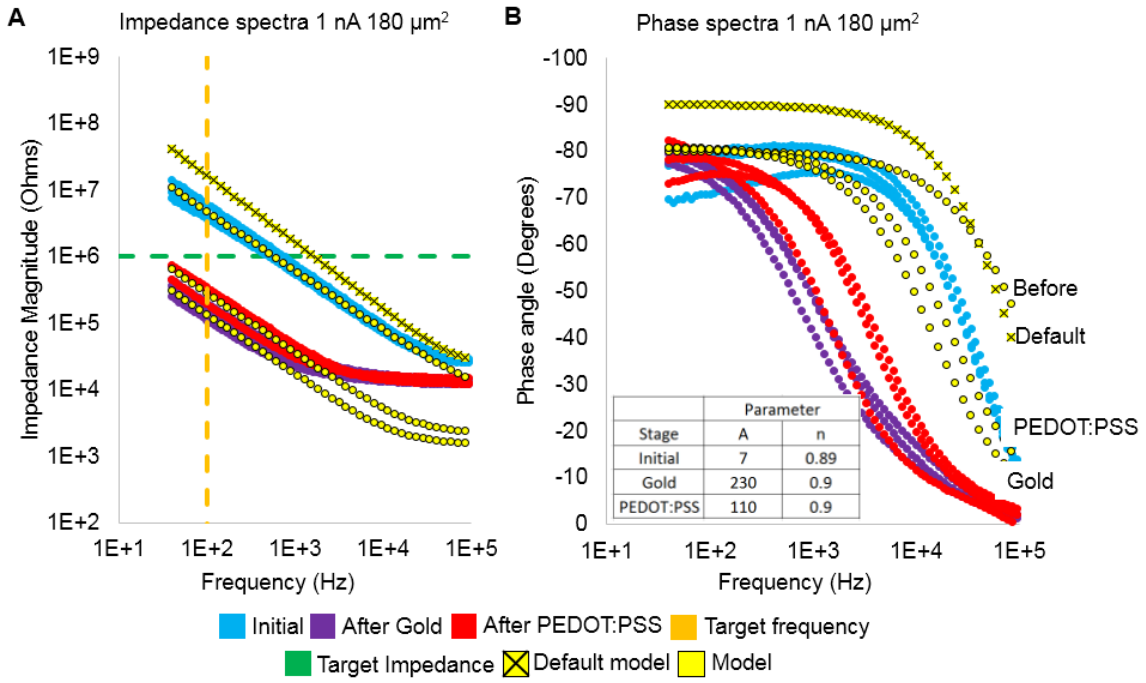

Figure 8.23 Impedance and phase spectras for plating/coating of 180 µm² electrodes. A) Impedance magnitude for each stage of the process. Initial (before plating), after gold plating and after the PEDOT:PSS coating. The results from three electrodes are shown for each. The model (from chapter 4) results are fitted by changing the parameters shown in B along with the default model result from an electrode of this area. Target impedance is (1 MΩ) at the target frequency (100 Hz), B) phase spectra for the same results. Associated model results are labelled.

The results of 6 nA and 16 nA currents are summarised in Figure 8.24 along with those from the 1 nA experiments with the impedance at 100 Hz given at each stage for each electrode along with the decrease compared to the initial impedance. The impedance and phase spectra for these results are given in Appendix A4 as they are largely similar to those already described. Figure 8.24 shows that although the 1 nA current did not lead to a reduction in impedance, the 6 nA and 16 nA currents did reduce the impedance of each electrode. A higher current requirement suggests that the electrode geometry being open ended at one side could be the cause, as

otherwise they are essentially the same as the electrodes used previously. The amount of reduction in impedance isn't as great but as mentioned the initial impedance was also lower. This suggests a limit as to how far the impedance can be reduced which is logical to assume as the surface area can only be increased by a certain amount. The 16 nA current appears to be the most effective but there is some variation between electrodes. All 6 six electrodes and the 3 that were tested with the 1 nA current are significantly below 1 MΩ. This is an excellent result as the aim was to reduce electrode impedance as much as possible. These impedances are within the same range as the previous results which confirms the impedance reduction methods were effective with the redesigned electrodes.

		Normal	Gold		PEDOT:PSS	
	Electrode	Mag (MΩ)	Mag (MΩ)	Decrease	Mag (MΩ)	Decrease
1 nA	1	6.18	0.20	31	0.147	42
	2	3.66	0.11	33	0.263	14
	3	4.24	0.16	27	0.241	18
6 nA	1	1.62	0.13	12	0.079	20
	2	6.44	0.21	31	0.065	98
	3	9.67	0.28	35	0.050	195
16 nA	1	4.14	0.15	27	0.027	156
	2	2.06	0.07	28	0.034	61
	3	8.25	0.19	43	0.028	298

Figure 8.24 Summary of plating/coating experiments. Impedance at 100 Hz is given for each electrode at each stage for each current used and for each electrode used. The reduction in impedance (factor) is also given in comparison to the initial impedance for each electrode after each stage.

8.3.3 Zebrafish measurement tests

After the plating/coating was confirmed to work with these new electrodes, they were again tested with the zebrafish with the help of Rhiannon Hurst who handled the zebrafish. Only a limited number of devices were able to be tested due to the release problems and the fragility of the electrodes. Figure 8.25 shows an example of these tests with different 3 dpf zebrafish in a variety of positions. 3 dpf zebrafish were positioned within the ring device using micropipette

suction as before but agarose was not used. The device connector was simply taped securely at the wires to the bottom of a petri dish and then the dish was filled with E3. Both 2 EPF (Figure 8.25) and 3 EPF ring devices were tested. It can be seen that the ring needed to be rolled much smaller than the designed size to fit the zebrafish which meant that only 10-12 electrodes were part of the ring and close to the heart. The extra slots on top of the ring helped to guide the zebrafish into the ring using a micropipette. Again, no ECG signal was measured using the Intan recording system for either style of electrode or zebrafish position.

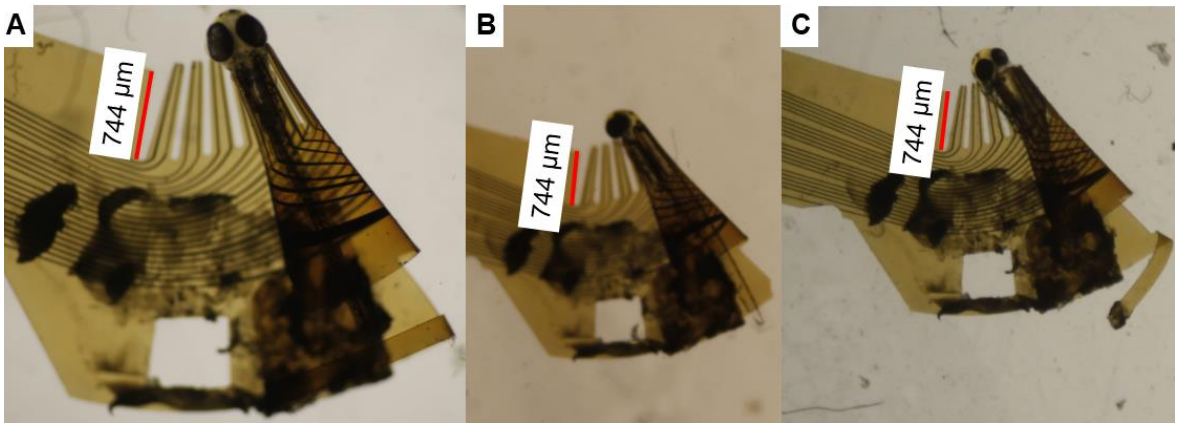

Figure 8.25 2 EPF 180.2 µm^2 electrode area ring device test with 3 dpf zebrafish showing multiple zebrafish positions.

The reason for no signal being measured could have again been due to the lack of contact between the zebrafish and the electrodes. It was difficult to judge whether there was contact or not as before. The lack of contact is partially due to the different thicknesses of PSPI used which results in a small outward (away from the zebrafish) curve to the fingers of the ring device which was most prominent at the electrode ends. These different thicknesses were chosen, as described before, to provide the required stiffness while still providing access to the electrodes. The stiffness of the devices fingers seemed to be sufficient to supply pressure, they perhaps even too rigid. The yolk sack of the zebrafish shown in Figure 8.25 appeared to be compressed upon entering the ring. The heart did seem to be beating for each zebrafish used after removal

from the device, but entry into the devices could have injured the zebrafish which would make it more difficult to measure a signal. The thicknesses could be made equal as before to prevent the bending of the fingers but then the device would likely not be rigid enough if two thin layers were used. The insulation thickness could also be changed on its own down to ~1 µm which could expose the electrodes more and make contact more likely.

A possible explanation for the outward bending of the device fingers and the curling up of the devices (after release) could be the different stresses associated with the thickness of the substrate and insulation layers. Measurements of stress in polyimide from the literature indicate that stress increases with thickness (fully cured polyimide) from 5 to 45 MPa for 8 to 120 µm layers [160]. This mismatched stress could therefore be the cause of the bending/curling of the devices.

The angle of the fingers of the ring device are also quite close to parallel against the zebrafish. Ideally, the fingers would be closer to a right angle with the zebrafish. There was not much room for changing this angle during the rolling/folding process with the design as it is as the devices were difficult to roll in any size because of their small dimensions. It could also be likely that firm contact with some pressure is required. As mentioned in chapter 4 the successful measurement with the 4-channel device required significant pressure to be applied to the zebrafish. Even when using a micropipette electrode, the electrode needs to be positioned on the zebrafish so that it can be seen to be applying pressure in order for a signal to be measured. It could also be the case that although the electrodes have low impedances, impedance spectroscopy may not have been sufficient to characterise whether or not the electrodes were capable of measuring the signal.

8.3.4 Artificial signal

As a biological signal could not be measured an artificial signal was used to show that the electrodes were functioning and able to measure a signal that differed between electrodes. The original plan was to use a current source consisting of a twisted pair of wires connected to a signal generator, this was not used as it was difficult to position within the ring device as well as determine the position of it relative to each electrode. Alternatively, one of the electrodes of the device was used as the source which allowed the distance to be approximately determined from photographs of the device.

The experimental setup is shown in Figure 8.26. A National Instruments (NI) BNC-2120 with a NI data acquisition card (DAQ) was used to generate and measure the signals. This was operated using a custom LabView (National Instruments) program. The signal was supplied to the electrode using a coax cable from the analogue output of the BNC-2120 which was split with the ground being placed in the solution and the positive side connected via the pin adapter to one of the electrodes on the ring device. Signals were then measured by connecting a second coax cable to the analogue input of the BNC-2120 with the ground connected to the source ground and the positive side to one of the other ring electrodes. A sine wave voltage was then applied to the source electrode with a frequency of 600 Hz (to be above 50 Hz electrical noise) and an amplitude of 100 mV. The signal from each of the other electrodes was then measured. The source electrode was then switched to different electrodes and the signal from each of the other electrodes was again measured. The measured waveforms were recorded and saved to files for analysis.

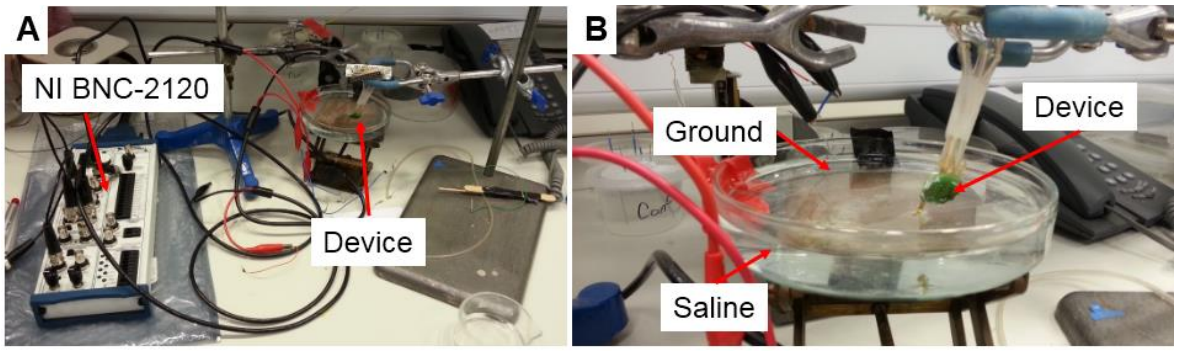

Figure 8.26 A) Wide view of experimental setup, B) expanded view of saline dish.

Saved waveforms were analysed using a custom Matlab (MathWorks) program. They were Fourier transformed with the magnitude of each signal determined from the peak at 600 Hz for each waveform for each electrode (19 as one is the source). This signal was above the noise level for each measurement. It was expected that voltages would be highest closest to the source and reduce with distance. To help interpret the results, a COMSOL model was created of the electrode geometry using the mask designs which were imported in to COMSOL and then extruded to create a 3D geometry which was then positioned based on images of the ring devices used. These models were the same as those described in chapter 7, but used a 3D geometry rather than 2D, i.e. saline block (0.7 S/m) containing electrodes with high conductivity (5.99×10^9 S/m) with a ground point on the edge of the block and insulated electrode fingers. These were also static models with a current source applied to the same electrodes as the experiment with the voltages determined at the other electrodes.

Two ring devices were used for these experiments, one of the 3 EPF devices (ring 1) with the 278.9 μm^2 electrodes and one of the 2 EPF devices with the 180.2 μm^2 (ring 2) electrodes (Figure 8.27). The 3 EPF ring was just used as a rolled device whereas ring 2 was used flat and then as a ring. The ring shape is poor for ring 2 as it is difficult to roll the ring devices when they are fixed to the PCB as it only requires a small amount of force to severe the neck of the device. The electrodes used in these tests were unmodified as an impedance

reduction was not required to measure the magnitude of signal used. The COMSOL models were constructed from the images as shown with the electrodes assumed to be lying in a single plane (to simplify model construction). This was approximately true for ring 1 but less true for ring 2. The extremely fine mesh setting in COMSOL was used with each of these models.

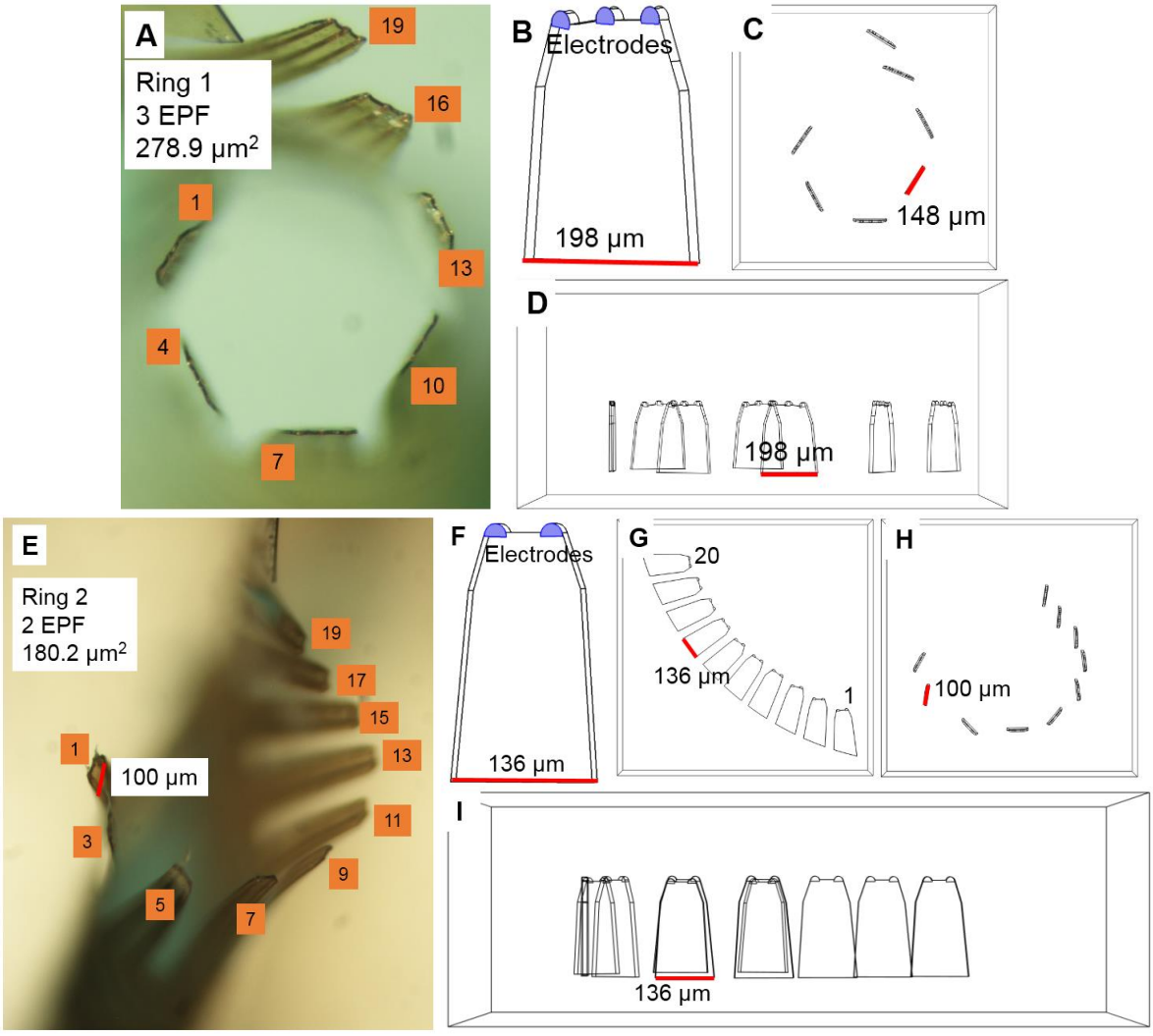

Figure 8.27 A) Ring 1 3 EPF image with electrode numbers labelled, B) individual modelled electrode finger, C) top view of model reproduction of device image, D) side view, E) ring 2 2 EPF image with electrodes labelled, F) single modelled electrode finger, G) unrolled (flat) ring model, H) rolled ring model top view, I) rolled ring model side view.

An example frequency spectrum is shown in Figure 8.28 for electrode 11 of ring 1 when electrode 18 was the source. This shows that the 600 Hz signal is above the noise and clearly

defined within the spectrum, which was the case for all of the signals. Each measurement was repeated three times with results consistent between repetitions.

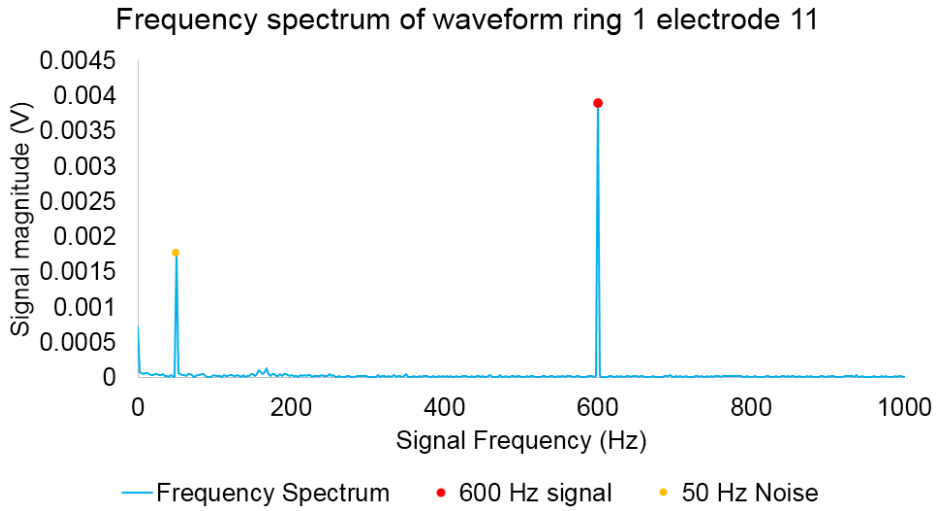

Figure 8.28 Ring 1 electrode 11 frequency spectrum with electrode 18 as the source.

The magnitude of the voltages from each signal are plotted together with the results from the model (Figure 8.29) for ring 1 (source on electrodes 15 and 18) against the distance to the source electrode which was calculated from the model (that was based on device images). The magnitude of the model voltages were scaled to the measurements so that the maximum model voltage was the same as the maximum measured voltage. This is the voltage measured by the electrode closest to the source and this was done so that the reduction in voltage could be compared on the same terms. Measured values from electrodes that were not functioning (from the initial impedance measurement) were removed from the results. It can be seen that the general trend of the model and measurement is the same as the voltage decreases with distance. There is also a difference between distributions for the different electrode sources. The model voltages reduced more quickly than the measured voltages. The differences between the model voltages could be due to the actual distance between electrodes being different to what the

modelled distance is. Each physical electrode is also likely not to be the same size due to differences in alignment.

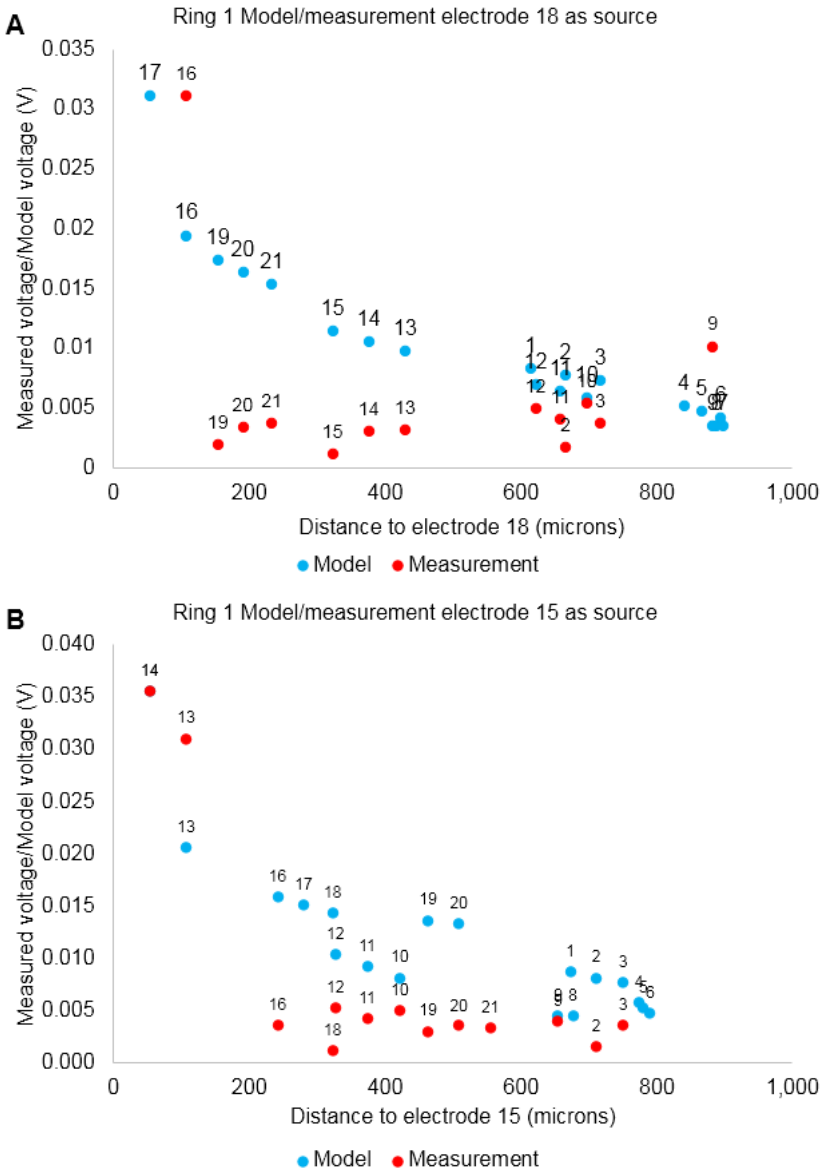

Figure 8.29 Ring 1 A) Electrode 18 as source, B) electrode 15 as source.

The measured and model voltages were also plotted for ring 2, with electrode 7 as the source and electrode 13 as the source. As well as the flat ring 2 with electrode 1 as the source. These plots are shown in Figure 8.29. These results are similar to those from ring 1 but the model voltages are more similar to the measured voltages with a similar reduction in voltage over the

distances, especially when the electrode is flat. There is again a difference in distribution for each position of the source as well as a difference between when the device is flat and rolled.

These results and the results from ring 1 show that the electrodes were functioning and capable of measuring a signal, with differences in model and measured voltages likely to be mostly due to the unknown electrode spacing. A larger signal was measured close to the source with a reduction in voltage measured at as the distance to the source increased. Different electrode sources led to a difference in the signal measured as expected. The measurement of different signals from each electrode is what would be expected when measuring ECG signals where different ECG's could be measured from the same zebrafish at the same time.

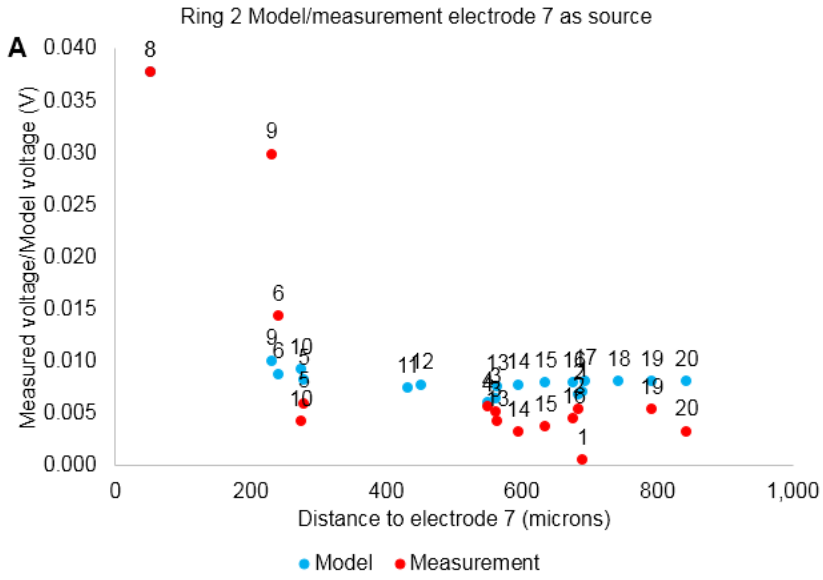

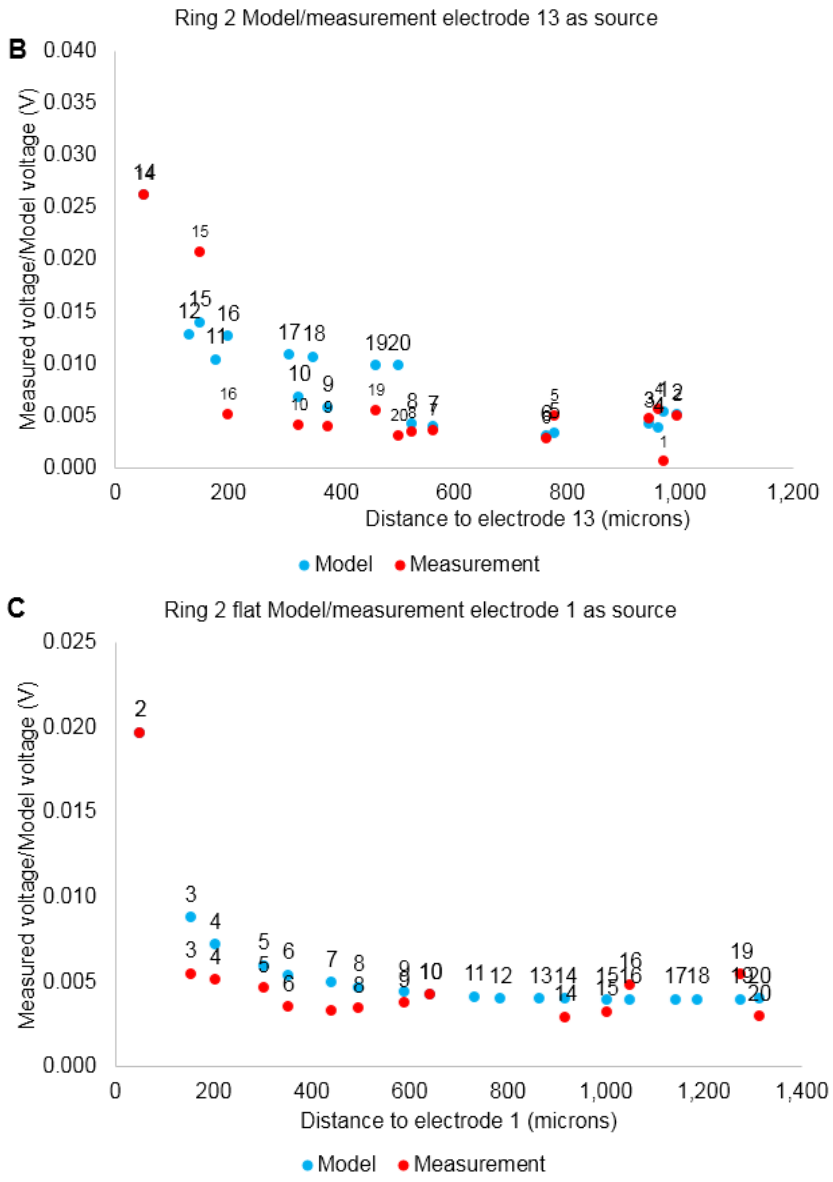

Figure 8.30 Ring 2. A) Electrode 7 as source, B) electrode 13 as source.

8.4 Summary of this chapter

This chapter has described the design, fabrication and testing of microelectrode arrays towards the development of a high throughput system for measuring the larval zebrafish ECG. The successful testing of impedance reduction methods was described along with the testing of devices with the zebrafish which was unsuccessful in measuring the zebrafish ECG. The original contribution from this section of work toward the electrode development was the use

of impedance reduction methods with zebrafish probes, modification of the sacrificial layer process, the use of unequal thickness substrate and insulation PI layers in the fabrication of the electrodes, testing of the original 20 channel ring device with the zebrafish, the modified ring electrode designs (2 EPF and 3 EPF) and the testing of these new electrodes with the impedance reduction methods, the zebrafish and artificial signals.

Firstly, the impedance reduction methods were tested on circular microfabricated zebrafish probe electrodes with a 30 µm diameter which were successfully found to lower the electrode impedance below 1 MΩ after performing tests with a series of varying current and plating combinations. This was the target impedance which corresponds to that of a micropipette which is known to measure a good ECG signal. Gold plating and PEDOT:PSS coating were used in combination and it was discovered that by adding 10% IPA to the PEDOT:PSS solution mixture these methods could also be applied to reduce the impedance of 15 µm diameter circular electrodes below 1 MΩ. These results were then applied to a similar four channel microfabricated electrode probe that was successfully able to measure an ECG signal from a zebrafish (chapter 4).

Due to this success the focus of this work was shifted from probe devices to a ring device which was thought to be more suitable for a high throughput application. This is because the ring forms an electrode array around the zebrafish with the intention that manual positioning of the electrodes/zebrafish would not be required. This positioning issue is not solved by the ring on its own but an additional device could perhaps solve this problem. Development of this was put on hold so manual positioning of the zebrafish within the devices was performed. Some tests with this ring device had been performed previously but no signal had been measured. The fabrication method of these devices was changed so that a 10 µm substrate was used with a 3

µm insulation layer rather than equal layers. This was done to maximise exposure of the electrodes which have a well design. Problems occurred during the release process which meant limited devices could be tested. The plating/coating methods were applied to the ring device and then tested with the zebrafish. Unfortunately, no signal was able to be recorded which was thought to be due to a lack of contact, either because of the well design or because the electrodes were not located at the end of the device's fingers.

Therefore, the ring device was redesigned with the electrodes modified to be similar to those of the 4-channel device which had previously worked. These were then fabricated with the 10 µm substrate and 3 µm insulation. A solution to the release problem was also found which allowed some devices to be tested. A retest was conducted of the plating/coating methods to confirm results with a higher application of current required to achieve similar results with the PEDOT:PSS. These devices were then tested on the zebrafish and still no signal could be measured. This was again thought to be a contact issue which could require another redesign of the electrodes. As no biological signal could be measured the electrodes were tested with an artificial signal which showed they were functioning as intended. Different signals could be measured in different electrodes due to the distance between them and the source which showed similar trends to a COMSOL model of the same geometry. Differences in the predicted model voltages to the experimental voltages could be due to the uncertainty in the position of the electrodes which was difficult to determine and only based on images and an assumption that the electrodes were all within a single plane. The conductivity of the experimental solution could have also been different to that used in the model as well as electrode interface effects.

The PEDOT:PSS work could be improved in the future by using scanning electron microscopy (SEM) and cyclic voltammetry (CV) to investigate further the nature of the coatings

as has been shown in the literature [158]. The robustness of the coatings could also be investigated as this would be a requirement in a high through put system. A different equivalent circuit model could also be used to help analyse the impedance and phase spectra [161]. For the ECG measurements the focus should be on trying to measure a signal. The existing devices could be used as probes to at least confirm the previous results. Contact was thought to be the main issue which could be improved by redesigning the angle of the ring so that the fingers of the devices are closer to a right angle with the zebrafish. Pressure could also be applied to the fingers in some way to increase contact, this was tried using a pipette but the device is so small it was difficult to apply pressure to the end of the fingers.

9. CONCLUSIONS AND AREAS FOR FUTURE WORK

The main accomplishments of the work presented in this thesis are the development of the first electrical model of the larval zebrafish heart using COMSOL Multiphysics, the application of impedance reduction methods to novel zebrafish MEA's and their testing on the larval zebrafish.

The heart model incorporates realistic geometry with the bidomain model and Fitzhugh-Nagumo equations used as the electrical model. It is capable of simulating ECG's that are comparable to those that are experimentally measured. Thus, the model successfully achieved the aim of the heart modelling work. The use of COMSOL Multiphysics shows that it and similar software can be used to create such a model, and, as it is widely available software the use of it in this work could lead to its greater use in heart modelling for the zebrafish, human or other animal models. The prediction capability of the model is mainly limited to ECG prediction at different positions and not finer drug effects. Therefore, the model is developed but could be expanded upon in future work to incorporate further details such as a more realistic ionic model or mechanical contraction to enable it to be able to make further predictions.

Gold plating and PEDOT:PSS electropolymerisation impedance reduction methods were successfully used to reduce the impedance of microelectrodes of various sizes to below 1 MΩ which was an excellent result. Of particular significance was the application of these methods to small 180 μm^2 electrodes whose impedance was reduced via the discovery that the addition of 10% IPA to the PEDOT:PSS coating solution improves the processes effectiveness. This is significant as ideally the smallest electrodes possible need to be used for their increased

voltage sensitivity as shown by the electrode modelling. These methods were applied to well electrodes, and also edge electrodes with similar results which showed the process was repeatable.

Electrode arrays for ECG were designed and tested with the zebrafish toward the development of a high throughput system. Several modifications were made to existing designs and previous fabrication processes of ring electrode arrays. In addition to the aforementioned impedance reduction, these included the use of unequal PSPI thicknesses, electrode shape/position/distribution changes and changes to the sacrificial layer/release process. Unsuccessful measurement experiments were performed with both the original and modified ring electrode arrays which could suggest that the modifications resulted in no improvement in their ability to measure a signal. However, this cannot be stated with certainty, as only a limited number of devices were tested due to the problems with the device release. It was found that the problem with the measurements was not due to non-functioning devices as successful impedance and artificial signal tests were performed. This most likely suggests that the main issue with the electrodes was poor contact with the zebrafish.

It was clear from this work that further work is needed to develop a high throughput system and that there could be some problems using the devices tested in such a system even if some signals could have been measured. The fabrication process of the devices can be unreliable and time consuming to produce even one device, as shown by the problems with the device release. The arrays are also fragile and would perhaps not withstand repeated use. In addition, the difficulty in being able to measure a signal could indicate manual positioning of the zebrafish may be required, which would not be suitable for such a system. However, as the number of devices that were tested was limited, solutions could still be found to these problems.

Future work could attempt to solve these problems, starting with the verification of the ability of the microfabricated devices to measure the ECG in any configuration.

9.1 Future work

9.1.1 Discrete heart model

One of the main improvements to model could be to use a discrete model of the electrical activity rather than the continuum model presented in thesis. This would involve modelling individual cells connected by gap junctions. Addition of this cellular level architecture would cause a decrease in overall wave velocity due to the relatively low conducting gap junctions which would mean the required realistic wave velocity could be realised without artificially reducing the conductivity to achieve those velocities. This could possibly be achieved by simply modelling the gap junctions as a high resistance region with the cells as a higher conducting region. This would likely mean geometrically modelling individual cells and their interconnections. Such models have been created previously for small sections of human tissue, for example by Bruce [146] or Stinstra [162] or hybrid model by Costa [163] but not for a whole heart. Bruce *et al* present a comparison of both discrete and continuum models with and without gap junctions, to show that they have a significant effect. Stinstra *et al* report a geometric and electrical model of a section of cellular tissue Figure 9.1. A good place to start would be to reproduce some of the results of these models within COMSOL and then apply them to different geometries such as a simplified heart where individual cells would be simpler to create.

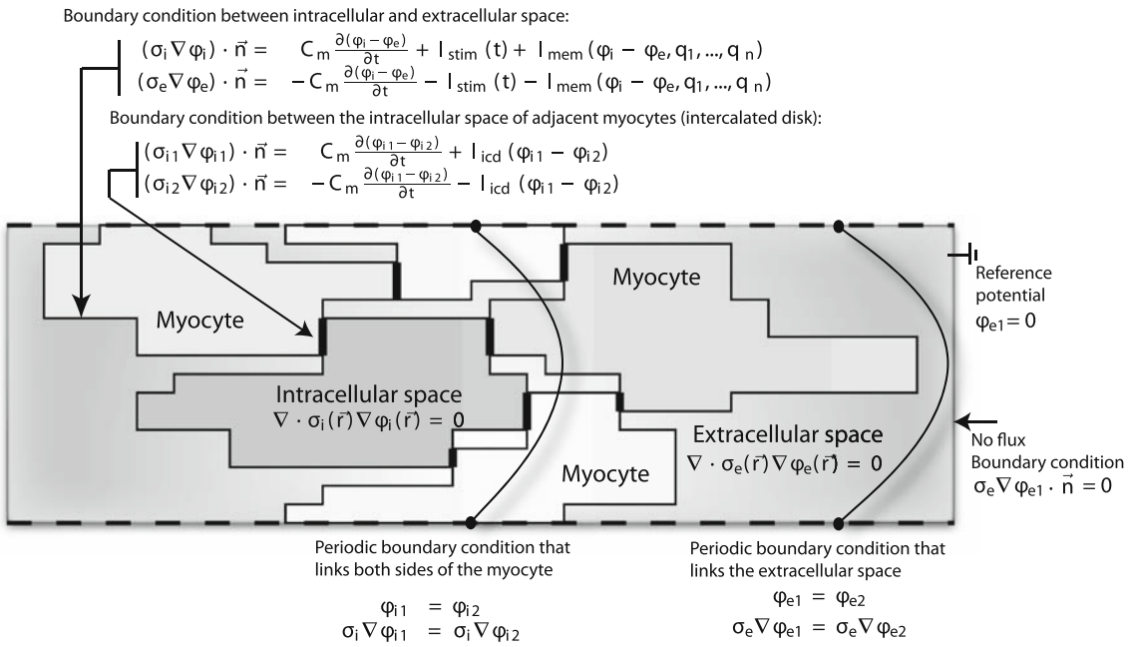

Figure 9.1 Schematic image of discrete heart model. Depicting the equations that describe each region and boundary [162]

9.1.2 Heart movement

The heart is obviously not a static object as it was treated by the models in this thesis and as described previously the mechanical properties of the heart effect the ECG [28]. Therefore, another improvement that could be made to the heart model would be to include either movement of the heart simply by just moving the boundaries in prescribed way, including full electromechanical coupling or by the use of hybrid model. Simple movement of the heart can be accomplished in COMSOL by using the deformed mesh feature and by prescribing displacements to interior and exterior boundaries. Application of this to the simplified model heart is shown in which was achieved by applying a time varying waveform to the heart boundaries (Figure 9.2). This would then need to be applied to the more complex geometry as well interfacing with the electrical model.

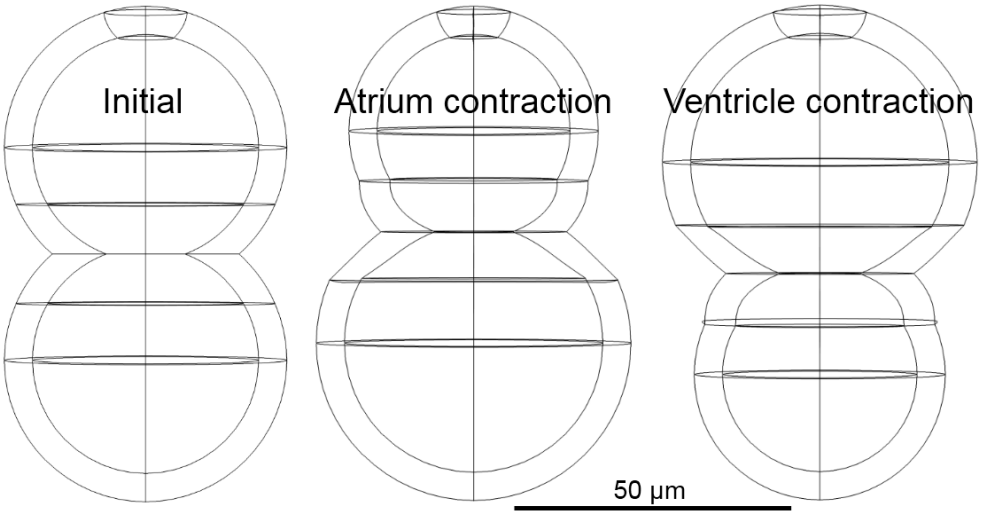

Figure 9.2 Simplified 3D heart model boundary movement using deformed mesh

9.1.3 Future experimental work

The priority for future experimental work should be to reliably demonstrate the ability of the microfabricated devices to measure the larval zebrafish ECG. Progression on to the use of the ring device should have perhaps been delayed to confirm the effectiveness and use of the probe style devices. This could be accomplished using the redesigned ring devices as probes by keeping them flat and then moving them in to contact with the zebrafish. If successful, different angles of contact with the zebrafish could be investigated to determine the ideal angle of ring shape which could then be incorporated in to a redesign if required. If these attempts are successful, the rolled ring could again be tested. This could then lead to use additional devices or methods to possibly remove the requirement of zebrafish positioning.

If use of the devices is still unsuccessful or as an extra component. The characterisation of the PEDOT:PSS coatings could be further investigated as described earlier using SEM or CV. Artificial signals could also be used to test whether the PEDOT:PSS coating is an improvement over the bare gold.

Appendix

A.1 Zebrafish devices designs 1: Mask set 1

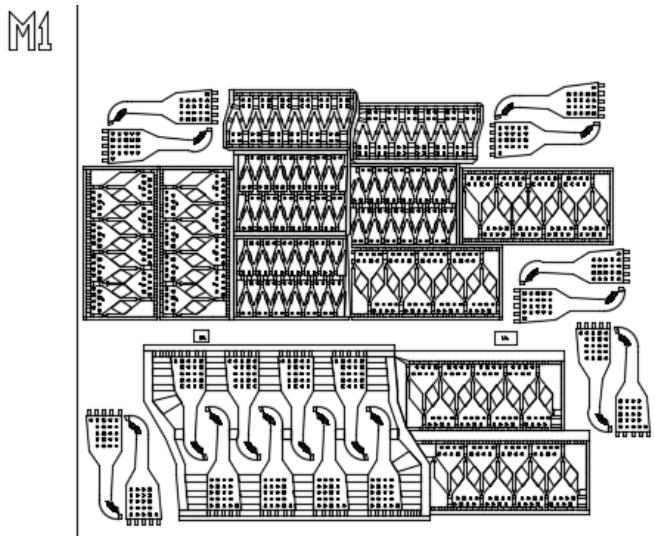

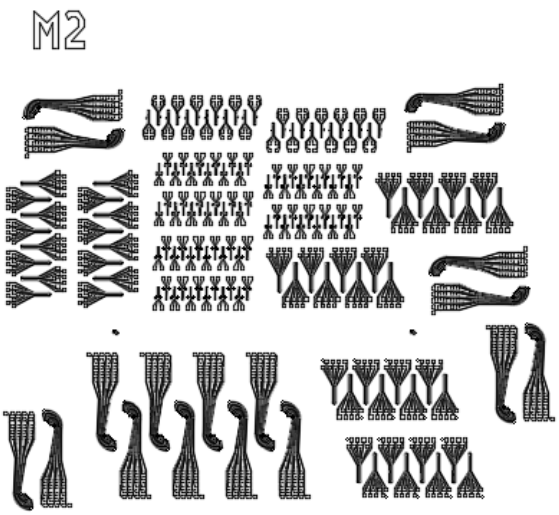

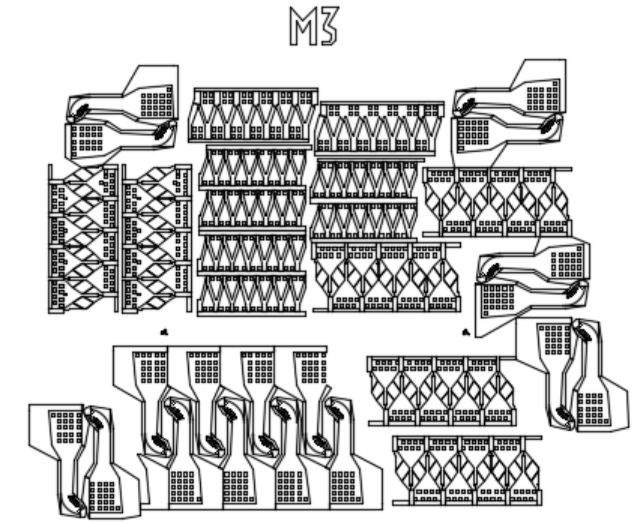

Figure A.1 Zebrafish devices mask set 1. Designed by Richard Barrett. M1 used to pattern substrate layer. M2 used to pattern photoresist for metal layer. M3 used to pattern insulation layer.

A.2 Zebrafish devices designs 2: Mask set 2

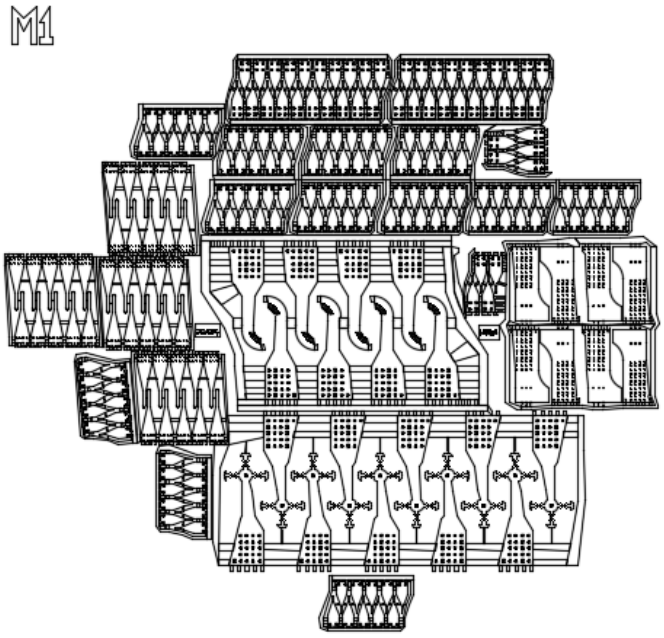

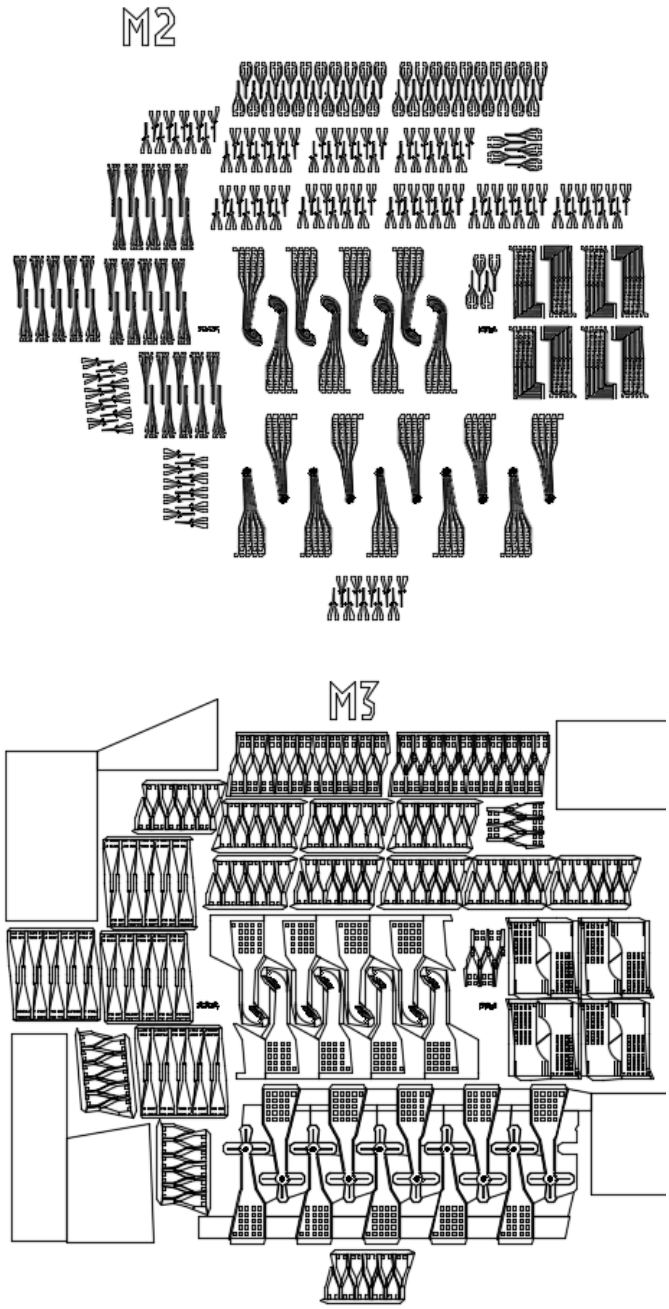

Figure A.2 Zebrafish devices mask set 2. Designed by Richard Barrett. M1 used to pattern substrate layer. M2 used to pattern photoresist for metal layer. M3 used to pattern insulation layer.

A.3 Zebrafish devices designs 3: Mask set 3

M1

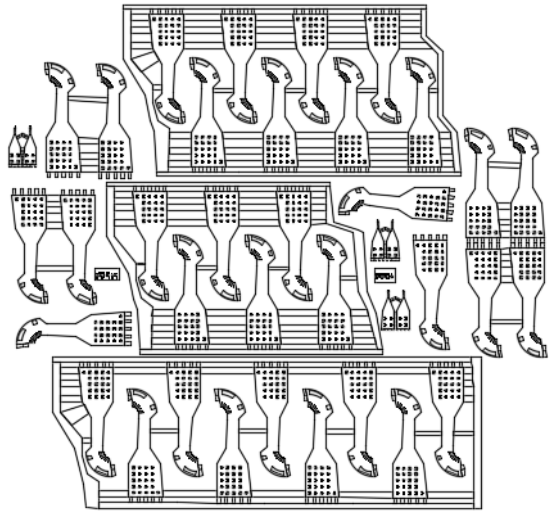

M2

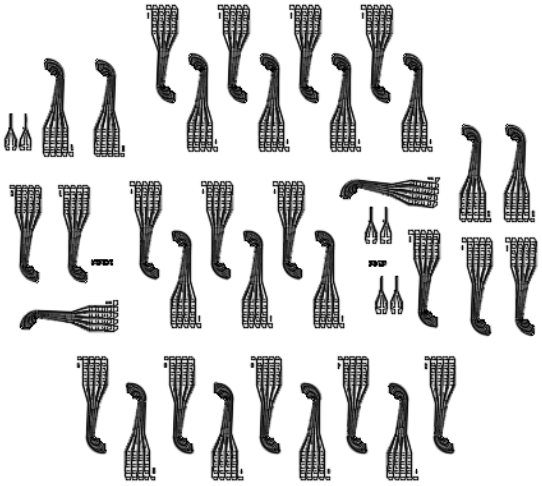

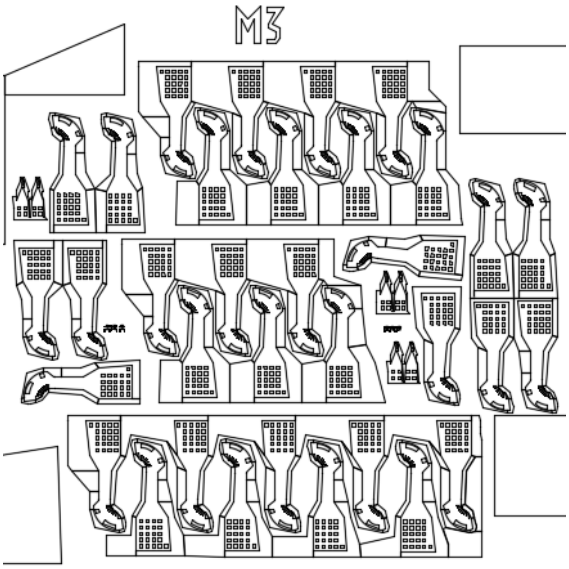

Figure A.3 Zebrafish devices mask set 3. Based on ring device foot print by Richard Barrett. M1 used to pattern substrate layer. M2 used to pattern photoresist for metal layer. M3 used to pattern insulation layer.

A.4 6 nA and 16 nA impedance and phase spectra

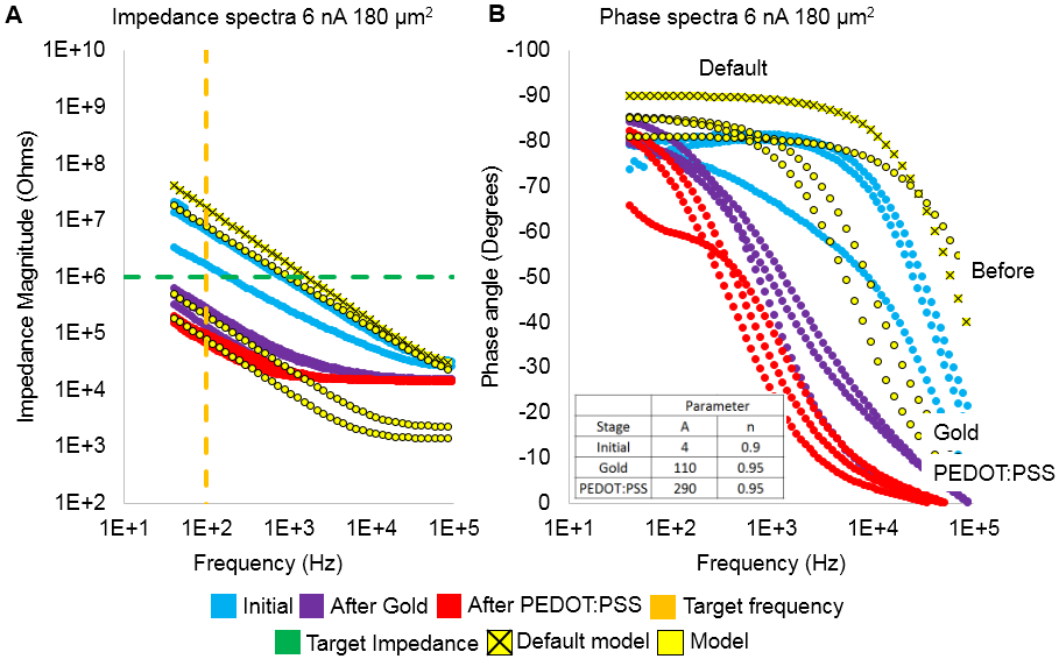

Figure A.4 Impedance and phase spectras for plating/coating of 180 µm² electrodes. 6 nA current for 2 mins. A) Impedance magnitude for each stage of the process. Initial (before plating), after gold plating and after the PEDOT:PSS coating. The results from three electrodes are shown for each. The model (from chapter 4) results are fitted by changing the parameters shown in B along with the default model result from an electrode of this area. Target impedance is (1 MΩ) at the target frequency (100 Hz). B) Phase spectra for the same results. Associated model results are labelled.

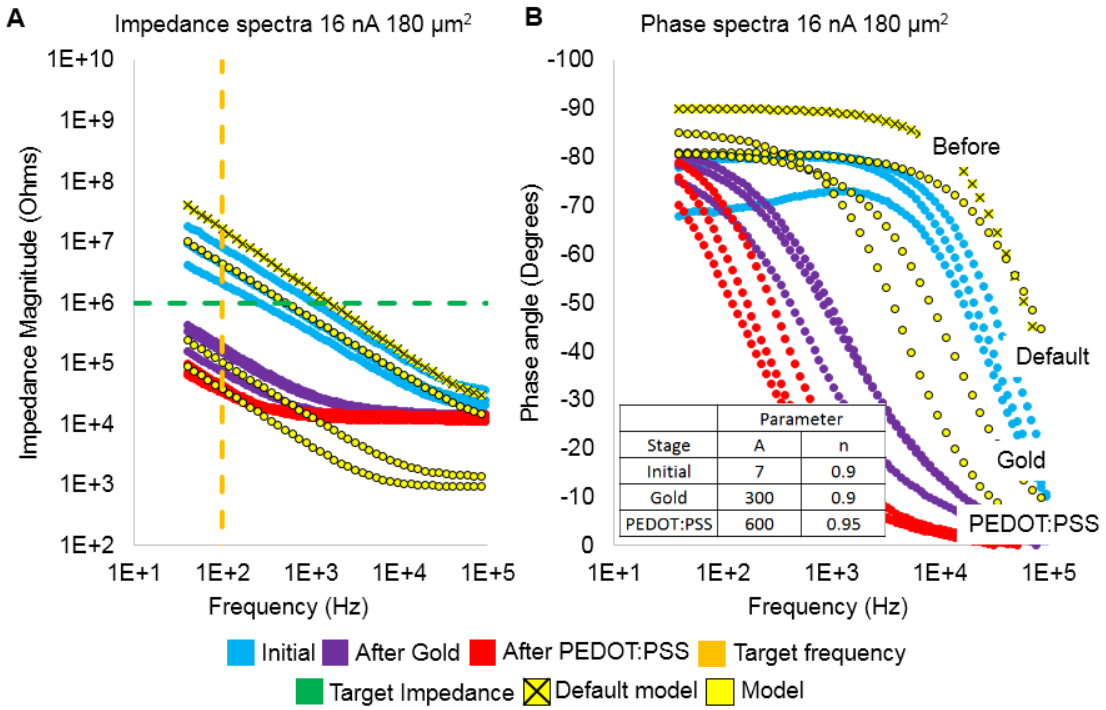

Figure A.5 Impedance and phase spectras for plating/coating of 180 µm² electrodes. 16 nA current for 2 mins. A) Impedance magnitude for each stage of the process. Initial (before plating), after gold plating and after the PEDOT coating. The results from three electrodes are shown for each. The model (from chapter 4) results are fitted by changing the parameters shown in B along with the default model result from an electrode of this area. Target impedance is (1 MΩ) at the target frequency (100 Hz). B) Phase spectra for the same results. Associated model results are labelled.

A.5 Fabrication process

5. Layer 1 – Sacrificial layer on silicon wafer
    - Chrome 100 nm
    - Aluminium 125 nm
    - Chrome 25 nm
    - Allows release of devices from wafer deposited using Cressington 380R
6. Layer 2 - Substrate PSPI Durimide 7020 10 µm
    - Spun at 500 rpm 5 seconds, 4000 rpm 30s, 300 rpm 1s.
    - Bake 30°C:5 mins, 40:5, 50:5, 60:5, 80:5, 90:8
    - Exposed for 12 seconds and then post exposure bake 90:3

- Cool 5 mins
- Developed using HTRD2 + RER600
- Forms the outline of each device

7. Layer 3 – Metallisation
    - Chrome (for adhesion) ~18 nm
    - Gold 100 nm
    - For wiring, connection pads and electrode sites
8. Layer 4 – Metal patterning
    - SPR 220 photoresist spun on to sample
    - 500 rpm 10 s, 3000 rpm 20s, 700 rpm 10s
    - Drop down bake 90°C:2 mins, 130:6
    - Edge bead removal with acetone if required
    - Exposure 4*35 s with 25 second rest between each exposure
    - Development in MF-26A

    Wet etching

    - To remove unwanted Gold and chrome
    - Cover slip placed in each solution for exact timing
    - Sample in gold etchant ~50 s and chrome etchant ~15 s with wash in water in between
    - Forms wiring, connection pads and electrode sites

    Plasma/UVO cleaning

    - 5 mins plasma cleaning at 50% power
    - 10 mins UVO
    - To remove remnants of photo resist and improve adhesion of next layer

10. Layer 5 – PSPI insulation/passivation Durimide 7505

    - 3 µm layer
    - Spun at 3800 rpm 30s
    - 30°C:5 mins, 40:3, 50:5, 60:3, 70:5, 80:3, 90:8
    - Exposed for 8 seconds and then post exposure bake 90:3
    - Insulates all wiring except for electrodes and connection pads

    Plasma/UVO cleaning

    - Plasma 10 mins at 70% power
    - UVO 20 mins
    - Final descum to remove unwanted material

    Hard bake in furnace

    - To remove oxide and give final properties

11. Release in NaCl

    - Anodic dissolution of the sacrificial layer as described in chapter 8. Process takes 24+ hrs

A.6 20 channel ring device PCB

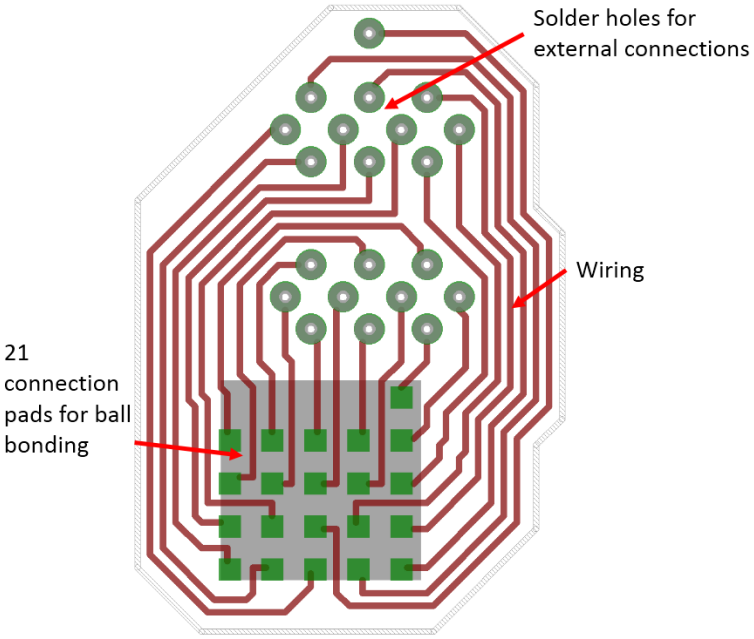

Figure A.6 21 Channel PCB for ring electrode array. Designed by Richard Barrett.

A.7 Publication plan

A paper has been published in PLOS One regarding the larval zebrafish bidomain heart model. There is potential for a paper that describes the larval zebrafish ECG measurements using the microfabricated electrodes.

BIBLIOGRAPHY

1. Milan, D.J., et al., *In vivo recording of adult zebrafish electrocardiogram and assessment of drug-induced QT prolongation.* Am J Physiol Heart Circ Physiol, 2006. **291**(1): p. 269-73.
2. Verkerk, A.O. and C.A. Remme, *Zebrafish: a novel research tool for cardiac (patho)electrophysiology and ion channel disorders.* Front Physiol, 2012. **3**(3): p. 255.
3. Hecker L, et al., *Functional evaluation of isolated zebrafish hearts.* Zebrafish, 2008. **5**(4): p. 319-22.
4. Stainier DY, et al., *Mutations affecting the formation and function of the cardiovascular system in the zebrafish embryo.* Development, 1996. **123**(285-292).
5. Rottbauer W, et al., *Growth and function of the embryonic heart depend upon the cardiac-specific L-type calcium channel alpha1 subunit.* Developmental Cell, 2001. **1**(2).
6. Forouhar AS, et al., *Electrocardiographic Characterization of embryonic zebrafish.* Proceedings of the 26th Annual International Conference of the IEEE EMBS, 2004.
7. Yu F, et al., *Evolving cardiac conduction phenotypes in developing zebrafish larvae: implications to drug sensitivity.* Zebrafish, 2010. **7**(4): p. 325-31.
8. Zhang X, et al. *Flexible MEA for adult zebrafish ECG recording covering both ventricle and atrium*. in *Micro Electro Mechanical Systems (MEMS), 2014 IEEE 27th International Conference on*. 2014.
9. Tsai CT, et al., *In-vitro recording of adult zebrafish heart electrocardiogram - a platform for pharmacological testing.* Clinica chimica acta; international journal of clinical chemistry, 2011. **412**(21-22): p. 1963-7.
10. Sun P, et al., *Micro-electrocardiograms to study post-ventricular amputation of zebrafish heart.* Annals of Biomedical Engineering, 2009. **37**(5): p. 890-901.
11. Dhillon SS, et al., *Optimisation of embryonic and larval ECG measurement in zebrafish for quantifying the effect of QT prolonging drugs.* PLoS One, 2013. **8**(4).
12. Berghmans S, et al., *Zebrafish based assays for the assessment of cardiac, visual and gut function--potential safety screens for early drug discovery.* Journal of pharmacological and toxicological methods, 2008. **58**(1): p. 59-68.
13. Nemtsas P, et al., *Adult zebrafish heart as a model for human heart? An electrophysiological study.* Journal of Molecular and Cellular Cardiology, 2010. **48**(1): p. 161-71.
14. Sanguinetti MC and Mitcheson JS, *Predicting drug–hERG channel interactions that cause acquired long QT syndrome.* . Trends in Pharmacological Sciences, 2006. **26**: p. 119-124.
15. Letamendia A, et al., *Development and Validation of an Automated High-Throughput System for Zebrafish In Vivo Screenings.* PLoS ONE, 2012. **7**(e36690).
16. CA, M., *Cardiac Arrhythmia: In vivo screening in the zebrafish to overcome complexity in drug discovery.* Expert Opin Drug Discov, 2010. **5**: p. 619-632.
17. Crumb W and Cavero I, *QT interval prolongation by non-cardiovascular drugs: issues and solutions for novel drug development.* Pharmaceutical Science & Technology Today, 1999. **2**: p. 270-280.

18. Broach JR and Thorner J, *High-throughput screening for drug discovery.* Nature, 1996. **384**(6604): p. 14-6.
19. Chapman T, *Drug discovery: the leading edge.* Nature, 2004. **430**(6995): p. 109-15.
20. Lieschke G J and Currie P D, *Animal models of human disease: zebrafish swim into view.* Nature Reviews Genetics, 2007. **8**: p. 353-367.
21. Eggert SU and Mitchison TJ, *Smal molecule screeening by imaging.* Current Opinion In Chemical Biology, 2006. **10**: p. 232-237.
22. Gehrig J, et al., *Automated high-throughput mapping of promoter-enhancer interactions in zebrafish embryos.* Nature Methods, 2009. **6**(12): p. 911-6.
23. Hochberg LR, et al., *Neuronal ensemble control of prosthetic devices by a human with tetraplegia.* Nature Reviews Genetics, 2006. **442**(7099): p. 164-71.
24. Stett A, et al., *Biological application of microelectrode arrays in drug discovery and basic research.* Analytical and Bioanalytical Chemistry, 2003. **377**(3): p. 486-95.
25. Okada J, et al., *Patient specific simulation of body surface ECG using the finite element method.* Pacing and clinical electrophysiology, 2013. **36**(3): p. 309-21.
26. Taylor CA, Fonte TA, and Min JK, *Computational Fluid Dynamics Applied to Cardiac Computed Tomography for Noninvasive Quantification of Fractional Flow: Reserve Scientific Basis.* Journal of the American College of Cardiology, 2013. **61**(22): p. 2233-2241.
27. Gurev V, et al., *Distribution of Electromechanical Delay in the Heart: Insights from a Three-Dimensional Electromechanical Model,.* Biophysical Journal, 2010. **99**(3): p. 745-754.
28. Adeniran I, Hancox JC, and Zhang H, *Effect of cardiac ventricular mechanical contraction on the characteristics of the ECG: A simulation study.* Journal of Biomedical Science and Engineering, 2013. **06**(12): p. 47-60.
29. Noble D, *A modificaiton of the hodkin-huxley equations applicable to purkinje fibre action and pace-maker potentials.* J . Physiology, 1962. **160**: p. 317-352.
30. Garny A and Kohl P, *Mechanical Induction of Arrhythmias during Ventricular Repolarization - Modeling cellular mechanisms and their interaction in two dimensions.* Annals of the New York Academy of Sciences, 2004. **1015**: p. 133-143.
31. Dokos S, Cloherty SL, and Lovell NH, *Computational Model of Atrial Electrical Activation and Propagation.* Proceedings of the 29th Annual International Conference of the IEEE EMBS, 2007.
32. Harrild DM and Henriquez CS, *A Computer Model of Normal Conduction in the Human Atria.* Circulation Res., 2000. **87**: p. 25-36.
33. Trayanova NA, *Whole-heart modeling: applications to cardiac electrophysiology and electromechanics.* Circulation research, 2011. **108**(1): p. 113-28.
34. Clayton RH, et al., *Models of cardiac tissue electrophysiology: progress, challenges and open questions.* Progress in biophysics and molecular biology, 2011. **104**(1-3): p. 22-48.
35. Henriquez CS, *A Brief History of Tissue Models for Cardiac Electrophysiology.* IEE Transcations on Biomedical Engineering, 2014. **61**(5): p. 1457-1465.
36. MacLeod R and Buist M, *The Forward Problem of Electrocardiography.* Comprehensive Electrocardiology, 2010. **8**(3): p. 247-298.

37. Lines GT, et al., *Mathematical models and numerical methods for the forward problem in cardiac electrophysiology.* Computing and Visualization in Science, 2002. **5**(4): p. 215-239.
38. Malmivuo J and Plonsey R, *Bioelectromagnetism*. 1995, New York: Oxford University Press.
39. Zemzemi N, et al., *Computational assessment of drug-induced effects on the electrocardiogram: from ion channel to body surface potentials.* British Journal of Pharmacology, 2013. **168**(3): p. 718-733.
40. Boulakia M, et al., *Mathematical modeling of electrocardiograms: a numerical study.* Annals of biomedical engineering, 2010. **38**(3): p. 1071-97.
41. Gurev V, et al., *Models of cardiac electromechanics based on individual hearts imaging data.* Biomechanics and Modeling in Mechanobiology, 2011. **10**(3): p. 295-306.
42. Butters TD, et al., *A novel computational sheep atria model for the study of atrial fibrillation.* Interface Focus, 2013. **3**(2).
43. Lee J, et al., *Moving Domain Computational Fluid Dynamics to Interface with an Embryonic Model of Cardiac Morphogenesis.* PLoS ONE, 2013. **8**(8).
44. Kochová P, et al., *A mathematical model of the carp heart ventricle during the cardiac cycle.* Journal of Theoretical Biology, 2015. **373**: p. 12-25.
45. Tirziu D, Giordano FJ, and Simons M, *Cell Communications in the Heart.* Circulation, 2011. **122**(9): p. 928-937.
46. Molina DK and DiMaio VJ, *Normal organ weights in men: part I-the heart.* The American Journal of Forensic Medicine and Pathology, 2012. **33**(4): p. 362-7.
47. *Anatomy of animals*. Available from: https://universe-review.ca/R10-33-anatomy09.htm.
48. Grimes AC, et al., *PCB126 exposure disrupts zebrafish ventricular and branchial but not early neural crest development.* Toxicological sciences, 2008. **106**(1): p. 193-205.
49. Chi NC, et al., *Genetic and physiologic dissection of the vertebrate cardiac conduction system.* PLoS Biology, 2008. **6**(5): p. e109.
50. Dietrich AC, et al., *Blood flow and Bmp signaling control endocardial chamber morphogenesis.* Development Cell, 2014. **30**(4): p. 367-77.
51. Kimmel CB, et al., *Stages of Embryonic Development of the Zebrafish.* Developmental Dynamics, 1995. **203**(3): p. 253-310.
52. Takeuchi JK, et al., *Chromatin Remodeling Complex Dosage Modulates Transcription Factor Function in Heart Development.* Nature Communications, 2011. **2**(187).
53. Rohr S, *Role of gap junctions in the propagation of the cardiac action potential.* Cardiovascular research, 2004. **62**(2): p. 309-22.
54. Gordon Betts J, et al., *Openstax - Anatomy and physiology*. 2013.
55. Ruiz M. *Connexon and connexin structure*. 2006; Available from: https://en.wikipedia.org/wiki/File:Connexon_and_connexin_structure.svg.
56. Nernst WH, *Die elektromotorische Wirksamkeit der Ionen.* Z. Phys. Chem, 1889. **4**: p. 129-81.
57. Einstein A, *Über die von der molekularkinetischen Theorie die wärme Gefordertebewegung von in ruhenden flüssigkeiten suspendierten Teilchen.* Ann. Physik, 1905. **17**: p. 549-60.
58. Hodgkin AL and Huxley AF, *A quantitative description of membrane current and its application to conduction and excitation in nerve.* J Physiol, 1952. **117**(4): p. 500-544.

59. Panakova D, Werdich AA, and Macrae CA, *Wnt11 patterns a myocardial electrical gradient through regulation of the L-type Ca(2+) channel.* Nature, 2010. **466**(7308): p. 874-8.
60. Pullan AJ, et al., *Cardiac electrical activity--from heart to body surface and back again.* Journal of Electrocardiography, 2003. **36**(Suppl): p. 63-7.
61. Siregar P, et al., *A Cellular Automata Model of the Heart and Its Coupling with a Qualitative Model.* Computers and Biomedical Research, 1996. **29**(3): p. 222-246.
62. Frank E, *Electric Potential Produced by Two Point Current Sources in a Homogeneous Conducting Sphere.* Journal of Applied Physics, 1952. **23**(11).
63. Barber MR and Fischmann EJ, *Heart Dipole Regions and the Measurement of Dipole Moment.* Nature, 1961. **192**: p. 141-142.
64. Geselowitz DB, *Multipole Representation for an Equivalent Cardiac Generator.* Proceedings of the IRE, 1960. **48**(1): p. 75-79.
65. Zablow L, *An Equivalent Cardiac Generator Which Preserves Topography.* Biophysical Journal, 1966. **6**(4): p. 535-536.
66. Colli-Franzone P, et al., *Potential fields generated by oblique dipole layers modeling excitation wavefronts in the anisotropic myocardium. Comparison with potential fields elicited by paced dog hearts in a volume conductor.* Circulation Research, 1982. **51**(3): p. 330-46.
67. Horácek BM and Clements JC, *The inverse problem of electrocardiography: a solution in terms of single- and double-layer sources of the epicardial surface.* Mathematical Biosciences, 1997. **144**(2): p. 119-54.
68. Geselowitz DB, *Dipole theory in electrocardiography.* The American Journal of Cardiology, 1964. **14**(3): p. 301-306.
69. Plonsey R, *Limitations on the equivalent cardiac generator.* Biophysical Journal, 1966. **6**(2): p. 163-173.
70. Luo CH and Rudy Y, *A model of the ventricular cardiac action potential. Depolarization, repolarization, and their interaction.* Circulation Research, 1991. **68**(6): p. 1501-26.
71. Karma A, *Spiral breakup in model equations of action potential propagation in cardiac tissue.* Physical Review Letter, 1993. **71**: p. 1103.
72. Fitzhugh R, *Impulses and physiological states in theoretical models of nerve membrane.* Biophysical Journal, 1961. **1**: p. 445-466.
73. Nagumo J, Arimoto S, and Yoshizawa S, *An Active Pulse Transmission Line Simulating Nerve Axon.* Proceedings of the IRE, 1962. **50**(10): p. 2061-2070.
74. Rogers JM and McCulloch AD, *A Collocation-Galerkin Finite Element Model of Cardiac Action Potential Propagation.* IEE Transcations on Biomedical Engineering, 1994. **41**(8): p. 743-756.
75. Courtemanche M, Skaggs W, and Winfree AT, *Stable three-dimensional action potential circulation in the Fitzhugh-Nagumo model.* Physica D: Nonlinear Phenomena, 1990. **41**(2): p. 173-182.
76. Winfree AT, *Varieties of spiral wave behavior: An experimentalist's approach to the theory of excitable media.* Chaos, 1991. **3**: p. 303-334.
77. Berenfeld O and Abboud S, *Simulation of cardiac activity and the ECG using a heart model with a reaction diffusion action potential.* Med Eng Phys, 1996. **18**(8): p. 615-625.

78. Plonsey R and Heppner DB, *Considerations of quasi-stationarity in electrophysiological systems.* The Bulletin of mathematical biophysics, 1967. **29**(4): p. 657-64.
79. Vigmond EJ, Aguel F, and Trayanova NA, *Computational techniques for solving the bidomain equations in three dimensions.* IEEE Transactions on Biomedical Engineering, 2002. **49**(11): p. 1260-1269.
80. Sovilj S, et al., *A simplified 3D model of whole heart electrical activity and 12-lead ECG generation.* Computational and mathematical methods in medicine, 2013. **2013**: p. 134208.
81. Pullan AJ, Cheng LK, and Buist ML, *Mathematically Modelling the Electrical Activity of the Heart*. 2005.
82. Irimia A, *Electric field and potential calculation for a bioelectric current dipole in an ellipsoid.* Journal of Physics A: Mathematical and General, 2005. **38**(37).
83. Pullan AJ, Cheng LK, and Buist ML, *Mathematically Modelling the Electrical Activity of the Heart: From Cell to Body Surface and Back Again*. 2005: World Scientific.
84. Reddy JN, *An introuction to the finite element method*. 1993.
85. Fischer G, et al., *A bidomain model based BEM-FEM coupling formulation for anisotropic cardiac tissue.* Ann Biomed Eng, 2000. **28**(10): p. 1229-43.
86. Humphrey DR and Schmidt EM, *Extracellular Single-Unit Recording Methods*. 1990: Humana Press.
87. Day S, *Important Factors in Surface EMG Measurement*. 2002, Calgary.
88. Kipke DR, Pellinen DS, and Rousche PJ, *Neuroprosthetics: Theory and Practice*. 2007: Michigan.
89. Yoshida RK, *Neuroprothetics: Theory and Practice*. 2007: Aalborg.
90. Hua C and Wang P, *Cell-based Biosensors: Principles and Applications*, ed. W.P. Liu Q. 2010: Artech House.
91. Botter A, Gazzoni M, and Merletti R, *Introduction to neural engineering for motor rehabiliation*, ed. J.W. Farina D, Akay M. 2013: IEEE Press.
92. Halliwell J, Whitaker M, and Ogeden D, *Using microelectrodes*.
93. Halliwell J, Whitaker M, and Ogden D, *Microelectrode techniques: Chapter 1*. 1994: Cambridge: The company of biologists. 1-15.
94. Neuman MR, *The Biomedical Engineering Handbook: Second Edition*. 2001.
95. Ignell R and Hansson B, *Methods in Insect Sensory Neuroscience: Types of Electrodes*. 2000: Boca Raton: CRC Press.
96. Franssila S, *Introduction to microfabrication*. 2004.
97. Barrett R, *Novel processing routes for neural interfaces*. 2013, University of Birmingham.
98. Kovacs GTA and et al, *Introduction to the theory, design, and modeling of thin-film microelectrodes for neural interfaces.* 1994.
99. Fischer A, *Electrode Dynamics*. 1996: Oxford University Press.
100. *CRC Handbook of Chemistry and Physics*. Vol. 93rd Edition internet version 2013. 2013.
101. Pajkossy T, *Impedance spectroscopy at interfaces of metals and aqueous solutions — Surface roughness, CPE and related issues.* Solid State Ionics, 2005. **176**(25-28): p. 1997-2003.

102. Fromhold A, *Nanotexurisation of Gold Surfaces and its Application to Neural Implants*. 2010, University of Birmingham.
103. Israelachvili JN, *Intermolecular and surface forces*. 1985: London: Academic.
104. Morrow D, Mckenzie R, and Bilek M, *The time-dependent development of electric double layers in saline solutions.* J. Phys. D:Applied Physics, 2006.
105. Najafi K and Wise KD, *An implantable multielectrode array with on-chip signal processing.* Solid-State circuits, IEEE Journal of, 1986. **21**(6): p. 1035-1044.
106. Boussey J, *Microsystems technology: Fabrication, test and reliability*. 2003: Kogan Page Science.
107. Metz S, Bertsch A, and Renaud P, *Partial Release and Detachment of Microfabircated MEtal and Polymer Structures by Anoidc Metal Dissolution.* Journal of Microelectromechanical Systems, 2005. **14**(2): p. 383-391.
108. Cheung, K., et al., *Flexible polyimide microelectrode arrays for in vivo recordings and current source density analysis.* Biosensors and Bioelectronics, 2007. **22**: p. 1783-1790.
109. *Shipley. Megaposit spr-220-7 photoresist datasheet.*
110. *Fujifilm. Durimide 7020 datasheet.*
111. Zong X, Zhu R, and Guo X, *Nanostructured gold microelectrodes for SERS and EIS measurements by incorporating Zn0 nanrod growth with electroplating.* Scientifc Reports, 2015. **5**.
112. Cui XY, et al., *Surface modifcation of neural recording electrodes with conducting polymer/biomolecule blends.* J Biomed Mater Res, 2001. **56**: p. 261-72.
113. Cui XY and Martin DC, *Electrochemical deposition and characterisation of poly(3,4-ethlyenedioxthiophene) on neural microelectrode arrays.* Sens Actuator B-Chem, 2003. **89**: p. 92-102.
114. Ferguson JE, Boldt C, and Redish AD, *Creating low-impedance tetrodes by electroplating with additives.* Sensors and Actuators A: Physical, 2009. **156**(2): p. 388-393.
115. Cui XT and Zhou DD, *Poly (3,4-Ethylenedioxythiophene) for Chronic Neural Stimulation.* IEEE Transactions on neural systems and rehabilitation engineering, 2007. **15**(4).
116. Nyberg T, Shimada A, and Torimitsu K, *Ion conducting polmer microelectrodes for interfacing with neural networks.* Journal of Neuroscience Methods, 2007. **160**: p. 16-25.
117. Group, H. *Conductive polymers* 2017; Available from: https://www.heraeus.com/en/group/products_and_solutions_group/conductive_polymers/cpolymers/conductive-polymers.aspx.
118. Cogan SF, *Neural stimulation and recording electrodes.* Annual reviews in biomedical engineering, 2008. **10**: p. 275-309.
119. Agilent, *Network analyser hp 9424, user manual and technical guide.*
120. Stieglitz T, Beutel H, and Meyer JU, *"microflex" new assembling technique for interconnects.* Journal of Intelligent Material Systems and Structures, 2000. **11**(6): p. 417-425.
121. Fau GN and Yelon DD, *Cardiac development in zebrafish: coordination of form and function.* Cell and Developmental Biology, 2002. **13**.
122. Li J and et al, *A modified Fitzhugh-Nagumo model that allows control of action potential duration and refractory period.* Computers in Cardiology, 2009.

123. Salgao D, et al. *Zebrafish anatomy portal*. Available from: http://www.zfap.org/download.php.
124. Bryson-Richardson RJ and Currie PD, *Optical projection tomography for spatio-temporal analysis in the zebrafish.* Methods Cell Biol, 2004. **76**: p. 37-50.
125. Fedorov A, et al., *3D Slicer as an Image Computing Platform for the Quantitative Imaging Network.* Magn Reson Imaging, 2012. **30**(9): p. 1323-41.
126. *Slicer*. Available from: http://www.slicer.org/.
127. Hami D, et al., *Zebrafish cardiac development requires a conserved secondary heart field.* Development, 2011. **138**(11): p. 2389-98.
128. Renz M, et al., *Regulation of beta1 integrin-Klf2-mediated angiogenesis by CCM proteins.* Developmental cell, 2015. **32**(2): p. 181-90.
129. Just S, et al., *Protein kinase D2 controls cardiac valve formation in zebrafish by regulating histone deacetylase 5 activity.* Circulation, 2011. **124**(3): p. 324-34.
130. Nakazaki T, et al., *Mobilization of a transposon in the rice genome.* Nature, 2003. **421**(6919): p. 170-2.
131. Zhou Y, et al., *Latent TGF-beta binding protein 3 identifies a second heart field in zebrafish.* Nature, 2011. **474**(7353): p. 645-8.
132. Zhang R, et al., *In vivo cardiac reprogramming contributes to zebrafish heart regeneration.* Nature, 2013. **498**(7455): p. 497-501.
133. Mickoleit M, et al., *High-resolution reconstruction of the beating zebrafish heart.* Nature Methods, 2014. **11**(9): p. 919-22.
134. Thomas NA, et al., *Hedgehog signaling plays a cell-autonomous role in maximizing cardiac developmental potential.* Development, 2008. **135**(22): p. 3789-99.
135. Liebling M, et al., *Four-dimensional cardiac imaging in living embryos via postacquisition synchronization of nongated slice sequences.* Journal of Biomedical Optics, 2005. **10**(5).
136. Peralta M, et al., *The Epicardium in the Embryonic and Adult Zebrafish.* Journal of Developmental Biology, 2014. **2**(2): p. 101-116.
137. Arrenberg AB, et al., *Optogenetic control of cardiac function.* Science, 2010. **330**(6006): p. 971-4.
138. Riegel J, Mayer W, and van Havre Y. *FreeCAD*. 2002; Available from: www.freecadweb.org.
139. BJ, R., *Electrical Conductivity Values Used with the Bidomain Model of Cardiac Tissue.* IEEE TRANSACTIONS ON BIOMEDICAL ENGINEERING, 1997. **44**(4): p. 326-328.
140. Stinstra JG, Hopenfeld B, and Macleod RS, *On the passive cardiac conductivity.* Annals of biomedical engineering, 2005. **33**(12): p. 1743-51.
141. Clerc L, *Directional differences of impulse spread in trabecular muscle from mammalian heart.* The Journal of Physiology, 1976. **255**(2): p. 335-346.
142. Roberts DE, Hersh LT, and Scher AM, *Influence of cardiac fiber orientation on wavefront voltage, conduction velocity, and tissue resistivity in the dog.* Circulation, 1979. **44**(5): p. 701-12.
143. Roberts DE and Scher AM, *Effect of tissue anisotropy on extracellular potential fields in canine myocardium in situ.* Circulation, 1982. **50**(3).

144. Clayton, R.H., et al., *Models of cardiac tissue electrophysiology: Progress, challenges and open questions.* Progress in Biophysics and Molecular Biology, 2011. **104**(1–3): p. 22-48.
145. Johnston BM and Johnston PR, *Determining six cardiac conductivities from realistically large datasets.* Mathematical Biosciences, 2015. **266**: p. 15-22.
146. Bruce D, Pathmanathan P, and Whiteley JP, *Modelling the effect of gap junctions on tissue-level cardiac electrophysiology.* Electronic Proceedings in Theoretical Computer Science, 2012. **92**(2): p. 1-15.
147. Wang J, et al., *The regenerative capacity of zebrafish reverses cardiac failure caused by genetic cardiomyocyte depletion.* Development, 2011. **138**(16).
148. Potse M, et al., *A comparison of monodomain and bidomain reaction-diffusion models for action potential propagation in the human heart.* IEEE Trans Biomed Eng, 2006. **53**(12): p. 2425-35.
149. Lin E, et al., *Optical mapping of the lectrical activity of isolated adult zebrafish hearts - acute effects of temperature.* Am J Physiol Regul Integr Comp Physiol, 2014. **306**: p. 823-836.
150. Jensen B, et al., *Identifying the evolutionary building blocks of the cardiac conduction system.* PLoS One, 2012. **7**(9): p. e44231.
151. Sedmera D, et al., *Functional and morphological evidence for a ventricular conduction system in zebrafish and Xenopus hearts.* Am J Physiol Heart Circ Physiol, 2003. **284**(4): p. H1152-60.
152. Merletti R, et al., *Technology and instrumentation for detection and conditioning of the surface electromyographic signal: State of the art.* Clinical Biomechanics, 2009. **24**(2): p. 122-134.
153. Fish RM and Geddes LA, *Conduction of Electrical Current to and Through the Human Body: A Review.* Eplasty, 2009. **9**(44).
154. Gauza M and Kubisz L, *Electrical Conductivity of Fish Skin Collagen in the Temperature Range 290-380 K.* Acoustic and BIomedical Engineering, 2010. **118**.
155. Migliaro A, Caputi AA, and Budelli R, *Theoretical Analysis of Pre-Receptor Image Conditioning in Weakly Electric Fish.* PLoS Computational Biology, 2005.
156. Castagnola E, et al., *pHEMA Encapsulated PEDOT-PSS-CNT Microsphere Microelectrodes for Recording Single Unit Activity in the Brain.* Front Neurosci, 2016. **10**(151).
157. Tian HC, et al., *Enhanced Flexible Tubular Microelectrode with Conducting Polmer for Multi-Functional Implantable Tissue-Machine Interface.* Scientific Reports, 2016. **6**.
158. Abidan MR, et al., *Conducting-Polymer Nanotubes Improve Electrical Properties, Mechanical Adhesion, Neural Attachment, and Neurite Outgrowth of Neural Electrodes.* Biomaterials, 2010. **6**(3): p. 421-429.
159. Lu N, et al., *Metal films on polymer substrates stretched beyond 50%.* Applied Physics Letters, 2007. **91**(22).
160. Chung H, Joe YI, and Han H, *Effects of Thickness on the Residual Stress Behaviour of High Temperature Polyimide Films.* Polymer Journal, 2000. **32**(3): p. 215-221.
161. Mandal H, et al., *Improving the performance of poly(3,4-ethylenedioxythiophene) (PEDOT) for brain machine interface applications.* Acta biomaterialia, 2014. **10**(6).

162. Stinstra J, MacLeod R, and Henriquez C, *Incorporating histology into a 3D microscopic computer model of myocardium to study propagation at a cellular level.* Annals of Biomedical Engineering, 2010. **38**(4): p. 1399-414.
163. Costa MC, Silva PAA, and dos Santos RW, *Mind the Gap: A semicontinuum Model for Discrete Electrical Propagation in Cardiac Tissue.* IEE Transcations on Biomedical Engineering, 2016. **63**(4): p. 765-773.